DOT/FAA/AR-05/17

Office of Aviation Research
Washington, D.C. 20591

Fundamental Studies of Nickel Billet Materials—Engine Titanium Consortium Phase II

June 2005

Final Report

This document is available to the U.S. public
through the National Technical Information Service (NTIS),
Springfield, VA 22161.

U.S. Department of Transportation
Federal Aviation Administration

NOTICE

This document is disseminated under the sponsorship of the U.S. Department of Transportation in the interest of information exchange. The United States Government assumes no liability for the contents or use thereof. The United States Government does not endorse products or manufacturers. Trade or manufacturers names appear herein solely because they are considered essential to the objective of this report. This document does not constitute FAA certification policy. Consult your local FAA aircraft certification office as to its use.

This report is available at the Federal Aviation Administration William J. Hughes Technical Center's Full-Text Technical Reports page: actlibrary.tc.faa.gov in Adobe Acrobat portable document format (PDF).

Technical Report Documentation Page

1. Report No.	2. Government Accession No.	3. Recipient's Catalog No.
DOT/FAA/AR-05/17		

4. Title and Subtitle	5. Report Date
FUNDAMENTAL STUDIES OF NICKEL BILLET MATERIALS—ENGINE TITANIUM CONSORTIUM PHASE II	June 2005
	6. Performing Organization Code

7. Author(s)	8. Performing Organization Report No.
Frank Margetan[1], Edward Nieters[2], Pranaam Haldipur[1], Lisa Brasche[1], Thomas Chiou[1], Mike Keller[2], Andrei Degtyar[3], Jeff Umbach[3], Waled Hassan[4], Thadd Patton[2], Kevin Smith[3]	

9. Performing Organization Name and Address		10. Work Unit No. (TRAIS)
[1]Iowa State University Center for Nondestructive Evaluation Ames, IA 50011	[2]General Electric Cincinnati, Ohio	
[3]Pratt & Whitney East Hartford, Connecticut	[4]Honeywell Engines Phoenix, Arizona	11. Contract or Grant No. DTFA0398FIA029

12. Sponsoring Agency Name and Address	13. Type of Report and Period Covered
U.S. Department of Transportation Federal Aviation Administration Office of Aviation Research Washington, DC 20591	Final Report
	14. Sponsoring Agency Code ANE-110

15. Supplementary Notes

The FAA William J. Hughes Technical Monitor was Cu Nguyen.

16. Abstract

Nickel (Ni) alloys are used for their high-temperature strength properties in jet engine disks and other propulsion components. To ensure safe operation, typical Ni components are ultrasonically inspected to detect defects such as white spots, dirty white spots, and freckles. A fundamental understanding of the ultrasonic properties and their relationship to microstructural conditions is useful in design of optimal inspection parameters. The report provides details of such studies for IN718 and Waspaloy, the two most prevalent Ni alloys.

17. Key Words	18. Distribution Statement
Nickel billet, Ultrasonic inspection, Probability of detection	This document is available to the public through the National Technical Information Service (NTIS), Springfield, Virginia 22161.

19. Security Classif. (of this report)	20. Security Classif. (of this page)	21. No. of Pages	22. Price
Unclassified	Unclassified	230	

Form DOT F1700.7 (8-72) Reproduction of completed page authorized

TABLE OF CONTENTS

		Page
EXECUTIVE SUMMARY		xv
1.	INTRODUCTION	1-1
1.1	Purpose	1-1
1.2	Background	1-1
1.3	Program Objectives	1-2
1.4	Related Activities and Documents	1-2
2.	APPROACH	2-1
2.1	Alloy Selection and Sample Fabrication	2-1
2.2	Ultrasonic Property Measurements	2-1
2.3	Synthetic Inclusion Samples	2-2
2.4	Defect Characterization	2-2
3.	DISCUSSION	3-1
3.1	Ultrasonic Property Measurements of Billets and Correlation With Microstructure	3-1
3.1.1	Background and Specimen Selection	3-1
3.1.2	Preliminary UT Examinations of the Billet Strip Coupons	3-11
3.1.3	Methods Used for Detailed UT Property Measurements	3-25
3.1.4	Results of UT Property Measurements	3-48
3.1.5	Metallography Characterization and the Relationship Between UT Properties and Grain Size	3-64
3.2	Summary	3-89
4.	SYNTHETIC INCLUSION SAMPLES	4-1
4.1	Introduction	4-1
4.2	Synthetic Defects	4-1
4.3	Flat-Bottom Hole Block	4-6
4.4	Trial Seed Block Design	4-8
4.4.1	IN718-IN718 Interface	4-11
4.4.2	Freckle-IN718 Interface Defects	4-11
4.4.3	White Spot-IN718 Interface Defects	4-12

4.4.4 Dirty White Spot-IN718 Interface Defects 4-13

4.5 Final Block Design 4-14
4.6 Summary 4-20

5. CONCLUSIONS 5-1

6. REFERENCES 6-1

APPENDICES

A—Defect Characterization of Naturally Occurring Anomalies
B—Ultrasonic Data Acquisition Procedure for ETC Real Defects

LIST OF FIGURES

Figure		Page
3-1	Typical Production of Ni Alloy Billets Used for Fabricating Rotating Jet Engine Components	3-2
3-2	Noise Banding and UT Property Variations in a 6″ Diameter Ti-6-4 Billet	3-3
3-3	Coupon Layout for 10″ Diameter Ni Alloy Billets	3-4
3-4	C-Scan Image of Backscattered Noise for Zone 2 of the IN718 V-Die Billet	3-6
3-5	Average Noise Levels in the Multizone Inspections of Four Ni Alloy Billets	3-7
3-6	Degree of Noise Banding in the Multizone Inspections of Four Ni Alloy Billets	3-8
3-7	C-Scan Image of Backscattered Noise for Zone 3 of the 12″ Long IN718 GFM Billet	3-9
3-8	C-Scan Image of Backscattered Noise for Zone 5 of the 40″ Long Waspaloy Billet	3-9
3-9	Stamped Markings Used to Label the Surfaces of the Ni Billet Strip Coupons	3-10
3-10	Volume Determination for Ni Billet Strip Coupons	3-11
3-11	Experimental Setups Used to Measure (a) Back-Wall Amplitude and TOF and (b) Backscattered Grain Noise Amplitude	3-12
3-12	Back-Wall TOF C-Scan Images for the V-Die-B Strip Coupon	3-13
3-13	Back-Wall Amplitude C-Scan Images for the Waspaloy Strip Coupon	3-14
3-14	Back-Wall Amplitude C-Scan Images for the GFM-A Strip Coupon	3-14
3-15	Back-Wall Amplitude C-Scan Images for the V-Die-A Strip Coupon	3-15
3-16	Back-Wall Amplitude C-Scan Images for the V-Die-B Strip Coupon	3-15
3-17	Rescaled C-Scan Images of Back-Wall Echo Amplitude for Axial (Side 2) and Hoop (Side 3) Inspections of the Four Ni Billet Strip Coupons	3-17
3-18	Dependence of Average Back-Wall Amplitude on Radial Position in the Four Ni Billet Strip Coupons	3-17
3-19	Backscattered Noise C-Scan Images for the Waspaloy Strip Coupon	3-19
3-20	Backscattered Noise C-Scan Images for the GFM-A Strip Coupon	3-19

3-21	Backscattered Noise C-Scan Images for the V-Die-A Strip Coupon	3-20
3-22	Backscattered Noise C-Scan Images for the V-Die-B Strip Coupon	3-20
3-23	Construction of Radial Profiles of Backscattered Grain Noise	3-21
3-24	Dependence of Backscattered Noise on Radial Position for Each of the Four Strip Coupons, Relative to a #1 FBH at the Same Depth (0.5″) in the IN100 Reference Block	3-22
3-25	Comparison of Backscattered Noise C-Scans and Back-Wall Amplitude C-Scans for the GFM-A Strip Coupon	3-23
3-26	The Five Sites on a Given Strip Coupon Where Detailed UT Property Measurements Were Made	3-24
3-27	Cutting and Labeling Protocols for the Ni Alloy Strip Coupons, Illustrated for the GFM-A Billet Strip	3-24
3-28	Setup for UT Velocity Measurements Using the Successive Back-Surface Reverberations Observed at a Fixed Measurement Site	3-26
3-29	(a)-(b) A-Scans Showing the Front-Wall (Truncated) and First Three Back-Wall Echoes for the Slice Coupons From the Centers of the Waspaloy and GFM-A Billets and (c)-(d) Overlap of the First Two Back-Wall Echoes After the Second Has Been Increased in Amplitude and Time Shifted	3-26
3-30	Results of Sound Velocity Measurements Performed on the Waspaloy Strip Coupon Before Slicing	3-27
3-31	The Two Methods Used for L-Wave Attenuation Versus Frequency Measurements	3-28
3-32	Computed Radiation Patterns for the Sonic Beam From a 0.25″ Diameter Transducer at Four Frequencies of Interest	3-30
3-33	Attenuation Measurement for Axial Sound Propagation at the Center of the IN718 GFM-A Billet Strip Coupon	3-31
3-34	Attenuation Measurement for Axial Sound Propagation at the Center of the Waspaloy Billet Strip Coupon	3-32
3-35	Measured Attenuation Values in the 5-15 MHz Range at the Five Sites in the GFM-A Billet Strip	3-34
3-36	Deduced Attenuation Values at Various Sites for Axial and Hoop Propagation in the (a) Waspaloy and (b) IN718 GFM-A Strip Coupons	3-35

3-37 Power-Law Fits to Measured Attenuation Values at Two Locations in the IN718 GFM-A Billet Specimen 3-36

3-38 Power-Law Fits to Measured Attenuation Values at Two Locations in the Waspaloy Billet Specimen 3-36

3-39 Immersion Setup for Grain Noise FOM Measurement 3-37

3-40 (a) The Independent Scatterer Noise Model Neglects Grain Noise Contributions From Multiple-Scattering Events and (b) Relationship Between the Average Measured Noise Spectrum and Various Microstructure and Measurement System Factors in the Noise Model 3-39

3-41 (a) Root Mean Square Noise Levels Measured at Five Sites in the GFM-A IN718 Billet (Axial Propagation), and Time Gates Used for FOM Determination and (b) Deduced FOM Values for Selected GFM-A Cases Using the Principal Time Gate (G7) 3-40

3-42 (a) Root Mean Square Noise Levels Measured at Five Sites in the Waspaloy Billet (Axial Propagation) and Time Gates Used for FOM Determination and (b) Deduced FOM Values for Selected Waspaloy Cases Using the Principal Time Gate (G7) 3-42

3-43 Grain Noise FOM Values for Axial Propagation at the Center of the GFM-A IN718 Billet Deduced Using the Seven Time Gates Indicated in Figure 40(a) 3-43

3-44 Measured and Predicted rms Grain Noise Levels for Axial Beam Propagation at the Center of the IN718 GFM-A Billet 3-44

3-45 Additional FOM Measurements and Analyses at the Center of the IN718 GFM-A Billet Specimen 3-45

3-46 Examples of Local Linear Fits Used to Determine the Best Estimate of the Grain Noise FOM at 7.5 MHz 3-46

3-47 Comparison of Measured FOM and Attenuation Values at 7.5 MHz for the GFM IN718 Billet 3-47

3-48 Comparison of Measured FOM and Attenuation Values at 7.5 MHz for the Waspaloy Billet 3-48

3-49 Measured Longitudinal-Wave Sound Velocities as Functions of Radial Depth in the Billet 3-51

3-50 Measured Attenuation Values at 7.5 MHz for the Ni Alloy Billet Specimens 3-57

3-51 Measured Grain Noise FOM Values at 7.5 MHz for the Ni Alloy Billet Specimens 3-58

3-52	Correlation Between Backscattered Noise FOM and Attenuation	3-59
3-53	Predicted Attenuation-Versus-Frequency Curves and Associated Power-Law Fits for Pure Ni Microstructures Having Average Grain Diameters of 10, 20, and 30 Microns	3-61
3-54	Predicted Relationship Between the Average Grain Diameter, the Attenuation at 7.5 MHz, and the Exponent in the Power-Law Fit to the Attenuation-Versus-Frequency Curve for Pure Ni Microstructures	3-61
3-55	Predicted FOM-Versus-Frequency Curves for Pure Ni Microstructures Having Average Grain Diameters Ranging From 10 to 100 Microns	3-62
3-56	Relationship Between FOM and Attenuation at 7.5 MHz	3-62
3-57	Predicted Behavior of the Absolute Grain Noise Level Seen at Three Depths in Pure Ni as a Function of Mean Grain Diameter	3-63
3-58	Metallography Coupons	3-65
3-59	Axial View of Microstructure at the Center (0″) of the Waspaloy Billet	3-65
3-60	Axial, Radial, and Hoop Views of the Waspaloy Microstructure at Four Metallography Sites	3-66
3-61	Radial Views of the IN718 GFM-A Microstructure at Two Sites	3-66
3-62	Example of Processing a Grain Structure	3-67
3-63	(a) Micrograph Subsection With Several Presumed Twin Boundaries Identified and (b) Boundaries Ignored in the Final Digitized Image	3-67
3-64	Mean Chord Length Method for Determining Average Grain Diameter	3-69
3-65	P(L) Method for Determining Average Grain Diameter	3-69
3-66	Examples of Exponential Fits to Measured P(L) Curves for a Typical Case	3-70
3-67	Effect of Twin Grain Treatment on Deduced Mean Diameter	3-77
3-68	Comparisons of Average Grain Diameters in the X and Y Directions of Ni Alloy Micrographs Using the MCL Method	3-77
3-69	Comparisons of Average Grain Diameters in the 12 V-Die-B Micrographs as Estimated Using the MCL and P(L) Methods	3-78
3-70	Comparisons of Average Grain Diameters as Estimated by the MCL and P(L) Methods for Each of the 4 x 12 Micrographs Analyzed	3-79

3-71	(a) Locations and Designations of the 12 Original Metallography Coupons From Each Rough-Cut Specimen and (b) Locations and Shapes of the four New Metallography Coupons for V-Die-A	3-80
3-72	Local Microstructures of the Four New Metallography Coupons From the V-Die-A Rough-Cut Slab	3-80
3-73	Backscattered Grain Noise C-Scans of the GFM-A Strip Coupon and Metallography Slab	3-82
3-74	Backscattered Grain Noise C-Scans of the V-Die-A Strip Coupon and Metallography Slab	3-83
3-75	Backscattered Grain Noise C-Scans of the V-Die-B Strip Coupon and Metallography Slab	3-83
3-76	Best Estimates of Grain Diameters Versus Radial Position	3-84
3-77	Relationship Between Average Grain Diameter and Measured Attenuation (at 7.5 MHz) for Each of the Four Strip Coupons	3-85
3-78	Relationship Between Average Grain Diameter and Measured Noise FOM (at 7.5 MHz) for Each of the Four Strip Coupons	3-86
3-79	Example of Determining IN718 Single-Crystal Elastic Constants by Fitting to Measured Velocity and Attenuation Data	3-88
4-1	Microstructure of White Spot Casting	4-3
4-2	Microstructure of White Spot Forging	4-3
4-3	Microstructure of Freckle Ingot	4-4
4-4	Microstructure of Freckle Forging, Exhibiting Refinement Due to Forging	4-4
4-5	Microstructure of Dirty White Spot Button	4-5
4-6	Microstructure of Dirty White Spot Forging	4-5
4-7	#1 FBH IN718 Block Design	4-7
4-8	Ultrasonic C-Scan of #1 FBH IN718 Block	4-8
4-9	Trial Block Design	4-9
4-10	Ultrasonic C-Scans of Trial Blocks	4-10
4-11	IN718 to IN718 Bond Line in the Dirty White Spot Test Block	4-11

4-12	Bond Between Freckle Seed 1 and IN718	4-12
4-13	Detail of Bond Line Between Freckle Seed 2 and IN718 Showing Small Discontinuities	4-12
4-14	Large Grain Structure of White Spot Seed 1	4-13
4-15	IN718 and White Spot Seed 2 Interface	4-13
4-16	IN718 Dirty White Spot 6 Bond Line in Which Large Ceramic Particles Create a Nonbonded Region Greater Than 0.5 mm Long	4-14
4-17	Dimensions and Seed Map for the Dirty White Spot Synthetic Seed Block	4-15
4-18	Dimensions and Seed Map for the Freckle Synthetic Seed Block	4-16
4-19	Dimensions and Seed Map for the White Spot Synthetic Seed Block	4-17
4-20	A 10-MHz F/7 C-Scan of Blocks Containing Synthetic Defects	4-19
4-21	A 10-MHz C-Scan of Blocks With Synthetic Defects After Second HIP	4-20

LIST OF TABLES

Table		Page
1-1	Typical Ni-Based Alloys Used in Rotating Components of Aircraft Engines	1-1
3-1	Multizone Inspection Parameters for 10″ Diameter Billet	3-5
3-2	Dimension, Mass, and Density Values for Ni Billet Strip Coupons	3-11
3-3	Approximate Upper Frequency Limit for Trustworthy Attenuation Measurements as a Function of the Material Attenuation Near 8 MHz	3-33
3-4	Results of Longitudinal-Wave Sound Velocity Measurements	3-50
3-5	Results of Shear-Wave Sound Velocity Measurements	3-52
3-6	Summary of Measured Attenuation Values for the Ni Alloy Billet Specimens	3-53
3-7	Summary of Measured Grain Noise FOM Values for the Ni Alloy Billet Specimens	3-55
3-8	Ranges of Attenuation and FOM Values Measured Within Each of the Ni Alloy Billet Strip Coupons	3-58
3-9	Summary of Grain-Sizing Analyses for One Micrograph of Metallography Coupon C of the GFM-A Specimen	3-71
3-10	Average Grain Diameters Deduced From Waspaloy Metallography	3-72
3-11	Average Grain Diameters Deduced From GFM-A Metallography	3-73
3-12	Average Grain Diameters Deduced From V-Die-A Metallography	3-74
3-13	Average Grain Diameters Deduced From V-Die-B Metallography	3-75
3-14	Best Estimates of Average Grain Diameters at Radial Sites in the Four Ni Alloy Metallography Slabs	3-79
3-15	Best Estimates of Average Grain Diameters at Radial Sites in the V-Die-A Metallography Slab	3-81
3-16	Preliminary Values of Deduced Single-Crystal Elastic Constants for the V-Die-B, GFM-A, and Waspaloy Billet Specimens	3-89
4-1	Compositions, in Weight Percent, of Synthetic Defects	4-2
4-2	Results of UT Velocity Measurements on Rectangular Coupons of Synthetic Ni Billet Defect Material	4-6

4-3 Anomalous Indications From IN718 Trial Blocks 4-10

4-4 Seed Types and Dimensions for Synthetic Blocks 4-18

4-5 Synthetic Seed Dimensions and Sound Velocities 4-19

LIST OF ACRONYMS

2D	Two-dimensional
EB	Electric beam
EDM	Electron discharge machining
ESR	Electroslag remelting
ETC	Engine Titanium Consortium
FAA	Federal Aviation Administration
FBH	Flat-bottom hole
FOM	Figure of merit
FQ	Fused quart
FSH	Full-screen height
GE	General Electric
GFM	Gesellschaft fur Maschinenbau-und-Fertigungstechnik
IFPP	Ideal focus piston probe
ISU	Iowa State University
MCL	Mean chord length
N/cm	Nepers per centimeter
Ni	Nickel
OD	Outer diameter
P&W	Pratt & Whitney
PoD	Probability of Detection
RF	Radio frequency
rms	Root mean square
SHA	Synthetic hard alpha
SMPC	Specialty Metals Processing Consortium
SNR	Signal-to-noise ratio
Ti	Titanium
TOF	Time-of-flight
UT	Ultrasonic
VAR	Vacuum arc melting

EXECUTIVE SUMMARY

Selection of engine materials is a balance between the ability to operate at temperature, adequate creep, fatigue, and strength properties, and acceptable weight. The primary materials considered for modern-day rotating components are titanium (Ti) alloys, valued for their lower weight but limited to intermediate temperature ranges, and nickel (Ni) alloys, higher-temperature materials with better damage tolerance properties but also heavier. Phase I of the Engine Titanium Consortium (ETC) research focused on Ti, particularly Ti-6Al-4V, and the detection of hard alpha defects. In Phase II, ETC extended this focus to include Ni-based alloys, which serve as the primary alloy in turbine and compressor disks. Extensive materials property data exists for Ni alloys, as is also the case for Ti materials. However, fundamental data relating microstructural features to inspectability are not available. Given the importance of understanding the relationship between material properties and inspectability, this program set about generating data for typical alloys used in commercial jet engines.

The steps to inspection implementation include gathering base material property data, defect characterization, and application of this knowledge to inspection development. Several melt-processing approaches and billet conversion practices are used by the industry, and samples were selected that are representative of these variations. Ni alloys such as IN718 (cast/wrought), IN901 (cast/wrought), Waspaloy (cast/wrought), IN100 (powder metal), and R95 (powder metal) are used extensively in high-temperature jet engine applications. Multiple defect types can exist in forged alloys, including dirty white spots, clean white spots, segregation, and slag. Defect types found in powder alloys include ceramic particles, porosity, and powder lot anomalies. This program generated inspection property data for the two most common alloys, IN718 and Waspaloy.

In cooperation with the Specialty Metals Processing Consortium, several naturally occurring defects were characterized using ultrasonics and metallography. These results assist the inspection community in understanding flaw morphology and its relationship to inspectability. They also provide valuable information to the lifing community for consideration in design and life management. While information about natural defects is valuable, benefit also comes from the ability to measure signal response from control samples. Processes to develop synthetic defects in Ni alloys were also completed and representative samples were fabricated. The key accomplishments from the program are listed below.

- Ultrasonic velocity was found to be relatively uniform for a given alloy. Since sonic velocity influences the ultrasonic beam radiation pattern, sizeable velocity variations can shift the focal depth and impact detectability. Given the uniformity of velocity measurements for IN718 and Waspaloy, it is unlikely that velocity variations will cause noticeable affects on detectability for these alloys.

- In contrast to velocity, attenuation and backscattered grain noise capacity were found to vary significantly with frequency and position. Attenuation and grain noises were highly correlated, i.e., billet regions of high attenuation also were found to have high grain noise capacity. Attenuation and noise capacity values were generally found to be larger in Waspaloy than in IN718.

- Grain size is the predominant factor controlling noise and attenuation in the Ni alloys studied in this program. In Ni processing, there is a significant amount of recrystallization that occurs due to the mechanical working of the billet during the conversion process. This leads to approximately equiaxed grains as determined by metallographic characterization performed during the program. As the mean grain size increased, the attenuation and grain noise capacity were also found to increase.

- Billet conversion practice was also found to affect the attenuation and grain noise characteristics of the alloys studied. Values of both properties were found to be lower for V-Die processing than for GFM (Gesellschaft fur Maschinenbau-und-Fertigungstechnik) processing.

- At a given location in a billet, attenuation and grain noise were found to be approximately isotropic with little difference between the axial, radial, and hoop directions.

- Methods to produce synthetic defects with similar chemistries to naturally occurring defects were developed, and several specimens were fabricated that contain so-called white spot, dirty white spot, and freckle defects.

1. INTRODUCTION.

1.1 PURPOSE.

Nickel (Ni) alloys such as IN718 (cast/wrought), IN901 (cast/wrought), Waspaloy (cast/wrought), IN100 (powder metal), and R95 (powder metal) are used extensively in high-temperature jet engine applications. Multiple defect types exist in forged alloys, including dirty white spots, clean white spots, segregation, and slag. In powder alloys, defect types include ceramic particles, porosity, and powder lot anomalies [1]. Typically, dirty white spots contain a microstructure of Nb-lean alloy with fine oxides and nitrides. Typical freckle segregation consists of Nb-rich regions in billets that produce undesirable, brittle phases. Slag defects are Ca-rich ceramic phases originating from the electroslag remelting (ESR) melting step and result from poor ingot surface preparation. An analysis of the acoustic properties of these materials and defect types will facilitate improvements to current Ni billet inspections as well as provide data for analysis of the probability of detection (PoD) of the inspections for various defect types.

1.2 BACKGROUND.

Selection of engine materials is a balance between the ability to operate at temperature, adequate creep, fatigue, and strength properties, and acceptable weight. For the fabrication of modern-day rotating components, two classes of materials are principally used: (1) titanium (Ti) alloys, which are valued for their lower weight but have limited intermediate temperature ranges and (2) Ni alloys, which are heavier but can operate at higher temperatures, and have operated at these higher temperatures, with better damage tolerance properties. Phase I of the Engine Titanium Consortium (ETC) focused on Ti, particularly Ti-6Al-4V, and the detection of hard alpha defects. In Phase II, ETC extended this focus to include Ni-based alloys. Typical Ni-based alloys are listed in table 1-1.

TABLE 1-1. TYPICAL Ni-BASED ALLOYS USED IN ROTATING COMPONENTS OF AIRCRAFT ENGINES

Alloy	Composition	Typical Usage
IN718	Ni-19Fe-19Cr-5Nb-3Mo-0.5Al-1Ti-0.1C-0.006B	Turbine disks, final stage compressor disks
IN901	43Ni-35Fe-13Cr-6Mo	High-pressure compressor
Waspaloy	56Ni-19Cr-14Co-4Mo	High-pressure compressor
IN100	60Ni-15Co-10Cr-5Al-5Ti	Turbine disks
Rene 95	Ni-13Cr-8 Co-3.5Mo-2.5Ti-3.5 Al-3.5 W-3.5 Nb-.06 C-.05 Zr-.01 B	Turbine disks

Extensive materials property data exists for these Ni alloys as it does for Ti materials. However, fundamental data relating microstructural features to inspectability are not available. The steps to inspection implementation include gathering base material property data, defect characterization, and application of this knowledge to inspection development. Several melt-processing approaches are used by the industry and consideration was given to choosing samples that address the broad classes of material processing in the industry.

1.3 PROGRAM OBJECTIVES.

- To establish the basic ultrasonic (UT) properties of Ni-based alloy billet materials and relevant inclusions as an appropriate foundation for selection of UT inspection approaches.

- To manufacture and characterize flat-bottom hole (FBH), synthetic inclusion, and real defect standards to provide data for determining defect detectability and developing improved inspections.

- To improve the understanding of the relationship of defect size, shape, and composition on defect detectability in Ni alloys.

1.4 RELATED ACTIVITIES AND DOCUMENTS.

The ETC was established in 1993 and includes Iowa State University (ISU), General Electric Aircraft Engines, Honeywell Engines Systems and Services, and Pratt & Whitney (P&W) in a partnership to perform research that contributes to improvements in flight safety. The Phase I program, which was completed in 1998, led to improvements in production inspection of Ti billet [2], improved physics models for UTs [3 and 4], and a feasibility study for phased array for UT inspection of billets [5]. In-service inspection efforts led to a commercially available portable scanner [6] and eddy-current probes [7] as well as improved probe designs [8] and eddy-current probe design tools [9]. Considerable progress was also made in developing a new approach [10] to quantifying inspection performance as reported in the Federal Aviation Administration (FAA) report "A Methodology for the Assessment of the Capability of Inspection Systems for Detection of Subsurface Flaws in Engine Components" [11].

The technical approach of the ETC Phase I program included the characterization of material properties, which impact inspectability and the subsequent use of that information in inspection design. Ti alloys typically suffer from UT noise, which implies a lower signal-to-noise ratio (SNR) and can lead to false indications or missed flaws. Full details of this study are provided in the final report for the program. Key accomplishments of the ETC Phase I program were as follows:

- Synthetic hard alpha (SHA) material, essentially Ti-N-O alloys, can be manufactured by either powder metallurgical or arc-melting techniques. Batches of such SHA material with nitrogen contents ranging from 1.5 to 16.2 wt.% were made for basic property measurements and for insertion as defects into HIPped test specimens.

- The UT reflectance of a hard alpha inclusion in a Ti alloy host depends on the difference in impedance (product of sound velocity and density) between the two materials. For each 1 wt.% increase in nitrogen content, the longitudinal sound speed of SHA increases by about 3% and the density increases by 1%. The reflectance of hard alpha in a Ti alloy host rises approximately linearly from zero at 0 wt.% N to 0.14 at 10 wt.% N.

- Uncracked, cylindrically shaped SHA inclusions in Ti alloy host material could be imaged and detected with compositions as low as 1.5 wt.% N. The SNR for such inclusions rose linearly as the nitrogen content was increased.

- Ti alloys are ultrasonically anisotropic within a single metal grain or within a colony of aligned grains. A plate of Ti-6-4 alloy with very large alpha-grain colonies was produced to study this anisotropy. The minimum longitudinal sound velocity (0.6063 cm/μs) was measured in a colony whose hexagonal symmetry axis was perpendicular to the direction of sound propagation. The maximum sound velocity (0.6712 cm/μs) was measured for propagation parallel to the symmetry axis. The anisotropy in longitudinal sound velocity in Ti-6-4 was roughly twice that reported for pure Ti.

- The above study of velocity anisotropy in the enlarged grain block suggests that uncracked hard alpha inclusions with compositions less than 3 wt.% N might not be detectable if present in a region of large alpha colonies. Based on the measured velocities, the UT reflectance at the boundary between two alpha-Ti colonies can be as high 0.051. This value exceeds the typical reflectance of uncracked hard alpha inclusions with less than 3 wt.% N (see bullet 2 above). Thus, signals from such inclusions could be masked by UT grain-boundary echoes.

- UT property measurements were carried out on rectangular coupons cut from representative Ti-17 and Ti-6-4 billets and forgings. Longitudinal wave velocity, attenuation, and backscattered noise figure of merit (FOM) were systematically measured for the radial, axial, and hoop propagation directions in 14 coupons labeled A-N. Additional measurements using these and a dozen other specimens were then made to further investigate the effects of Ti microstructure on UT inspections.

- For a given coupon, all measured properties showed a dependence on propagation direction. This dependence was generally greatest for backscattered noise, less (but still large) for attenuation, and smallest for velocity. There were also large noise and attenuation differences between coupons from different sources.

- Attenuation and backscattered noise depended strongly on frequency (f), while velocity did not. If the dependence on frequency is approximated as a power function, cf^p, then for attenuation, p typically ranged from 1 to 2, and for noise FOM, p typically ranged from 0.5 to 1.5.

- Attenuation and backscattered noise exhibited opposite dependencies on propagation direction within a given coupon. Attenuation was highest and noise FOM was lowest when sound propagated parallel to macrograin elongation (billets) or flow lines (forgings). Conversely, attenuation was lowest and noise highest for propagation perpendicular to macrograins or flow lines.

- Beam-mapping measurements revealed that the Ti microstructure could cause significant distortion of the sonic amplitude and phase profiles. These distortions were worse for propagation along macrograins and worse at higher frequencies. They affected all types of UT measurements.

- When beam distortions were large, there were significant fluctuations in the UT signal amplitudes of nominally identical reflectors. In addition, different methods for measuring attenuation yielded different results. For example, the average attenuation of back-surface echoes was larger than that expected due to energy loss alone and different from the attenuation deduced from FBH echoes.

- In current billet inspection procedures, 5-MHz transducers are used and the sonic beam travels radially inward, perpendicular to the columnar macrograins. Thus, the effects of beam distortion on the inspection are generally modest. However, beam distortion effects may significantly degrade inspections at higher frequencies, particularly Ti forging inspections at locations where the sound beam is not perpendicular to the flow lines.

- Some models for predicting backscattered noise attributes assume Gaussian noise statistics at each fixed observation time. The noise measurements indicate that these models should be applicable to 5-MHz Ti billet inspections. One such model was in fact used for detection reliability studies by the ETC PoD subtask.

Alloy selection for jet engine applications is dictated by operational parameters such as temperature, stress, and environment. Operational requirements for jet engine alloys are some of the most stringent, placing critical demands on the integrity and purity of both Ni and Ti alloys. The Specialty Metals Processing Consortium (SMPC) was established to improve melting practices and other manufacturing processes associated with the production of jet engine materials. Details of their work are available from Sandia National Laboratories [12].

2. APPROACH.

The approach for this research effort included the following:

- Alloy selection and sample fabrication
- UT property measurements
- Synthetic inclusion samples
- Defect characterization

2.1 ALLOY SELECTION AND SAMPLE FABRICATION.

Two alloys were selected for fundamental property measurements. The most widely used alloy, IN718, was selected to receive the primary focus, and it was decided that a more limited sample set would be generated for Waspaloy. Waspaloy was selected because it tends to exhibit higher levels of UT backscattered noise and, therefore, would offer an opportunity to study a material that is traditionally more difficult to inspect. The sequence of manufacturing the properties specimens and the specimen configuration was planned to yield as much data as possible on properties as a function of depth and orientation.

2.2 ULTRASONIC PROPERTY MEASUREMENTS.

Using rectangular coupons cut from Ni alloy billets, baseline UT properties (velocity, attenuation, and backscattered noise) were measured to determine the impact of properties on inspectability. In Phase I, the UT properties of Ti billets were found to vary with position, and similar variations were expected in Ni alloy billets and forgings. The selection of representative Ni billets to serve as sources for property measurement specimens was based on an initial screening inspection. The grain noise-banding patterns observed in the screening inspections were then used to select the locations where rectangular property measurement coupons were cut. This guaranteed that billet coupons with a range of representative microstructures would be studied.

The sequence for manufacturing and using the property measurement coupons was planned to yield as much data as possible on the variation of UT properties with radial depth and orientation. Strip-like coupons were initially cut along billet diameters and used to survey UT properties for beam propagation in the axial and hoop directions. The strip-like coupons were later cut into smaller slices to facilitate measurements in the radial direction. UT velocity, attenuation, and backscattered noise capacity were measured using the same methods developed in Phase I for Ti specimens. These measurements on billet coupons allowed the team to assemble a more comprehensive picture of UT property variations within representative billets and to better understand the effect of these variations on inspectability. In addition to the UT measurements, metallographic studies were performed and average grain diameters were deduced from optical micrographs. The grain size data were then correlated with the measured UT properties.

2.3 SYNTHETIC INCLUSION SAMPLES.

Synthetic inclusions were embedded into Ni test standards for the purpose of evaluating the inspection sensitivity of UTs on melt-related defects. Public literature [1] of metallurgical analysis on the naturally occurring defects was used to identify the candidate inclusion types for sample manufacture. Construction methods were developed at General Electric (GE) Corporate Research and Development to chemically manufacture the synthetic inclusions and to embed the inclusions into Ni alloy test blocks. After the successful development of synthetic inclusion manufacturing methods, three blocks containing synthetic inclusions of different geometry and composition were manufactured. The types of inclusions were determined by the team based on the ability to manufacture the synthetic inclusions, the criticality of the defect to part life, and the sensitivity of the inspection to the composition and geometry of the defect type. The team ultrasonically evaluated the synthetic inclusion samples to determine the sensitivity of the inspections for detecting and characterizing melt-related defects.

2.4 DEFECT CHARACTERIZATION.

Samples were also acquired with real defects in cooperation with SMPC, reflecting both vacuum induction melting (VIM)/vacuum arc melting (VAR) and VIM/ESR/VAR material defects in IN718 and Waspaloy. The initial effort will focus on evaluation of natural defects to establish typical compositions and properties and their detectability. Five samples were evaluated using a limited UT characterization and a simplified metallographic process. UT measurements were performed at two stages: original samples prior to sectioning and defects machined to regular shapes.

3. DISCUSSION.

3.1 ULTRASONIC PROPERTY MEASUREMENTS OF BILLETS AND CORRELATION WITH MICROSTRUCTURE.

3.1.1 Background and Specimen Selection.

3.1.1.1 Background.

As part of the ongoing effort to quantify and improve inspection practices, the ETC investigated the UT properties of Ni alloy, cylindrical billets used in the fabrication of rotating jet engine components. A primary goal of the Fundamental Studies was to determine, for representative 10″ diameter billets, the manner in which the UT inspection properties depended on position, inspection direction, and frequency. The inspection properties of interest were the density and the sonic velocity, attenuation, and backscattered grain noise capacity. These properties influence UT inspections in a direct manner. For a given transducer and billet diameter, the density, sonic velocity, and attenuation determine the shape and strength of the incident pressure field within the billet and, thus, directly influence the amplitude of the echo from an internal defect. The backscattered noise capacity then determines the average strength of the grain-boundary echoes that can mask or obscure the defect echo.

This section summarizes the methods and results of the Ni billet survey study. The review of the specimen selection begins with the cutup procedures used to obtain rectangular coupons for property measurements. The various UT measurement techniques are then reviewed and representative results are shown. The UT measurements themselves fall into two classes. In preliminary work, C-scans of back-surface amplitude, back-surface time-of-flight (TOF), and backscattered grain noise amplitude were performed to determine the degree of property variability with position and inspection direction. Careful measurements of velocity, attenuation, and grain noise capacity were then made at selected sites, with site locations based on the earlier C-scans. After summarizing the results of these more-detailed UT property measurements, two complementary metallographic analyses used to estimate average grain diameters at the UT measurement sites are discussed. The correlations between mean grain diameter, UT attenuation, and UT backscattering are then discussed. Experimental results are also compared to model predictions for simple microstructures consisting of equiaxed, randomly oriented, pure Ni crystallites. An approach for using the combined UT and metallographic data to estimate the single-crystal elastic constants of IN718 and Waspaloy is discussed next. Finally, a summary of the findings and their implications for billet inspections is presented.

Currently, most Ni alloy billet inspections are performed using 5-MHz transducers. In the future, if greater inspection sensitivity is desired, it may be advisable to increase the frequency to take advantage of the greater focusing ability of higher-frequency transducers. UT attenuation and backscattered noise capacity are strongly frequency-dependent, with both quantities tending to rise as the frequency is increased. In the Ni alloy survey study, it was endeavored to measure these quantities within the frequency range of greatest present and future interest, namely, from about 5 to 12.5 MHz. The manner in which attenuation and noise capacity depend on frequency will be shown explicitly for selected cases. To illustrate the manner in which attenuation and noise capacity vary with billet position and inspection direction, graphical results will be shown

for a fixed inspection frequency, typically 7.5 MHz. Results for other frequencies (5, 10, and 12.5 MHz) are presented in tabular form and have similar dependencies on billet position and inspection direction as the 7.5 MHz results (see section 3.1.4.2).

3.1.1.2 Specimen Selection.

Ni alloy material intended for the fabrication of rotating jet engine components generally begins as a cast ingot. As illustrated in figure 3-1, the initial ingot, which may have a rectangular or cylindrical cross section, was subjected to mechanical-working processes that result in a reduced diameter cylindrical billet. Although the final billet shape has cylindrical symmetry, the UT properties of the billet do not share this symmetry even if the cast ingot is cylindrical. This is because the billet is generally rotated in fixed increments, rather than continuously, when mechanical working is done. The UT properties are dependent, to some extent, on the mechanical-working history, and the lack of cylindrical symmetry during working leads to noncylindrically symmetric UT properties.

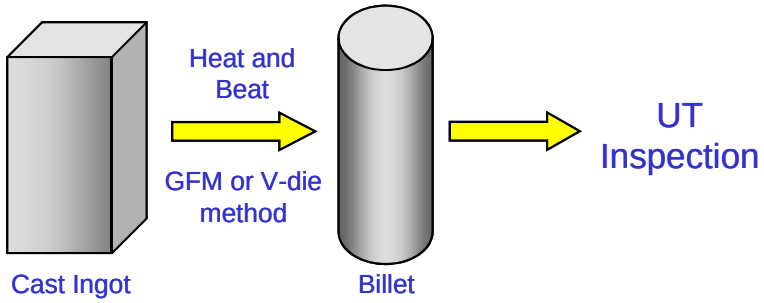

FIGURE 3-1. TYPICAL PRODUCTION OF Ni ALLOY BILLETS USED FOR FABRICATING ROTATING JET ENGINE COMPONENTS

UT property measurements are most easily carried out on rectangular specimens. The Ti billet research conducted during ETC Phase I provided guidance for choosing a scheme for cutting rectangular coupons from Ni alloy billets [13-19]. An example of UT property variations in cylindrical Ti billets is illustrated in figure 3-2, in this case, for a 6″ diameter Ti-6-4 billet. Panel 3-2(a) displays the backscattered grain noise pattern that was seen when an axial-cylindrical scan of the specimen was made using a 5-MHz, bicylindrically focused (multizone) transducer, and the resulting gated-peak noise amplitude was displayed as a function of scan position. Prominent bands of high and low backscattered noise amplitude are seen. As shown in panel 3-2(b), two sets of coupons were cut from the billet for property measurements. Each set of three coupons was cut along a radius of the billet, one set from a region having a low-noise amplitude near the outer diameter (OD) (at 1″ depth) and the other set having a high-noise amplitude near the OD. For sonic beam propagation in the radial direction, figure 3-2(c) shows measured longitudinal wave speeds, attenuations, and FOM values for each coupon. The FOM is a measure of the noise generation capacity of the microstructure that (ideally) is a property of the microstructure alone and independent of the details of the measurement procedure [20-22]. One sees that the UT properties vary significantly throughout the billet, and that the differences are greatest near the OD. It is important to note that changes in velocity and attenuation values are well correlated

with changes in backscattered noise capacity. This indicates that the backscattered noise patterns that are seen in routine inspections can be used to identify coupon sites with differing UT properties.

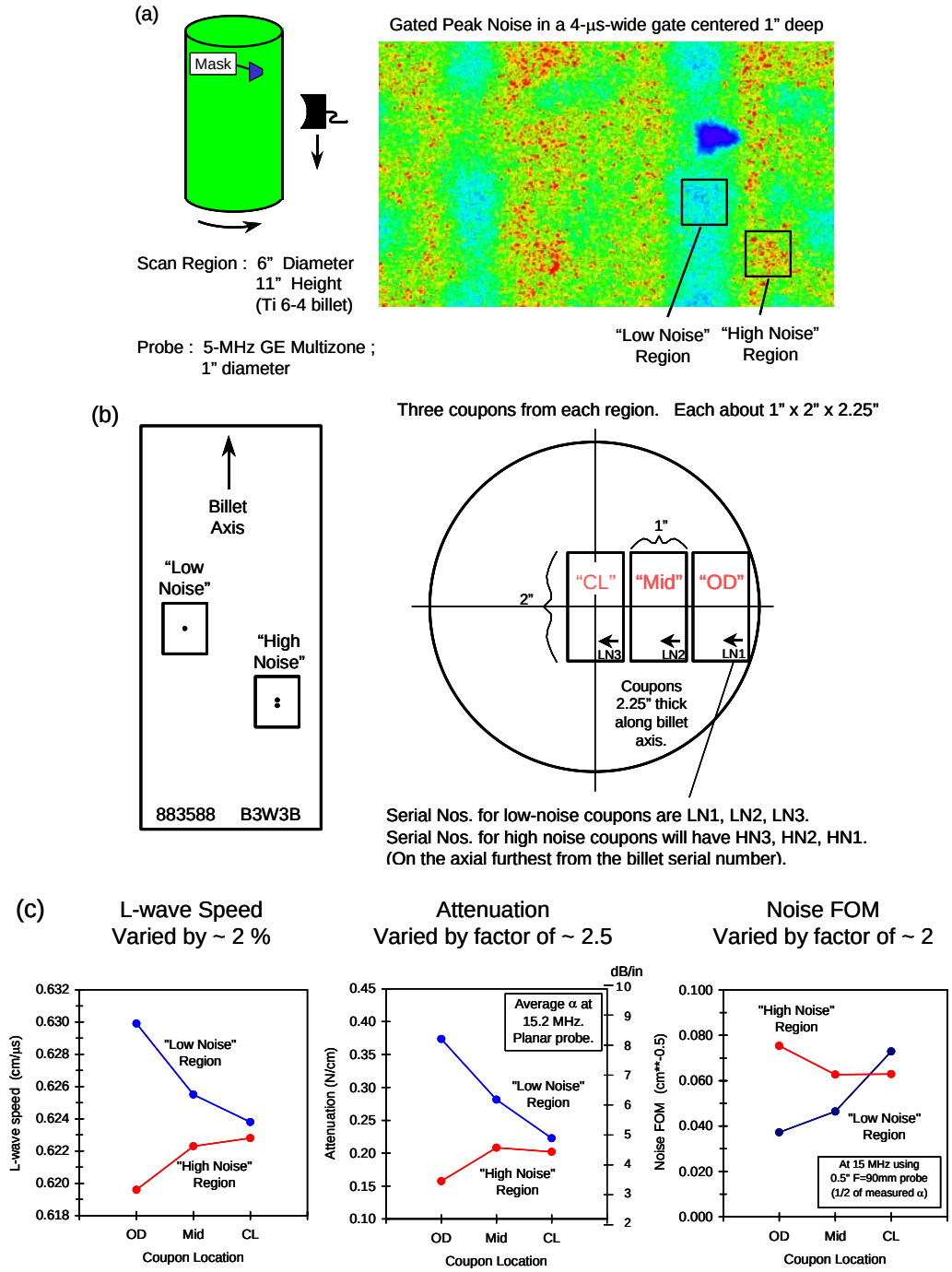

FIGURE 3-2. NOISE BANDING AND UT PROPERTY VARIATIONS IN A 6″ DIAMETER Ti-6-4 BILLET (a) NOISE-BANDING PATTERN, (b) RECTANGULAR COUPON LOCATIONS, AND (c) UT PROPERTY VARIATIONS FOR RADIAL SOUND PROPAGATION

To construct a coherent picture of how UT velocity, attenuation, and backscattered noise vary with position and sound propagation, the coupon-cutting scheme shown in figure 3-3 was used in this study of Ni billets. Rectangular strip coupons with approximate dimensions of 2″ x 2″ x 10″ were cut along billet diameters, as illustrated in figure 3-3(a), and used for UT measurements in the axial and hoop directions. The 2″ thickness in the axial and hoop directions was chosen because: (1) it provided ample lateral width so that the incident sonic beams of the transducers being used did not appreciably interact with the sides of the specimen during measurements of back-wall echoes and (2) a 2″ thick fused-quartz (FQ) reference block (used for comparative attenuation measurements) was already in hand. The strip coupons would be later cut into slices for UT measurements in the radial direction, figure 3-3(b), with the number and thickness of the slices dependent upon the radial variation of UT properties observed in the strip coupon themselves. If the perceived radial variation was small, thicker slices would be used; if the radial variation was large, thinner slices would be used. As will be discussed in section 3.1.2.3, the slice thickness was eventually chosen to be 1.0″ for all the slice coupons studied. In addition to the property measurement coupons, which had smooth (ground) surfaces, a rough-cut slice of adjacent material was obtained for use in metallographic studies. As shown in figure 3-3(a), this measured approximately 0.5″ x 2″ x 10″ and abutted the strip coupon in the axial direction. Small coupons were obtained from the rough-cut slice at selected radial positions, and these were polished and etched to reveal the metal grain structure.

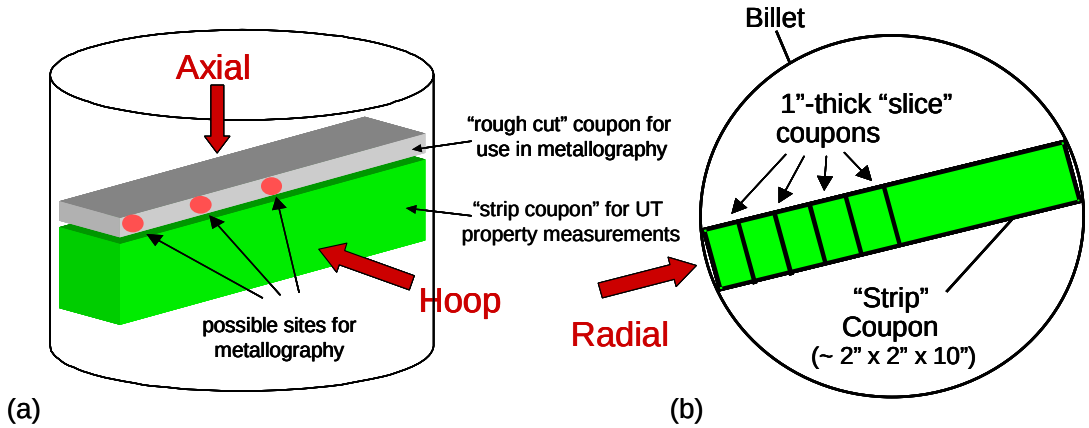

FIGURE 3-3. COUPON LAYOUT FOR 10″ DIAMETER Ni ALLOY BILLETS
(a) STRIP COUPON FOR AXIAL AND HOOP MEASUREMENTS, AND ITS ASSOCIATED ROUGH-CUT (METALLOGRAPHY) COUPON AND
(b) SLICE COUPONS FOR RADIAL PROPERTY MEASUREMENTS

Four strip coupons and their associated slices were studied. It was decided by consensus that two Ni alloys would be studied: IN718 and Waspaloy. Their nominal chemical compositions were listed in table 1-1. Two different forging methods known as GFM (Gesellschaft fur Maschinenbau-und-Fertigungstechnik) and V-Die, respectively, are commonly used to transform IN718 cast ingot into finished billet. GFM employed multiple hammers oriented at 90 degrees to one another, which pound the ingot while it rotates, while V-die used a single hammer to strike the ingot while it rotates within in a V-shaped trough. IN718 billets produced by both methods were studied.

The precise locations of the strip coupons within the candidate billets were determined from measured backscattered grain noise patterns. Four 10″ diameter billets having typical backscattered grain noise levels were selected by the original engine manufacturers (OEM):

- A 30″ length of V-Die-processed IN718 billet
- A 30″ length of GFM-processed IN718 billet
- A 12″ length of GFM-processed IN718 billet
- A 40″ length of Waspaloy billet

These candidate billets were then inspected in the radial direction using a multizone inspection system [23] for 10″ diameter billets located at GE in Cincinnati. That system contains six focused 5-MHz transducers each designed to inspect a different depth zone. The depth zones and associated transducer properties are listed in table 3-1. Except for the shallowest inspection zone, the multizone transducers have bicylindrically curved lenses with different focal lengths (in water) in the radial/axial and radial/hoop planes. The transducer diameters and focal lengths are chosen to produce focal spots of similar size at the centers of each of the six inspection zones. Each transducer is nominally operated at a 3.0″ water path, although small adjustments are sometimes made to better balance the beam focus within the inspection zone.

TABLE 3-1. MULTIZONE INSPECTION PARAMETERS FOR 10″ DIAMETER BILLET

Zone Number	Zone Depth Range (inches)	Transducer Diameter (nominal, inches)	Transducer Focal Depth in Metal (nominal, inches)
1	0.2-0.9	0.75	0.55
2	0.9-1.8	1.25	1.35
3	1.8-2.7	1.50	2.25
4	2.7-3.6	1.75	3.15
5	3.6-4.5	2.00	4.05
6	4.5-5.5	2.35	5.00

For the Ni alloy billet inspections, the usual multizone setup and calibration procedure was generally followed [23], although the gain settings were increased to emphasize the grain noise. The calibration specimen was a 10″ diameter Ti-6-4 billet containing #2 FBHs at various depths. The gain setting for each transducer was adjusted to bring the amplitudes of FBH signals in the associated zone of the standard to 80% full-screen height (FSH). Then, prior to scanning a given Ni billet, an additional gain was applied to boost the average gated peak-to-peak noise level in the highest-noise zone to approximately 50% FSH. The amount of added gain was different for each Ni billet inspected and ranged from 20 to 31.5 dB. The electronic noise level of the measurement system was determined by performing a similar rotational/axial scan beyond the end of the billet (i.e., in water only).

For each billet inspected, six gated-peak noise C-scan images were obtained, one for each depth zone. Some degree of grain noise banding was seen in all C-scans. An example is shown in figure 3-4 for the IN718 V-Die billet. For the full useable area of each C-scan image, the average and peak values of the observed noise were measured and tabulated. Small subregions with areas of several square inches on the billet OD were identified, where the average noise level was approximately highest and lowest, respectively. Gated-peak noise statistics (mean noise; peak noise) were then computed for these subregions as well. For example, in figure 3-4, the high- and low-noise subregions are denoted by A and B, respectively, and have average noise levels of 45% and 17% FSH, respectively, at the gain used for this particular inspection (31.5 dB above standard).

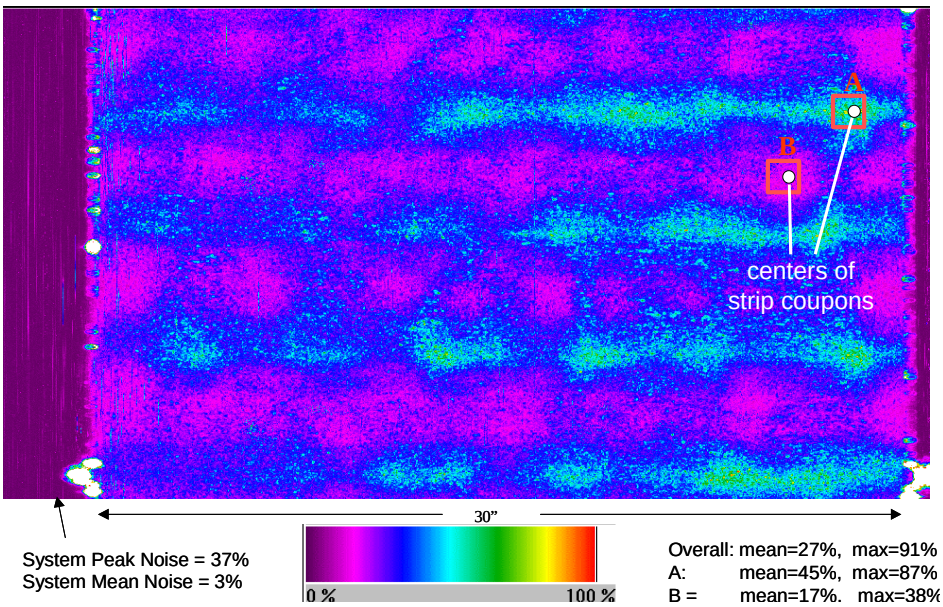

FIGURE 3-4. C-SCAN IMAGE OF BACKSCATTERED NOISE FOR ZONE 2 OF THE IN718 V-DIE BILLET
(Locations are shown where two strip coupons were later cut.)

Average noise levels seen in the four Ni alloy billets are compared in figure 3-5. The measured noise values have been renormalized to a common gain setting, namely, the gain needed to raise #2 FBH signals in the calibration standard to 80% FSH plus an additional 30 dB. At this gain, the noise is shown as a percentage of FSH. The measured noise values are seen to be well above the electronic noise level of the inspection system, which tends to increase with inspection depth. Note that the observed system noise is expected to increase linearly with the absolute voltage amplification applied by the receiver. Also, because of material attenuation in the calibration standard, the absolute gain required to bring a calibration FBH echo to 80% FSH tends to increase with inspection depth. In figure 3-5, results are shown for inspection zones 2-6 only. At the large gain settings used, ring-down of the front-surface echo affected the zone 1 noise level in a manner which was very sensitive to probe alignment. Since the measured noise levels in zone 1 were generally not reproducible, they have been excluded from the figure.

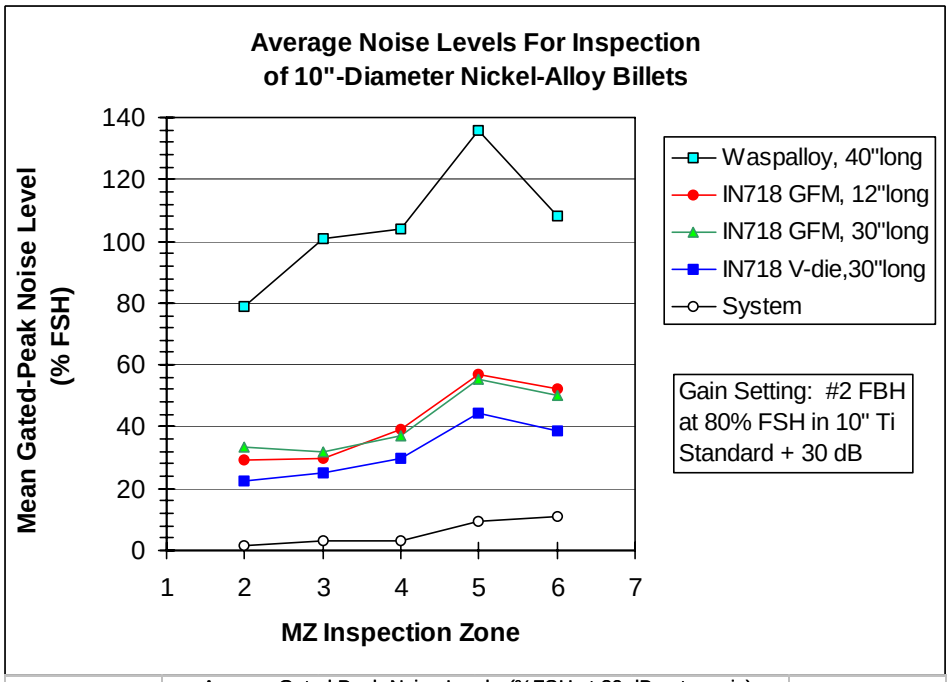

	Average Gated-Peak Noise Level (%FSH at 30 dB extra gain)				
Zone	System Noise	GFM (12"-long)	GFM (30"-long)	V-die (30"-long)	Wasp. (40"-long)
2	2	29	34	23	79
3	3	30	32	25	101
4	3	39	37	30	104
5	10	57	56	44	136
6	11	52	50	39	108

FIGURE 3-5. AVERAGE NOISE LEVELS IN THE MULTIZONE INSPECTIONS OF FOUR Ni ALLOY BILLETS

Note in figure 3-5 that the Waspaloy billet has a mean noise level approximately 2-3 times higher than those of the three IN718 billets. This will later be traced to the significantly larger mean grain diameters in the Waspaloy billet. Also note in figure 3-5 that the two IN718 GFM billets have very similar noise levels. These two billets had similar noise-banding patterns as well. It was decided that the shorter of the two billets would be used for UT property specimens and the longer would be used to construct an FBH calibration standard for 10″ diameter Ni alloy billets. Finally, note in figure 3-5 that the average noise level of each Ni billet (relative to the #2 FBH standard) is always greatest in zone 5. Since noise-to-signal ratios tend to increase as the UT pulse volume increases [24], this may indicate that the zone 5 transducer has a broader focal spot than the transducers used for the other inspection zones. Alternatively, it may indicate that for all four billets, average grain diameters are largest near the billet center.

Figure 3-6 displays the ratio of the average noise levels seen in the high- and low-noise subregions of the Ni alloy billets. This ratio serves as a measure of the severity of noise banding. For the Waspaloy and IN718-GFM billets, noise banding was relatively moderate with the average noise level in high-noise bands about 1.5 times that in low-noise bands. For the IN718 V-Die billet, however, noise banding in the shallower depth zones was much more severe, and it was decided that strip coupons would be cut from both high- and low-noise bands of that billet.

It was also decided that a single strip coupon would be cut from each of the Waspaloy and IN718-GFM billets, with that single coupon taken from a high-noise band because high-noise regions generally present more challenging inspection difficulties. Thus, the four strip coupons that the budget permitted, together with their short-hand designations, were:

- V-Die-A: Strip coupon from a high-noise band in an IN718 V-Die billet
- V-Die-B: Strip coupon from a low-noise band in the above V-Die billet
- GFM-A: Strip coupon from a high-noise band in an IN718-GFM billet
- Waspaloy: Strip coupon from a high-noise band in a Waspaloy billet

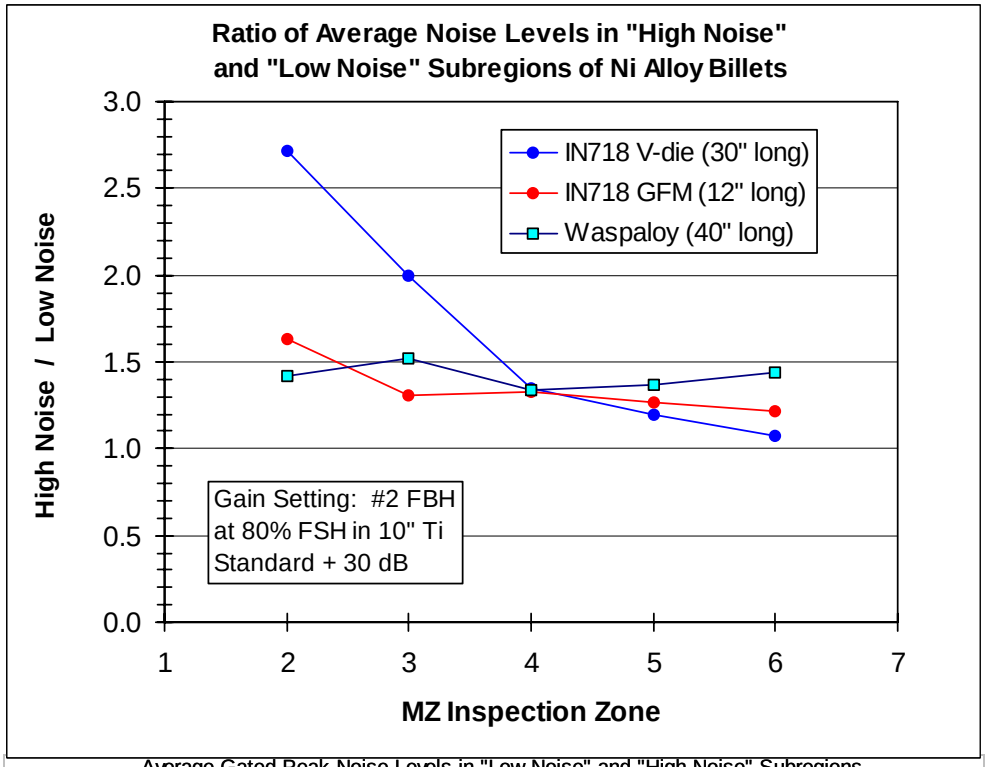

Average Gated-Peak Noise Levels in "Low-Noise" and "High-Noise" Subregions
(%FSH at 30 dB extra gain)

Zone	GFM (12"-long)	V-die (30"-long)	Wasp. (40"-long)
2	22, 36	14, 38	60, 85
3	26, 34	18, 36	73, 111
4	34, 45	26, 35	85, 114
5	49, 62	41, 49	104, 142
6	47, 57	39. 42	79, 114

FIGURE 3-6. DEGREE OF NOISE BANDING IN THE MULTIZONE INSPECTIONS OF FOUR Ni ALLOY BILLETS

For the IN718 V-Die billet, the locations of the two strip coupons within the noise-banding pattern were shown in figure 3-4. Noise-banding patterns and strip coupon locations for the other two billets are displayed in figures 3-7 and 3-8. The single strip coupon for the Waspaloy

billet was cut near an end of the 40″ length, allowing the remainder to be used for the construction of a full-round calibration standard containing FBHs at selected depths.

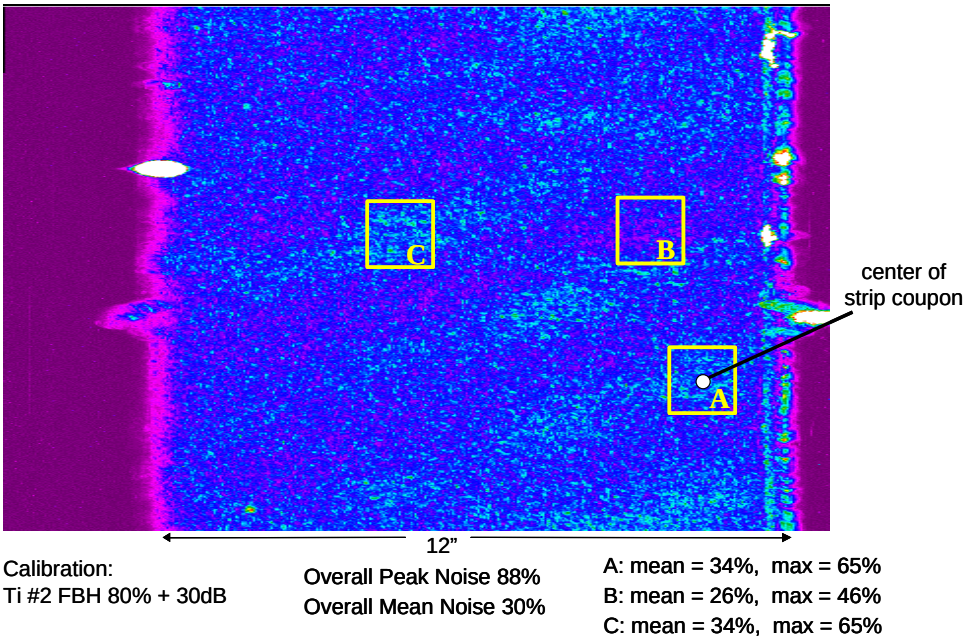

FIGURE 3-7. C-SCAN IMAGE OF BACKSCATTERED NOISE FOR ZONE 3 OF THE 12″ LONG IN718 GFM BILLET
(A strip coupon was cut at site A within a high-noise band.)

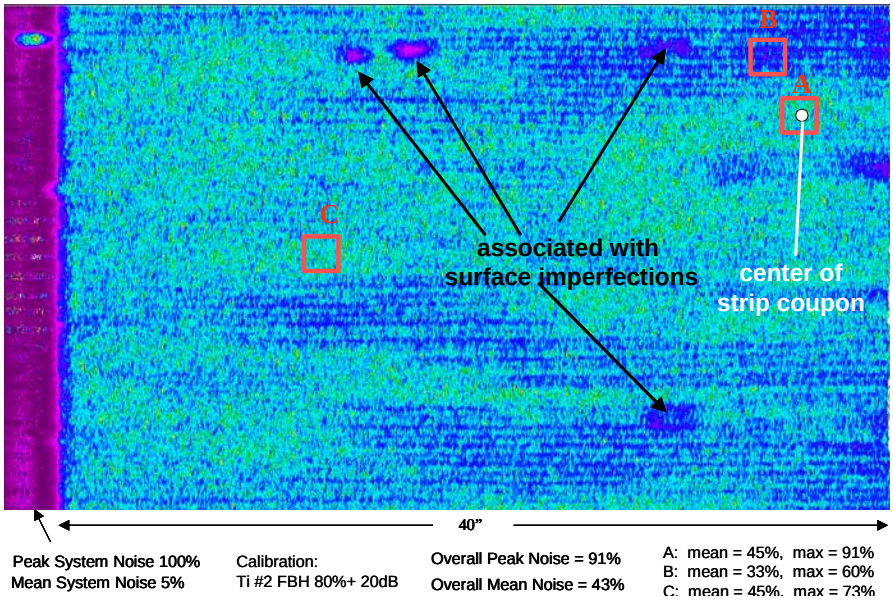

FIGURE 3-8. C-SCAN IMAGE OF BACKSCATTERED NOISE FOR ZONE 5 OF THE 40″ LONG WASPALOY BILLET
(A strip coupon was cut at site A within a high-noise band.)

The four strip coupons were cut from their respective billets using electron discharge-machining (EDM) techniques. The four large (2″ x 10″) surfaces of each coupon having normal vectors pointing in the axial or hoop directions were then ground smooth to facilitate accurate UT measurements. The six surfaces of each specimen were labeled 1-6 in the manner shown in figure 3-9. Note that the outward normal vectors to sides 1, 2, and 3 point in the radial, axial, and hoop directions of the billet respectively. Sides 4, 5, and 6 are opposite to sides 1, 2, and 3 respectively. Note that both sides 1 and 4 are slightly curved before finish machining, and both are portions of the OD billet surface. In all cases, side 1 denotes the OD face that was the sound entry surface for the backscattered noise C-scan used to select the coupon location.

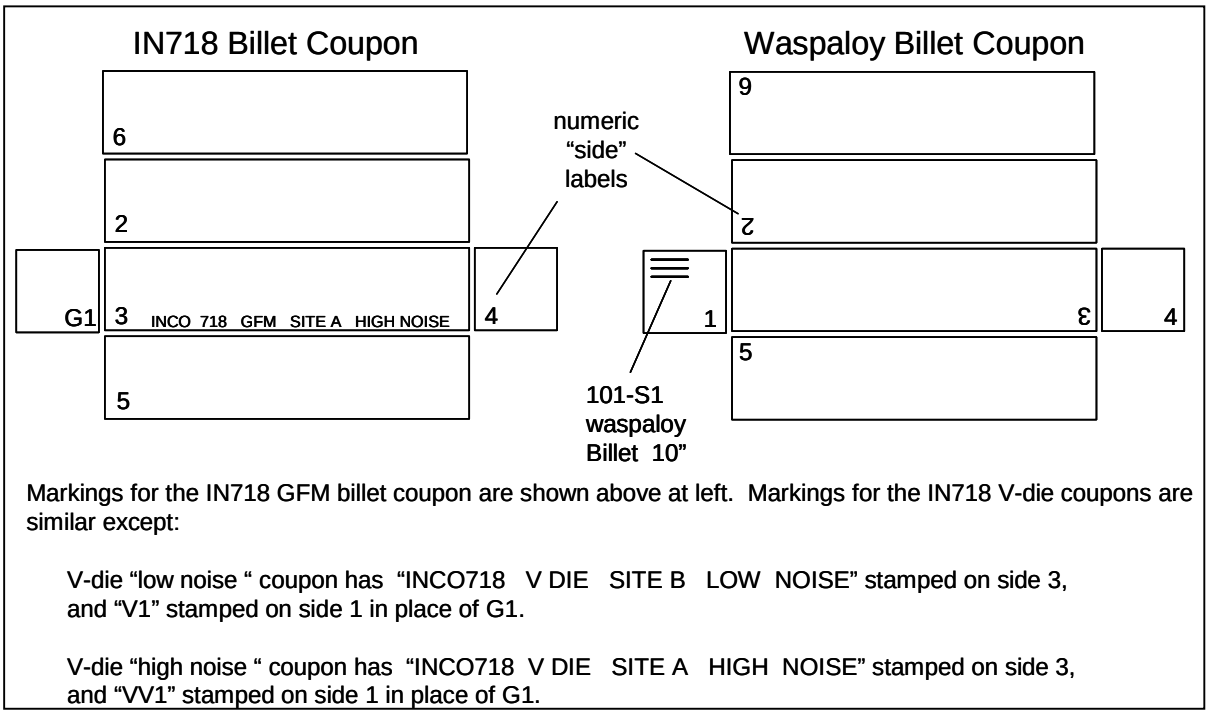

FIGURE 3-9. STAMPED MARKINGS USED TO LABEL THE SURFACES OF THE Ni BILLET STRIP COUPONS
(Here, the six faces of a given coupon have been unfolded into a plane.)

For each of the four strips, the density was determined in the standard manner by dividing the measured mass by the computed volume. The three strips cut from the IN718 billets had curved ends (sides 1 and 4) whose cylindrical curvatures were those of the billet OD surfaces. For the Waspaloy strip coupon, the two curved ends had been machined flat, resulting in a rectangular prism. Formulas used to compute the volumes of the strip coupons from the measured dimensions are shown in figure 3-10. The measured dimensions and masses are listed in table 3-2, together with the deduced density values. For the three IN718 strip coupons, the measured densities were the same to within 1 part in 2000, averaging 8.259 gm/cm. The measured density for the Waspaloy specimen, which has a different alloy chemistry, was slightly lower at 8.209 gm/cm.

Strip coupon volume was computed using:

$$V = (L_{hoop})(L_{axial})(L_{radial})$$

for the rectangular Waspalloy coupon, and

$$V = \left[\frac{L_{axial}}{2}\right]\left\{\left[L_{hoop}\sqrt{(L_{radial})^2 - (L_{hoop})^2}\right] + (L_{radial})^2 \, Sin^{-1}\left(\frac{L_{hoop}}{L_{radial}}\right)\right\}$$

for the IN718 coupons which each had two cylindrically-curved surfaces.

Here, L_{xxx} denotes the full length in the xxx direction. For the IN718 coupons L_{radial} is effectively the billet diameter:

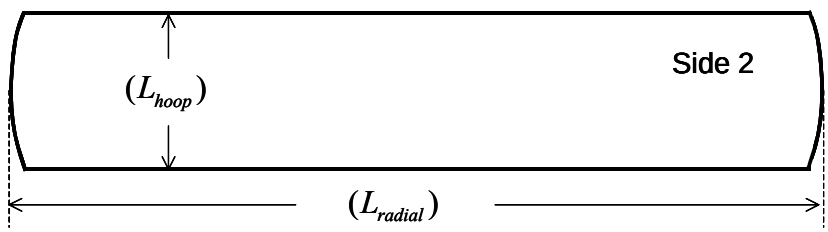

FIGURE 3-10. VOLUME DETERMINATION FOR Ni BILLET STRIP COUPONS

TABLE 3-2. DIMENSION, MASS, AND DENSITY VALUES FOR Ni BILLET STRIP COUPONS

Specimen	L_radial (inches)	L_axial (inches) (ave.)	L_hoop (inches) (ave.)	Mass (grams)	Density (gm/cc)
Waspaloy-A	10.000	1.9975	2.0000	5374	8.209
GFM-A	10.025	1.9645	1.9905	5272	8.262
V-Die-A	9.983	2.0050	1.9945	5366	8.258
V-Die-B	9.980	2.0080	2.0070	5406	8.258

A = high-noise site
B = low-noise site

3.1.2 Preliminary UT Examinations of the Billet Strip Coupons.

Before performing detailed UT property measurements, the strip coupons were scanned at normal incidence using the two experimental setups shown in figure 3-11. The object was to produce C-scan images of back-wall TOF, back-wall amplitude, and backscattered grain noise amplitude. To produce C-scan images of back-wall amplitude and TOF, a 10-MHz, 0.25″ diameter planar transducer was used, and a 2″ thick FQ block served as a low-attenuation reference. To produce C-scan images of backscattered noise, a 15-MHz focused transducer having a 0.5″ diameter and a 3.5″ focal length in water was used. The beam was focused 0.5″ deep in metal, i.e., midway between the front surface and the center plane. For the noise

measurements, a 1/64″ diameter (#1 FBH) in a low-attenuation Ni alloy step block (IN100) served as the reference. For producing the various C-scan images of a given strip coupon, each of the four 2″ x 10″ surfaces served in turn as the sound entry surface. All C-scan images were produced using a SONIX scanning system with the digitization rate set at 100 MHz. For backscattered noise measurements, local signal averaging (64 averages at each transducer position) was used to reduce the effect of electronic noise. No signal averaging was required when digitizing the much stronger back-wall echoes. The SONIX system had an eight-bit analog-to-digital voltage converter, resulting in 256 amplitude levels.

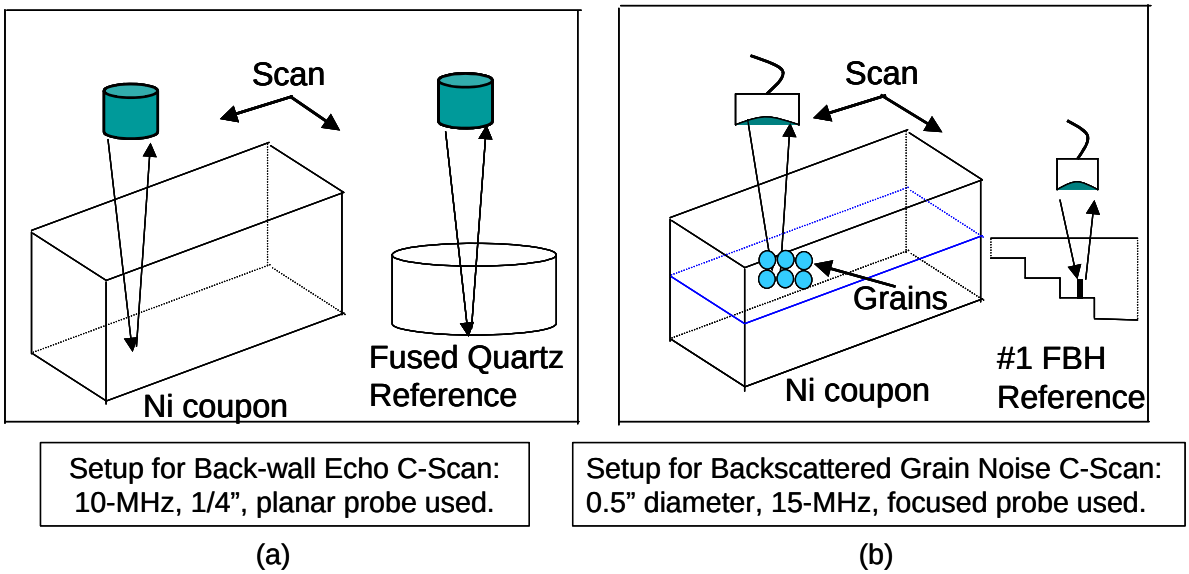

FIGURE 3-11. EXPERIMENTAL SETUPS USED TO MEASURE (a) BACK-WALL AMPLITUDE AND TOF AND (b) BACKSCATTERED GRAIN NOISE AMPLITUDE

3.1.2.1 Back-Wall TOF and Amplitude C-Scans.

For the back-wall echo measurements using the 10-MHz planar transducer, the water path was fixed at 5.0 cm (1.97″) for both the strip coupons and the FQ reference block, guaranteeing that the specimen back walls were located well within the far field of the sonic beam. If a specimen block is simply laid upon a flat support and back-wall echoes are acquired, the echoes will usually be affected by reverberations of sound within a thin water layer trapped between the specimen and its support. For these measurements, the strip coupons and reference block were each supported only by their far edges so that a thick layer of water was immediately below each back wall. Thus, the reflecting back-wall surface was a simple water/metal or water/FQ interface without complicating factors. For radio frequency (RF) waveform digitizations, a time gate of 2 μsec duration was used, which was approximately centered at the arrival time of the back-wall echo. Amplitude C-scans were constructed, which displayed the peak rectified back-wall amplitude within the time gate. TOF C-scans were also constructed, which displayed the time at which the leading edge of the back-wall echo crossed a preset threshold level. For the strip coupons, the scan area typically measured 10.4″ (radial) by 2.4″ (axial or hoop) with a step size of 0.04″ in each direction. A smaller scan region of 2.2″ x 2.2″ was used for the FQ block, but

the same 0.04″ step size was used. As illustrated in figure 3-12 for the V-Die-B case, the back-wall TOF images showed very little variation. Note that for figures in the style of figure 3-12, the sound entry surface is indicated below each separate C-scan image. The four numbers listed immediately above, below, left, and right of an image are the labels of the four adjacent lateral surfaces, which are parallel to the insonification direction, following the earlier notational scheme of figure 3-9. The TOF images were found to be consistent with having velocity variations of less than about 0.2% throughout each coupon. Longitudinal velocities measured in the axial and hoop directions of the strip coupons were found to range over 0.5808 ±0.0008 cm/µsec (or ±0.14%) for the group of three IN718 coupons, and over 0.6012 ±0.0003 cm/µsec (or ±0.05%) within the Waspaloy coupon.

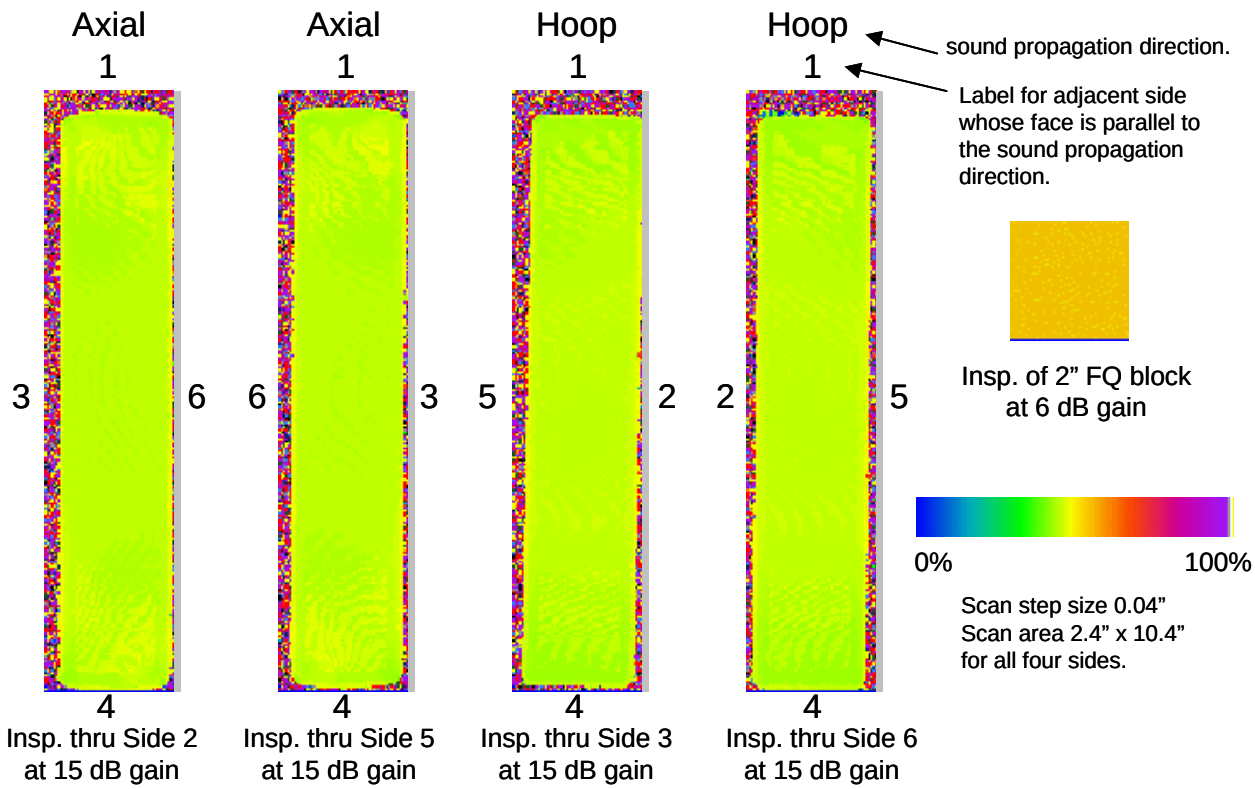

FIGURE 3-12. BACK-WALL TOF C-SCAN IMAGES FOR THE V-DIE-B STRIP COUPON

Although the sound velocities were quite uniform, a strong dependence of back-wall echo amplitude on radial position was typically seen. Back-wall amplitude C-scan images for the four strip coupons are shown in figures 3-13 through 3-16, respectively. Note that back-wall amplitude images made from opposite sides of the same strip coupon (e.g., sides 2 and 5) are essentially mirror versions of each other, as expected. Also note that for a given strip coupon, the images for beam propagation in the axial direction (through sides 2 and 5) tend to closely resemble those for propagation in the hoop direction (through sides 3 and 6).

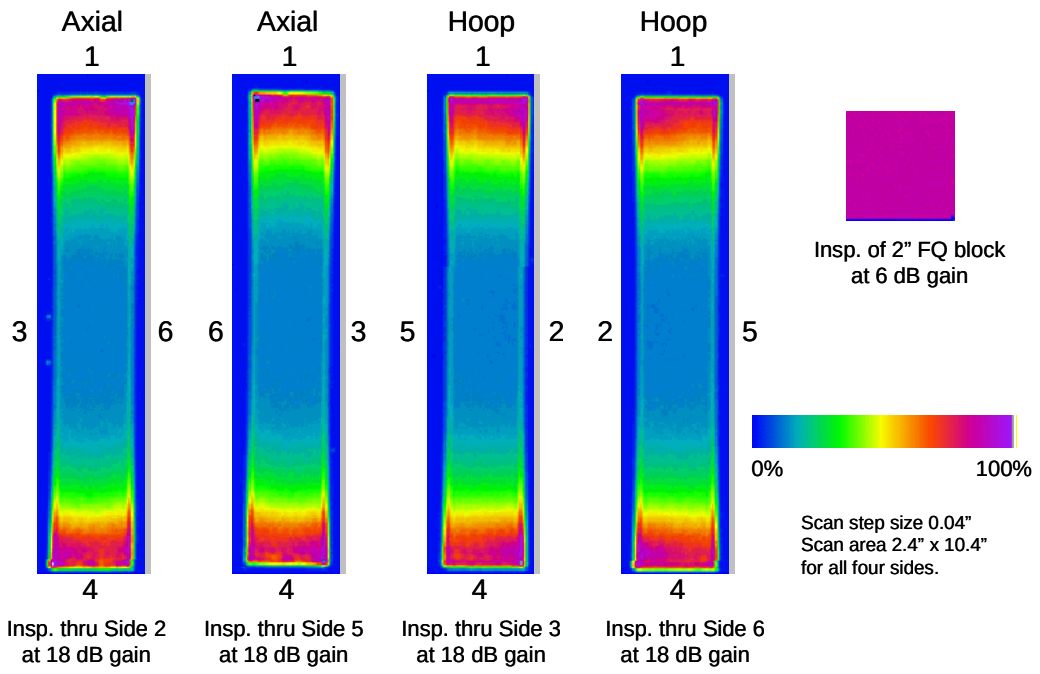

FIGURE 3-13. BACK-WALL AMPLITUDE C-SCAN IMAGES FOR THE WASPALOY STRIP COUPON

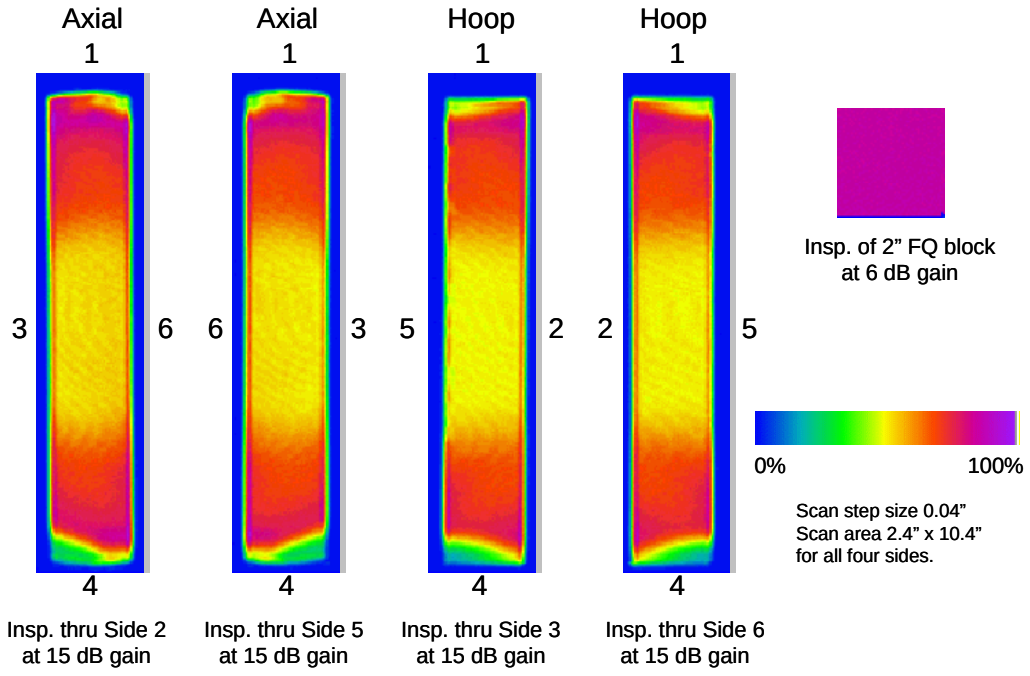

FIGURE 3-14. BACK-WALL AMPLITUDE C-SCAN IMAGES FOR THE GFM-A STRIP COUPON

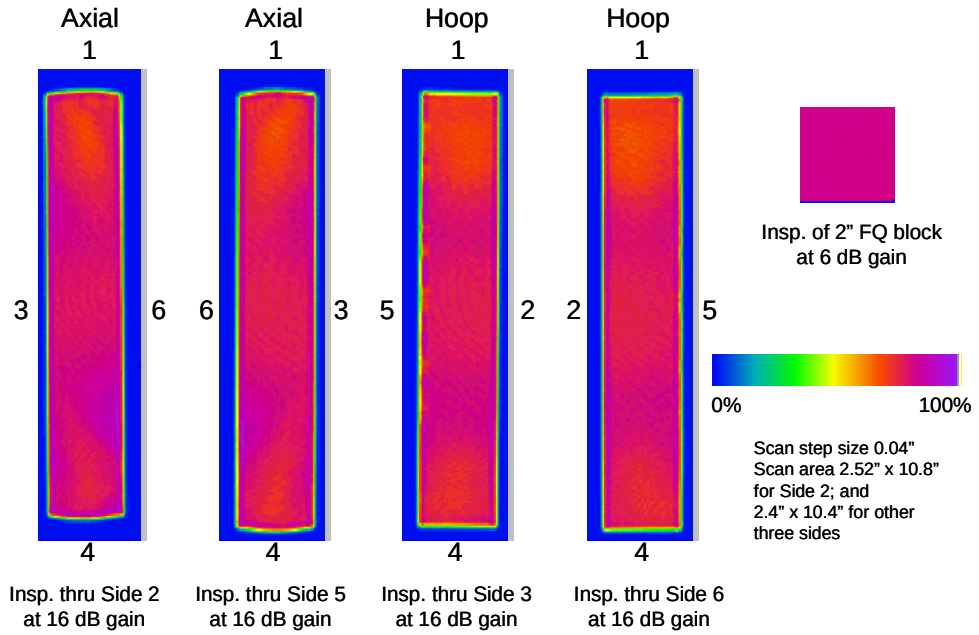

FIGURE 3-15. BACK-WALL AMPLITUDE C-SCAN IMAGES FOR THE V-DIE-A STRIP COUPON

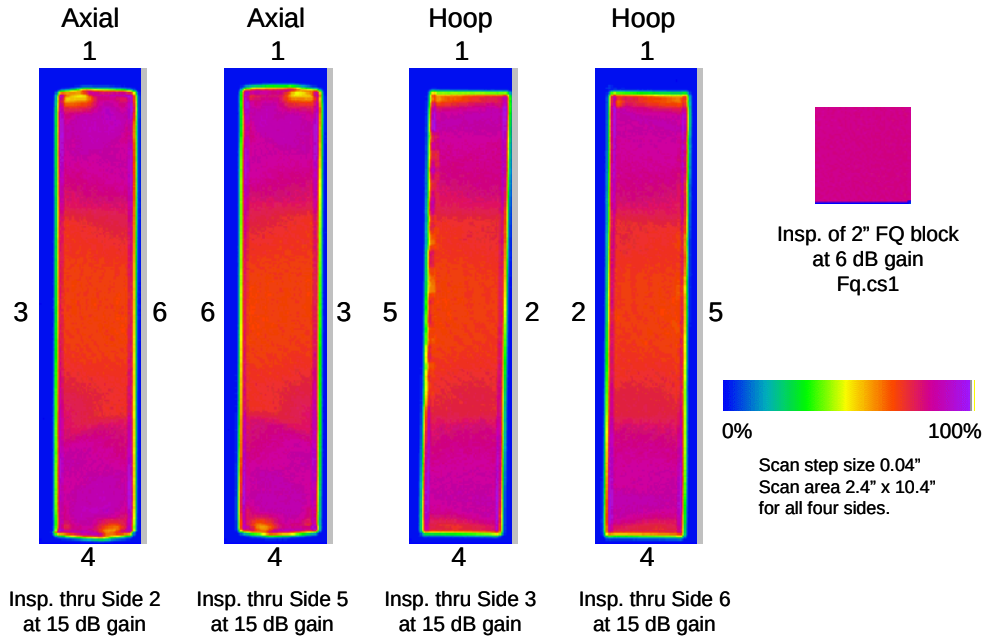

FIGURE 3-16. BACK-WALL AMPLITUDE C-SCAN IMAGES FOR THE V-DIE-B STRIP COUPON

The back-wall amplitude C-scan images for the four strip coupons are directly compared to one another in figure 3-17. There, the images have been rescaled so that the coloration is related to the average attenuation in dB/inch units. The rescaling process assumed that the FQ reference block had negligible attenuation, and corrected for the different gain settings used during the scans and for the differences in interface transmission/reflection losses. The rescaling process involved four major steps:

1. All measured back-wall amplitudes were first multiplied by a constant scale factor chosen such that the rescaled FQ image had a mean amplitude of 100% FSH. Since FQ was assumed to have zero attenuation, an amplitude of 100% FSH was then associated with zero attenuation.

2. The Ni alloy images were then rescaled to correct for gain differences between the Ni and FQ scans. These gain differences ranged from 9 to 12 dB.

3. The Ni images were then rescaled to correct for differences (between Ni and FQ) in the reflection and transmission losses at water/solid interfaces. These losses were quantified by the product of one reflection and two transmission coefficients, denoted here by $T_{01}R_{11}T_{10}$, where subscripts 0 and 1 refer to water and solid, respectively. Plane-wave transmission and reflection coefficients were used; these can be easily calculated from the measured densities and sound velocities [22]. The product $T_{01}R_{11}T_{10}$ was computed to be 0.291, 0.109, and 0.107 for FQ, IN718, and Waspaloy respectively.

4. After the above rescalings, all Ni back-wall amplitudes were found to be less that 100%, and the reduction below 100% was assumed to result from UT attenuation. The attenuation value (α) was then estimated using

$$Amplitude/100\% = exp(-2\alpha z)\ ;\ \ z = 2 \text{ inches.}$$

The resulting rescaled back-wall amplitude images are shown in figure 3-17.

Figure 3-18 provides a second depiction of the same rescaled amplitude data. There, for both axial and hoop sound propagation, the rescaled amplitude and estimated attenuation of each coupon are shown as functions of radial position. Each radial profile shown is an average (in the axial or hoop direction) over the central 1/3 of the coupon surface. The coupon region used in the averaging and the sign choice for the radial coordinate axis are both indicated in the right-hand portion of figure 3-18. Note that the attenuation estimates shown in figures 3-17 and 3-18 are only approximate. This is because UT attenuation tends to increase with frequency, and a broadband pulse is being used. The center frequency of the sonic pulse is near 10 MHz when the pulse initially leaves the transducer, but that center frequency shifts downward during propagation since the high-frequency components of the beam are attenuated more that the low-frequency ones. Figures 3-17 and 3-18 may be thought of as providing estimates of the material attenuation averaged within the bandwidth of the back-wall echo. These estimates are useful for quick visual comparisons of the relative attenuations of the four specimens.

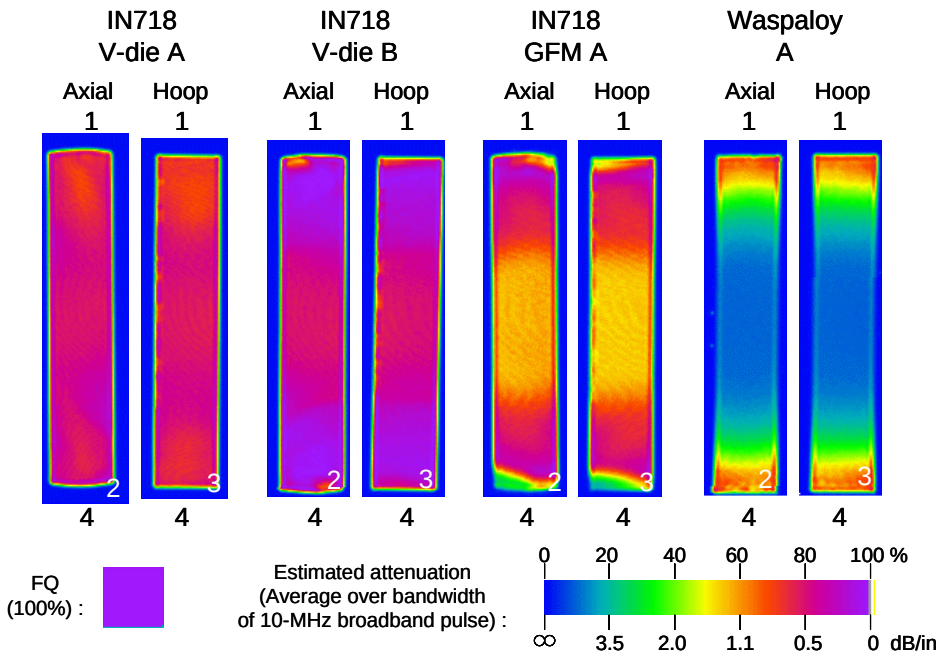

FIGURE 3-17. RESCALED C-SCAN IMAGES OF BACK-WALL ECHO AMPLITUDE FOR AXIAL (SIDE 2) AND HOOP (SIDE 3) INSPECTIONS OF THE FOUR Ni BILLET STRIP COUPONS

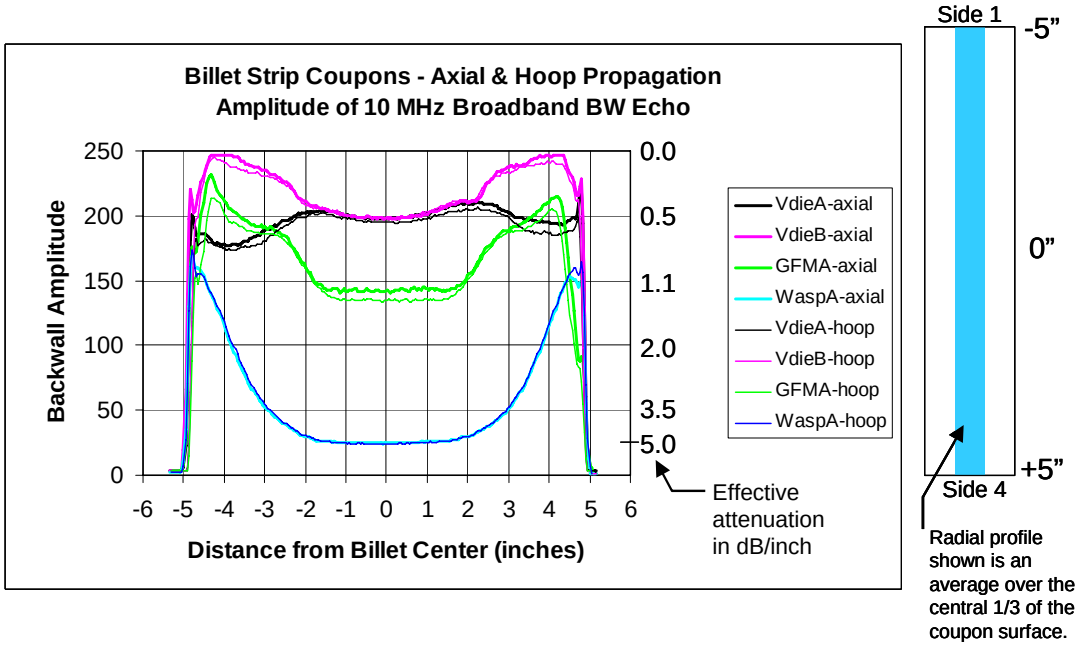

FIGURE 3-18. DEPENDENCE OF AVERAGE BACK-WALL AMPLITUDE ON RADIAL POSITION IN THE FOUR Ni BILLET STRIP COUPONS

As shown in figures 3-17 and 3-18, there are significant differences in the back-wall amplitude (or attenuation) values of the four strip coupons. Note that for each coupon there is a clear dependence of back-wall amplitude on radial depth, but at a given radial depth, there is generally little difference between the results for the axial and hoop directions. Such a behavior is consistent with strip coupon microstructures that have equiaxed grains whose average grain diameter varies with radial depth. It is also interesting to note that the V-Die-A and V-Die-B strip coupons, which were cut from high- and low-noise bands of the same IN718 billet, differ significantly in their effective attenuation values near the coupon ends (OD regions) but have very similar attenuation values near their centers. Such a coalescing of attenuation values at the billet center has also been seen for coupons cut from high- and low-noise bands of Ti-6-4 billets. One instance of this behavior was shown in figure 3-2. As might be expected, the asymmetries in the mechanical working of the billet, which led to noise-banding and other property variations in the hoop direction, evidently have a diminished effect near the billet center.

3.1.2.2 C-Scans of Backscattered Noise Amplitude.

The measurement setup used to produce backscattered grain noise C-scan images was shown in figure 3-11. The 15-MHz, 0.5″ diameter transducer used had a nominal focal length of 9.0 cm (3.54 inches) in water. Its geometric focal length and actual focal length (peak amplitude from a small ball target in water) were measured to be 9.65 cm (3.80 inches) and 9.2 cm (3.62 inches) respectively [22]. For the inspections of the strip coupons, a 1.66″ water path was used so that the actual focal depth in metal was about 0.5″ deep, or one-quarter of the specimen thickness. The scan plan used for backscattered grain noise was similar to that used in section 3.1.2.1. The scan area was 10.4″ x 2.4″ and the step size was 0.04″. The time gate extended from 2.9 μsec to 6.9 μsec after the front-surface echo, or approximately from 0.33″ to 0.79″ deep in the metal. This bracketed the center of the focal zone where the absolute backscattered noise amplitudes tended to be the greatest. The resulting C-scan images of the Ni alloy strip coupons displayed the rectified gated-peak noise amplitude, i.e., the largest absolute noise amplitude seen anywhere within the time gate at a given transducer position. For a given strip coupon, the inspection gain was fixed; however, the gain varied from coupon to coupon. A #1 FBH located 0.5″deep in a fine-grain IN100 step block served as a reference for absolute amplitude. The FBH was scanned at the same water path used for the noise scans; the scan area was 0.078″ by 0.078″ with a step size of 0.002″. The peak amplitude seen in the reference scan differed slightly from day-to-day (by 1% to 3%) due to minor differences in water temperature and beam normalization.

The four large (2″ x 10″) surfaces of each strip coupon were scanned to produce images of backscattered grain noise amplitudes. The results are shown in figures 3-19 through 3-22, respectively, for the four strip coupons, together with the associated images of the #1 FBH reference. It was found that grain noise, like attenuation, depended primarily on radial depth in the billet. At a given radial depth, noise measurements in the hoop and axial directions tended to yield similar results.

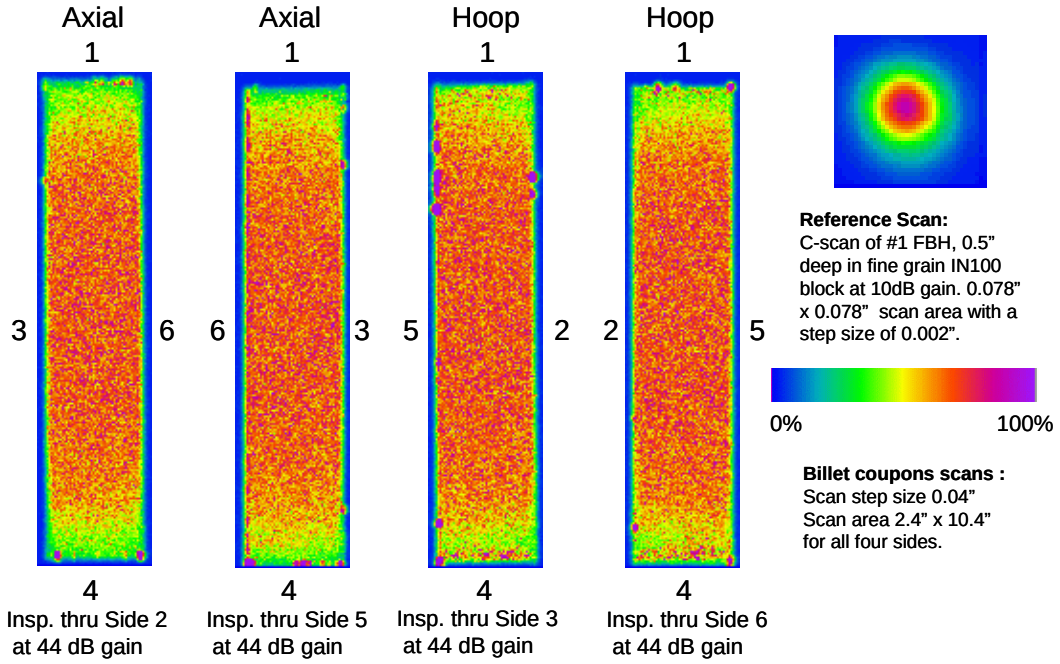

FIGURE 3-19. BACKSCATTERED NOISE C-SCAN IMAGES FOR THE WASPALOY STRIP COUPON

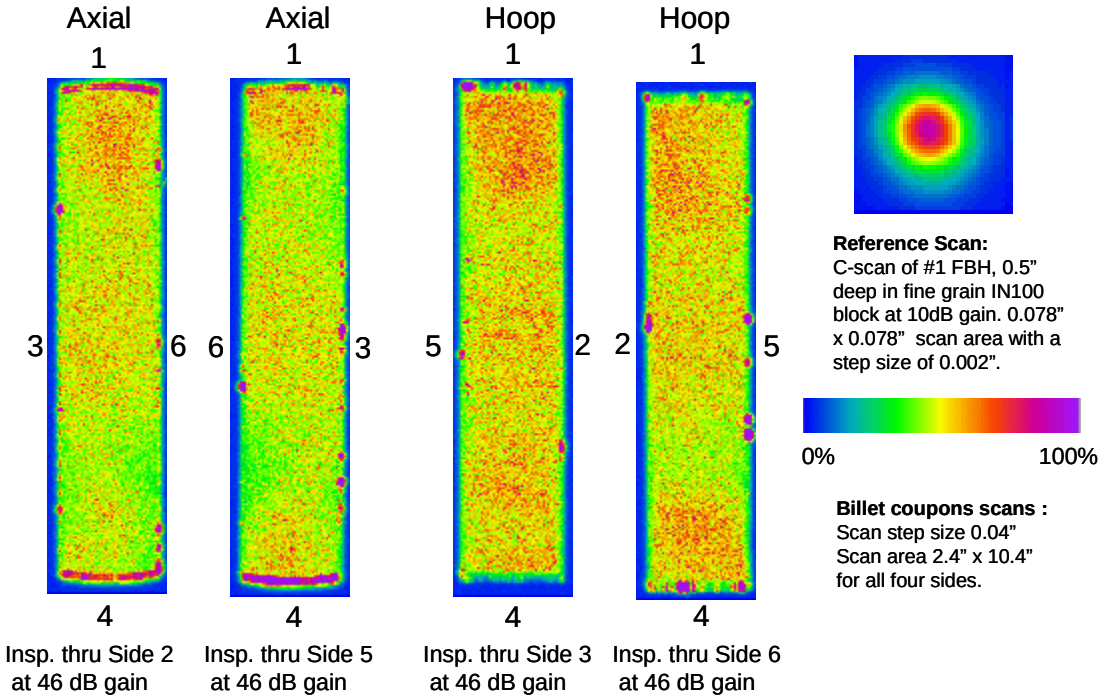

FIGURE 3-20. BACKSCATTERED NOISE C-SCAN IMAGES FOR THE GFM-A STRIP COUPON

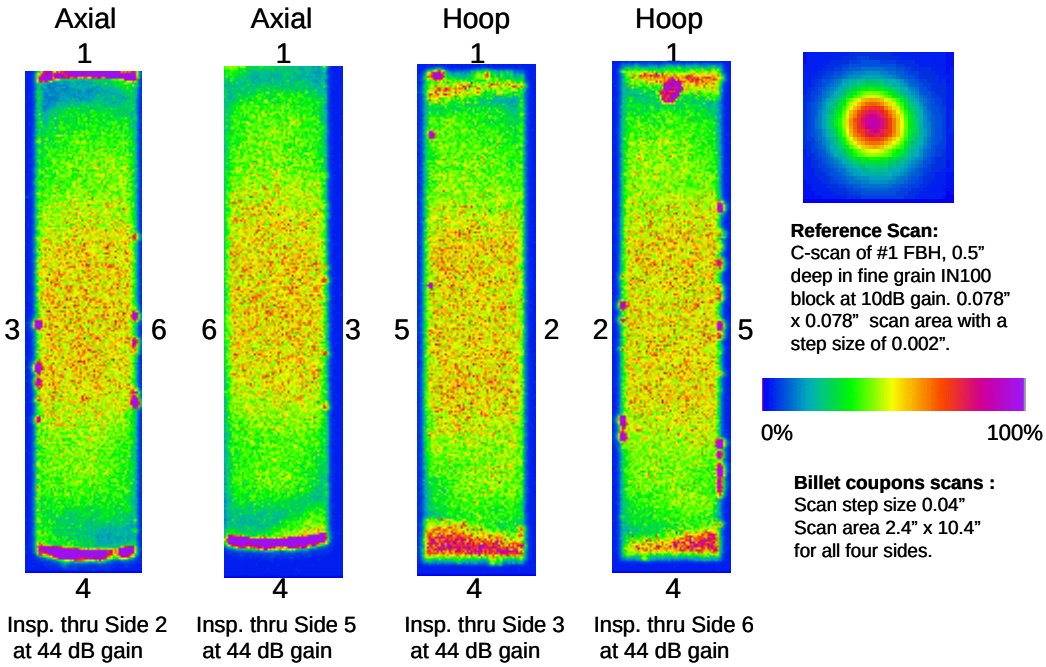

FIGURE 3-21. BACKSCATTERED NOISE C-SCAN IMAGES FOR THE V-DIE-A STRIP COUPON

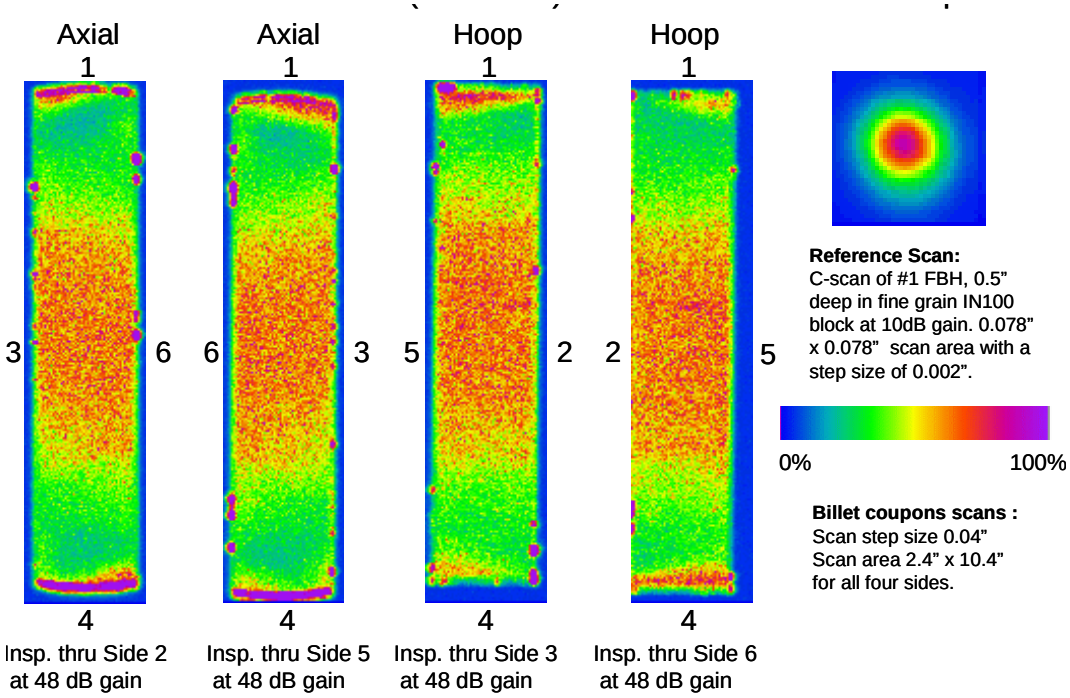

FIGURE 3-22. BACKSCATTERED NOISE C-SCAN IMAGES FOR THE V-DIE-B STRIP COUPON

To better display the dependence of noise on radial depth, radial profiles of averaged noise amplitudes were constructed. The procedure used is illustrated in figure 3-23 using noise data from the Waspaloy coupon. Within each C-scan image, a rectangular area of dimension 0.52″ (axial or hoop) by 10.4″ (radial) was studied. This area, outlined by the dotted rectangle in figure 3-23(a), was centered at the center of the strip coupon. At each radial position, the noise amplitudes within the rectangle were averaged over the lateral coordinate (axial or hoop) to produce a noise-amplitude-versus-radial-position profile. Because of the random nature of backscattered noise, the radial profiles thus constructed have a somewhat jagged appearance. As shown in figure 3-23(b), a 9-point running average was performed to obtain a smoother curve that better displays the general trend of the data.

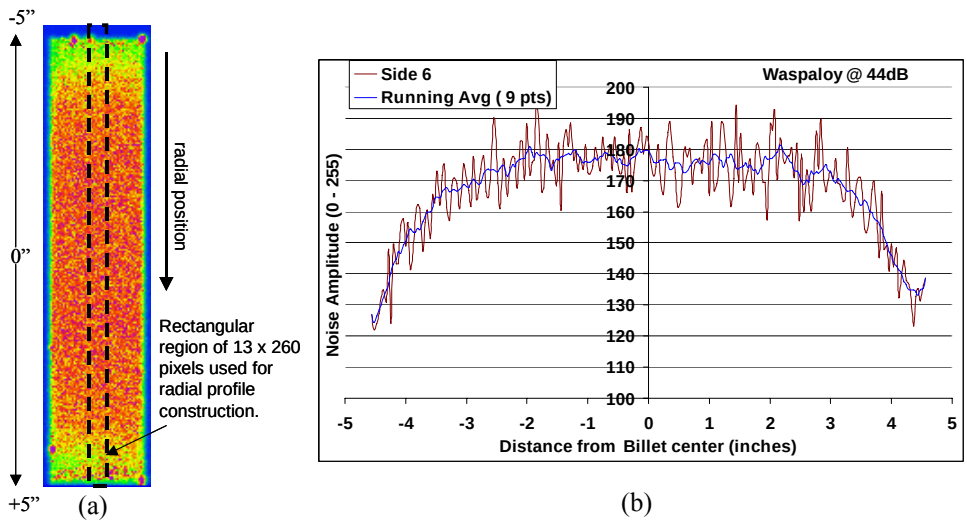

FIGURE 3-23. CONSTRUCTION OF RADIAL PROFILES OF BACKSCATTERED GRAIN NOISE (a) NOISE ANALYSIS REGION FOR THE INSPECTION THROUGH SIDE 6 OF THE WASPALOY STRIP COUPON AND (b) RESULTING CALCULATED AND SMOOTHED RADIAL NOISE PROFILES

The smoothed versions of the radial noise profile are compared in figure 3-24, with the results shown for four sides of each strip coupon. Recall that the sonic beam propagates in the axial direction for inspections through sides 2 and 5 and in the hoop direction for inspections through sides 3 and 6. Note in figure 3-24 that a uniform amplitude scale has been adopted in which the peak amplitude of the FBH reference has a value of 100. Thus, all the grain noise amplitudes shown are less than 2% of that #1 FBH amplitude. The observed grain noise amplitudes depend on both the inherent noisiness of the microstructure (i.e., the FOM value) and on the UT attenuation, which varies greatly among the suite of specimens. Because of the effects of attenuation, one must not assume that relative FOM values are in the same proportion as the corresponding measured gated-peak noise amplitudes. For example, in figure 3-24, the displayed noise amplitude near the center of the Waspaloy coupon is only about 30% higher than that near the center of the GFM-A coupon. However, as discussed in section 3.1.4.2, the FOM values for these cases differ by about a factor of 4. The UT attenuation within the Waspaloy coupon is much larger than that within the GFM-A coupon; this attenuation difference acts to bring the measured noise amplitudes in figure 3-24 closer together.

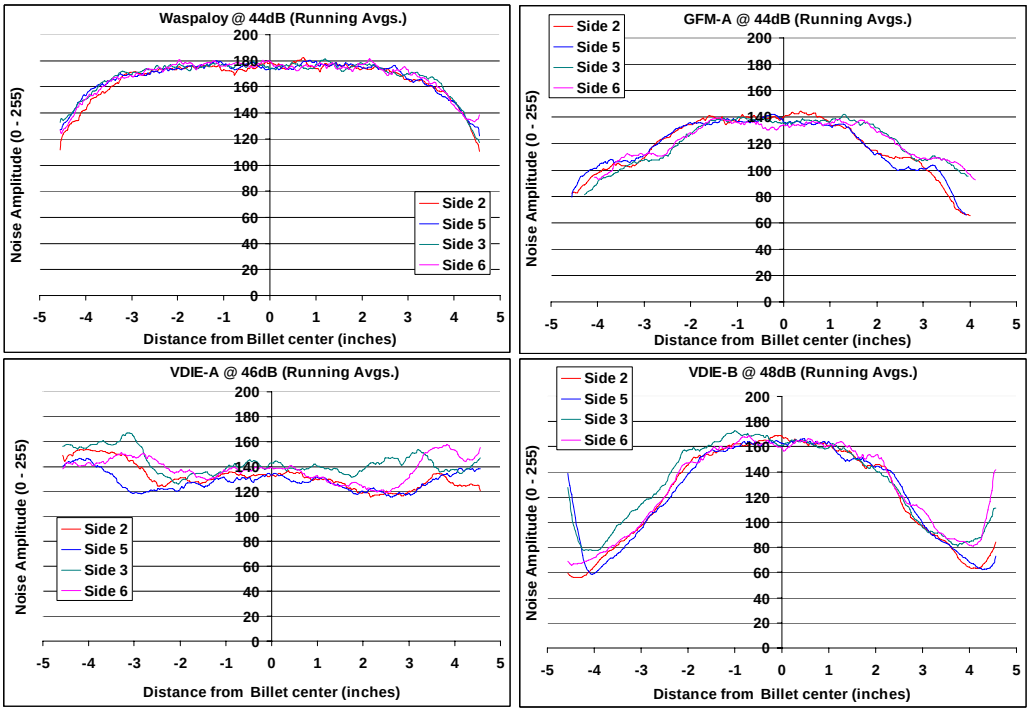

FIGURE 3-24. DEPENDENCE OF BACKSCATTERED NOISE ON RADIAL POSITION FOR EACH OF THE FOUR STRIP COUPONS, RELATIVE TO A #1 FBH AT THE SAME DEPTH (0.5″) IN THE IN100 REFERENCE BLOCK

In each panel of figure 3-24, four curves are shown corresponding to measurements through the central regions of the four major surfaces. Because of the choices of gate depth and lateral width, the insonified volumes for these four measurements do not overlap. However, the four curves for a given coupon tend to be quite similar in overall amplitude and shape. This indicates that backscattered noise levels at a given radial depth are (1) similar for axial and hoop sound propagation and (2) relatively unchanged by translations of an inch or so in either the axial or hoop direction. Again, this finding is consistent with having, within a given strip coupon, equiaxed microstructures in which the mean grain size principally varies with radial position. For example, under this interpretation, grain sizes would tend to decrease as one moved radially away from the center of the Waspaloy, GFM-A, or V-Die-B strip coupon. Although the dependence of backscattered noise on radial position is clear in figures 3-20 through 3-23, there are also dependences of noise (and hence microstructure) on axial and hoop position within a given billet. This fact is clear from the noise-banding patterns observed in the C-scans of the original billets (e.g., see figures 3-4, 3-7, and 3-8. It is also evident from the differences between the V-Die-A and V-Die-B curves in figure 3-24, since both strips were cut from different axial/hoop locations in the same billet. Recall that V-Die-A was cut from a high-noise band, and V-Die-B from a low-noise band. Thus, as expected, the measured noise amplitudes for V-Die-A, seen in figure 3-24, are generally larger than those for V-Die-B. However, the grain noise levels in the two V-Die coupons are much more similar to one another near the billet center than at other radial depths. This mirrors the behavior of back-wall echo amplitudes that were shown in section 3.1.2.1 to be most similar near the centers of these two coupons.

In summary, back-wall echo and backscattered noise C-scans were performed at normal incidence through the four large surfaces of each strip coupon. Results were consistent with the hypothesis that the Ni billet microstructures have approximately equiaxed, randomly oriented grains whose mean diameter varies systematically with position (principally radial depth). Note that this hypothesis implies that local values of attenuation and backscattered noise should be well correlated with one another, with both attenuation and noise FOM increasing with mean grain diameter. A review of figures 3-18 and 3-24 does indeed reveal that for a given strip coupon, large (small) values of estimated attenuation are seen at sites having large (small) values of backscattered noise amplitude. This correspondence is also made clear by figure 3-25, which directly compares the back-wall and noise C-scan images for axial and hoop inspections of the GFM-A strip coupon. One sees that the sites having low back-wall amplitude (high attenuation) also have high backscattered noise. Similar visual comparisons for the other three strip coupons can be made by the interested reader by comparing figures 3-13 through 3-16 with figures 3-19 through 3-22.

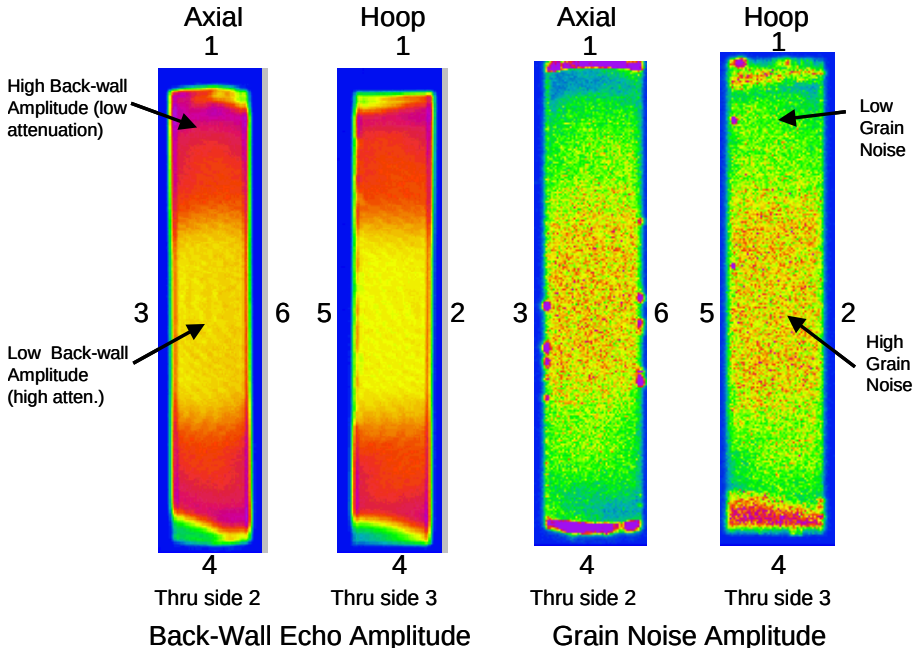

FIGURE 3-25. COMPARISON OF BACKSCATTERED NOISE C-SCANS (RIGHT TWO IMAGES) AND BACK-WALL AMPLITUDE C-SCANS (LEFT TWO IMAGES) FOR THE GFM-A STRIP COUPON
(Results are shown for sound propagation in both the axial and hoop directions.)

3.1.2.3 Site Selection.

The preliminary back-wall and backscattered noise C-scans revealed that the UT properties of the strip coupons were primarily dependent on radial depth and were approximately symmetric about the billet center. It was decided that detailed property measurements would be made at sites along a single billet radius rather than along a full diameter. Since the property variations with radial depth tended to be systematic and relatively smooth, it was decided that detailed measurements at five sites on each strip coupon would be sufficient to obtain a good general

understanding of the degree of variability. The five sites selected are shown in figure 3-26 and were located 0″, 1″, 2″, 3″, and 4″, respectively, from the billet center. For sonic beam propagation in the axial and hoop directions, UT measurements at these sites were made on the intact strip coupons. For measurements in the radial direction, the strip coupons were later cut into approximately 1″ thick slices centered at these five sites (see figure 3-27).

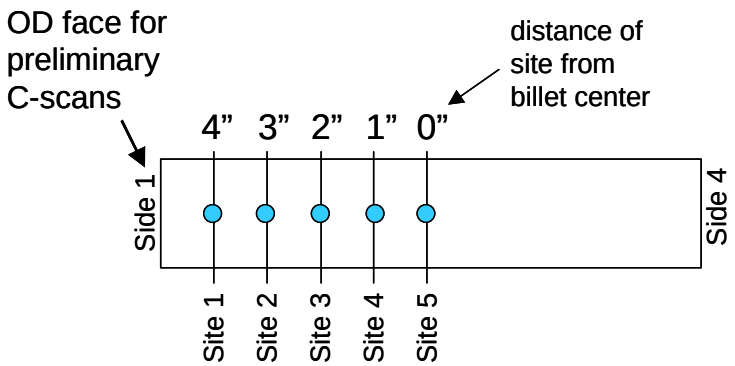

FIGURE 3-26. THE FIVE SITES ON A GIVEN STRIP COUPON WHERE DETAILED UT PROPERTY MEASUREMENTS WERE MADE

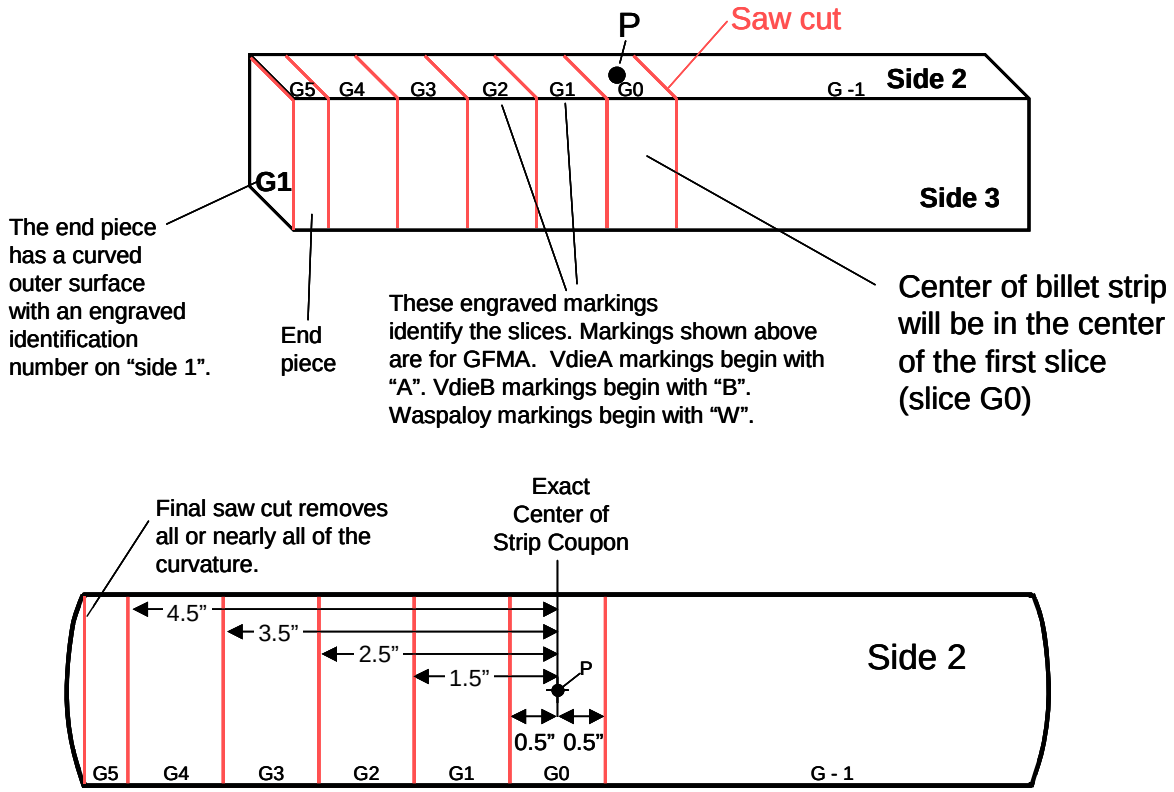

FIGURE 3-27. CUTTING AND LABELING PROTOCOLS FOR THE Ni ALLOY STRIP COUPONS, ILLUSTRATED FOR THE GFM-A BILLET STRIP

3.1.3 Methods Used for Detailed UT Property Measurements.

This section will discuss the procedures used for detailed UT property measurements and show representative examples of the results. For a given site and beam propagation direction, longitudinal-wave measurements were performed in the following order: sound velocity, attenuation, and backscattered noise. This order was necessary because (1) sound velocity is a required input for the attenuation measurement procedure that was used and (2) both velocity and attenuation are inputs for the grain noise FOM extraction procedure. All the measurements were performed with the specimens immersed in distilled water using the same two transducers that were used for the preliminary C-scans. However, a different UT measurement system was used consisting of a Panametrics 5052 pulser/receiver, a Lecroy 9400A digitizing oscilloscope, a Testek water tank with a motorized XY scanning bridge, a manual gimble-gimble goniometer for adjusting the transducer orientation, and a personal computer to control scanning and data acquisition. The A-scans (RF waveforms) required for attenuation and FOM determination were digitized at a 100-MHz sampling rate.

3.1.3.1 Velocity Measurements.

The velocity at each measurement site was determined from the average time delay between successive back-wall echoes using the setup shown in figure 3-28. The first three back-wall (or back-surface) echoes were generally used, denoted BS1, BS2, and BS3, respectively, in figure 3-28. The two transducer orientation angles were adjusted so that the incident beam was as normal as possible to the front and back surfaces of the specimen; this was usually done by maximizing the amplitude of the second back-wall echo, BS2. The time delay between two echoes was specifically defined as the time difference between the corresponding zero crossing points just preceding the dominant positive peaks in the waveforms. In practice, time delays were measured with the LeCroy oscilloscope alone by (1) amplifying the second echo until its peak-to-peak amplitude approximately matched that of the first echo and (2) shifting the second echo to the left by the amount necessary to overlap the designated zero crossing points. This procedure is illustrated in figure 3-29 for two typical cases. Note in the figure that the successive back-wall echoes decrease more quickly in amplitude for Waspaloy than for GFM-A, indicating a higher attenuation in the Waspaloy specimen. Because of this higher attenuation, there are more pronounced changes in the shapes of the successive back-wall echoes. Early measurements for selected cases using both 5- and 10-MHz planar transducers found very little difference between the two measured velocities, i.e., typically less than one-tenth of 1 percent. Consequently, the dependence of velocity on frequency was deemed to have little impact on practical inspections, and subsequent velocity measurements were made using only the 10-MHz transducer.

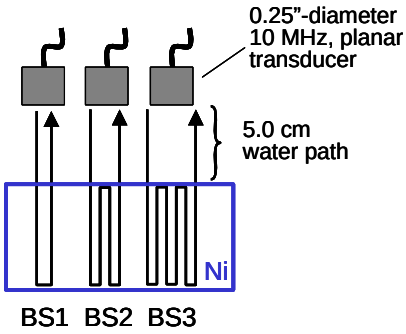

FIGURE 3-28. SETUP FOR UT VELOCITY MEASUREMENTS USING THE SUCCESSIVE BACK-SURFACE REVERBERATIONS OBSERVED AT A FIXED MEASUREMENT SITE

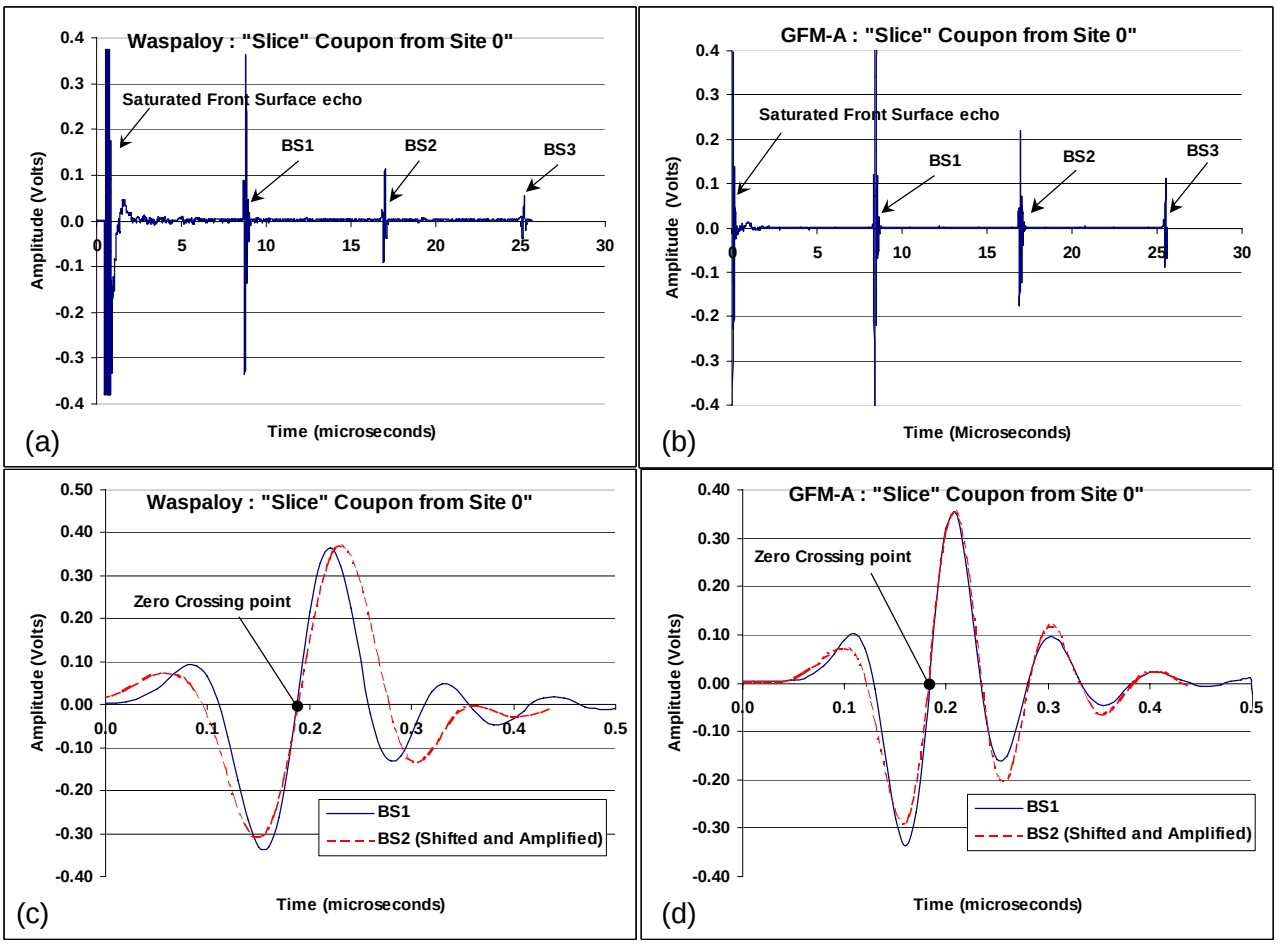

FIGURE 3-29. (a)-(b) A-SCANS SHOWING THE FRONT-WALL (TRUNCATED) AND FIRST THREE BACK-WALL ECHOES FOR THE SLICE COUPONS FROM THE CENTERS OF THE WASPALOY AND GFM-A BILLETS AND (c)-(d) OVERLAP OF THE FIRST TWO BACK-WALL ECHOES AFTER THE SECOND HAS BEEN INCREASED IN AMPLITUDE AND TIME SHIFTED

Examples of measured sound speeds within the Waspaloy coupon strip are shown in figure 3-30. The measured velocities occupied a narrow range of 0.6012 ±0.0003 cm/μsec (or ±0.05%). Absolute velocity measurements are typically believed to be accurate to about 1 part in 1000 (0.10%), usually limited by the accuracy of the thickness measurement (via calipers). For example, a thickness measurement error of 1 mil out of 2″ would shift a given plotted value, in figure 3-30, up or down by about 0.0003 cm/μsec. Figure 3-30 shows that measured velocities in the Waspaloy strip coupon tend to be slightly lower in the center of the billet than near the OD. The results for the full set of sound speed measurements on the Ni alloy coupons will be presented and discussed in section 3.1.4.1.

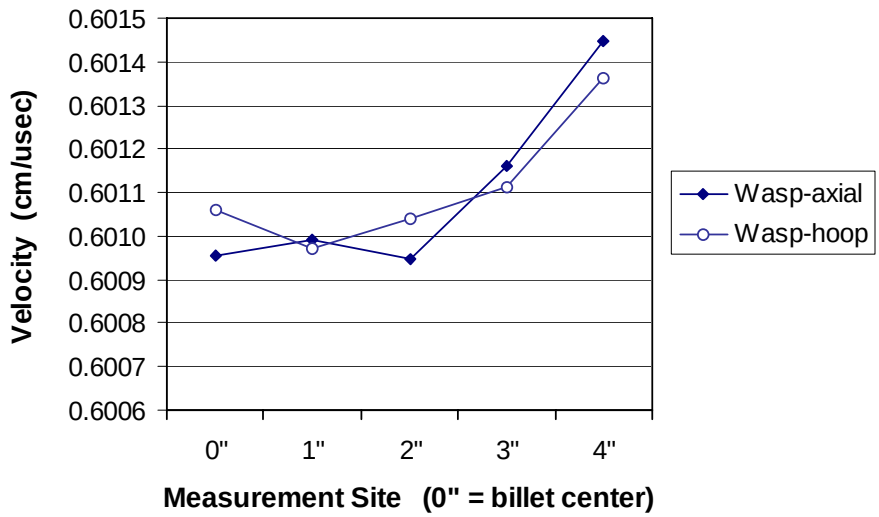

FIGURE 3-30. RESULTS OF SOUND VELOCITY MEASUREMENTS PERFORMED ON THE WASPALOY STRIP COUPON BEFORE SLICING

3.1.3.2 Attenuation Measurements.

In the preliminary study, two competing immersion methods for attenuation measurement were used, as illustrated in figure 3-31. Method 1 is based on comparing the first back-wall echo in the metal specimen to that in an FQ reference block of similar thickness [22]. The attenuation of the reference block is assumed to be negligible. Method 2 is based on comparing the first three metal back-wall echoes with one another [25]. Method 1 was originally developed for scanning applications where the effective attenuation varies from point to point and an average attenuation value within a scan region is desired. However, it can also be used for single-point measurements, as was the case here. Method 2 does not require a reference block; in addition, it is preferred for low-attenuation materials because longer sonic path lengths allow the effects of attenuation to accumulate, resulting in greater (and more readily measured) reductions to back-wall amplitudes. In these attenuation measurements, a 1/4″ diameter, 10-MHz, broadband planar transducer was used. The water path was typically 5 cm, and the incident sonic beam was perpendicular to the entry surface of the FQ, or metal block, with beam normalization accomplished in the same manner as discussed above for sound velocity measurements.

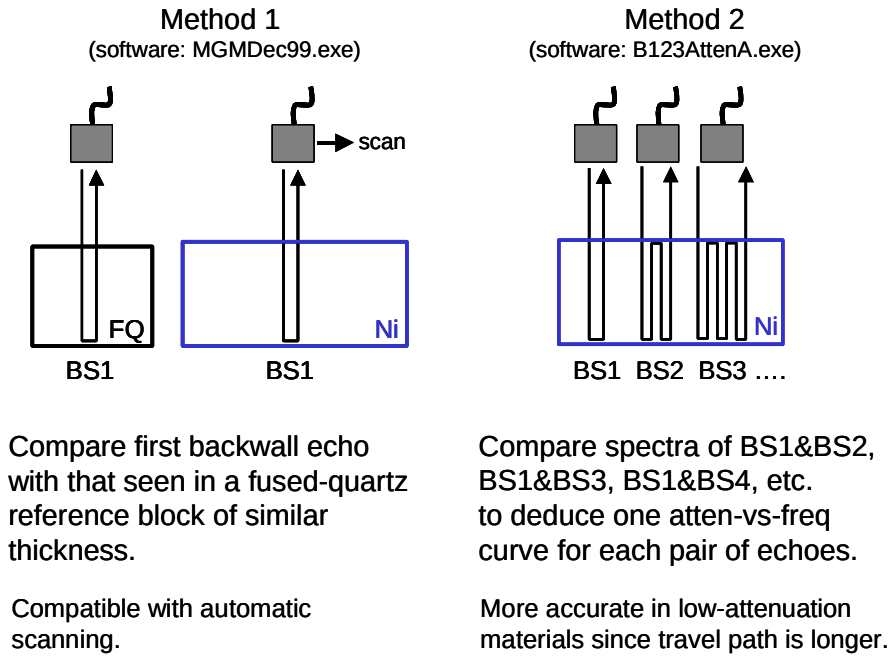

FIGURE 3-31. THE TWO METHODS USED FOR L-WAVE ATTENUATION VERSUS FREQUENCY MEASUREMENTS

In either method, the metal attenuation coefficient at a given frequency (f) is deduced from measured spectral components of two back-surface echoes. For any given back-surface echo, the spectral component at frequency (f), denoted by Γ(f), is written as a product of factors, which account for the effects of the measurement system, beam diffraction, interface losses, and attenuation, respectively. For example, in Method 2, the spectral amplitudes of the first two back-surface echoes are written respectively as

$$\left|\Gamma_{BS1}(f)\right| = \left|\beta(f)D(f)T_{01}R_{11}T_{10}\right|\exp\left[-2\alpha_0(f)Z_0 - 2\alpha_1(f)Z_{01}\right] \tag{3-1}$$

$$\left|\Gamma_{BS2}(f)\right| = \left|\beta(f)D(f)T_{01}(R_{11})^3T_{10}\right|\exp\left[-2\alpha_0(f)Z_0 - 4\alpha_1(f)Z_{01}\right] \tag{3-2}$$

Here, β is related to the efficiency with which electric energy is converted to sound by the measurement system, and D describes the effect of beam spread (diffraction) on the back-wall echo. T_{01} and T_{10} are displacement field transmission coefficients for water-into-solid and solid-into-water, respectively, and R_{11} is the similar solid-into-solid reflection coefficient at the water/solid interface. α_0 and α_1 are attenuation coefficients for water and solid respectively, and Z_0 and Z_1 are the respective thickness of the water layer and the solid specimen. When evaluating the reflection and transmission coefficients, plane-wave values were used [22], which are independent of frequency and depend solely on the densities and sound speeds of the water and solid media. The diffraction correct D is calculated using the well-known Lommel formula [22] for diffraction from an ideal planar piston transducer. D depends on the sonic frequency, the sound speeds in the fluid and solid, the path lengths in each media, and the diameter of the

transducer. The nominal diameter of the transducer (i.e., 0.25 in. = 0.635 cm) was assumed when diffraction corrections were computed. By measuring the spectral amplitudes Γ and using models, as described, to calculate the *R*, *T*, and *D* factors, equations 3-1 and 3-2 may be regarded as a system of two equations with two unknowns: the system efficiency factor β and the metal attenuation coefficient α_1. β can be eliminated by dividing the two equations, leaving a single equation that expresses α_1 in terms of the ratio of the spectral components of the two back-surface echoes. Since Fast Fourier Transform operations are applied to the discretized back-wall A-scan signals, the spectral components (and hence the deduced attenuation values) are obtained at a number of discrete frequencies within the transducer's bandwidth.

Two systems of units are commonly used for quoting attenuation values. The attenuation coefficient α_1, as it appears in equation 3-1 or 3-2, is usually specified in Nepers per centimeter (N/cm), with the Neper being a dimensionless unit. In industrial settings, it is common to describe the loss in signal amplitude (in dB units) due to attenuation while propagating over a given distance (say, in inches). The attenuation value in dB/inch units can be obtained by multiplying the value in N/cm by 22.06. For example, 0.1 N/cm would be equivalent to 2.206 dB/inch.

It has been described in detail how the metal attenuation coefficient α_1 is determined using Method 2 and the first two back-surface echoes. A similar logic can be followed for other cases in which α_1 is deduced from the spectral components of a pair of echoes (e.g., Method 1, or Method 2 with other reflections). Additional discussion of the attenuation measurement techniques can be found in references 1, 17, 19, 26, and 29. Note that when Method 2 is used together with the first three back-surface echoes, there are three different ways of choosing a pair of echoes (BS1+BS2, BS1+BS3, BS2+BS3) and each such pair leads to an attenuation estimate. However, one can show that only two of the three estimates are independent results, and that the third estimate can be expressed in terms of the other two. BS1+BS2 and BS1+BS3 were regarded as the independent pairs.

When making the diffraction corrections, it is tacitly assumed that the sound beam does not appreciably interact with the lateral sides of the specimen. The multi-Gaussian beam model [26 and 27] was used to calculate the lateral size of the propagating beam within the metal coupons, with examples shown in figure 3-32. Theory predicts that the strength of the back-wall response should be proportional to the square of the incident pressure field integrated over the back wall [15]. Thus, the square of the pressure amplitude for various frequencies was plotted, as shown in figure 3-32. A 0.25″ diameter planar transducer operating at a 5-cm water path was assumed and a metal sound speed appropriate for Waspaloy was (0.601 cm/μsec). A distance-amplitude correction has been applied to keep the peak pressure-squared value independent of depth. This makes it easier to discern, at each metal depth, the relative decrease in field strength as one moves laterally away from the beam center. The vertical lines indicate the effective locations of the reflecting surface for the BS1, BS2, and BS3 echoes when measurements are made on the 2″ thick strip specimens. For the 1″ thick slice specimens, the three reflecting surfaces would be half as deep. For either the strip or slice coupons, the lateral width (perpendicular to the beam propagation direction) is 2″, which is indicated on the figure. In figure 3-32, it is of interest to identify those cases in which the beam appreciably intersects the specimen's sidewalls while on its way to the back wall. Note, for example, that the 3-MHz component of the beam for the BS3

echo clearly interacts with the sidewalls of the 2″ wide coupon. Based on such calculations, it was estimated that Method 2 diffraction corrections could likely be trusted above about 3.5 MHz when BS1 and BS2 echoes were used and above about 5.0 MHz when BS1 and BS3 echoes were used.

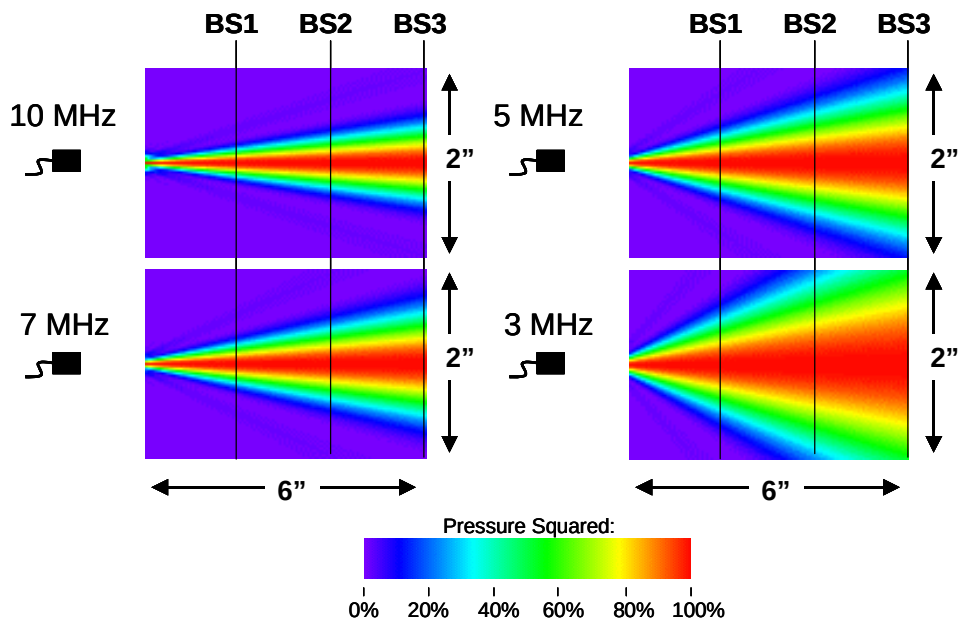

FIGURE 3-32. COMPUTED RADIATION PATTERNS FOR THE SONIC BEAM FROM A 0.25″ DIAMETER TRANSDUCER AT FOUR FREQUENCIES OF INTEREST

When deciding upon the valid frequency range for an attenuation measurement at a given site, one must also consider the bandwidths of the two echoes from which the attenuation determination is to be made, as illustrated in figure 3-33. For one site on the GFM-A strip coupon, the spectral components are shown for the various echoes used in the attenuation determination and the attenuation curves deduced from the spectra. Note that metal attenuation causes the peak frequency in the spectrum to shift downward from its nominal value of 10 MHz and, hence, to influence the bandwidths of the various back-surface echoes. For each analysis (using a pair of echoes), the resulting attenuation versus frequency curve possesses a general systematic trend (monotonically increasing faster than linear) with some scatter about that trend. The scatter tends to be larger at the lowest and highest frequencies in the plotted range where the spectral amplitudes of the echoes are weakest. Accurate attenuation measurements are most difficult for low-attenuation materials, since small errors in setup (probe alignment and position) can induce small back-wall echo changes on the same order as those resulting from material attenuation. For this reason, the scatter typically appears worse at low frequencies where the attenuation is smallest, other factors being equal.

(a)

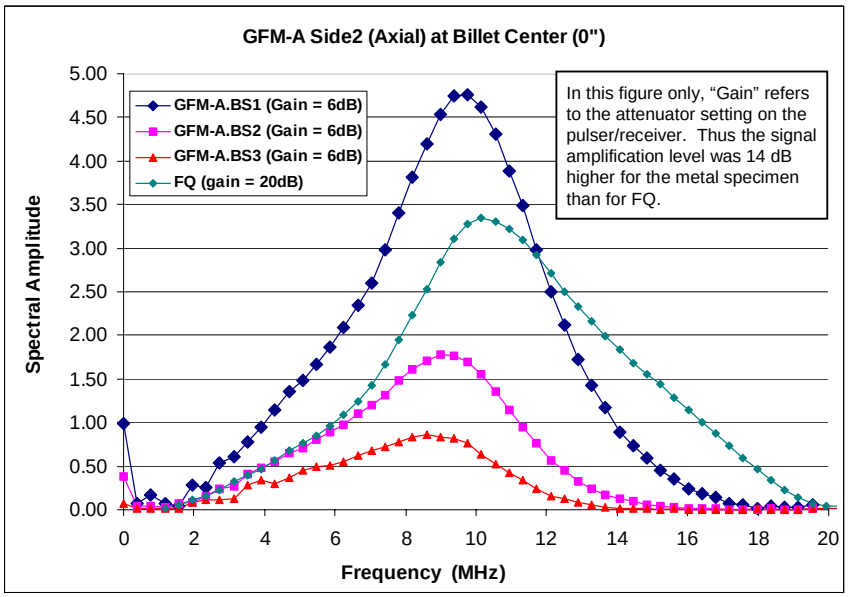

(b)

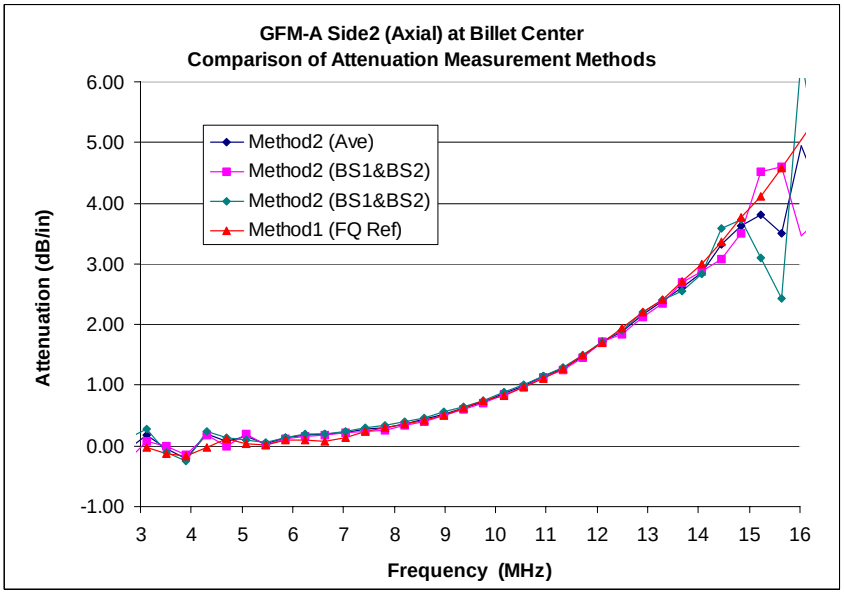

FIGURE 3-33. ATTENUATION MEASUREMENT FOR AXIAL SOUND PROPAGATION AT THE CENTER OF THE IN718 GFM-A BILLET STRIP COUPON (a) SPECTRA OF BACK-WALL ECHOES ON WHICH THE MEASUREMENTS ARE BASED AND (b) DEDUCED ATTENUATION VS FREQUENCY CURVES

Another example of measured back-wall spectra and the resulting attenuation values is shown in figure 3-34. For this specific Waspaloy case, the largest attenuation seen anywhere within the suite of specimens was observed. This large attenuation results in a pronounced downshifting of the center frequency with increasing travel path. Note that in both figures 3-33(b) and 3-34(b) good agreement between the Method 1 and Method 2 attenuation results is generally seen in the frequency range for which the relevant spectral components are all appreciable. This frequency range is significantly wider for the GFM-A example.

(a)

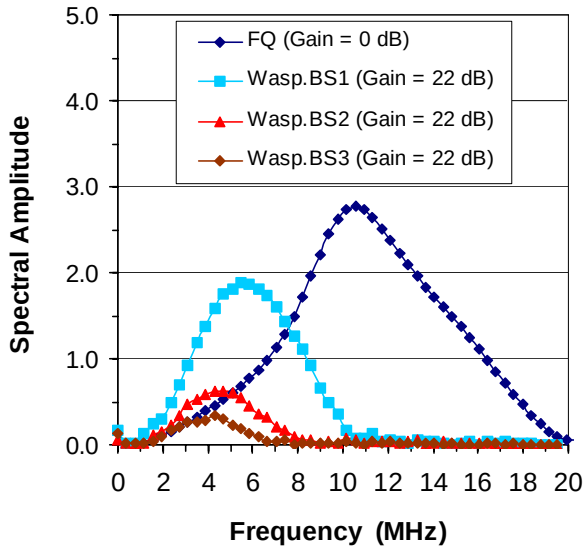

(b)

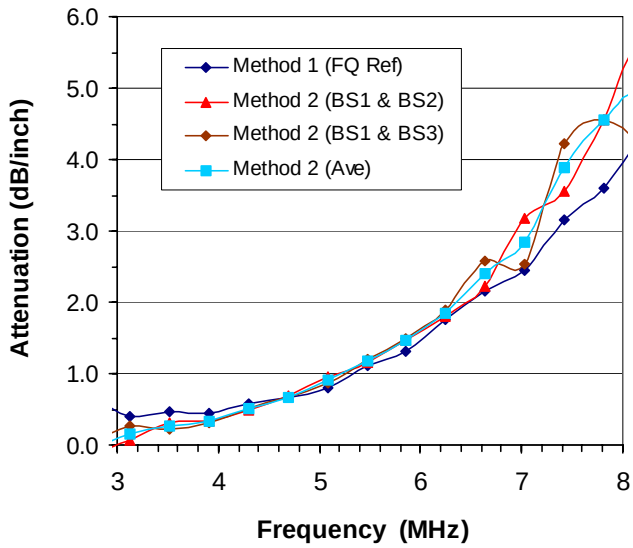

FIGURE 3-34. ATTENUATION MEASUREMENT FOR AXIAL SOUND PROPAGATION AT THE CENTER OF THE WASPALOY BILLET STRIP COUPON (a) SPECTRA OF BACK-WALL ECHOES ON WHICH THE MEASUREMENTS ARE BASED AND (b) DEDUCED ATTENUATION VS FREQUENCY CURVES

In summary, it was found that good agreement between the two methods was generally obtained if one

- takes care to carefully reposition the transducer so that comparative measurements are made at the same physical location in the specimen.
- discounts results where the sonic beam interacts appreciably with the lateral edges of the coupon.
- examines the spectra of the back-wall echoes being used to determine the valid frequency range for the measurement.

- uses the same equipment gain setting for all echoes that contribute to the measured attenuation at a given site. The measured attenuation was quite low for many of the specimen/measurement site combinations considered.

In such cases, the small effect of attenuation on the spectrum of an echo could be similar to that caused by small-equipment nonlinearities introduced when gain settings were changed. For a given measurements system, a gain change of 10 dB may not alter every frequency component of an echo by exactly 10 dB. To limit such nonlinearities, the gain setting of the pulser/receiver was fixed at each measurement site, and only the volts/division setting of the digitizing oscilloscope was altered.

Because attenuation values for the suite of specimens as a whole tended to be rather small, a decision was made to adopt Method 2 as the preferred measurement technique. Two attenuation estimates were then made for each measurement case: one from the BS1 and BS2 echoes and one from BS1 and BS3. For each estimate, the valid frequency range was then estimated from beam spread and bandwidth considerations. At frequencies where both the BS1+BS2 and BS1+BS3 estimates were deemed valid, the two estimates were averaged. Otherwise, the quoted result is that for the BS1+BS2 analysis alone. In some cases, to check repeatability, multiple measurement trials were made. In those cases, the reported values are an average over trials. The decision was to only trust results for which the spectral amplitudes of both echoes were deemed to be appreciable. Appreciable was usually interpreted as meaning "having a spectral amplitude of at least 10%-15% of the maximum amplitude for that echo." In practice, the lower limit on frequency was usually determined by the beam spread considerations (see figure 3-32), while the upper limit was determined by the 15% spectral amplitude rule. As the attenuation of the specimen increased, the upper limit on the trustworthy frequency range decreased. Table 3-3 relates the upper frequency limit for trustworthy measurements to the deduced attenuation at one frequency of interest, namely, 8 MHz. This table was used in most instances to rapidly estimate frequency limits for quoted attenuation values.

TABLE 3-3. APPROXIMATE UPPER FREQUENCY LIMIT FOR TRUSTWORTHY ATTENUATION MEASUREMENTS AS A FUNCTION OF THE MATERIAL ATTENUATION NEAR 8 MHz

Atten. at 8 MHz (N/cm)	Attn. at 8 MHz (dB/inch)	Max freq. for BS1+BS2	Max freq. for BS1+BS2
0.18	4.0	7.7	6.6
0.08	1.8	9.8	8.9
0.02	0.4	13.2	12.4
0.005	0.1	15.1	14.2
<0.005	<0.1	15.7	~15.7

Note: Measurements used a 0.25″ diameter, 10-MHz broadband planar probe.

In C-scan studies (see section 3.1.2.1) of back-wall echo amplitude, it was noted that the amplitude varied significantly with radial position in all four of the strip coupons. As expected,

the same trends were seen for measured UT attenuation values. Figure 3-35 shows one example of how measured attenuation-versus-frequency curves vary with radial position. For the case shown, namely, hoop propagation at sites in the IN718 GFM billet, the measured attenuation at a given frequency is highest near the billet center and decreases as the billet OD is approached. A similar behavior of decreasing attenuation with increasing distance from the billet center was also seen for the Waspaloy and V-Die-B coupons (but not for V-Die-A). Measured attenuation values, like those shown in figure 3-35, are typically believed to be reproducible to within about ±0.01 N/cm or ±0.2 dB/inch, meaning that trained operators performing measurements at the same site on different days would generally obtain results differing by 0.01 N/cm or less. This error estimate is based on duplicate measurements made on selected specimens. When sufficient spectral strength is present to easily perform an attenuation measurement, the final accuracy of the measurement is usually dependent on the operator's ability to adjust the two probe orientation angles so that the incident beam is normal to the entry surface. For low-attenuation materials, a small angulation error of 0.1 or 0.2 degrees can introduce an appreciable error into the measured attenuation.

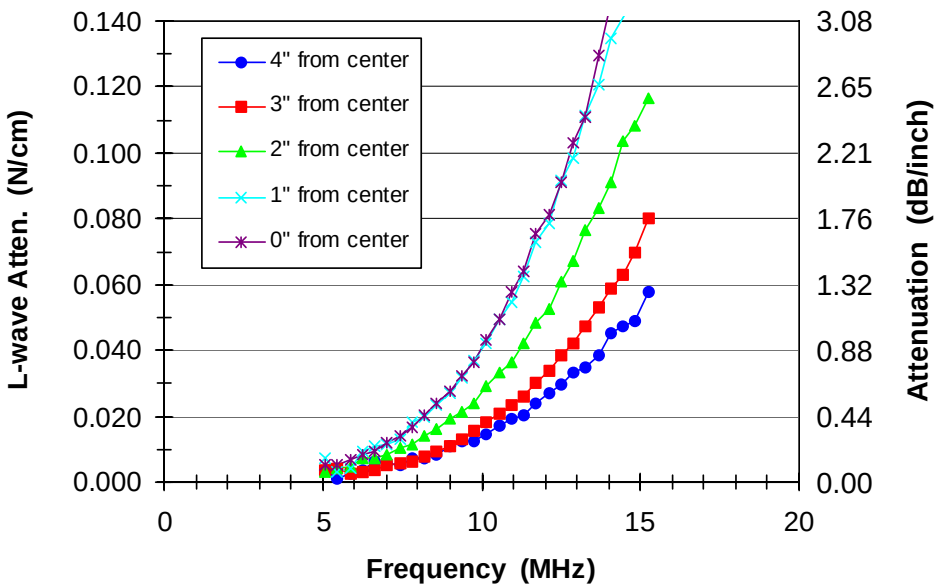

FIGURE 3-35. MEASURED ATTENUATION VALUES IN THE 5-15 MHz RANGE AT THE FIVE SITES IN THE GFM-A BILLET STRIP
(Beam propagation is in the hoop direction, i.e., perpendicular to side 3 of the strip coupon.)

In C-scan studies of the strip coupons (section 3.1.2.1), it was also noted that at a given radial site there was generally little difference in the back-wall amplitudes, as measured in the axial and hoop directions. As expected, this tendency was also seen in the measured attenuation values. Examples are shown figure 3-36, where one sees both the variation in measured attenuation with radial position and the similarity in attenuation values for propagation in the axial and hoop directions. In fact, as discussed in section 3.1.4.2, measured attenuation values at a given site in a given specimen tended to be fairly isotropic, i.e., similar for all three orthogonal propagation directions.

(a)

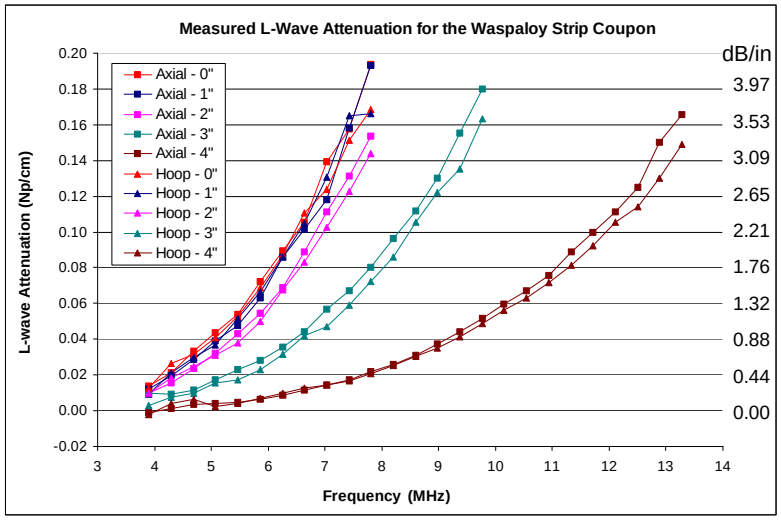

(b)

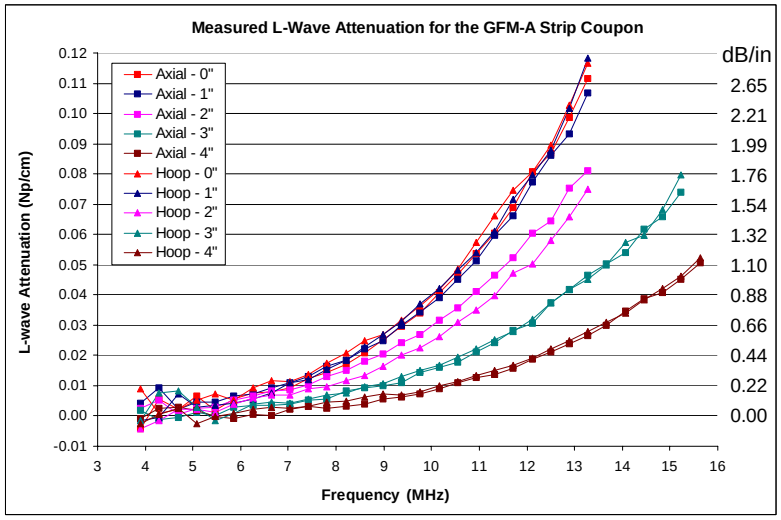

FIGURE 3-36. DEDUCED ATTENUATION VALUES AT VARIOUS SITES FOR AXIAL AND HOOP PROPAGATION IN THE (a) WASPALOY AND (b) IN718 GFM-A STRIP COUPONS

ISU models for simulating inspections often assume that the attenuation can be approximated as a power law in frequency:

$$\textit{Attenuation in N/cm units} = C\ (\textit{frequency}\ \text{in MHz})^{p} \tag{3-3}$$

For this reason, each measured attenuation-versus-frequency curve was fit to such a power law. The fitting process consisted of adjusting the values of the multiplicative constant (C) and exponent (p) to minimize the sum of the squares of the differences between the measured attenuation values and those obtained by evaluating the power law at the discrete frequencies in question. Examples of four such fits are shown in figures 3-37 and 3-38.

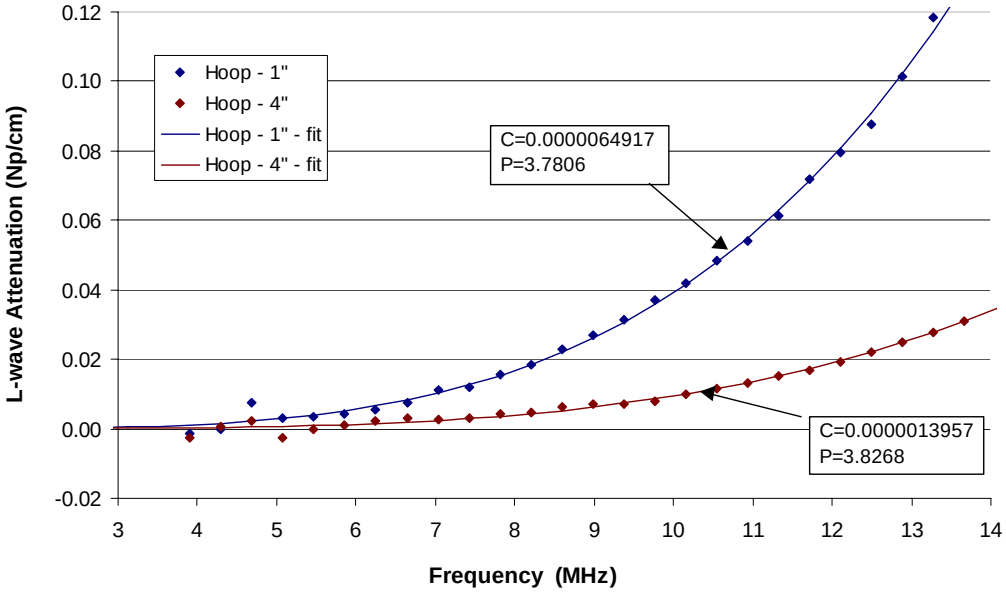

FIGURE 3-37. POWER-LAW FITS TO MEASURED ATTENUATION VALUES AT TWO LOCATIONS IN THE IN718 GFM-A BILLET SPECIMEN
(Measurements are for hoop propagation at sites 1″ and 4″, respectively, from the billet center.)

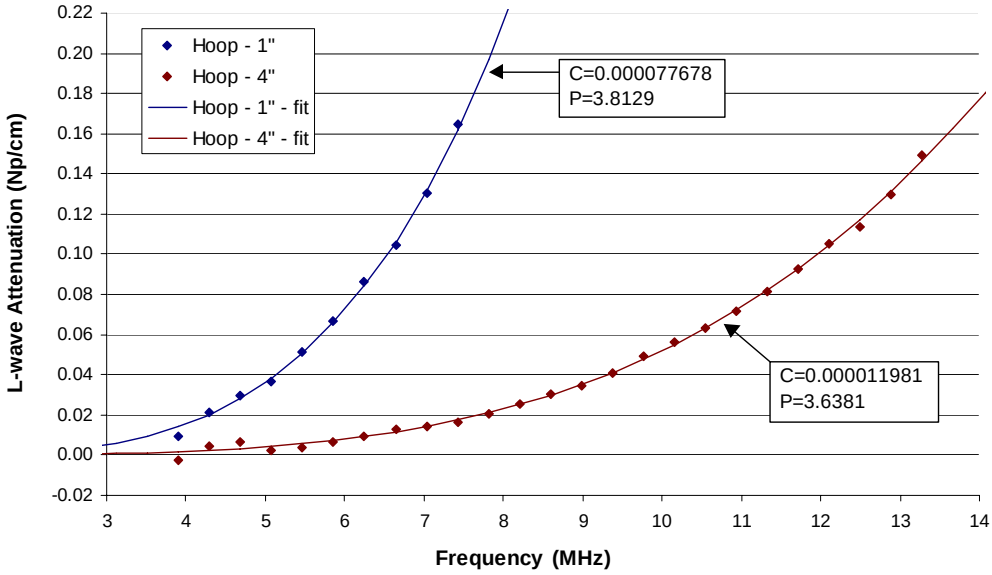

FIGURE 3-38. POWER-LAW FITS TO MEASURED ATTENUATION VALUES AT TWO LOCATIONS IN THE WASPALOY BILLET SPECIMEN
(Measurements are for hoop propagation at sites 1″ and 4″, respectively, from the billet center.)

Generally speaking, it was found that each of the power-law fits provided a good overall summary of the trend of the measured data. One should be aware, however, that there are often other $\{C, p\}$ pairs for a given case that provide a fit of similar overall quality to that of the quoted pair. Also, if one alters the frequency range of the measured data contributing to the fit, a different $\{C', p'\}$ pair will generally result. For two fits using different ranges of the same data, it is not too unusual to find differences in exponents of $|p-p'| > 0.2$ or more. For the Ni billet specimens in the frequency range of interest (5-15 MHz), power-law fits, in virtually all cases, yielded powers in the $3 < p < 4$ range.

In all, attenuation-versus-frequency measurements were carried out for 60 cases: four billet specimens, five sites per specimen and three propagation directions per site. The results, including fitted power-law parameters, are summarized and discussed in section 3.1.4.2.

3.1.3.3 Grain Noise FOM Measurement.

Detailed backscattered noise measurements were made at the same sites where attenuation values were measured. The goal was to determine the frequency-dependent FOM parameter that is a measure of the noise-generating capacity of the microstructure. The basic measurement setup is shown in figure 3-39. A focused transducer, oriented at normal incidence, is scanned above the metal specimen. No distance-amplitude compensation is applied. For such a constant-gain measurement, the backscattered noise level tends to be highest for scattering from the focal zone [20, 21, and 22]. Digitized grain noise A-scans are acquired at a few hundred transducer positions and stored for later analysis. A reference echo is also acquired and subsequently used to deduce the measurement system efficiency factor. For FOM determination from measured noise data, it is important to accurately know the focal properties of the transducer being used. The same 1/2″ diameter, 15-MHz broadband transducer used earlier for the preliminary noise C-scans was used for the FOM measurements. This transducer had previously been characterized using beam-mapping methods to determine its true focal characteristics. The basic characterization procedure is described in reference 22 and involves comparing measured responses from a small reflecting target scanned along the beam axis to model predictions for an ideal focused piston transducer (IFPP). The transducer in question was found to have an effective diameter of 1.21 cm (0.48″), a geometric focal length in water of 9.65 cm (3.80″), and an actual focal length of 9.2 cm (3.6″) in water.

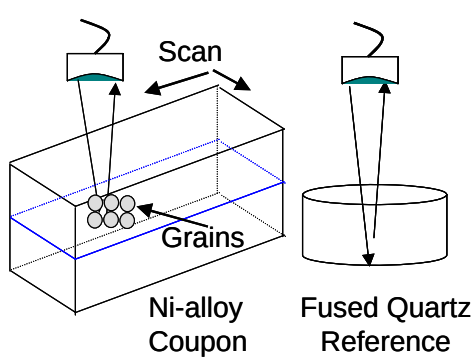

FIGURE 3-39. IMMERSION SETUP FOR GRAIN NOISE FOM MEASUREMENT

For the noise measurements on the Ni billet strip coupons, the water path was adjusted to place the actual beam focus 0.6″ deep in the metal. Because of metal sound speed differences, the water path varied slightly from specimen to specimen but was typically near 1.3″. For the slice coupons, the beam focus was approximately 0.5″ deep in the metal, and the water path was typically 1.7″. At each measurement site, the transducer was scanned over a 0.54″ by 0.54″ area using a step size of 0.03″ in each direction. Backscattered noise A-scans were digitized at a 100-MHz sampling rate and stored. The depth (time) region for which data was stored was approximately 1.8″ (16 μsec) for the strip coupons and 0.9″ (8 μsec) for the thinner slice coupons. At each transducer position, 500 A-scans were typically acquired, and these were averaged to reduce the contribution of measurement system (electronic) noise. In all cases, the reference signal was a back-wall echo from a 1/2″ thick FQ block with the water path adjusted to position the geometric focus at the back wall.

In deducing the value of the grain noise FOM at a given frequency, a time gate is first selected for the analysis, typically one bracketing the focal zone where the average noise level tends to be highest. Using that gate, the spectrum of each stored noise A-scan is computed, and the spectra are averaged. For technical reasons, a root mean-squared (rms) average is computed at each frequency rather than a simple average. The rms noise spectrum is then compared to the spectrum of the reference echo, and the formalism of the so-called independent scatterer noise model is used to deduce an FOM-versus-frequency curve.

The independent scatterer noise model, the associated FOM extraction procedure, and examples of deduced FOM-versus-frequency curves for metals are discussed in detail in references 20-22 and references 28-34. In addition, appendix B of reference 1 describes the historical development of the evolving grain noise models and summarizes their practical uses. As illustrated in figure 3-40(a), the independent scatterer model makes the assumption that the observed noise is dominated by single-scattering events, i.e., events in which sound energy is directly reflected back to the transducer by a metal grain. In particular, the model assumes that the received noise is an incoherent superposition of the direct echoes from all the insonified grains. As summarized in figure 3-40(b), the model formalism expresses the rms average spectral amplitude of the received noise at a given frequency in terms of a product of factors. The factors depend on both the details of the measurement system (e.g., transducer focal properties, time gate, system efficiency) and on the properties of the metal specimen (sound speed, attenuation, and noise capacity). One of the factors, known as the FOM, is a direct measure of the noise generation capacity of the microstructure. By using the measured reference signal spectrum to deduce the measurement system efficiency factor (β), the FOM can be deduced from the measured noise data. The standard unit for the FOM is $cm^{-1/2}$.

The determination of the grain noise FOM requires analysis of backscattered noise RF waveforms within some designated time gate. A time gate is generally used that brackets the focal zone of the transducer being used because the grain noise level tends to be highest there; this reduces the impact of any residual electronic noise that remains after signal averaging. In particular, for the results quoted in section 3.1.4.2, a time gate of 5.11 μsec duration (512 discrete time points with 0.01 μsec spacing) centered at the focal depth in the metal was used with the focal depth computed from the actual focal depth in water and the measured sound speeds in the water and metal. The locations of this principal time gate and several other time

gates used in preliminary analyses are illustrated in figure 3-41(a). Times are measured relative to the center of the front-surface echo (t = 0) so that noise arrival time is directly proportional to sound penetration depth. The smaller time gates are designated G1, G2, …, G6 from left to right in the figure, and the larger (principal) gate is designated G7.

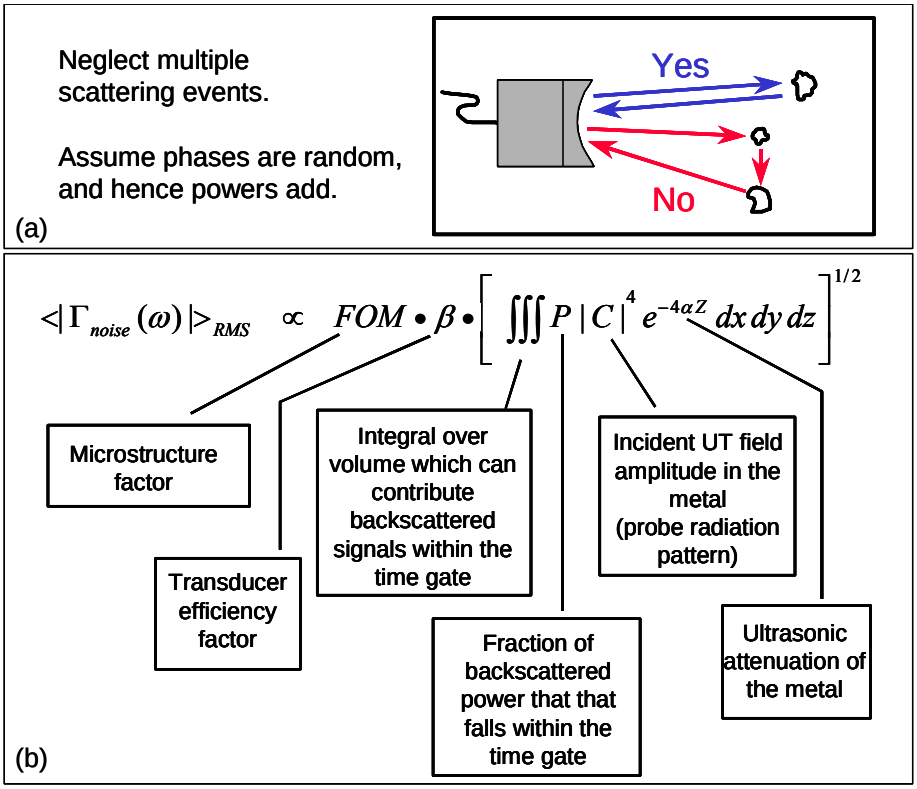

FIGURE 3-40. (a) THE INDEPENDENT SCATTERER NOISE MODEL NEGLECTS GRAIN NOISE CONTRIBUTIONS FROM MULTIPLE-SCATTERING EVENTS AND (b) RELATIONSHIP BETWEEN THE AVERAGE MEASURED NOISE SPECTRUM AND VARIOUS MICROSTRUCTURE AND MEASUREMENT SYSTEM FACTORS IN THE NOISE MODEL

Figure 3-41(a) also shows the depth dependence of the grain noise level at each of the five measurement sites. The plotted quantity is the so-called rms noise level [22, 28, and 29]. This is computed directly from the stored A-scan voltages. Recall that at a given measurement site (i.e., the billet center) several hundred A-scans are acquired by scanning the transducer over a small area centered at the site. At a fixed sound arrival time, i.e., 3.0 μsec after the front surface echo, the noise voltages seen at that time in the various A-scans are squared. These squares are then averaged and the square root of the average is taken. This process is repeated at each time instant. The resulting rms noise level curve generally has a slowly varying underlying trend with statistical jitter superimposed on it. The jitter decreases as the number of A-scans used in the average increases. In figure 3-41(a), a prominent focal maximum is seen in the rms noise level near t = 5 μsec at each of the five measurement sites. In addition, the absolute rms noise level is seen to systematically decrease as one moves from the center of the billet toward the OD. The

lower panel in figure 3-41(a) displays deduced FOM-versus-frequency curves for four of the measurement trials conducted on the GFM-A billet strip. The results are shown for two inspection directions (axial and hoop) at two sites (0″ and 4″ from the billet center). In each case, the principal time gate (G7 in figure 3-41(a)) was used in the analysis. One notices that the FOM values tend to rise with frequency at a rate faster than linear, and that the results are relatively independent of inspection direction at each site. The deduced FOM values are considerably higher near the billet center than near the OD for this specimen. This is as expected from the preliminary noise C-scans shown in figure 3-20.

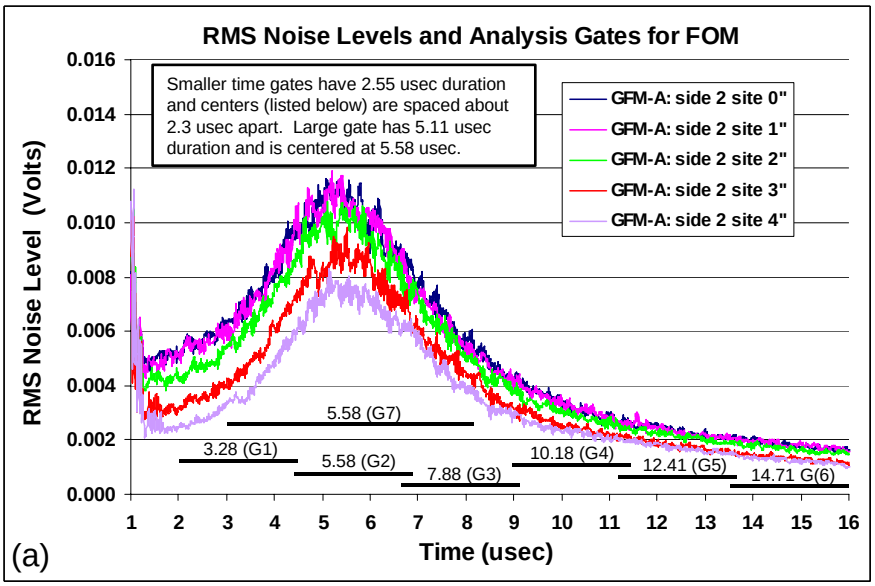

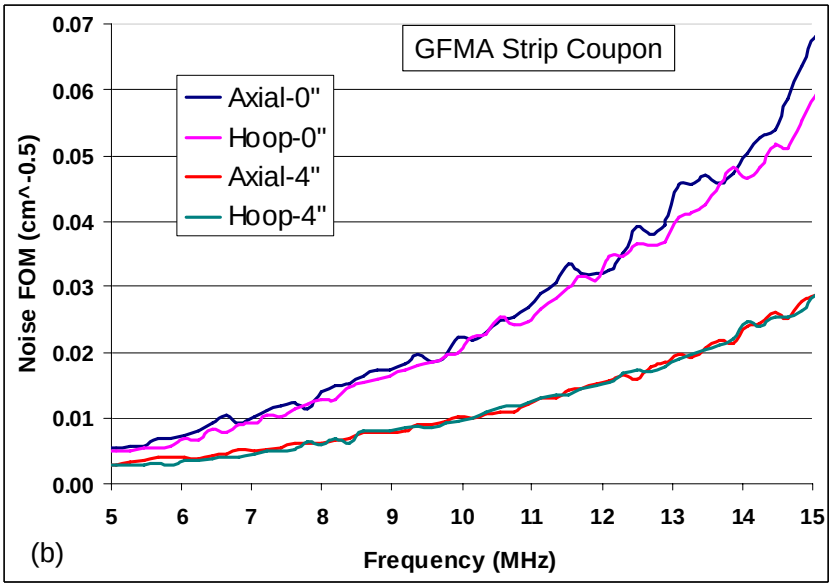

FIGURE 3-41. (a) ROOT MEAN SQUARE NOISE LEVELS MEASURED AT FIVE SITES IN THE GFM-A IN718 BILLET (AXIAL PROPAGATION), AND TIME GATES USED FOR FOM DETERMINATION AND (b) DEDUCED FOM VALUES FOR SELECTED GFM-A CASES USING THE PRINCIPAL TIME GATE (G7)

Figure 3-42 shows examples of rms noise levels and deduced FOM values for the Waspaloy billet. As the billet center is approached, the attenuation becomes substantial (approximately 11 dB/inch at 10 MHz). This large attenuation causes grain noise from sites deep within a billet specimens to be diminished relative to noise from shallower sites. When the attenuation is large enough, the focal maximum in the rms noise curve can be suppressed, as is the case in figure 3-42(a). It was noted that the UT attenuation, as measured earlier, is used in the FOM extraction procedure. As illustrated in figure 3-42(b), the noise analysis leads to FOM values near the center of the Waspaloy billet, which are significantly larger than those near the OD. Again, this is as expected from the preliminary noise C-scans shown in figure 3-19. As in the GFM-A example, the deduced FOM values for Waspaloy at a given measurement site are approximately independent of inspection direction, although some differences in the axial and hoop FOM values near the billet center are seen at the higher frequencies. This measured difference is believed to largely be a manifestation of the uncertainty in attenuation values at the higher frequencies. At the 0″ site in Waspaloy, measured attenuation values are trustworthy up to about 8 MHz. For FOM extraction at higher frequencies, the attenuation was estimated by extrapolating the fitted power law to higher frequencies. As was shown in figure 36(a), attenuation values below 8 MHz are very similar for axial and hoop propagation at the 0″ site in Waspaloy. However, at higher frequencies, the extrapolated attenuation values for axial propagation are somewhat larger than those for hoop propagation. This boost in assumed attenuation leads to a similar boost in the deduced FOM value and accounts for most of the difference between the axial and hoop results at the 0″ site that are seen at the higher frequencies in figure 3-42(b). Larger assumed attenuation values will always lead to larger deduced FOM values. This is because a larger attenuation value implies that grain noise echoes will be suppressed more by attenuation, thus requiring a larger FOM value (larger backscatter capacity) to produce the grain noise that is observed.

In principle, if the assumptions of the independent scatterer noise model hold, if the radiation pattern of the transducer is well modeled, and if the microstructure does not vary with inspection depth, then the FOM values deduced from the noise data should be independent of the time gate used in the analysis. Several analyses were carried out to examine the dependence of the deduced FOM values on the choice of time gate. In one set of calculations, the backscattered noise data for the GFM-A IN718 specimen was reanalyzed using the seven time gates shown in figure 3-41(a). The resulting FOM-versus-frequency curves are shown in figure 3-43. The extraction of FOM values from measured noise echoes requires knowledge of the attenuation of the specimen. In particular, the attenuation value used in the analysis should be that which describes the rate of loss of sound energy with increasing propagation distance [22, 28, and 31]. Two attenuation choices were made in the analyses leading to figure 3-43: (1) using the attenuation-versus-frequency curve deduced from earlier back-wall echo measurements and (2) assuming the energy loss attenuation to be negligible. The attenuation value appropriate for backscattered noise should be between these two limits. This is because attenuation values deduced from back-wall reverberations generally contain contributions from both energy loss and beam distortion during propagation [15]. Only the energy loss contribution is of importance in the backscattered noise analysis. Figure 3-43 shows that there is a systematic dependence of the deduced FOM on the time gate choice, especially at higher frequencies, with deeper gates generally leading to higher FOM values. This trend is less prominent, but still present, when negligible attenuation is assumed. One indication that beam distortion effects are a significant

contributor to back-wall signal attenuation is the observation of back-wall echo fluctuations when the probe is scanned over a region of uniform average attenuation [15]. Such fluctuations, which are often very prominent in Ti alloy billet specimens, were not seen in these Ni billet specimens at the inspection frequencies. This suggests that the energy loss attenuation is quite close to the measured back-wall attenuation. The measured back-wall attenuation values were consequently used as input energy loss values for the final FOM determinations; these results are summarized in section 3.1.4.2.

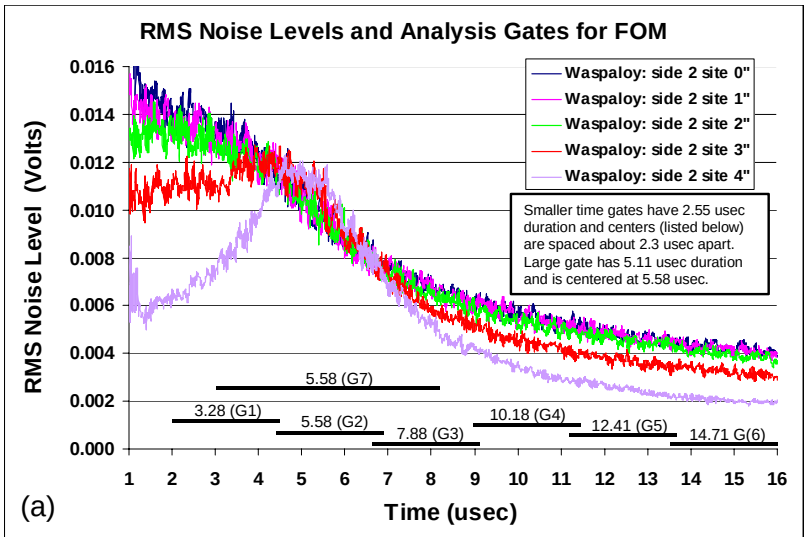

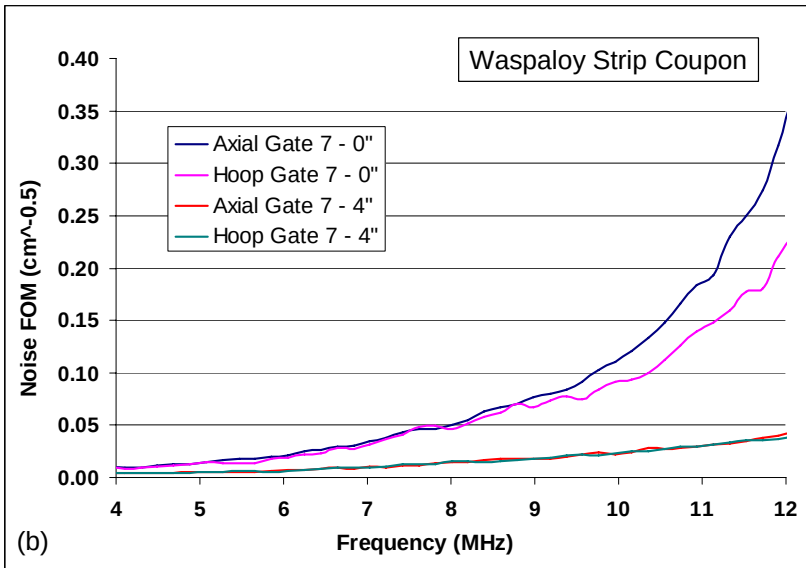

FIGURE 3-42. (a) ROOT MEAN SQUARE NOISE LEVELS MEASURED AT FIVE SITES IN THE WASPALOY BILLET (AXIAL PROPAGATION) AND TIME GATES USED FOR FOM DETERMINATION AND (b) DEDUCED FOM VALUES FOR SELECTED WASPALOY CASES USING THE PRINCIPAL TIME GATE (G7)

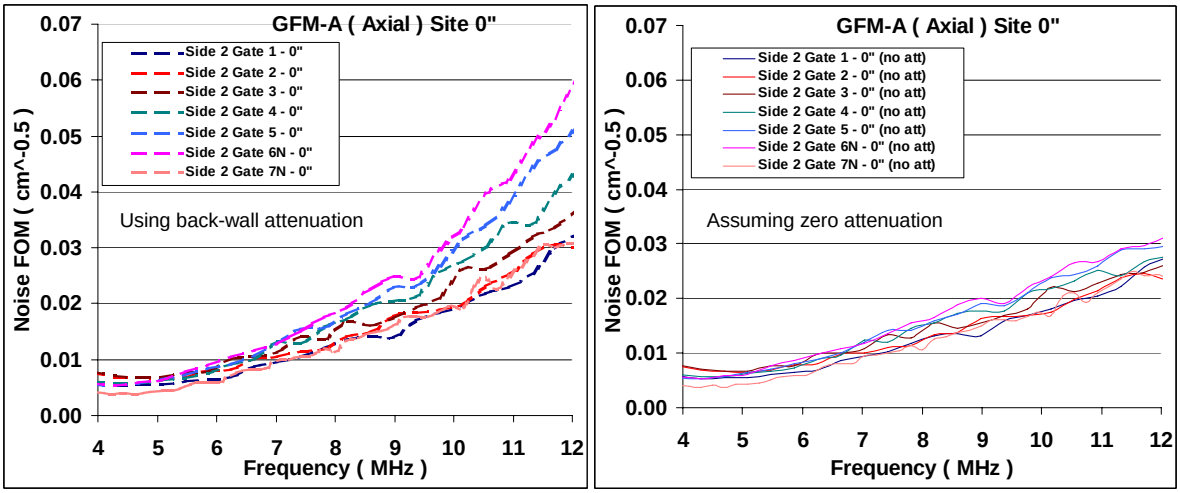

(a) (b)

FIGURE 3-43. GRAIN NOISE FOM VALUES FOR AXIAL PROPAGATION AT THE CENTER OF THE GFM-A IN718 BILLET DEDUCED USING THE SEVEN TIME GATES INDICATED IN FIGURE 40(a); (a) USING THE MEASURED BACK-WALL ATTENUATION FOR THE ENERGY LOSS ATTENUATION AND (b) ASSUMING THAT THE ENERGY LOSS ATTENUATION IS NEGLIGIBLE

The fundamental reasons behind the apparent dependence of FOM on gate choice are not fully understood. The gate dependence may arise from the neglect of multiple-scattering events by the underlying noise model. Near the centers of the Ni alloy billets, the UT properties are relatively uniform, suggesting that the microstructures are relatively uniform as well. This affords an opportunity to test some predictions of the independent scatterer noise model. For example, the model can be used to predict the depth dependence of the rms noise level from an input FOM-versus-frequency curve. Such model predictions, which assume a homogeneous (depth independent) microstructure, are compared with the experiment in figure 3-44 for axial sound propagation near the center of the GFM-A billet. Two model results are shown; these use the measured attenuation and zero, respectively, for the energy loss attenuation in the FOM extraction analysis and the ensuing rms noise level prediction. The model was shown to do a good job of predicting the overall shape and location of the focal maximum. However, the measured noise levels tend to be above the predicted result for times that are either well before or well after the focal maximum. Departures from the model predictions at early times are not unexpected, since ring-down of the front-wall echo tends to boost the measured rms noise level over that due to grain noise alone. Departures at later times are of more interest. One possible explanation is that multiple-scattering events are contributing significantly to the observed noise, particularly in the insonified regions away from the focal zone. These multiple-scattering contributions, which are not treated by the model, tend to boost the grain noise level above that expected based on single scattering alone. Consequently, when noise data is analyzed using the single-scattering model, the enhanced noise level is translated into an overstated FOM value.

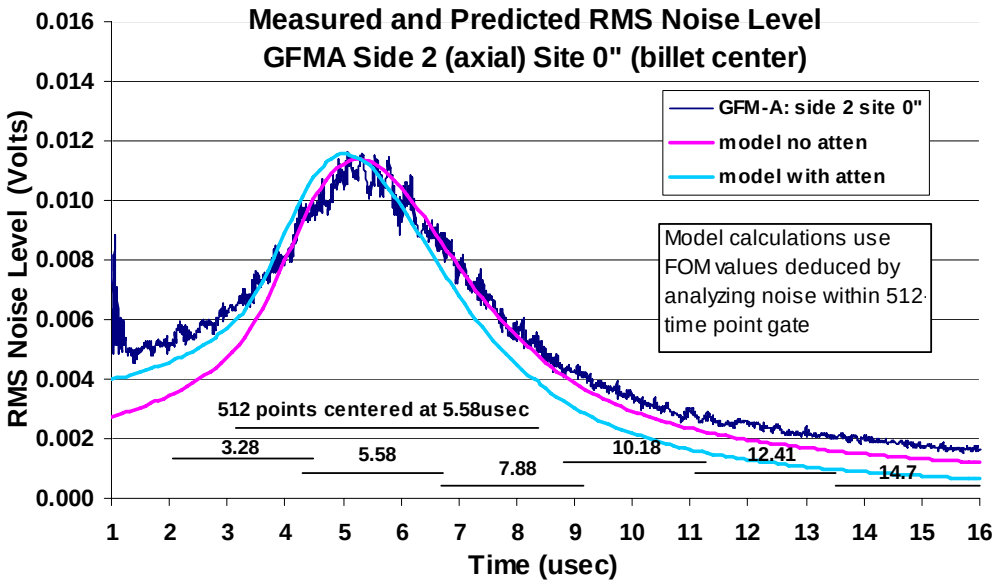

FIGURE 3-44. MEASURED AND PREDICTED RMS GRAIN NOISE LEVELS FOR AXIAL BEAM PROPAGATION AT THE CENTER OF THE IN718 GFM-A BILLET

The observed dependence of FOM on the time gate choice may indeed be due to multiple-scattering events and the manner in which they contribute to the observed noise in and away from the focal zone. Alternatively, the gate dependence may be due to the accuracy of the ideal piston probe assumption: the transducer's actual radiation pattern may be similar to that of a piston probe near the focal zone but depart from it systematically as one moves away from the focal zone. Since transducer characterization procedures tend to emphasize data acquired near the focal zone, noise data analyses and model predictions based on such transducer characterizations are likely more trustworthy in the focal zone.

Additional experiments were conducted to shed further light on the dependence of deduced FOM values on the choice of time gate. The experimental setups and results for two complementary FOM measurements in the GFM-A billet are contrasted in figure 3-45. In the first experiment, the inspection water path was fixed and grain noise data was gathered. The resulting rms noise-versus-time curve is shown in figure 3-45(b), together with three of the time gates that were subsequently used for FOM determination. The FOM-versus-frequency curves, deduced by analyzing the spectral components of the backscattered noise within each time gate, are shown in figure 3-45(c). One sees that backscattered noise data beyond the focal zone generally led to a larger deduced FOM value than noise data from within the focal zone. A second round of measurements was then made using the same transducer. As depicted in figure 3-45(d), the water path was varied to alter the depth of the beam focus in metal. Shifting the beam focus downward caused the peak in the rms grain noise level to shift to later arrival times, as expected. For each of the three water paths, the FOM-versus-frequency curve was deduced using a time gate enclosing the focal maximum, as shown in figure 3-45(e). The resulting FOM curves (figure 3-45(f)) were very similar to one another and in good agreement with the earlier result that used noise data from the focal zone. Thus, measured FOM does not appear to depend on metal depth per se but rather on the location of the analysis region relative to the focal zone.

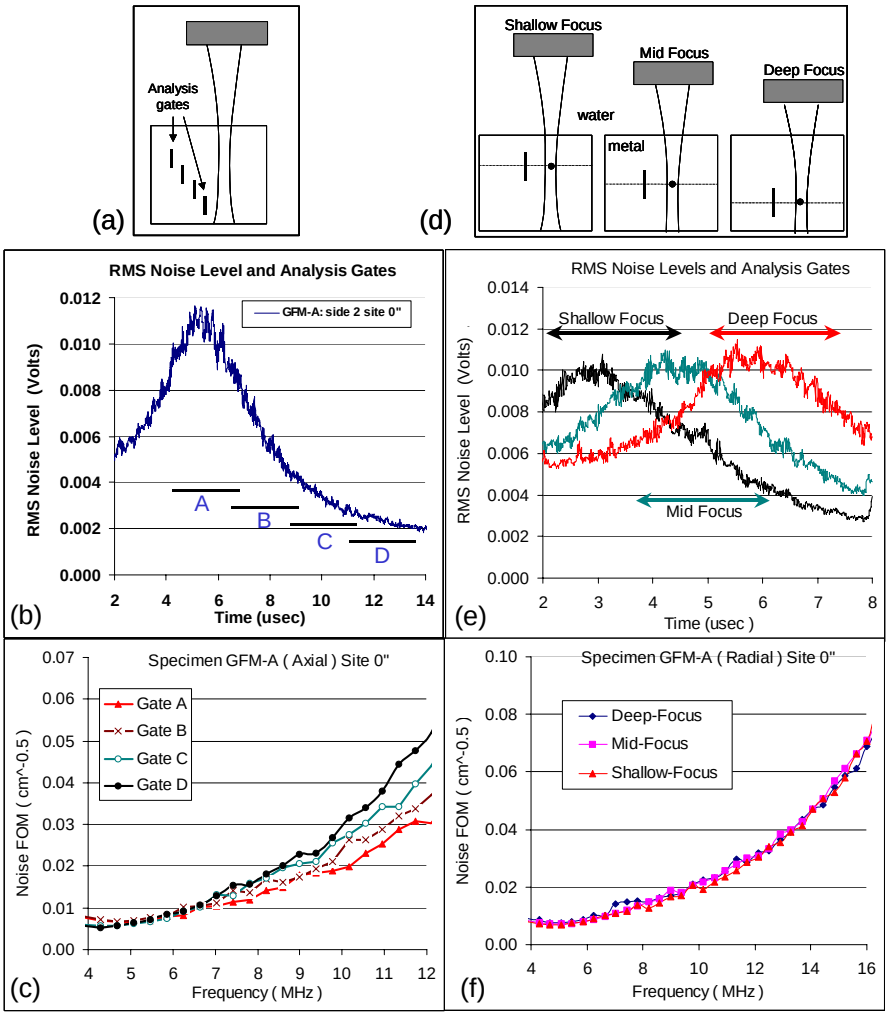

FIGURE 3-45. ADDITIONAL FOM MEASUREMENTS AND ANALYSES AT THE CENTER OF THE IN718 GFM-A BILLET SPECIMEN (a AND d) MEASUREMENT SETUPS (b AND e) RMS GRAIN NOISE PROFILES WITH ANALYSIS GATES INDICATED, AND (c AND f) RESULTING FOM VALUES

Note that the trends evident in figure 3-45 are consistent with preliminary computations of a two-dimensional noise model recently developed by R. Roberts and A. Li [35]. In those computations, ensembles of model grains are generated with each grain having a randomly selected sound velocity in the beam propagation direction (simulating random grain orientations). Backscattered rms grain noise levels were then computed, assuming an incident-focused sound beam. Two types of computations were made: one using the full-model formalism that includes both single- and multiple-scattering effects and another in which only single-scattering effects were accounted for. The difference in rms noise levels between the full-scattering computation (including multiple-scattering effects) and the single-scattering computation was found to increase as one moved away from the focal zone in either direction [35]. This led to deduced FOM values that increased away from the focal zone when the single-scatterer model was used in the extraction of FOM from measured noise data.

Alternatively, one can craft an explanation for the trends in figure 3-45 that does not rely on the presence of a significant multiple-scattering contribution to the observed grain noise. One could posit that the transducer in question has a radiation pattern that differs from that of an idea IFPP. If, as in figure 3-45(d), one performs a series of measurements that all use the same portion of the radiation field (e.g., the focal zone), the error made in assuming that the radiation field is the same as that of an IFPP would be similar for each measurement. Thus, the deduced FOM values, although in error, would be the same for each measurement, as is the case in figure 3-45(f). However, if different experiments use different regions of the radiation field in their analyses (as is the case for figure 3-45(a)), the error made by assuming an IFPP radiation field would be different for each experiment and hence lead to different deduced FOM values, as is the case in figure 3-45(c). Thus, although the results of figure 3-45 are quite interesting, they are open to different interpretations. The reasons underlying the dependence of deduced FOM on gate choice are expected to be the subject of future research that is beyond the scope of the current study.

Section 3.1.4.2 summarizes the grain noise measurements by tabulating the best estimates of FOM for several inspection frequencies of interest, namely, 5, 7.5, 10, and 12.5 MHz. For a given coupon site and inspection direction, this involves analyzing backscattered noise data within a time gate, fitting a curve through the data in a localized frequency region, and evaluating the fitted curve at the frequency of interest. Curve fitting was deemed necessary because the FOM-versus-frequency results deduced from a limited number of RF noise waveforms display a significant scatter about the general trend, as evidenced by the wiggles seen in the FOM curves shown in figures 3-41 through 3-43. The curve-fitting operation is demonstrated in figure 3-46 for a typical case. Since the fitting interval is relatively small in frequency (about 1.5 MHz in length), it was found that a simple linear fit suffices.

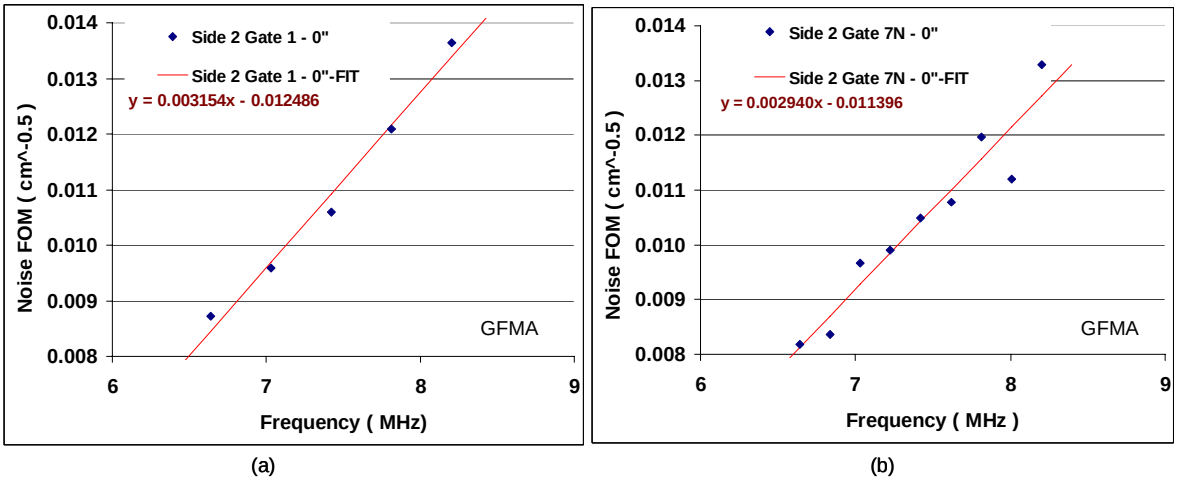

FIGURE 3-46. EXAMPLES OF LOCAL LINEAR FITS USED TO DETERMINE THE BEST ESTIMATE OF THE GRAIN NOISE FOM AT 7.5 MHz (a) USING A 256-POINT GATE CENTERED 2.38 μsec AFTER THE FRONT-WALL ECHO AND (b) USING A 512-POINT GATE CENTERED 5.58 μsec AFTER THE FRONT-WALL ECHO
(Both fits are for axial propagation near the center of the GFM-A billet.)

As a practical matter, the dependence of FOM on gate choice and assumed energy loss attenuation leads to an uncertainty in measured FOM values. For a given billet specimen, measurement site, and inspection direction, uncertainty can be quantified by repeatedly analyzing the stored noise data using different time gates and different attenuation choices and examining the spread in the resulting FOM values. Such studies have been performed, and typical results are shown in figures 3-47 and 3-48 for IN718 and Waspaloy examples, respectively. In each figure, the deduced FOM values at 7.5 MHz are plotted versus the measured back-wall attenuation, with results shown for each of the seven time gate choices indicated in figures 3-41(a) and 3-42(a). In the leftmost panel of figures 3-47 and 3-48, the energy loss attenuation assumed in the FOM analysis was equal to the measured back-wall attenuation. In the rightmost panel, the energy loss attenuation was assumed to be zero. In both figures 3-47 and 3-48, the dependence of deduced FOM on time gate choice is substantial, with time gates in or near the focal zone tending to yield the smaller FOM values, as discussed earlier in this section. It was believed that the most accurate FOM estimates are obtained when gate 7 is used because (1) this gate encloses the bulk of the focal zone where noise levels are high and, hence, easily measured and (2) when characterizing the radiation pattern of the transducer in question (to obtain the diameter and focal length subsequently used in FOM analyses), data from the focal zone were principally used. Thus, plotted and tabulated FOM values, discussed in section 3.1.4.2, are always those for gate 7, i.e., a wide gate centered in the focal zone.

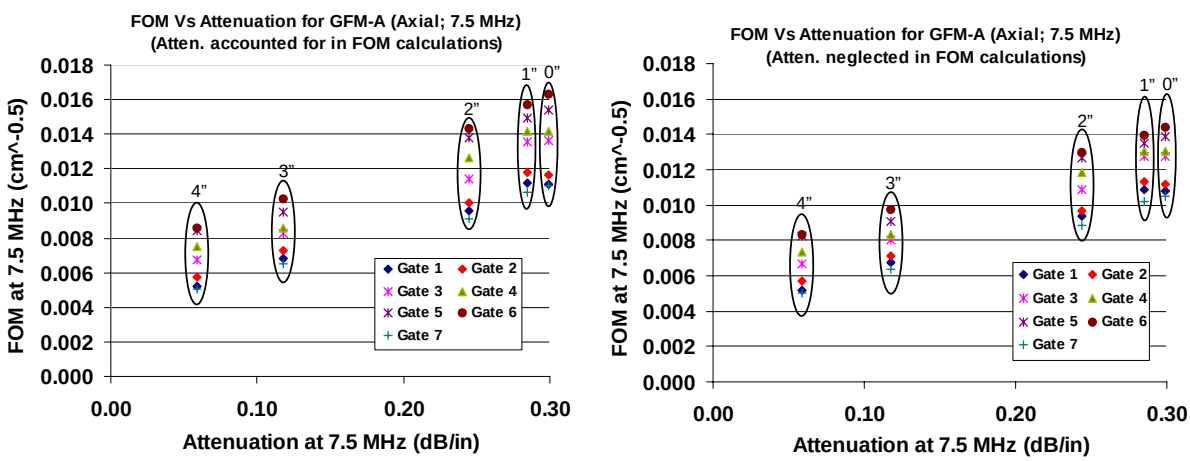

FIGURE 3-47. COMPARISON OF MEASURED FOM AND ATTENUATION VALUES AT 7.5 MHz FOR THE GFM IN718 BILLET

(Results are shown for axial beam propagation at five measurement sites located 0″, 1″, 2″, 3″, and 4″ from the billet center, respectively. Deduced FOM values depend on the time gate used in the analysis and the treatment of attenuation.)

For the IN718 specimens, the measured attenuations tend to be rather low and the influence of attenuation on the deduced FOM values is rather small, as can be seen by comparing the two panels of figure 3-48. For the Waspaloy billet, however, the attenuation is quite large, particularly near the billet center, and uncertainty in the knowledge of the energy loss attenuation can lead to a much larger uncertainty in the FOM value, as can be seen by comparing the two panels in figure 3-48. Because of the smooth variation of back-wall amplitudes seen during scanning, it was believed that the back-wall attenuation is a good estimate of the energy loss

attenuation in these Ni billet specimens. Consequently, unless explicitly stated otherwise, the back-wall attenuation was used in the FOM analysis for all the results quoted in the remainder of this report.

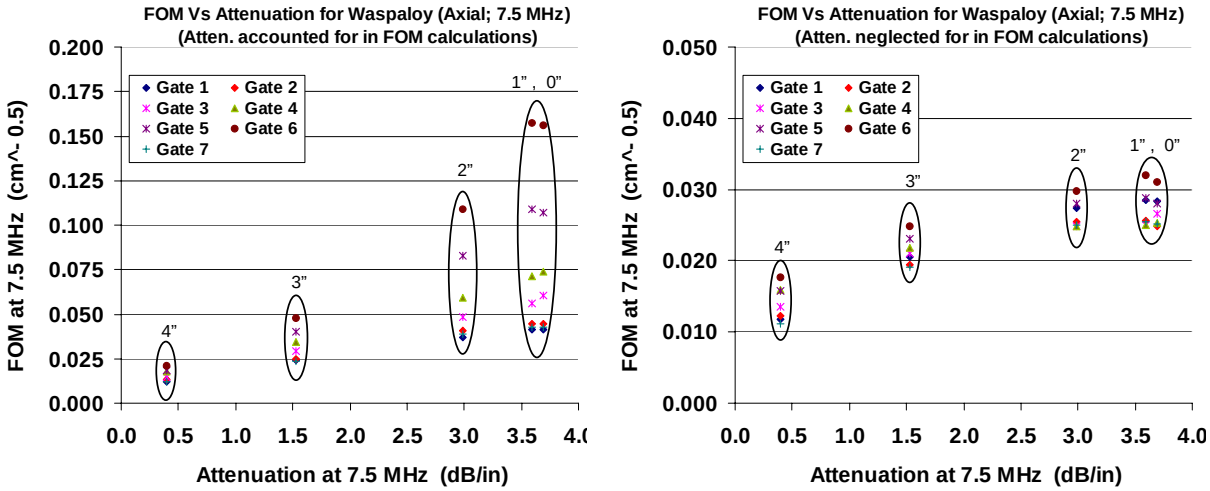

FIGURE 3-48. COMPARISON OF MEASURED FOM AND ATTENUATION VALUES AT 7.5 MHz FOR THE WASPALOY BILLET, AFTER THE FASHION OF FIGURE 3-47

Finally, it was noted that the spectra of the reference echo and the backscattered noise A-scans must be considered when assessing the reliability of the deduced FOM values. The situation is similar to that discussed at length for the attenuation measurements: one desires that spectral strength at a frequency of interest be appreciable, e.g., greater that 15% of the strength at the peak frequency. This policy has been followed as well for the FOM data. In addition, because FOM analysis requires knowledge of the attenuation, FOM values were not quoted for frequencies where the attenuation values were deemed to be unreliable, even if there was appreciable spectral strength in the reference and (averaged) noise echoes. For example, near the center of the Waspaloy billet, FOM values for 10 and 12.5 MHz are not quoted due solely to the unreliability of the attenuation data.

3.1.4 Results of UT Property Measurements.

This section summarizes the results of the longitudinal-wave velocity, attenuation, and backscattered grain noise FOM measurements. For each of these three basic UT properties, 60 measurement trials were conducted, corresponding to four billet strip specimens, five measurement sites per strip, and three inspection directions per site.

The focus will be on the manner in which UT properties vary with position and inspection direction and the correlation between attenuation and FOM values. As demonstrated earlier, attenuation and FOM are strong functions of frequency for these Ni alloys, as they are for metals in general. However, to maintain focus and to keep this section reasonably short, the main points will be graphically illustrated using data for just one frequency of interest, namely, 7.5 MHz.

Some of the results shown in this report have been published in other venues [36-38], and the latter reference in particular contains additional graphs and tables that do not appear here. These may be of interest to readers desiring a more detailed summary of certain aspects of the measured results, such as the manner in which deduced FOM values depend on the time gate used in the analysis.

3.1.4.1 Velocity Summary.

As noted in section 3.1.2.1, the TOF C-scan images for the strip coupons (like that shown in figure 3-12) were consistent with having velocity variations of less than about 0.2% throughout each coupon. This finding was confirmed by the subsequent detailed velocity measurements, which are summarized in table 3-4. For the set of 60 measurements, longitudinal velocities were found to range over 0.5805 ±0.0009 cm/μsec (or ±0.15%) for the IN718 specimens and over 0.6008 ±0.0006 cm/μsec (or ±0.10%) for the Waspaloy specimens. The measured velocities are also displayed graphically in figure 3-49. A horizontal line in each panel indicates the average for all measurements for a given alloy, i.e., 0.58075 cm/μsec for IN718 (average over GFM-A, V-Die-A, V-Die-B) and 0.60098 cm/μsec for Waspaloy. No obvious trends in the velocity results are seen in figure 3-49. The minor velocity variations within each of the four billet strips may simply reflect the inherent errors in the measurement process. As noted in section 3.1.3.1, the absolute velocity measurements are believed to typically be accurate to about 1 part in 1000 (0.10%), usually limited by the accuracy of the thickness measurement. For the axial and hoop directions, a thickness measurement error of 1 mil out of 2″ would shift a given plotted value in figure 3-49 up or down by about 0.0003 cm/μsec. For the radial direction, where the coupons are only about 1″ thick, a 1 mil error would result in a 0.0006 cm/μsec shift.

In practice, the small velocity variations seen in these Ni alloy billets, in and of themselves, are expected to have no significant impact on inspectability. The sonic velocity influences the radiation pattern within the billet that is produced by the insonifying transducer. Sizeable velocity inhomogeneities can shift the focal depth and alter the degree of focus at the focal zone. For the specimens studied, the velocity variations are very small and are unlikely to cause noticeable changes in the radiation pattern. For example, in typical multizone billet inspections, the focal depth and spot size are expected to be very similar for, say, the GFM billet studied here, and an ideal billet having a perfectly uniform sound velocity of 0.58075 cm/μsec, if other factors (e.g., attenuation) are the same for both.

Although this study was focused on gathering UT data to support longitudinal-wave inspections, a limited number of shear-wave velocity measurements were also made. These were carried out to obtain representative velocity values for testing models that relate sonic velocity to the single-crystal elastic constants of the metal. The measurements used a 1/2″ diameter, 5-MHz, shear-wave contact transducer with a thin layer of honey serving as a couplant. Time delays between successive back-wall echoes were measured (in essentially the same manner as described earlier for the longitudinal-wave case) and used to deduce velocities. Results are summarized in table 3-5.

TABLE 3-4. RESULTS OF LONGITUDINAL-WAVE SOUND VELOCITY MEASUREMENTS

Coupon	Inspection Direction		Inspection Site				
			0″ (center)	1″	2″	3″	4″
Waspaloy-A	axial	thickness (in.):	1.9975	1.9975	1.9975	1.9975	1.9975
		Dt (μsec):	16.8853	16.8843	16.8855	16.8795	16.8715
		v (cm/μsec):	0.6010	0.6010	0.6009	0.6012	0.6014
Waspaloy-A	hoop	thickness (in.):	2.0000	2.0000	2.0000	2.0000	2.0000
		Dt (μsec):	16.9035	16.9060	16.9040	16.9020	16.8950
		v (cm/μsec):	0.6011	0.6010	0.6010	0.6011	0.6014
Waspaloy-A	radial	thickness (in.):	0.9682	0.9722	0.9700	0.9700	0.9700
		Dt (μsec):	8.2065	8.2075	8.2115	8.19475	8.19425
		v (cm/μsec):	0.6006	0.6003	0.6002	0.6013	0.6014
GFM-A	axial	thickness (in.):	1.9645	1.9645	1.9645	1.9645	1.9645
		Dt (μsec):	17.1695	17.1663	17.1665	17.1758	17.1833
		v (cm/μsec):	0.5812	0.5814	0.5813	0.5810	0.5808
GFM-A	hoop	thickness (in.):	1.9905	1.9905	1.9905	1.9905	1.9905
		Dt (μsec):	17.4030	17.4038	17.4033	17.4023	17.4140
		v (cm/μsec):	0.5810	0.5810	0.5810	0.5811	0.5807
GFM-A	radial	thickness (in.):	0.9755	0.9755	0.9755	0.9755	0.9755
		Dt (μsec):	8.5340	8.5375	8.5425	8.5420	8.5412
		v (cm/μsec):	0.5806	0.5806	0.5801	0.5801	0.5802
V-Die-A	axial	thickness (in.):	2.0050	2.0050	2.0050	2.0050	2.0050
		Dt (μsec):	17.5183	17.5170	17.5220	17.5320	17.5440
		v (cm/μsec):	0.5814	0.5815	0.5813	0.5810	0.5806
V-Die-A	hoop	thickness (in.):	1.9945	1.9945	1.9945	1.9945	1.9945
		Dt (μsec):	17.4548	17.4550	17.4458	17.4358	17.4668
		v (cm/μsec):	0.5805	0.5805	0.5808	0.5811	0.5801
V-Die-A	radial	thickness (in.):	0.9755	0.9755	0.9755	0.9755	0.9755
		Dt (μsec):	8.54225	8.52625	8.543	8.5305	8.53775
		v (cm/μsec):	0.5801	0.5811	0.5804	0.5807	0.5805
V-Die-B	axial	thickness (in.):	2.0080	2.0080	2.0080	2.0080	2.0080
		Dt (μsec):	17.5480	17.5490	17.5503	17.5593	17.5648
		v (cm/μsec):	0.5813	0.5813	0.5812	0.5809	0.5807
V-Die-B	hoop	thickness (in.):	2.0070	2.0070	2.0070	2.0070	2.0070
		Dt (μsec):	17.5390	17.5378	17.5420	17.5553	17.5783
		v (cm/μsec):	0.5813	0.5813	0.5812	0.5808	0.5800
V-Die-B	radial	thickness (in.):	0.9820	0.9820	0.9820	0.9820	0.9820
		Dt (μsec):	8.5915	8.60175	8.5955	8.6065	8.6045
		v (cm/μsec):	0.5807	0.5800	0.5804	0.5796	0.5797

Note: Dt is the average time delay between two successive back-wall echoes.

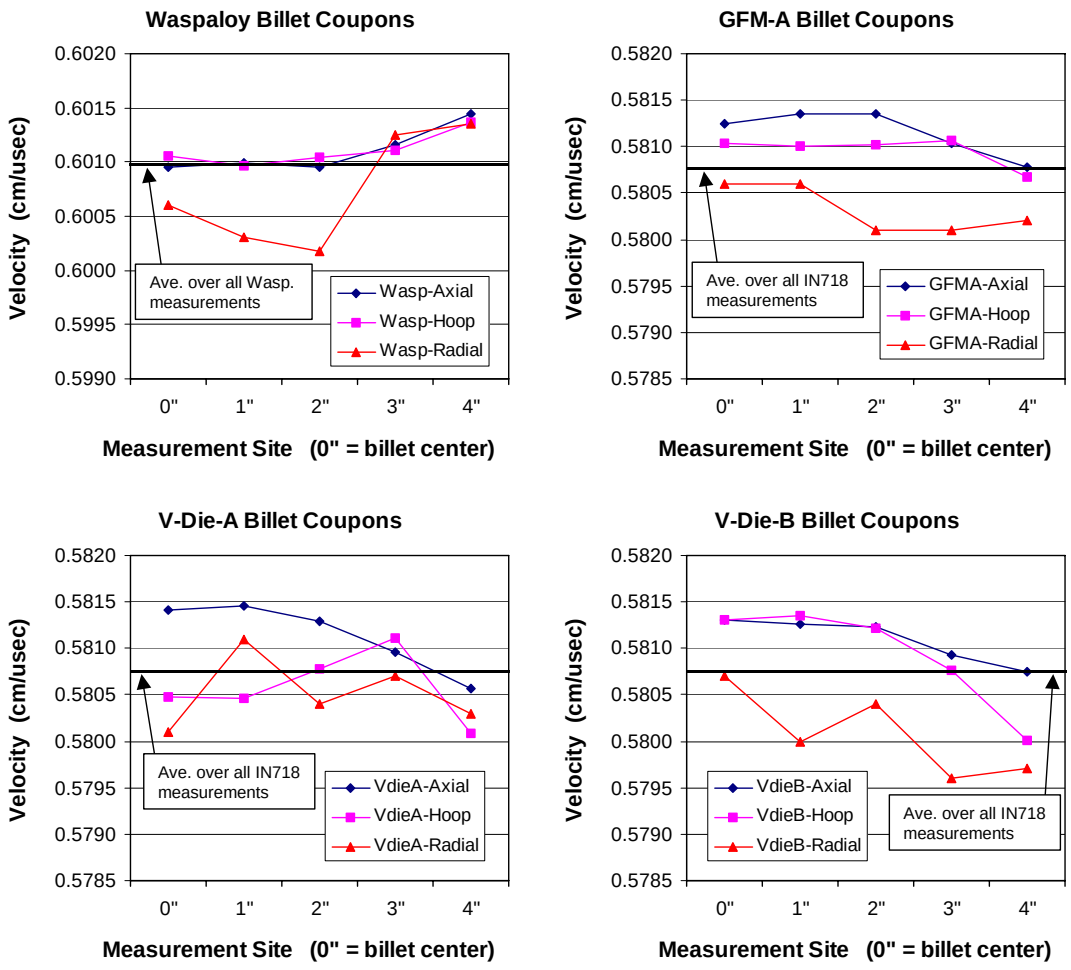

FIGURE 3-49. MEASURED LONGITUDINAL-WAVE SOUND VELOCITIES AS FUNCTIONS OF RADIAL DEPTH IN THE BILLET
(Results are shown for three sound propagation directions.)

3.1.4.2 Attenuation and Backscattered Noise FOM Summary.

In contrast to the velocity behavior, attenuation and FOM values varied significantly with both frequency and position. As illustrated in figures 3-37 and 3-38, a power law was fit to the measured attenuation-versus-frequency data for each case studied. Generally speaking, it was found that each of the power-law fits provided a good overall summary of the trend of the measured data. The power-law fits are summarized in table 3-6. For each measurement case, the following are listed: the frequency range for the data used in the fitting range, the multiplicative (C) and power (p) parameters resulting from the fitting, and a tabulation of attenuation values at selected frequencies obtained by evaluating the power law expressions. Tabulated attenuation values listed in blue indicate cases where an evaluation was made by extrapolating the power law slightly beyond the range of the trustworthy attenuation data used in the fit. Except for a few cases with very low measured attenuation (where measurement uncertainties will be a larger percentage of the attenuation value), fits to the Ni alloy data yielded power law exponents in the $3 < p < 4$ range.

TABLE 3-5. RESULTS OF SHEAR-WAVE SOUND VELOCITY MEASUREMENTS

Coupon	Inspection Direction	Measured Quantities	Results
Waspaloy	Radial	thickness (in.):	0.9682
0″ (center)		Dt (μsec):	15.2925
		v (cm/μsec):	0.3216
GFM-A	Radial	thickness (in.):	0.9755
0″ (center)		Dt (μsec):	16.0725
		v (cm/μsec):	0.3083
V-Die-A	Radial	thickness (in.):	0.9755
0″ (center)		Dt (μsec):	16.035
		v (cm/μsec):	0.3090
V-Die-B	Radial	thickness (in.):	0.9820
0″ (center)		Dt (μsec):	16.1975
		v (cm/μsec):	0.3080

Note: Dt is the average time delay between two successive back-wall echoes.

Note that table 3-6 is complete for 5 MHz (the center frequency for existing Ni billet inspections) and for 7.5 MHz (the likely center frequency for a next-generation inspection with improved sensitivity). However, for some high-attenuation cases, e.g., the 0″ site in Waspaloy at 10 MHz, no tabulated value is listed because the measured attenuation data at that frequency were not deemed to be sufficiently trustworthy. For such cases, the attenuation values are likely too high to permit practical billet inspections at those frequencies; lower-frequency inspections with enhanced focusing would probably present a better alternative. Since the billet specimens will be preserved, property measurements at the higher frequencies could be carried out in the future using other transducers if necessary.

The best estimates of the backscattered noise FOM values at the same five frequencies of interest are listed in table 3-7. The best estimate at a given frequency was obtained from a local linear fit to the measured FOM-versus-frequency curve that resulted from an analysis of the backscattered noise using the large time gate centered near the focal depth (gate 7 in figures 3-41 and 3-42). Deduced FOM values are listed for two separate analyses: one in which the measured attenuation power law of table 3-6 was used as an input, and one in which the input attenuation was assumed to be negligible. The first analysis (using measured attenuation) is believed to lead to the more accurate FOM value. By comparing the two results for a given case, the effect of attenuation on the FOM determination can be discerned.

TABLE 3-6. SUMMARY OF MEASURED ATTENUATION VALUES FOR THE Ni ALLOY BILLET SPECIMENS

Coupon	Side - Site	Power Law Parameters (N/cm Units)		Fitting Range		Atten. at 5 MHz (dB/inch)	Atten. at 7.5 MHz (dB/inch)	Atten. at 10 MHz (dB/inch)	Atten. at 12.5 MHz (dB/inch)	Atten. at 15 MHz (dB/inch)
		C	P	f_min (MHz)	f_max (MHz)					
Waspaloy	Axial - 0″	1.378E-04	3.526	3.91	7.81	0.885	3.696			
	Axial - 1″	7.279E-05	3.828	3.91	7.81	0.761	3.596			
	Axial - 2″	8.757E-05	3.644	3.91	7.81	0.681	2.986			
	Axial - 3″	5.070E-05	3.585	3.91	9.77	0.358	1.533	4.298		
	Axial - 4″	7.778E-06	3.849	3.91	13.3	0.084	0.400	1.211	2.858	
Waspaloy	Hoop - 0″	2.227E-04	3.242	3.91	7.81	0.907	3.376			
	Hoop - 1″	7.768E-05	3.813	3.91	7.42	0.793	3.719			
	Hoop - 2″	9.284E-05	3.582	3.91	7.81	0.653	2.791			
	Hoop - 3″	3.818E-05	3.667	3.91	9.77	0.308	1.362	3.912		
	Hoop - 4″	1.198E-05	3.638	3.91	13.3	0.092	0.403	1.149	2.587	
Waspaloy	Radial - 0″	1.280E-04	3.551	4.3	8.2	0.857	3.615			
	Radial - 1″	9.822E-05	3.685	4.3	8.2	0.815	3.632			
	Radial - 2″	6.200E-05	3.803	4.3	8.2	0.623	2.911			
	Radial - 3″	8.065E-05	3.394	4.3	8.2	0.420	1.661			
	Radial - 4″	1.794E-05	3.563	4.3	8.2	0.122	0.518			
GFM-A	Axial - 0″	6.558E-06	3.765	3.91	13.3	0.062	0.285	0.841	1.949	
	Axial - 1″	9.736E-06	3.593	3.91	13.3	0.070	0.299	0.840	1.873	
	Axial - 2″	9.686E-06	3.495	3.91	13.3	0.059	0.244	0.668	1.456	
	Axial - 3″	3.015E-06	3.713	3.91	15.2	0.026	0.118	0.343	0.786	1.546
	Axial - 4″	7.931E-07	4.029	3.91	15.6	0.011	0.059	0.187	0.459	0.958
GFM-A	Hoop - 0″	1.075E-05	3.585	3.91	13.3	0.076	0.325	0.912	2.030	
	Hoop - 1″	6.492E-06	3.781	3.91	13.3	0.063	0.291	0.864	2.009	
	Hoop - 2″	3.968E-06	3.801	3.91	13.3	0.040	0.185	0.553	1.292	
	Hoop - 3″	3.174E-06	3.703	3.91	15.2	0.027	0.122	0.354	0.808	1.587
	Hoop - 4″	1.396E-06	3.827	3.91	15.6	0.015	0.069	0.207	0.485	0.975
GFM-A	Radial - 0″	1.132E-05	3.567	3.91	16	0.078	0.330	0.920	2.039	3.907
	Radial - 1″	7.136E-06	3.724	3.91	16	0.063	0.286	0.835	1.916	3.778
	Radial - 2″	9.800E-06	3.478	3.91	16	0.058	0.239	0.650	1.412	2.663
	Radial - 3″	3.033E-06	3.735	3.91	16	0.027	0.124	0.364	0.837	1.654
	Radial - 4″	1.601E-05	2.896	3.91	16	0.037	0.121	0.278	0.530	0.898

Values in blue require extrapolations of the power-law curve beyond the frequency range of the measured data.

TABLE 3-6. SUMMARY OF MEASURED ATTENUATION VALUES FOR THE Ni ALLOY BILLET SPECIMENS (Continued)

Coupon	Side - Site	Power Law Parameters (N/cm Units)		Fitting Range		Atten. at 5 MHz (dB/inch)	Atten. at 7.5 MHz (dB/inch)	Atten. at 10 MHz (dB/inch)	Atten. at 12.5 MHz (dB/inch)	Atten. at 15 MHz (dB/inch)
		C	P	f_min (MHz)	f_max (MHz)					
V-Die-A	Axial - 0″	2.985E-06	3.734	3.91	15.2	0.027	0.122	0.357	0.821	1.621
	Axial - 1″	2.995E-06	3.697	3.91	15.2	0.025	0.114	0.329	0.750	1.472
	Axial - 2″	3.021E-06	3.691	3.91	15.2	0.025	0.113	0.327	0.745	1.460
	Axial - 3″	5.663E-06	3.563	3.91	14.5	0.039	0.164	0.456	1.010	1.935
	Axial - 4″	1.795E-05	3.199	3.91	13.3	0.068	0.249	0.626	1.278	
V-Die-A	Hoop - 0″	1.899E-06	3.889	3.91	15.2	0.022	0.106	0.324	0.773	1.570
	Hoop - 1″	2.914E-06	3.715	3.91	15.2	0.025	0.114	0.333	0.763	1.502
	Hoop - 2″	2.776E-06	3.736	3.91	15.2	0.025	0.114	0.334	0.768	1.518
	Hoop - 3″	1.189E-05	3.331	3.91	14.5	0.056	0.216	0.562	1.182	2.170
	Hoop - 4″	1.330E-05	3.292	3.91	13.3	0.059	0.223	0.574	1.197	
V-Die-A	Radial - 0″	1.003E-05	3.249	6.25	14.1	0.041	0.154	0.392	0.810	
	Radial - 1″	7.161E-06	3.363	6.25	14.1	0.035	0.138	0.364	0.771	
	Radial - 2″	4.178E-06	3.603	6.25	14.1	0.030	0.131	0.369	0.825	
	Radial - 3″	1.371E-05	3.348	6.25	14.1	0.066	0.257	0.674	1.422	
	Radial - 4″	1.137E-06	3.454	6.25	14.1	0.065	0.264	0.713	1.542	
V-Die-B	Axial - 0″	1.699E-06	3.898	3.91	15.2	0.020	0.097	0.296	0.707	1.439
	Axial - 1″	3.952E-06	3.558	3.91	15.2	0.027	0.113	0.315	0.697	1.334
	Axial - 2″	4.298E-06	3.440	3.91	15.2	0.024	0.097	0.261	0.563	1.054
	Axial - 3″	2.634E-06	3.322	3.91	15.6	0.012	0.047	0.122	0.256	0.469
	Axial - 4″	1.998E-09	5.474	10	15.6	0.000	0.003	0.013	0.045	0.121
V-Die-B	Hoop - 0″	1.707E-06	3.889	3.91	15.6	0.020	0.095	0.292	0.695	1.412
	Hoop - 1″	2.809E-06	3.668	3.91	15.6	0.023	0.100	0.289	0.654	1.277
	Hoop - 2″	8.309E-06	3.243	3.91	15.2	0.034	0.126	0.321	0.662	1.195
	Hoop - 3″	6.766E-06	2.995	3.91	15.6	0.018	0.062	0.147	0.288	0.496
	Hoop - 4″	9.009E-08	4.361	10	13.3	0.002	0.013	0.046	0.121	
V-Die-B	Radial - 0″	3.791E-06	3.606	7.43	14.1	0.028	0.120	0.338	0.755	
	Radial - 1″	3.004E-06	3.681	7.43	14.1	0.025	0.110	0.318	0.722	
	Radial - 2″	7.937E-06	3.249	7.43	14.1	0.033	0.122	0.311	0.642	
	Radial - 3″	2.750E-06	3.342	7.43	14.1	0.013	0.051	0.133	0.281	
	Radial - 4″	6.444E-06	2.881	7.43	14.1	0.015	0.047	0.108	0.206	

Values in blue require extrapolations of the power-law curve beyond the frequency range of the measured data.

TABLE 3-7. SUMMARY OF MEASURED GRAIN NOISE FOM VALUES FOR THE Ni ALLOY BILLET SPECIMENS

Coupon	Side - Site	Noise FOM at 5 MHz ($cm^{-0.5}$) Measured Atten. Used	Noise FOM at 7.5 MHz ($cm^{-0.5}$) Measured Atten. Used	Noise FOM at 10 MHz ($cm^{-0.5}$) Measured Atten. Used	Noise FOM at 12.5 MHz ($cm^{-0.5}$) Measured Atten. Used	Noise FOM at 5 MHz ($cm^{-0.5}$) Atten. = 0 Assumed	Noise FOM at 7.5 MHz ($cm^{-0.5}$) Atten. = 0 Assumed	Noise FOM at 10 MHz ($cm^{-0.5}$) Atten. = 0 Assumed	Noise FOM at 12.5 MHz ($cm^{-0.5}$) Atten. = 0 Assumed
Waspaloy	Axial - 0″	0.0142	0.0425			0.0124	0.0251		
	Axial - 1″	0.0135	0.0427			0.0120	0.0254		
	Axial - 2″	0.0122	0.0386			0.0110	0.0250		
	Axial - 3″	0.0086	0.0238			0.0081	0.0190		
	Axial - 4″	0.0049	0.0119			0.0048	0.0112		
Waspaloy	Hoop - 0″	0.0128	0.0413			0.0112	0.0256		
	Hoop - 1″	0.0130	0.0407			0.0115	0.0239		
	Hoop - 2″	0.0114	0.0360			0.0103	0.0241		
	Hoop - 3″	0.0088	0.0250			0.0084	0.0205		
	Hoop - 4″	0.0049	0.0122			0.0048	0.0115		
Waspaloy	Radial - 0″	0.0156	0.0473			0.0136	0.0291		
	Radial - 1″	0.0153	0.0454			0.0134	0.0278		
	Radial - 2″	0.0134	0.0401			0.0121	0.0266		
	Radial - 3″	0.0099	0.0275			0.0093	0.0219		
	Radial - 4″	0.0062	0.0144			0.0060	0.0134		
GFM-A	Axial - 0″	0.0045	0.0107	0.0201	0.0360	0.0045	0.0102	0.0178	0.0271
	Axial - 1″	0.0049	0.0110	0.0201	0.0351	0.0048	0.0105	0.0178	0.0267
	Axial - 2″	0.0040	0.0092	0.0171	0.0291	0.0040	0.0088	0.0155	0.0235
	Axial - 3″	0.0030	0.0065	0.0122	0.0214	0.0030	0.0064	0.0116	0.0191
	Axial - 4″	0.0026	0.0051	0.0093	0.0163	0.0026	0.0050	0.0091	0.0152
GFM-A	Hoop - 0″	0.0047	0.0109	0.0201	0.0360	0.0046	0.0104	0.0178	0.0271
	Hoop - 1″	0.0048	0.0112	0.0201	0.0351	0.0047	0.0108	0.0178	0.0267
	Hoop - 2″	0.0040	0.0093	0.0171	0.0291	0.0040	0.0091	0.0155	0.0235
	Hoop - 3″	0.0030	0.0070	0.0122	0.0214	0.0030	0.0069	0.0116	0.0191
	Hoop - 4″	0.0026	0.0054	0.0093	0.0163	0.0026	0.0054	0.0091	0.0152
GFM-A	Radial - 0″	0.0050	0.0118	0.0214	0.0361	0.0049	0.0113	0.0190	0.0279
	Radial - 1″	0.0050	0.0110	0.0204	0.0334	0.0049	0.0106	0.0183	0.0262
	Radial - 2″	0.0048	0.0102	0.0188	0.0306	0.0047	0.0098	0.0173	0.0256
	Radial - 3″	0.0041	0.0076	0.0128	0.0211	0.0041	0.0740	0.0122	0.0190
	Radial - 4″	0.0032	0.0066	0.0118	0.0196	0.0032	0.0065	0.0113	0.0184

TABLE 3-7. SUMMARY OF MEASURED GRAIN NOISE FOM VALUES FOR THE Ni ALLOY BILLET SPECIMENS (Continued)

Coupon	Side - Site	Noise FOM at 5 MHz ($cm^{-0.5}$) Measured Atten. Used	Noise FOM at 7.5 MHz ($cm^{-0.5}$) Measured Atten. Used	Noise FOM at 10 MHz ($cm^{-0.5}$) Measured Atten. Used	Noise FOM at 12.5 MHz ($cm^{-0.5}$) Measured Atten. Used	Noise FOM at 5 MHz ($cm^{-0.5}$) Atten. = 0 Assumed	Noise FOM at 7.5 MHz ($cm^{-0.5}$) Atten. = 0 Assumed	Noise FOM at 10 MHz ($cm^{-0.5}$) Atten. = 0 Assumed	Noise FOM at 12.5 MHz ($cm^{-0.5}$) Atten. = 0 Assumed
V-Die-A	Axial - 0″	0.0034	0.0064	0.0121	0.0204	0.0034	0.0063	0.0115	0.0181
	Axial - 1″	0.0032	0.0061	0.0119	0.0199	0.0031	0.0060	0.0114	0.0179
	Axial - 2″	0.0030	0.0063	0.0117	0.0197	0.0030	0.0062	0.0111	0.0177
	Axial - 3″	0.0036	0.0074	0.0129	0.0218	0.0036	0.0072	0.0120	0.0188
	Axial - 4″	0.0040	0.0089	0.0174	0.0304	0.0040	0.0086	0.0159	0.0252
V-Die-A	Hoop - 0″	0.0036	0.0080	0.0137	0.0223	0.0036	0.0079	0.0130	0.0199
	Hoop - 1″	0.0035	0.0073	0.0126	0.0201	0.0035	0.0072	0.0120	0.0180
	Hoop - 2″	0.0034	0.0072	0.0122	0.0197	0.0034	0.0071	0.0116	0.0176
	Hoop - 3″	0.0036	0.0080	0.0145	0.0242	0.0036	0.0078	0.0133	0.0203
	Hoop - 4″	0.0037	0.0082	0.0149	0.0251	0.0037	0.0079	0.0137	0.0211
V-Die-A	Radial - 0″	0.0038	0.0080	0.0214	0.0361	0.0038	0.0078	0.0190	0.0279
	Radial - 1″	0.0034	0.0075	0.0204	0.0334	0.0034	0.0073	0.0183	0.0262
	Radial - 2″	0.0035	0.0076	0.0188	0.0306	0.0035	0.0074	0.0173	0.0256
	Radial - 3″	0.0048	0.0109	0.0128	0.0211	0.0048	0.0107	0.0122	0.0190
	Radial - 4″	0.0045	0.0102	0.0118	0.0196	0.0045	0.0099	0.0113	0.0184
V-Die-B	Axial - 0″	0.0030	0.0061	0.0111	0.0193	0.0030	0.0060	0.0106	0.0174
	Axial - 1″	0.0030	0.0059	0.0105	0.0185	0.0030	0.0058	0.0100	0.0167
	Axial - 2″	0.0026	0.0052	0.0094	0.0167	0.0026	0.0051	0.0090	0.0153
	Axial - 3″	0.0020	0.0033	0.0058	0.0101	0.0020	0.0033	0.0057	0.0098
	Axial - 4″	0.0018	0.0022	0.0037	0.0065	0.0018	0.0022	0.0037	0.0065
V-Die-B	Hoop - 0″	0.0033	0.0071	0.0116	0.0193	0.0033	0.0070	0.0111	0.0174
	Hoop - 1″	0.0037.	0.0078	0.0122	0.0196	0.0037	0.0077	0.0117	0.0178
	Hoop - 2″	0.0030	0.0064	0.0112	0.0179	0.0030	0.0062	0.0107	0.0162
	Hoop - 3″	0.0025	0.0045	0.0076	0.0124	0.0025	0.0044	0.0074	0.0119
	Hoop - 4″	0.0017	0.0029	0.0048	0.0076	0.0017	0.0029	0.0048	0.0075
V-Die-B	Radial - 0″	0.0038	0.0078	0.0137	0.0230	0.0038	0.0077	0.0131	0.0209
	Radial - 1″	0.0037	0.0074	0.0137	0.0233	0.0036	0.0073	0.0131	0.0213
	Radial - 2″	0.0030	0.0059	0.0111	0.0191	0.0030	0.0058	0.0106	0.0176
	Radial - 3″	0.0021	0.0040	0.0072	0.0125	0.0021	0.0039	0.0071	0.0121
	Radial - 4″	0.0019	0.0028	0.0046	0.0077	0.0019	0.0028	0.0045	0.0075

The attenuation values of the various coupons are displayed graphically in figure 3-50 for one frequency of interest, namely, 7.5 MHz. The plotted values shown were obtained from table 3-6, i.e., by evaluating the power-law fits at that frequency. Figure 3-51 displays, in a similar format, the measured FOM values at 7.5 MHz. The plotted values have been taken from table 3-7 for the analysis that used the measured attenuation as an input.

The same trends seen earlier in the preliminary C-scans of back-wall echo strength and backscattered noise are also evident in figures 3-50 and 3-51.

1. The attenuation or FOM value varies significantly with radial position, being largest near the billet center (0″) for Waspaloy, GFM-A, and V-Die-B, and largest near the OD for V-Die-A.

2. On average, at a given measurement site, there is little difference between the results for the axial, radial, and hoop directions.

3. Averaged over radial position, the attenuation or FOM value increases for the sequence: V-Die-B, V-Die-A, GFM-A, and Waspaloy.

4. Attenuation and FOM values tend to be correlated: sites with higher (lower) attenuation also have higher (lower) FOM.

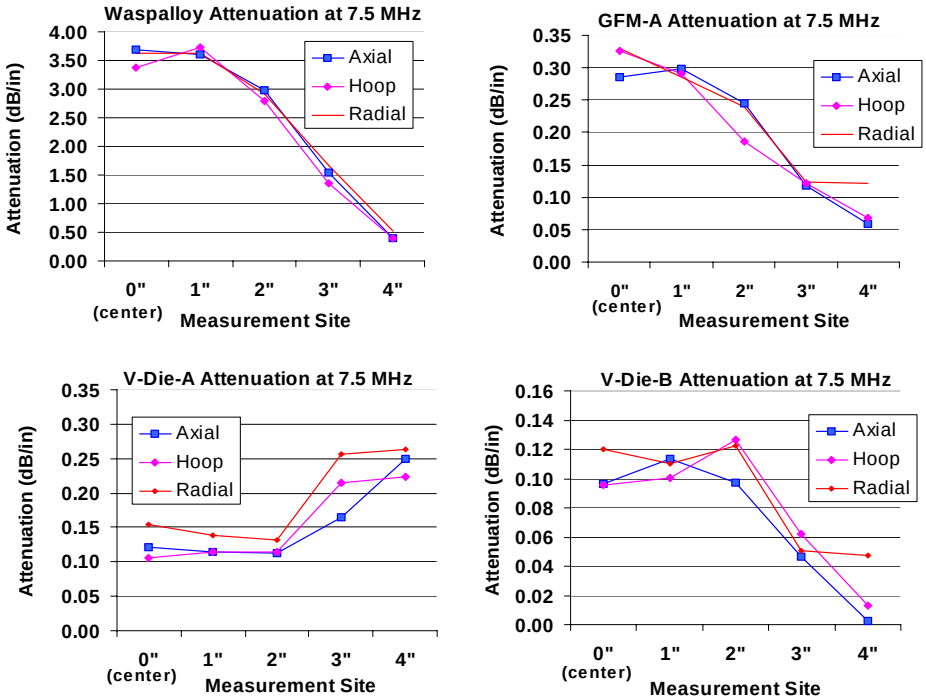

FIGURE 3-50. MEASURED ATTENUATION VALUES AT 7.5 MHz FOR THE Ni ALLOY BILLET SPECIMENS
(Results are shown for three orthogonal inspection directions. The distance from each measurement site to the billet center is indicated.)

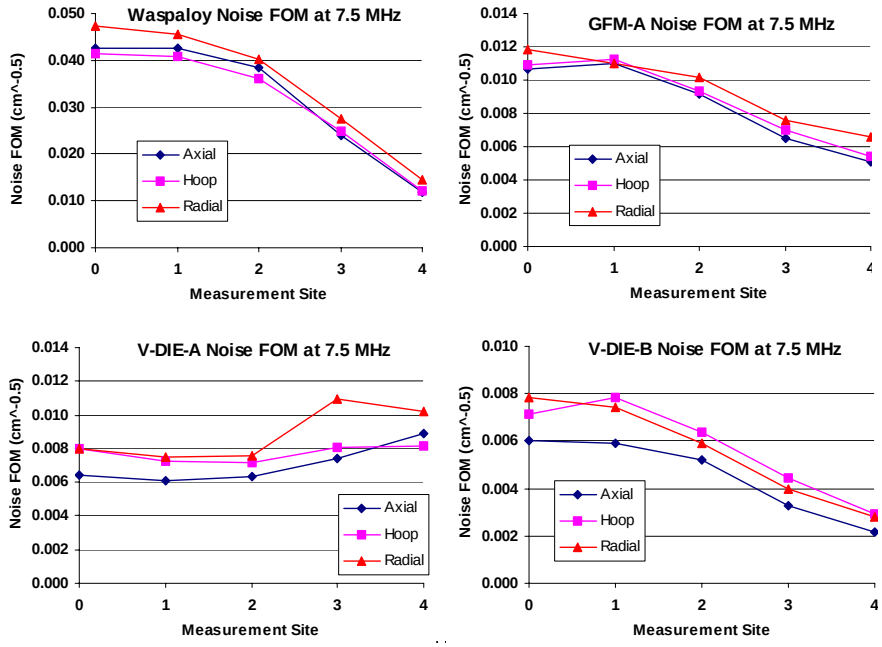

FIGURE 3-51. MEASURED GRAIN NOISE FOM VALUES AT 7.5 MHz FOR THE Ni ALLOY BILLET SPECIMENS
(Results are shown for three orthogonal inspection directions. The distance from each measurement site to the billet center is indicated.)

The attenuation and FOM values vary widely over the suite of specimens. Values for both properties tend to be much larger for Waspaloy than for IN718. Averaged over all the coupons and all inspection directions, the Waspaloy attenuation at 5 MHz (0.56 dB/inch) is 15 times larger than the IN718 attenuation (0.036 dB/inch). At 7.5 MHz, the average Waspaloy attenuation is 16 times larger (2.41 dB/inch versus 0.15 dB/inch). The average FOM values for Waspaloy at 5 and 7.5 MHz are larger than the corresponding averages for IN718 by factors of 3.1 and 4.5, respectively. Within a given billet strip coupon, attenuation values at these frequencies can vary by as much as an order of magnitude with position, and FOM values can vary by as much as a factor of 3. Table 3-8 lists the range of measured attenuation and FOM values at 5 and 7.5 MHz for each strip coupon.

TABLE 3-8. RANGES OF ATTENUATION AND FOM VALUES MEASURED WITHIN EACH OF THE Ni ALLOY BILLET STRIP COUPONS

Coupon	Range of Attenuation Values		Range of FOM Values	
	(dB/inch) at 5 MHz	(dB/inch) at 7.5 MHz	($cm^{-0.5}$) at 5 MHz	($cm^{-0.5}$) at 7.5 MHz
Waspaloy	0.084-0.907	0.400-3.719	0.0049-0.0156	0.0119-0.0473
GFM-A	0.011-0.078	0.059-0.330	0.0026-0.0050	0.0051-0.0118
V-Die-A	0.022-0.068	0.106-0.264	0.0030-0.0048	0.0061-0.0109
V-Die-B	0.000-0.034	0.003-0.126	0.0017-0.0038	0.0022-0.0078

It was noted that for the Ni alloy billet specimens, high-attenuation regions generally produce high backscattered noise levels. This correlation can now be demonstrated more explicitly. In figure 3-52(a)-(b), the measured noise FOM was plotted against the measured attenuation for a fixed frequency of 7.5 MHz. Each point on the plot represents data from one site on one coupon, inspected from one direction. Thus, for each of the four strip coupons, there are 15 plotted points in figure 3-52(a) (i.e., five sites with three directions per site). It was observed that the Ni alloys exhibit a clear general trend, with the noise FOM tending to increase with increasing attenuation. This general trend is expected for specimens with equiaxed grains: as the mean grain size increases, the attenuation and noise FOM both increase. However, this trend is not always seen in jet-engine materials. For example, for the Ti alloy billet specimens studied under ETC Phase I, the direction of maximum back-wall attenuation was usually the direction of minimum grain noise [15-17]. This led to an inverse relationship between attenuation and noise, as shown in figure 3-52(c) [17]. These two different trends were attributed to the role of recrystallization during the billet formation process. In Ni alloys, there is a significant amount of recrystallization that occurs due to mechanical working of the billet during its formation. This evidently leads to nearly equiaxed grains in the Ni billet specimens under study. In contrast, very little or no recrystallization occurs during working of titanium alloy billets. Hence, the large-scale macrograins present in the Ti ingot become elongated in the axial direction. These elongated grains are believed to be responsible for the inverse correlation between noise FOM and attenuation that is seen in figure 3-52(c) [17].

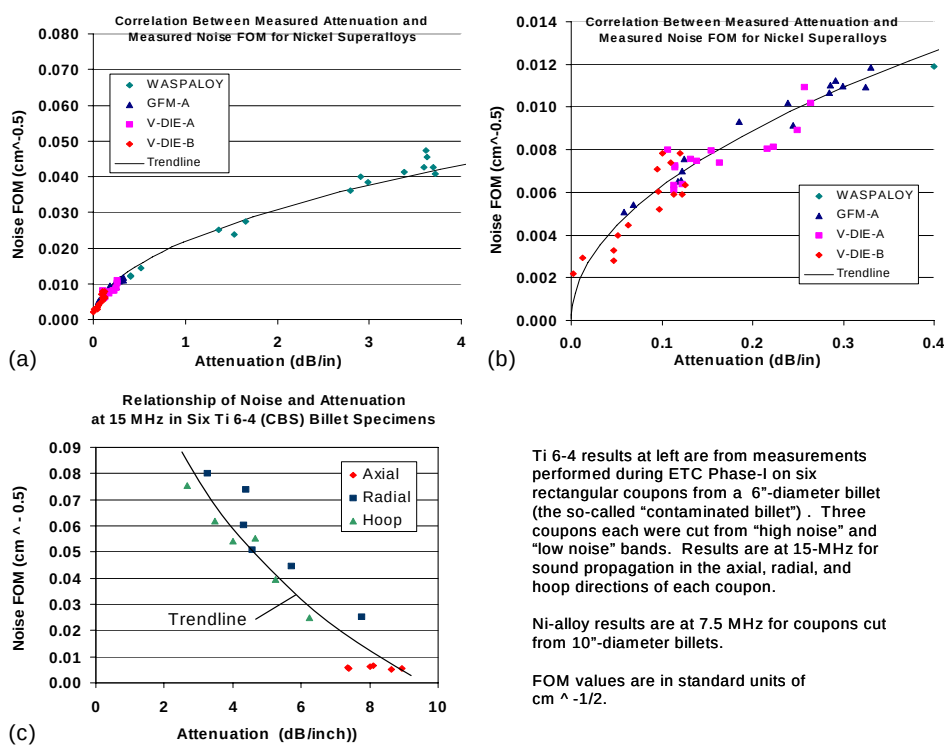

FIGURE 3-52. CORRELATION BETWEEN BACKSCATTERED NOISE FOM AND ATTENUATION (a)-(b) COUPONS FROM 10″ DIAMETER Ni BILLETS AT 7.5 MHz WITH PANEL (b) BEING A BLOWUP OF THE LOW-ATTENUATION PORTION OF PANEL (a), AND (c) COUPONS FROM A 6″ DIAMETER Ti-6-4 BILLET AT 15 MHz

The systematic variation of attenuation and FOM with position will make some locations within billets more difficult to inspect than others. For a given defect, SNR will vary with defect position, generally being smaller at locations having larger FOM values. The UT properties reported in this section can be used as inputs to model calculations that simulate billet inspections and estimate SNR values. Examples of such calculations performed during ETC Phase I were reported in reference 39.

3.1.4.3 The Relationship Between Attenuation and FOM in Equiaxed Pure Ni Microstructures.

As noted in section 3.1.4.2, for the Ni alloy specimens, the UT properties at a given measurement site are approximately independent of inspection direction, and attenuation and FOM values tend to rise or fall together as the measurement site is moved. This behavior is consistent with an equiaxed, untextured billet microstructure in which the average grain diameter varies systematically with position. It is informative to ask how attenuation and FOM are expected to depend upon grain size and frequency for such simple microstructures. Models were used to calculate attenuation and FOM values for pure Ni microstructures containing equiaxed, randomly oriented grains of constant density. Such calculations require, as inputs, the elastic stiffness constants of a single crystal. These constants are known for pure Ni but not for Waspaloy or IN718. Thus, the calculations were only performed for the pure Ni case. Attenuation values, as functions of frequency and average grain diameter, were obtained using an internet-available calculator developed by Joseph Turner [40]. It is based on the so-called first-order smoothing approximation to a stochastic elastic wave equation [41 and 42] and is equivalent to the formalism developed by Stanke and Kino [43] to describe attenuation resulting from grain scattering during sound propagation through a polycrystalline solid. FOM values were predicted using a model expression developed by James Rose [22 and 44]. Both the attenuation and FOM model calculations assume that each microstructure considered contains a distribution of grain sizes with a well-defined average diameter. Grain size information is input through a function P(L) that describes the probability (P) that a line segment of length (L), randomly drawn through the microstructure, has both ends in the same grain. Here, P(L) is assumed to be an exponential function, $P(L) = \exp(-L/b)$, where parameter b is equal to one-half of the average grain diameter. The P(L) function will be discussed further in section 3.1.5.2.

Selected results of the model calculations are shown in figures 3-53 through 3-55. Figure 3-53 displays predicted attenuation-versus-frequency curves for three pure Ni microstructures having average grain diameters of 10, 20, and 30 microns, respectively. As the average grain diameter increases, the attenuation is shown to increase rapidly. For each of the three diameters, the attenuation is a rapidly rising function of frequency, which, over a limited frequency range, can be well approximated by a power law [$\alpha = C f^{p}$]. Such power-law fits to the attenuation-versus-frequency curves in the 5-15 MHz range are also shown in figure 3-53. As shown in figure 3-54, the power-law exponent for pure Ni microstructures is near 4 for small grain diameters, and systematically decreases as the average grain diameter rises, being about 3.0 for 50-micron grains and 2.3 for 100-micron grains. Recall that power-law fits to the Ni alloy attenuation data generally yielded exponents in the 3 to 4 range. Figure 3-55 shows predicted FOM-versus-frequency curves for eight pure Ni microstructures with different average grain diameters. The curves all rise with frequency within the horizontal range shown, but in each case, the rate of rise is significantly lower than that of the associated attenuation-versus-frequency curve.

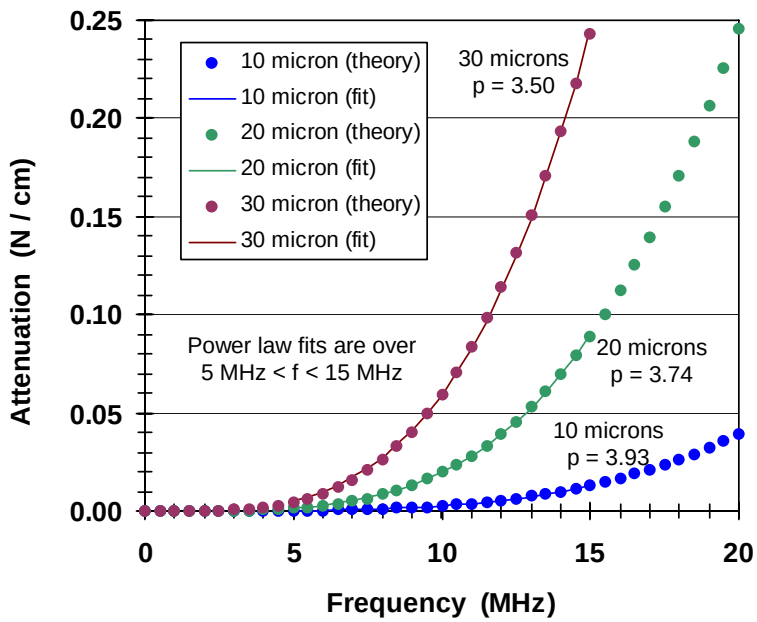

FIGURE 3-53. PREDICTED ATTENUATION-VERSUS-FREQUENCY CURVES AND ASSOCIATED POWER-LAW FITS FOR PURE Ni MICROSTRUCTURES HAVING AVERAGE GRAIN DIAMETERS OF 10, 20, AND 30 microns

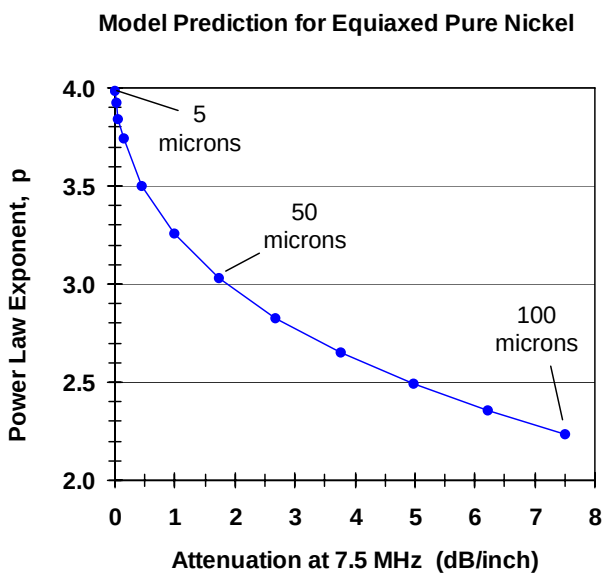

Ave. Grain Diameter (microns)	Attenuation at 7.5 MHz (dB/in)	Power Law Exponent
5	0.002	3.981
10	0.019	3.927
15	0.062	3.844
20	0.143	3.739
30	0.452	3.499
40	0.984	3.254
50	1.738	3.029
60	2.683	2.828
70	3.776	2.651
80	4.971	2.495
90	6.225	2.356
100	7.502	2.232

Power law fits are over
5 MHz < frequency < 15 MHz

FIGURE 3-54. PREDICTED RELATIONSHIP BETWEEN THE AVERAGE GRAIN DIAMETER, THE ATTENUATION AT 7.5 MHz, AND THE EXPONENT IN THE POWER-LAW FIT TO THE ATTENUATION-VERSUS-FREQUENCY CURVE FOR PURE Ni MICROSTRUCTURES

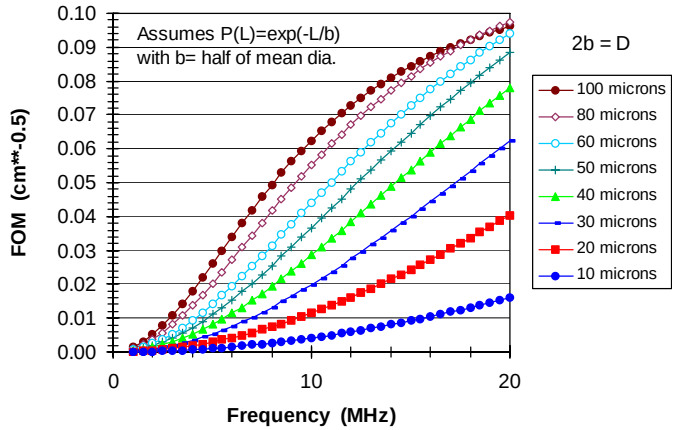

FIGURE 3-55. PREDICTED FOM-VERSUS-FREQUENCY CURVES FOR PURE Ni MICROSTRUCTURES HAVING AVERAGE GRAIN DIAMETERS RANGING FROM 10 TO 100 microns

The relationship between attenuation and FOM for the pure Ni microstructures is illustrated in figure 3-56, assuming a fixed frequency of 7.5 MHz. As the average grain size increases, the FOM value rises less rapidly than the attenuation, leading to a FOM-versus-attenuation curve whose slope decreases as one moves further to the right in the figure (i.e., as the average grain size increases). For the model curve, the FOM value is approximately proportional to the square root of the attenuation value. Also shown for comparison are the measured (attenuation, FOM) pairs at 7.5 MHz for the Ni alloy billet specimens (figure 3-52). The general trend of the Ni alloy data is similar to that predicted for pure Ni microstructures; however, the Ni alloy results tend to lie above the pure Ni curve. Attenuation and FOM values for polycrystals depend, in part, on the single-crystal elastic constants of the metal. The differences seen in figure 3-56 may be a result of associated differences in the elastic constants of pure Ni and the two alloys under study.

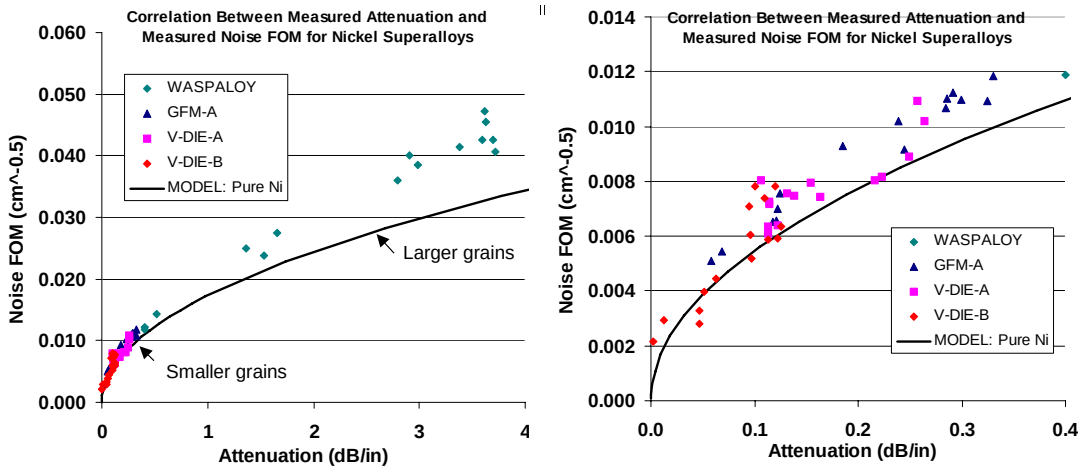

(Solid curve: model prediction for pure Ni. Plotted points: measured data for Ni alloy billet specimens. Right panel shows a blowup of the low attenuation region of the left panel.)

FIGURE 3-56. RELATIONSHIP BETWEEN FOM AND ATTENUATION AT 7.5 MHz

Because attenuation and FOM increase at different rates as the grain size grows, the absolute grain noise level seen in an inspection does not necessarily increase with grain size. The grain noise level (e.g., the rms noise voltage) seen at a particular frequency, f and depth z, in the metal is expected to be proportional to the product [exp(-2a(f)z)][FOM(f)], with the first factor describing the effect of attenuation on the backscattered noise. In addition, a third depth-dependent factor would describe the effect of beam focusing and diffraction. Consider the case of a nondiffracting sonic beam that maintains a constant lateral area during propagation through the metal. For such a beam, figure 3-57 shows the predicted manner in which the noise level depends on the average grain diameter. Results are shown for three depths in pure Ni microstructures. In each case, the noise level peaks at a particular average grain size; beyond that size, signal loss due to attenuation outpaces the increase in signal resulting from the stronger scattering by the larger grains. Note that as the depth in the metal increases, the grain size that produces the largest absolute noise level decreases. It is this interplay between attenuation and FOM that is responsible for the fact that observed absolute noise levels for the Waspaloy and IN718 specimens (figure 3-24) are much more similar than would be expected based on their relative FOM values (figure 3-51).

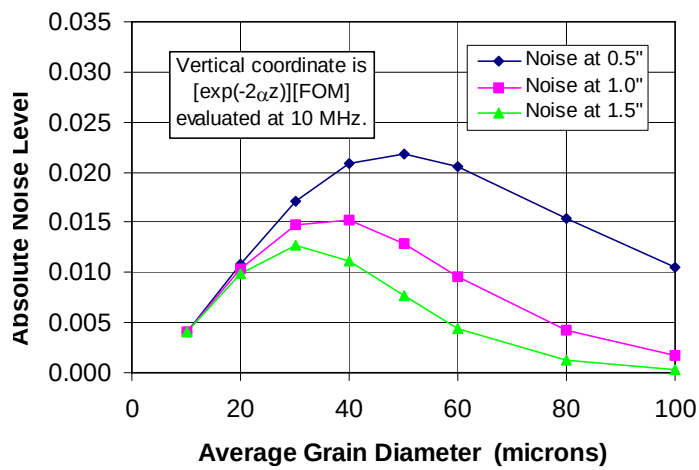

FIGURE 3-57. PREDICTED BEHAVIOR OF THE ABSOLUTE GRAIN NOISE LEVEL SEEN AT THREE DEPTHS IN PURE Ni AS A FUNCTION OF MEAN GRAIN DIAMETER

Note that figure 3-54 contains, for pure Ni microstructures, a short table relating the attenuation at 7.5 MHz to the average grain diameter. One can compare the values in that table to the measured attenuations for the Ni alloy specimens listed in tables 3-6 or 3-8. If one assumes that the relationship between attenuation and grain diameter for the Ni alloys is similar to that for pure Ni, one concludes that average grain diameters within the billet specimens range from approximately 5 to 70 microns. A similar comparison of measured FOM values at 7.5 MHz and those predicted for pure Ni (figure 3-55) leads to estimated grain diameters of 10-100 microns for the billet specimens. The measurement of average grain diameter is the topic of the next section.

3.1.5 Metallography Characterization and the Relationship Between UT Properties and Grain Size.

3.1.5.1 Metallography Coupons and Grain Structure Photography.

One goal of the study was to correlate the measured UT properties with the local billet microstructure. To this end, small metallography coupons from selected billet sites were polished and etched to reveal the grain structure, and grain sizes were then measured from associated photographs. The metallography coupons were not cut directly from the rectangular specimens used for UT property measurements because it was desired to keep these specimens fully intact. Instead, as shown in figure 3-58, the metallography coupons were cut from a 1/2″ thick rough-cut slab that was adjacent in the billet to a given strip coupon. For each of the four strip coupons studied, there were 12 metallography coupons: three each from sites located 0″, 2″, 3″, and 4″ from the billet center. To economize, the 1″ site was skipped because it typically showed very similar attenuation and noise values as the central (0″) site. One face of each metallography coupon was polished, as shown in figure 3-58(b), so that the collection of 12 coupons provided axial, radial, and hoop views of the microstructure at each of the four inspection sites. As shown in figure 3-58(b), the 12 coupons associated with a given UT property strip were denoted A-L. These can be divided into three groups based on their polished surfaces:

- Axial view coupons: A, D, G, and J
- Radial view coupons: B, E, H, and K
- Hoop view coupons: C, F, I, and L

The photographs that were used for grain-sizing work were taken at points located as close as possible to the center of the corresponding UT measurement site. Thus, in the axial-radial plane, the photographed regions of the polished metallography coupons were as close as possible to the blue dot shown in figure 3-58(c). That blue dot indicates a point precisely 0″, 2″, 3″, or 4″ from the billet center.

Grain structure photographs were printed on 8.5″ x 11″ stock, with the magnification chosen such that 150-300 grains were typically seen. An example is shown in figure 3-59(a). Figure 3-59(b) depicts a smaller, representative area of the entire micrograph. Such subimages are used in this document for discussion purposes and to illustrate variations in average grain size with position. For example, figure 3-60 uses subimages to compare the microstructures seen in the 12 Waspaloy metallography coupons. At a given radial location in the Waspaloy billet, the grains are approximately equiaxed, i.e., the grains tend to have approximately circular cross-sections rather than being systematically elongated, and the grain structure appears similar from the three viewing directions. In addition, figure 3-60 shows that the average grain size tends to decrease as one moves radially outward from the center of the billet. In section 3.1.4.2, the UT measurements on the Waspaloy coupons found both attenuation and grain noise to be approximately independent of inspection direction and largest near the billet center. Generally speaking, the grain structures were seen to be approximately equiaxed in all the Ni alloy billet specimens studied. A second example is shown in figure 3-61 for one of the IN718 cases. Note the different magnifications of the two images in figure 3-61; the average grain diameter for the

left-hand image (billet center) is approximately twice that of the right-hand image (1″ from billet OD).

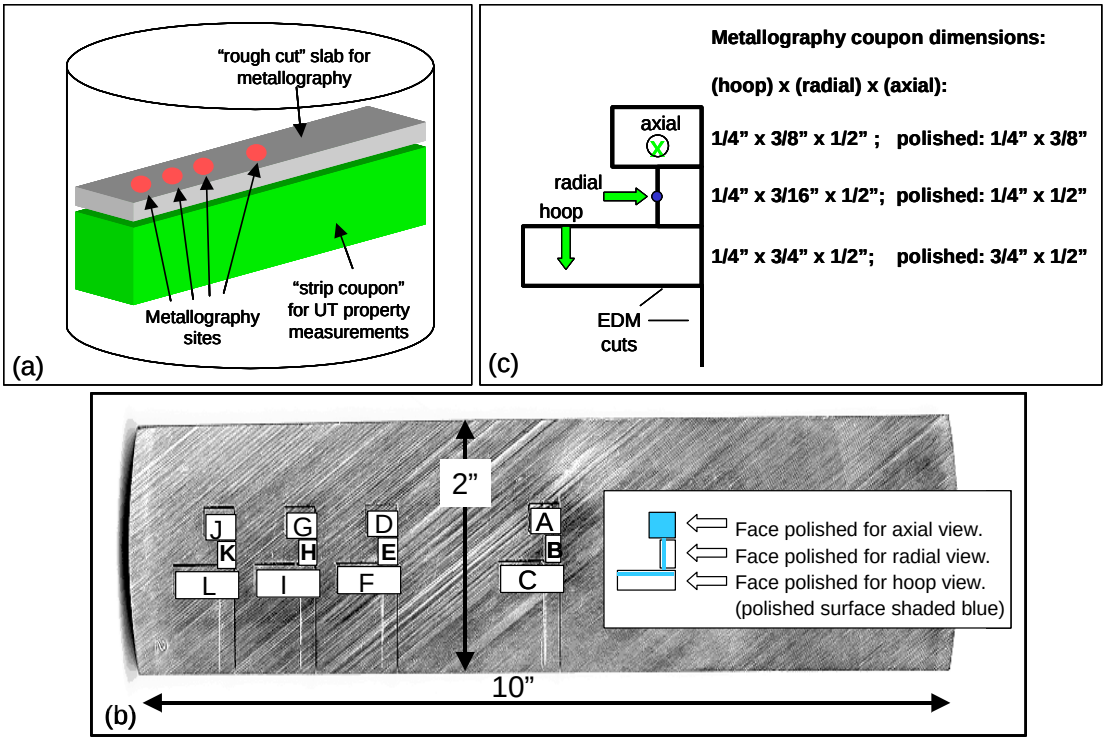

FIGURE 3-58. METALLOGRAPHY COUPONS (a) SLAB FROM WHICH COUPONS ARE CUT, (b) DESIGNATIONS OF THE 12 COUPONS FROM EACH SLAB, AND (c) COUPON DIMENSIONS

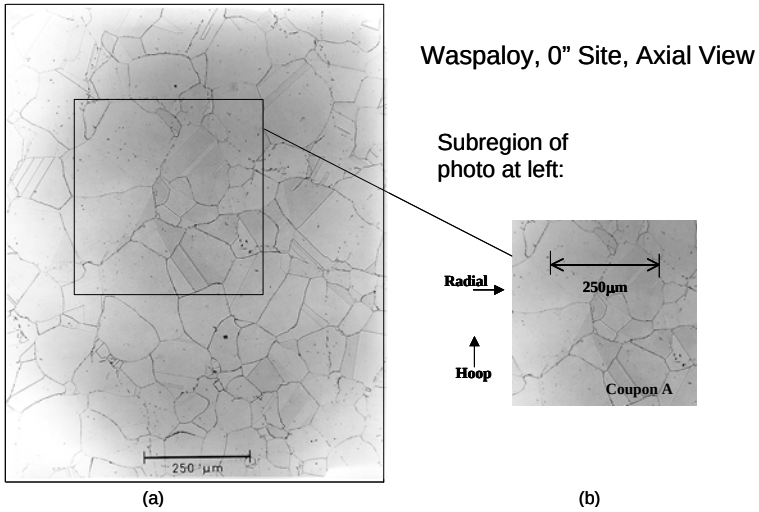

FIGURE 3-59. AXIAL VIEW OF MICROSTRUCTURE AT THE CENTER (0″) OF THE WASPALOY BILLET (a) FULL REGION USED FOR GRAIN SIZE ANALYSIS AND (b) SMALLER SUBREGION

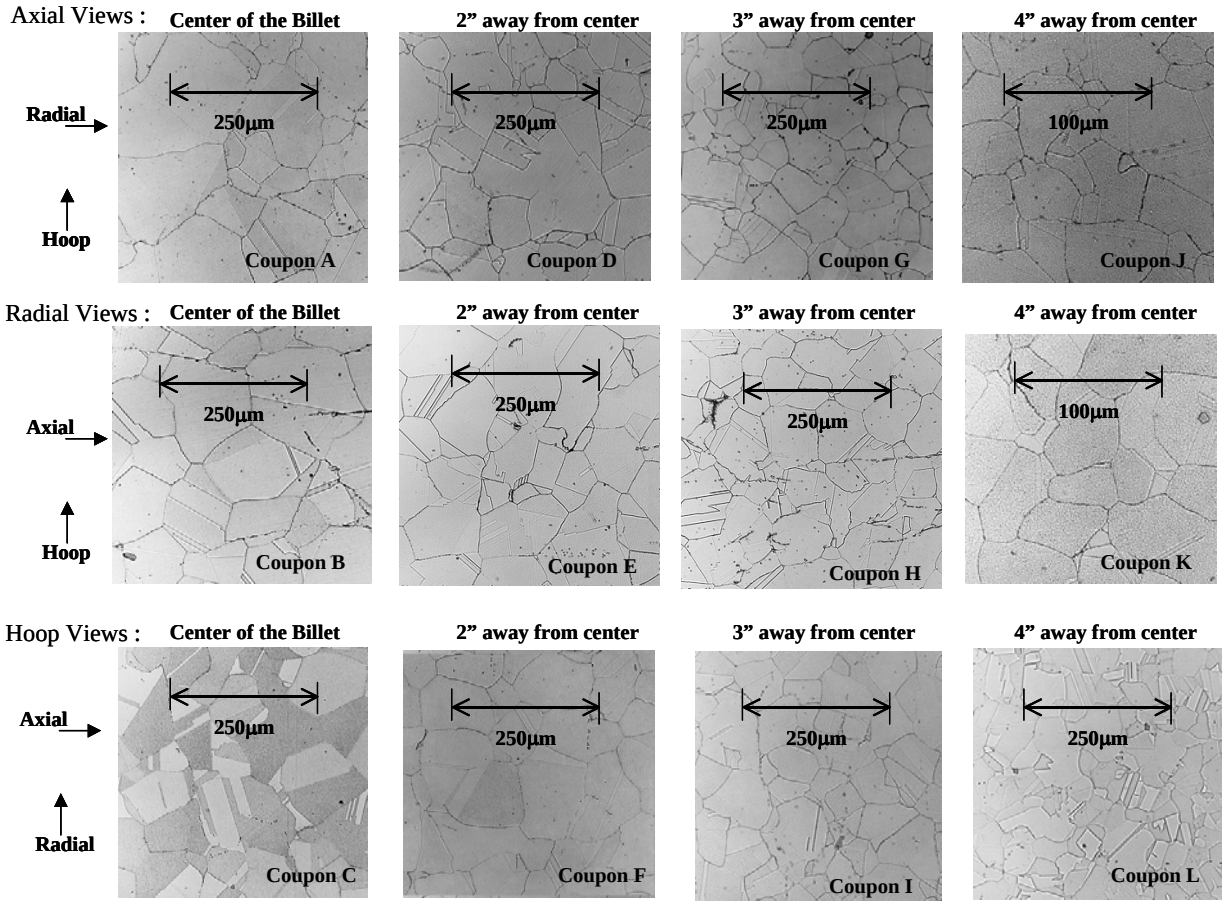

FIGURE 3-60. AXIAL, RADIAL, AND HOOP VIEWS OF THE WASPALOY MICROSTRUCTURE AT FOUR METALLOGRAPHY SITES

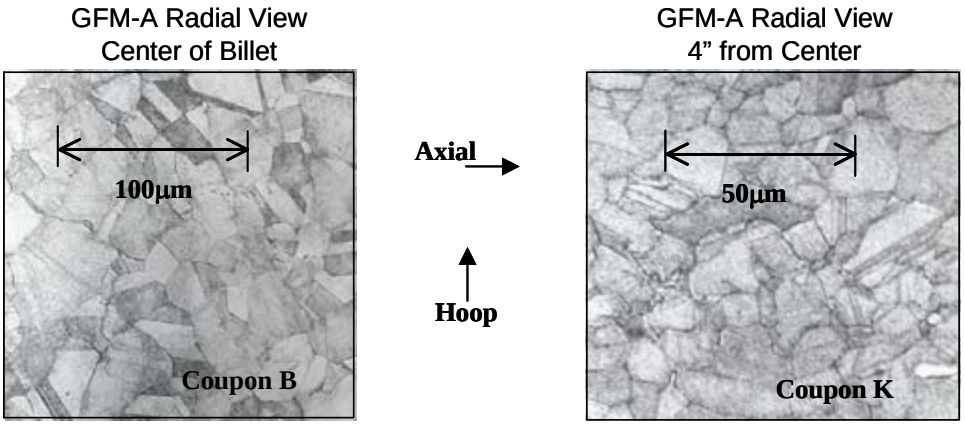

FIGURE 3-61. RADIAL VIEWS OF THE IN718 GFM-A MICROSTRUCTURE AT TWO SITES

3.1.5.2 Grain-Sizing Methods.

Grain size information was deduced from a digitized image of the grain boundaries. The first phase of the analysis is illustrated in figure 3-62. A clear transparency is placed over the microphotograph and the presumed grain boundaries are traced by hand in black ink. The image on the transparency, which has excellent black and white contrast, is scanned and digitized. Commercial software is then used to skeletonize the image, i.e., to reduce the thickness of each grain boundary line to a single pixel. When the tracings are made, an attempt is made to identify the so-called twin boundaries and exclude them from the tracing. This is done because it is believed that these boundaries do not significantly contribute to attenuation and backscattered noise. Twin grain pairs are characterized by a shared boundary that consists of one or more very straight-line segments. Typical examples of presumed twin boundaries are shown in figure 3-63.

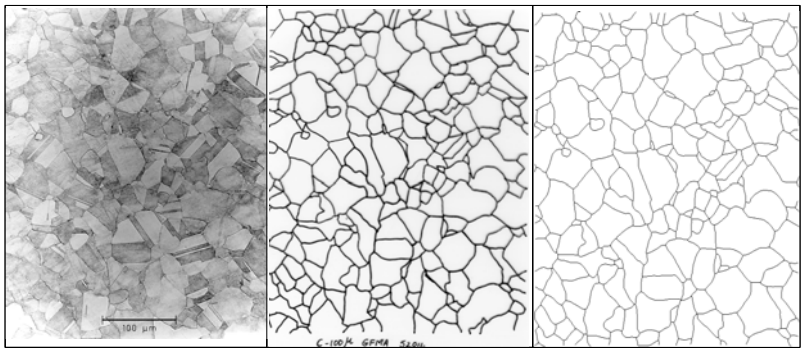

Photograph (a) | Digitized image of grain boundary tracing (b) | Skeletonized image (grain boundaries 1 pixel wide) (c)

FIGURE 3-62. EXAMPLE OF PROCESSING A GRAIN STRUCTURE (a) PHOTOGRAPH, (b) DIGITIZED IMAGE, AND (c) SKELETONIZED IMAGES OF GRAIN BOUNDARIES

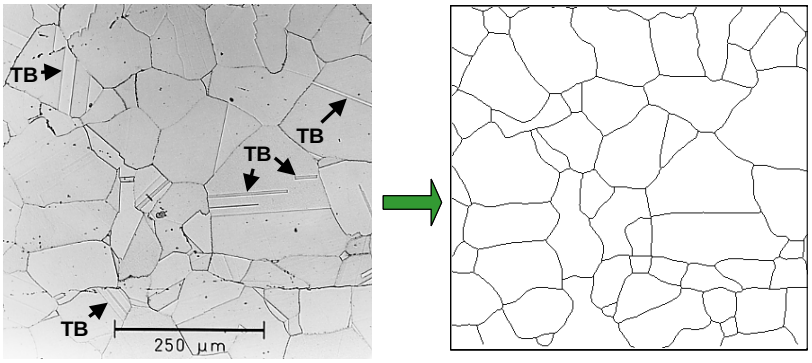

Microstructure photographed. (a)

Grain boundaries traced and digitized. (Twin boundaries ignored) (b)

FIGURE 3-63. (a) MICROGRAPH SUBSECTION WITH SEVERAL PRESUMED TWIN BOUNDARIES IDENTIFIED AND (b) BOUNDARIES IGNORED IN THE FINAL DIGITIZED IMAGE

Twin grains typically have atomic lattice directions that are nearly aligned with one another. Sound energy crossing the boundary between twin grains will, thus, encounter only a minor velocity shift, and the sonic reflection coefficient at the boundary consequently tends to be much smaller than at a typical grain boundary. Since relatively little energy is scattered at twin boundaries, they are not believed to play a major role in determining UT attenuation and backscattered noise levels. Since the goal is to correlate grain diameter estimates with these two UT properties, a conscious effort has been made to identify and exclude obvious twin boundaries from the grain size analysis. However, as will be discussed in section 3.1.5.3, some photographs were reanalyzed counting twin boundaries as bona fide boundaries. This allowed one to determine how the decision to exclude twin boundaries affected the deduced average grain diameter.

For grain size determinations, it is important to accurately determine the scaling factor that translates from pixel coordinates in the skelontonized image to physical coordinates on the metal specimen. This was done by (1) selecting two widely separated points on opposite corners of the image (e.g., easily recognizable vertices where three grains meet), (2) determining the separation between the two points on the skeletonized image in pixel coordinates, (3) determining the separation between the two points on the original photograph in microns, and (4) equating the two separation measurements to determine the scaling factor in microns/pixel. The process is discussed in more detail in references 38 and 45.

Two different methods were used to deduce average grain diameters from a given skeletonized image of the grain boundaries. The first, known as the mean chord length (MCL) method, is illustrated in figure 3-64. This method is equivalent to (1) drawing a set of parallel straight lines through the micrograph, (2) examining each line to determine the points where it crosses grain boundaries, (3) calculating the average length of the small line segments that connect the points (i.e., segments which lie within a single grain), and (4) multiplying this average chord length by 1.5 to obtain a grain diameter estimate. A computer program operating on the digital image of the grain boundaries is used to draw all possible lines in either the horizontal (X) or vertical (Y) direction, and to calculate the chord lengths for each line [45]. The conversion factor of 1.5, which translates from two-dimensional images to three-dimensional diameters, is believed to be appropriate for equiaxed grains of the kind seen in these billets. This is because if a line is randomly passed through a sphere, the length of the line segment within the sphere can range from 0 (line tangent to the sphere) to the sphere diameter (line passing through center of the sphere). If one considers all possible lines (parallel to some given direction) that intersect the sphere, the average line segment within the sphere is 2/3 of the sphere diameter. Hence, the sphere diameter is 3/2 of the MCL.

The second, known as the P(L) method, is an alternative approach to grain sizing and is summarized in figure 3-65. There, one begins by analyzing the skeletonized grain boundary image to determine:

> P(L) = the probability P that a line segment of length L, randomly placed on the micrograph, lies entirely within a single grain.

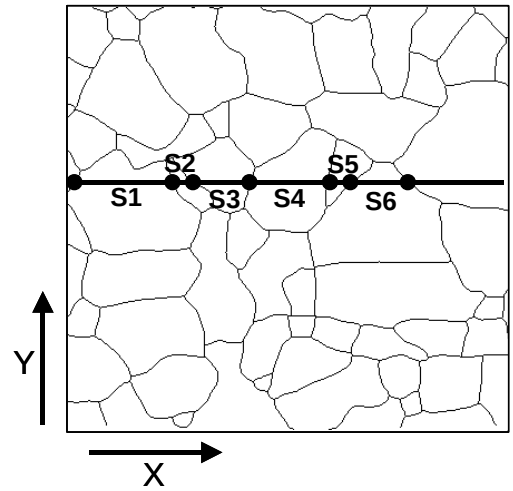

MCL Method:

Horizontal (X) or vertical (Y) lines are drawn through the tracing.

The average of the chord lengths (S_j) is calculated.

The average chord length is multiplied by 1.5 to obtain an estimate of the average grain diameter.

FIGURE 3-64. MEAN CHORD LENGTH METHOD FOR DETERMINING AVERAGE GRAIN DIAMETER

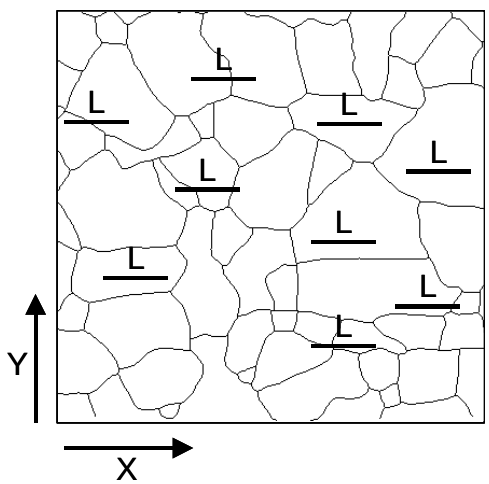

P(L) Method:

For a given length L, line segments of that length are randomly placed on the tracing. Some cross grain boundaries, some do not. Count each type to determine:

P(L) = probability that a segment of length L lies entirely within one grain.

Repeat for a series of different lengths.

Fit an exponential function $e^{-L/b}$ to P(L).

Use 2b as an estimate of the average grain diameter.

FIGURE 3-65. P(L) METHOD FOR DETERMINING AVERAGE GRAIN DIAMETER

For a given line segment length (L), a computer program is used to generate the line segments, place them on the image, and decide whether a given segment crosses a grain boundary [45]. One begins by considering short line segments having a length of one pixel and progresses systematically to longer lengths until the line segment becomes so large that it always crosses a grain boundary regardless of where it is placed on the image [P(L)=0]. As with the MCL method, the P(L) method can be applied separately in the X and Y directions of the image. The X or Y analysis of a micrograph yields a probability-versus-length curve, P(L). This curve is then fit to an exponential function P(L) = exp(-L/b), and 2b is used as an estimate of the mean grain diameter [43]. Typical measured P(L) curves do not exactly follow an exponential function, leading to some uncertainty in the fitting parameter b and the associated grain diameter estimate. To document this uncertainty, separate fits were performed to different regions of the

measured P(L) curve. This is illustrated in figure 3-66, where fits to the low L and high L halves of the data are shown for one case. In practice, separate fits were performed to ten overlapping regions of the measured P(L) curve, with each such region comprising 50% of the horizontal range of the P(L) data; the minimum, maximum, and mean values of b thus obtained are then tabulated. Note that the P(L) curve for a given microstructure, sometimes referred to as a two-point correlation function, is of interest because it appears in a direct manner in certain models of UT beam propagation and scattering, playing a key role in determining the levels of UT attenuation and backscattered grain noise [29 and 43].

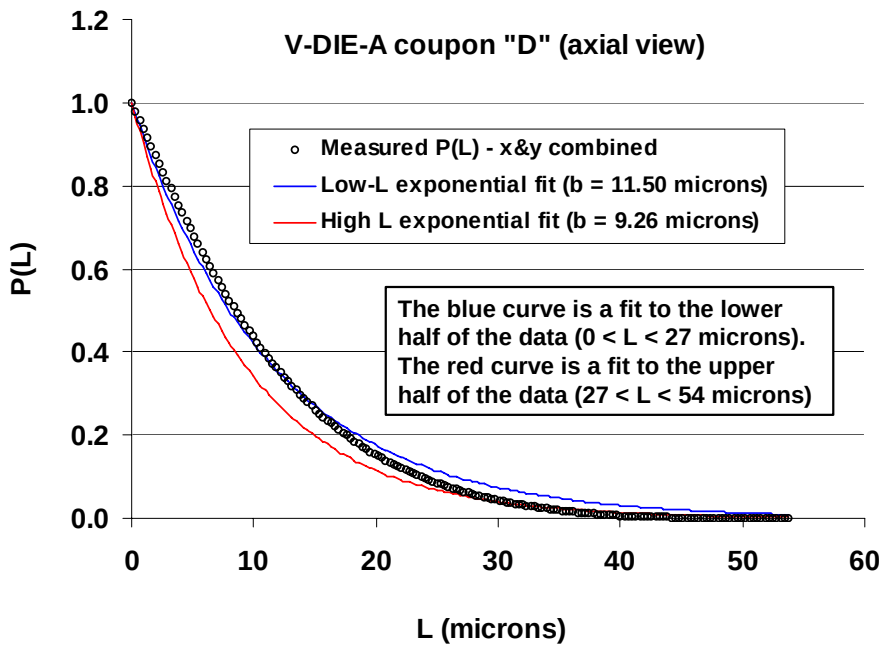

FIGURE 3-66. EXAMPLES OF EXPONENTIAL FITS TO MEASURED P(L) CURVES FOR A TYPICAL CASE

A Fortran program named GrnSize3 was developed at ISU to perform both the MCL and P(L) analyses [45]. For a given skeletonized image that is input to the program, grain-sizing results are summarized in the manner illustrated in table 3-9. The P(L) and MCL analyses are summarized in the upper and lower portion of the table, respectively. Note that for each sizing method, separate analyses are carried out for X alone, for Y alone, and for XY. The latter describes an analysis in which the data for the X and Y directions is combined and then processed to determine a grain size estimate. For the P(L) method, the third analysis involves averaging the measured X and Y P(L) curves, and then fitting exponentials to the average curve. For the MCL method, the third analysis is equivalent to simply averaging the MCL estimates from the separate X and Y analyses to obtain a new MCL estimate. Notice the "Where" parameter in table 3-9, which describes the portion of the measured P(L) curve that is being fit to an exponential function. As Where varies from 0 to 100, the 50% of the data being fit varies from the extreme low-L portion to the extreme high-L portion in a systematic manner. For the case shown in table 3-9, the P(L) method yielded an average grain diameter estimate of 30.20 microns for the analysis in which (1) the X and Y data were combined to determine the overall P(L) curve; (2) ten separate exponential fits were made to various portions of that P(L) curve;

and (3) the ten grain size estimates resulting from the 10 separate fits were averaged. For the case shown in table 3-9, the MCL method yielded an average grain diameter of 33.07 microns when averaged over the X and Y data. Details of the inner workings and use of the Grnsize3 software can be found in the User's Guide [45].

TABLE 3-9. SUMMARY OF GRAIN-SIZING ANALYSES FOR ONE MICROGRAPH OF METALLOGRAPHY COUPON C OF THE GFM-A SPECIMEN (0″ site; hoop view)

Table of b values for P(L) in microns:

"Where"	b for x	b for y	b for xy
0.00E+00	1.63E+01	1.77E+01	1.69E+01
1.00E+01	1.61E+01	1.75E+01	1.68E+01
2.00E+01	1.58E+01	1.73E+01	1.65E+01
3.00E+01	1.55E+01	1.69E+01	1.61E+01
4.00E+01	1.50E+01	1.64E+01	1.56E+01
5.00E+01	1.46E+01	1.59E+01	1.52E+01
6.00E+01	1.41E+01	1.54E+01	1.47E+01
7.00E+01	1.37E+01	1.49E+01	1.42E+01
8.00E+01	1.33E+01	1.44E+01	1.38E+01
9.00E+01	1.30E+01	1.40E+01	1.34E+01
1.00E+02	1.27E+01	1.35E+01	1.30E+01
AVE b =	14.55	15.81	15.10

	b	P(L) Ave. Grain Diameter
Highest b for x:	16.27	32.54
Lowest b for x:	12.66	25.32
Highest b for y:	17.72	35.44
Lowest b for y:	13.49	26.98
Highest b for xy:	16.91	33.83
Lowest b for xy:	12.99	25.99

AVE. GRAIN DIA. VIA P(L) (microns, for xy) = 2b = 30.20

		MCL Average Grain Diameter
Mean chord length along x (microns) :	21.4803	32.22
Mean chord length along y (microns) :	22.6075	33.91
Average MCL for x & y (microns) :	22.0439	33.07

AVE. GRAIN DIA. VIA MCL (microns, for xy) = 33.07

AVE. FROM THE TWO METHODS= 31.64 microns

3.1.5.3 Grain-Sizing Results.

The results of the grain-sizing analyses performed on micrographs from the 48 metallographic coupons are listed in tables 3-10 through 3-13. The first two columns of each table list the coupon site (distance from billet center) and coupon designation as defined in figure 3-58(b). The third column lists grain diameter estimates inferred from the attenuation measurements; the tabulated value is the mean grain diameter of an equiaxed pure Ni microstructure having a predicted attenuation-versus-frequency curve that approximately matches the measured curve. Note that the third column results are for reference only; one does not expect these predicted grain diameters to match measured ones because the elastic properties of pure Ni are different than those of the alloys. However, the predicted grain diameters serve to remind us of the trend of the attenuation data, with larger predicted diameters associated with larger measured

TABLE 3-10. AVERAGE GRAIN DIAMETERS DEDUCED FROM WASPALOY METALLOGRAPHY

WASP Coupon		From Atten.	From XY ave. of P(L) and MCL Methods	From P(L) Using Highest b for X	From P(L) Using Lowest b for X	From P(L) Using Highest b for Y	From P(L) Using Lowest b for Y	From P(L) Using Highest b for XY	From P(L) Using Lowest b for XY	From P(L) Using Average b for X	From P(L) Using Average b for Y	From P(L) Using Average b for XY
0″	A	69	115.88	125.01	92.21	128.93	101.78	126.52	95.90	110.40	117.01	113.01
0″	A*	69	82.33	89.18	73.74	92.41	79.51	90.54	75.88	82.63	87.03	84.37
0″	B		117.16	139.60	103.14	115.79	90.06	126.70	96.02	123.28	103.75	112.87
0″	C	66	113.08	119.26	87.93	130.89	106.31	123.85	95.98	105.14	119.32	110.91
2″	D	62	91.85	95.36	68.91	104.18	76.44	98.82	70.33	81.89	92.05	85.55
2″	D*	62	70.94	79.28	66.27	76.15	65.35	77.20	62.15	72.12	71.38	70.04
2″	E		65.29	102.24	74.80	102.85	79.88	102.03	76.45	90.03	92.49	90.59
2″	F	60	105.07	112.99	80.01	114.23	89.43	111.72	79.88	97.11	102.32	96.86
3″	G	47	74.83	83.37	61.36	76.52	55.87	79.78	58.73	73.75	67.40	70.54
3″	G*	47	63.37	69.48	53.76	66.56	51.16	67.82	51.75	62.72	59.93	60.91
3″	H		87.91	112.99	80.01	114.23	89.43	111.72	79.88	97.11	102.32	96.86
3″	I	45	72.76	80.71	60.24	78.38	56.83	78.27	55.04	71.74	69.17	68.42
4″	J	28	44.36	51.10	36.93	50.14	37.45	50.56	37.05	44.90	44.75	44.74
4″	J*	28	36.04	42.84	33.27	38.99	30.92	40.67	31.46	38.78	35.48	36.77
4″	K		50.01	54.22	40.61	58.48	45.40	55.80	41.86	48.35	52.77	49.80
4″	L	28	47.70	50.24	37.63	50.38	36.21	50.20	36.60	44.53	44.24	44.14

Coupon		From Atten.	From MCL for X	From MCL for Y	From MCL for XY
0″	A	69	116.70	120.82	118.76
0″	A*	69	79.07	81.49	80.28
0″	B		131.26	111.65	121.46
0″	C	69	111.05	119.46	115.25
2″	D	62	97.33	98.96	98.14
2″	D*	62	72.19	71.49	71.84
2″	E		102.08	97.88	99.98
2″	F	60	114.44	112.10	113.27
3″	G	47	81.12	77.13	79.13
3″	G*	47	66.40	65.25	65.83
3″	H		81.53	76.37	78.95
3″	I	45	75.97	78.22	77.09
4″	J	28	42.92	45.02	43.97
4″	J*	28	36.13	34.49	35.31
4″	K		49.46	51.00	50.23
4″	L	28	50.91	51.58	51.25

Notes: All numerical values are average grain diameters in microns.

A,B, C,…L identify the 12 metallography coupons:
A, D. G, J present axial views of the microstructure.
B, E, H, K present radial views of the microstructure.
C, F, I, L present hoop views of the microstructure.

Results are given for analyses in the X and Y directions of each micrograph, and for a combined (XY) analysis.

In most cases, apparent twin boundaries were not counted as bona fide grain boundaries when making tracings. However for entries denoted A*, D*, G*, and J*, twin boundaries were counted as bona fide grain boundaries (leading to a smaller average grain size.)

The result labeled “From Atten.” is the average grain diameter of a pure Ni microstructure, which has the same attenuation near 7.5 MHz as measured for the Ni alloy specimen in the corresponding inspection direction.

TABLE 3-11. AVERAGE GRAIN DIAMETERS DEDUCED FROM GFM-A METALLOGRAPHY

GFM-A Coupon		From Atten.	From XY Ave. of P(L) and MCL Methods	From P(L) Using Highest b for X	From P(L) Using Lowest b for X	From P(L) Using Highest b for Y	From P(L) Using Lowest b for Y	From P(L) Using Highest b for XY	From P(L) Using Lowest b for XY	From P(L) Using Average b for X	From P(L) Using Average b for Y	From P(L) Using Average b for XY
0″	A	25	36.28	41.07	39.68	39.17	37.57	39.47	38.20	40.74	38.14	39.09
0″	B		32.63	34.57	26.39	36.59	29.13	35.55	27.82	30.86	33.55	32.22
0″	C	26	31.64	32.54	25.32	35.44	26.98	33.83	25.99	29.10	31.61	30.20
2″	D	24	30.40	32.85	27.25	31.99	23.49	32.37	25.40	30.05	28.27	29.11
2″	E		26.58	30.22	25.16	30.01	22.68	29.68	22.84	27.52	26.79	26.46
2″	F	21	25.06	28.29	22.04	27.27	20.48	27.50	20.64	25.51	24.24	24.47
3″	G	18	24.69	26.23	21.82	27.12	26.23	26.68	23.04	24.61	26.92	25.54
3″	H		23.07	25.31	17.55	24.82	19.09	24.82	17.86	21.90	22.20	21.70
3″	I	18	19.84	21.84	15.60	22.54	15.43	21.56	13.93	19.05	19.58	18.29
4″	J	14	16.75	17.91	12.87	17.70	13.58	17.69	12.83	15.69	15.69	15.47
4″	K		17.27	19.29	15.41	17.62	15.20	18.22	14.94	17.48	16.24	16.44
4″	L	15	14.60	14.15	9.75	16.55	14.28	15.15	12.29	12.20	15.21	13.50

Coupon		From Atten.	From MCL Along X	From MCL Along Y	From MCL Along XY
0″	A	25	34.77	32.17	33.47
0″	B		31.89	34.21	33.05
0″	C	26	32.22	33.91	33.07
2″	D	24	32.49	30.92	31.70
2″	E		26.17	27.23	26.70
2″	F	21	26.14	25.17	25.66
3″	G	18	23.59	24.10	23.85
3″	H		24.66	24.21	24.44
3″	I	18	20.11	22.66	21.39
4″	J	14	17.96	18.10	18.03
4″	K		18.57	17.61	18.09
4″	L	15	14.67	16.72	15.69

Notes: All numerical values are average grain diameters in microns.

A,B, C,…L identify the 12 metallography coupons:
A, D. G, J present axial views of the microstructure.
B, E, H, K present radial views of the microstructure.
C, F, I, L present hoop views of the microstructure.

Results are given for analyses in the X and Y directions of each micrograph, and for a combined (XY) analysis.

In most cases, apparent twin boundaries were not counted as bona fide grain boundaries when making tracings.

The result labeled “From Atten.” is the average grain diameter of a pure Ni microstructure, which has the same attenuation near 7.5 MHz as measured for the Ni alloy specimen in the corresponding inspection direction.

TABLE 3-12. AVERAGE GRAIN DIAMETERS DEDUCED FROM V-DIE-A METALLOGRAPHY

V-Die-A Coupon		From Atten.	From XY Ave. of P(L) and MCL Methods	From P(L) Using Highest b for X	From P(L) Using Lowest b for X	From P(L) Using Highest b for Y	From P(L) Using Lowest b for Y	From P(L) Using Highest b for XY	From P(L) Using Lowest b for XY	From P(L) Using Average b for X	From P(L) Using Average b for Y	From P(L) Using Average b for XY
0″	A	19	24.84	27.05	20.74	28.85	24.89	27.72	21.27	24.31	27.06	25.08
0″	B		25.53	29.97	21.25	26.20	18.89	27.95	20.03	26.11	22.93	24.45
0″	C	18	21.15	25.47	22.96	21.73	16.68	21.87	19.63	23.67	19.48	20.63
2″	D	18	21.63	24.43	19.24	23.12	17.80	23.74	18.50	22.05	20.42	21.20
2″	E		20.48	22.48	18.83	21.48	18.91	21.88	18.41	20.51	20.22	20.15
2″	F	18	23.89	24.19	18.82	27.90	25.19	25.93	22.08	21.99	26.78	24.31
3″	G	21	17.89	19.38	16.16	18.84	15.62	19.10	15.89	17.79	17.31	17.55
3″	H		15.58	18.08	16.70	15.66	11.87	16.49	14.08	17.23	13.97	15.09
3″	I	22	14.14	14.99	13.29	14.55	11.48	14.76	12.43	14.07	12.97	13.51
4″	J	24	20.60	23.11	18.14	21.14	17.06	22.03	17.43	21.02	19.28	20.05
4″	K		23.78	31.11	29.28	20.02	16.66	25.00	23.69	29.99	18.37	24.28
4″	L	22	15.62	15.27	11.45	18.21	15.77	16.51	13.51	13.58	17.02	15.06

Coupon		From Atten.	From MCL Along X	From MCL Along Y	From MCL Along XY
0″	A	19	22.45	26.78	24.61
0″	B		27.06	26.21	26.63
0″	C	18	22.15	21.21	21.68
2″	D	18	21.92	22.23	22.08
2″	E		21.12	20.53	20.83
2″	F	18	22.33	24.65	23.49
3″	G	21	18.41	18.08	18.25
3″	H		16.60	15.55	16.08
3″	I	22	14.85	14.71	14.78
4″	J	24	21.65	20.65	21.15
4″	K		26.99	19.60	23.30
4″	L	22	15.47	16.90	16.18

Notes: All numerical values are average grain diameters in microns.

A,B, C,…L identify the 12 metallography coupons:
A, D. G, J present axial views of the microstructure.
B, E, H, K present radial views of the microstructure.
C, F, I, L present hoop views of the microstructure.

Results are given for analyses in the X and Y directions of each micrograph, and for a combined (XY) analysis.

In most cases, apparent twin boundaries were not counted as bona fide grain boundaries when making tracings.

The result labeled “From Atten.” is the average grain diameter of a pure Ni microstructure, which has the same attenuation near 7.5 MHz as measured for the Ni alloy specimen in the corresponding inspection direction.

TABLE 3-13. AVERAGE GRAIN DIAMETERS DEDUCED FROM V-DIE-B METALLOGRAPHY

V-Die-B Coupon		From Atten.	From XY Ave. of P(L) and MCL Methods	From P(L) Using Highest b for X	From P(L) Using Lowest b for X	From P(L) Using Highest b for Y	From P(L) Using Lowest b for Y	From P(L) Using Highest b for XY	From P(L) Using Lowest b for XY	From P(L) Using Average b for X	From P(L) Using Average b for Y	From P(L) Using Average b for XY
0″	A	17	23.41	26.24	22.97	24.80	19.15	25.49	21.02	24.87	22.43	23.59
0″	B		27.36	31.04	24.89	31.14	23.59	30.77	23.39	28.59	27.91	27.75
0″	C	17	24.58	25.89	18.95	29.11	25.66	26.29	21.08	22.77	27.42	23.65
2″	D	17	21.32	22.37	18.56	23.95	19.63	23.00	18.53	20.67	21.93	21.01
2″	E		21.25	23.42	17.14	22.89	18.77	23.06	17.68	20.60	21.04	20.66
2″	F	19	18.11	18.57	14.49	20.21	16.90	19.15	15.11	16.66	18.52	17.20
3″	G	13	16.73	18.36	12.79	18.15	13.76	17.84	12.46	15.86	16.22	15.47
3″	H		17.10	19.29	15.30	17.11	13.90	18.13	14.52	17.49	15.63	16.50
3″	I	14	15.49	15.99	13.44	17.07	13.19	16.39	12.89	14.65	15.36	14.78
4″	J	<5	13.24	14.57	11.01	13.02	9.27	13.75	10.11	12.95	11.35	12.11
4″	K		12.39	13.95	10.24	12.03	9.25	12.90	9.65	12.32	10.75	11.45
4″	L	7	13.82	14.30	10.80	14.52	10.04	14.35	10.30	12.69	12.52	12.51

Coupon		From Atten.	From MCL Along X	From MCL Along Y	From MCL Along XY
0″	A	17	23.18	23.28	23.23
0″	B		25.89	28.06	26.97
0″	C	17	23.90	27.11	25.51
2″	D	17	20.48	22.76	21.62
2″	E		22.77	20.91	21.84
2″	F	19	18.22	19.83	19.02
3″	G	13	17.94	18.03	17.98
3″	H		18.59	16.83	17.71
3″	I	14	15.82	16.57	16.20
4″	J	<5	14.96	13.80	14.38
4″	K		14.06	12.61	13.34
4″	L	7	14.97	15.29	15.13

Notes: All numerical values are average grain diameters in microns.

A,B, C,…L identify the 12 metallography coupons:
A, D. G, J present axial views of the microstructure.
B, E, H, K present radial views of the microstructure.
C, F, I, L present hoop views of the microstructure.

Results are given for analyses in the X and Y directions of each micrograph, and for a combined (XY) analysis.

In most cases, apparent twin boundaries were not counted as bona fide grain boundaries when making tracings.

The result labeled “From Atten.” is the average grain diameter of a pure Ni microstructure, which has the same attenuation near 7.5 MHz as measured for the Ni alloy specimen in the corresponding inspection direction.

attenuation values. The fourth column in the upper half of tables 3-10 through 3-13 lists an overall estimate of the mean grain diameter; this is obtained by averaging the results of the MCL and P(L) analyses, which use the combined data from the X and Y directions of the micrograph in question. The remainder of the columns in the upper half of each table list various results from the P(L) analyses. These include mean grain diameters deduced using the highest, lowest, and average b-parameters from the various exponential fits to the measured P(L) curve, with values listed separately for the X, Y, and combined (XY) micrograph directions. The lower half of tables 3-10 through 3-13 lists the mean grain diameters resulting from the MCL analyses of the X, Y, and combined (XY) data.

It was endeavored to make grain diameter estimates near the sites where UT property measurements were conducted without cutting the property measurement coupons themselves. Absolute errors in grain diameter estimates at the UT sites are believed to mainly arise from three factors: (1) the process of identifying nontwin grain boundaries is somewhat subjective, (2) a given micrograph containing a few hundred grains represents only a very minute fraction of the specimen volume that is insonified in a typical UT measurement, and (3) because the metallography coupons were taken from the rough-cut slab shown in figure 3-58(a), there is approximately a 1″ axial shift between the locations where metallography was done and the center of the associated UT property measurement region.

It is difficult to estimate the absolute grain diameter error that results from these combined factors, but it was suspected that it could be 25% or more in isolated cases.

The effect of eliminating the twin grain boundaries from the analysis was also studied. For four of the Waspaloy micrographs, two analyses were carried out: one in which apparent twin boundaries were identified and excluded from the tracing (the standard procedure) and another in which apparent twin boundaries were included in the tracing. The results, taken from column 4 of table 3-10, are graphically summarized in figure 3-67. Retaining twin boundaries as bona fide grain boundaries will, of course, reduce the average grain diameter below that obtained from the standard analysis. In the Waspaloy study, retaining twin boundaries decreased the mean grain diameter to about 76% of the standard treatment. That ratio is likely similar for the IN718 cases as well, since twin boundaries were observed to be present in roughly similar proportions in the micrographs of both alloys.

Each of the grain structure micrographs had its X and Y axes approximately aligned with the principal billet axes, i.e., with the axial, radial, or hoop directions. For example, in figure 3-58, the X and Y axes for micrographs of coupons A, D, G, and J are parallel to the radial and hoop directions, respectively. In all the cases examined, the grain cross-sections shown in the micrographs had roughly similar average dimensions in the X and Y directions. This indicated that there was no general tendency for grains to be preferentially longer, for instance, in the radial direction than in the hoop direction. It also reinforced the finding, from visual observation of the micrographs, that the grain structures were approximately equiaxed (i.e., spherical). This is demonstrated in figure 3-68 for the MCL method. For each of the $4 \times 12 = 48$ metallography coupons, the grain diameter estimate from the analysis in the Y direction is plotted versus the result for the X direction. The grain diameter estimates vary widely, from about 15 microns for some IN718 coupons to about 120 microns for some Waspaloy coupons. However, for each

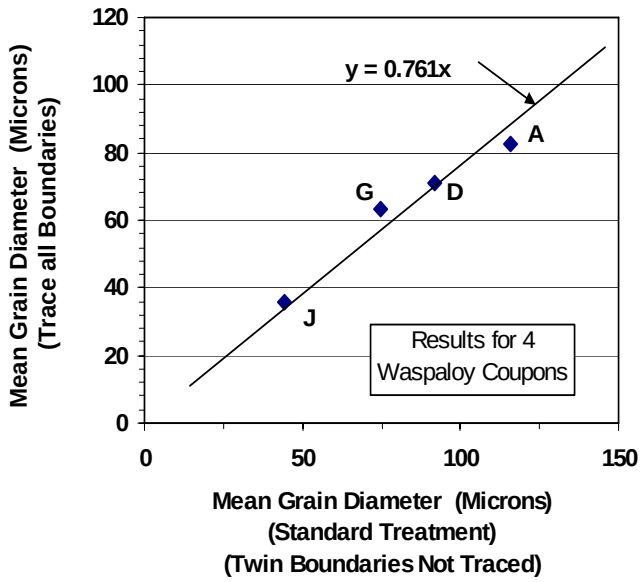

FIGURE 3-67. EFFECT OF TWIN GRAIN TREATMENT ON DEDUCED MEAN DIAMETER

micrograph, the X and Y diameter estimates tend to be very similar to each other, and thus, the plotted points in figure 3-68 lie close to the diagonal line that would result from a perfectly equiaxed microstructure. The P(L) analysis similarly finds nearly equiaxed grain diameters.

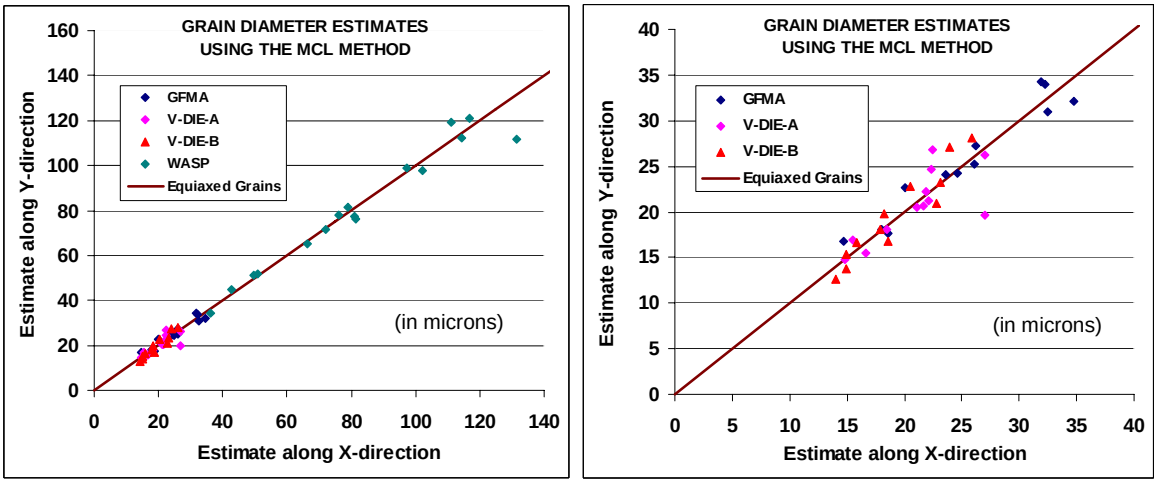

FIGURE 3-68. COMPARISONS OF AVERAGE GRAIN DIAMETERS IN THE X AND Y DIRECTIONS OF Ni ALLOY MICROGRAPHS USING THE MCL METHOD
(The right-hand panel is a blowup of the small diameter region where the IN718 values lie.)

When a given micrograph is analyzed, the MCL grain size estimate usually falls in between the minimum and maximum estimates from the P(L) method. This is demonstrated in figure 3-69 for average grain sizes deduced from the 12 V-Die-B metallography coupons. In the figure, the coupons have been arranged in order of increasing MCL grain size estimate to give the plot a

smoother appearance. When the P(L) method was applied to a given micrograph, exponentials were fitted separately to ten regions of the P(L) data as usual, and the resulting minimum, maximum, and mean estimates of average grain diameter are all shown in figure 3-69. One sees that in all but one case (coupon K), the MCL grain diameter estimate lies between the minimum and maximum estimates from the P(L) method.

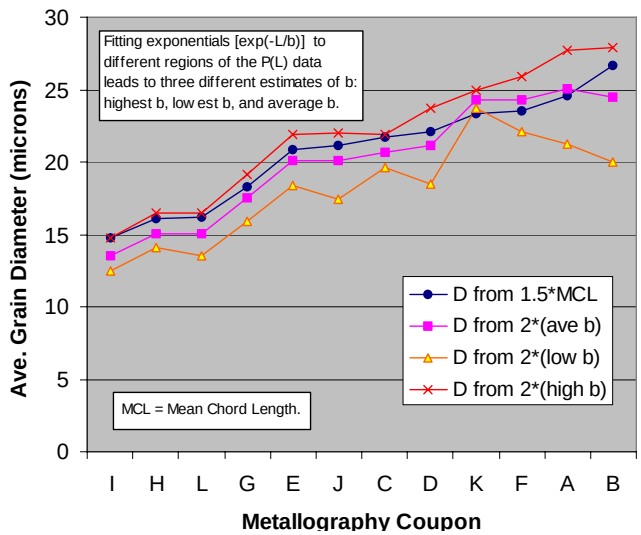

FIGURE 3-69. COMPARISONS OF AVERAGE GRAIN DIAMETERS IN THE 12 V-DIE-B MICROGRAPHS AS ESTIMATED USING THE MCL AND P(L) METHODS
(In each case, results are averaged over the X and Y directions.)

Overall, it was found that the average grain diameter estimate from the P(L) method tended to be about 5% below that from the MCL method. This is demonstrated in figure 3-70. For each of the 48 metallography coupons, the average grain diameter estimate from the P(L) method is plotted versus the estimate from the MCL method. For both methods, an average over the X and Y directions has been taken, and the P(L) results are averages over the ten exponential fits to various regions of the P(L) data. The plotted points in the figure lie nearly along a straight line, indicating a high degree of correlation between the two grain diameter estimates. A best-fit line through the plotted points is also shown and shows a slope of 0.946. This indicates that, on average, the P(L) grain diameter estimate is 94.6% of the MCL estimate.

Since the grains generally appear to be nearly equiaxed and the two analysis methods yield similar diameter estimates, the data were averaged over the two analysis directions for [X and Y] and over the two methods [MCL and average P(L)] to arrive at an overall best grain diameter estimate for each image. These best estimates for each micrograph were listed earlier in column four of tables 3-10 through 3-13. Finally, three viewing directions were averaged over each metallography site (e.g., over coupons A, B, and C at the billet center) to obtain the best estimate of the mean grain diameter at a given radial depth. These latter estimates are listed in table 3-14.

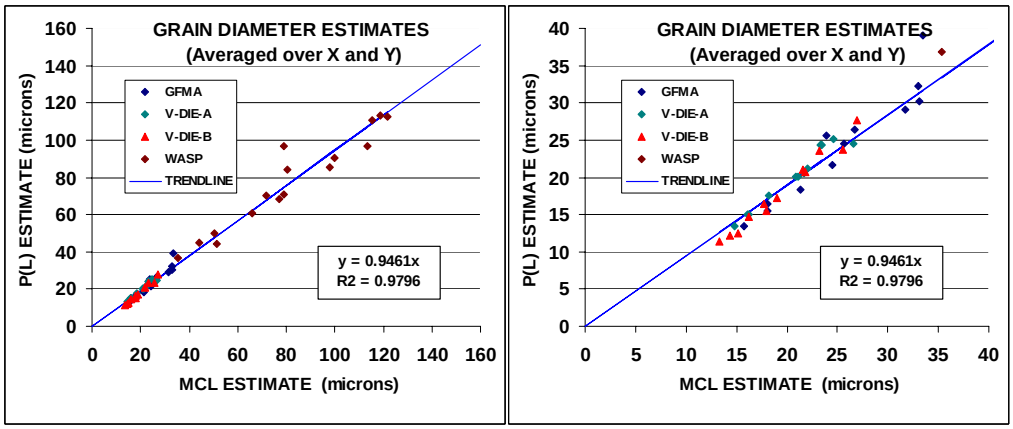

FIGURE 3-70. COMPARISONS OF AVERAGE GRAIN DIAMETERS AS ESTIMATED BY THE MCL AND P(L) METHODS FOR EACH OF THE 4 x 12 MICROGRAPHS ANALYZED (The right-hand panel is a blowup of the small diameter region where the IN718 values lie.)

TABLE 3-14. BEST ESTIMATES OF AVERAGE GRAIN DIAMETERS AT RADIAL SITES IN THE FOUR Ni ALLOY METALLOGRAPHY SLABS

Average Grain Diameter in Microns				
Site	WASP	GFM-A	V-Die-A	V-Die-B
0″	115.39	33.52	23.85	25.12
2″	97.40	27.35	22.01	20.23
3″	78.50	22.53	15.88	16.44
4″	47.36	16.20	20.00	13.15

Note: Site coordinate is the distance from the billet center.

As will be discussed in section 3.1.5.4, the grain-sizing results in tables 3-10 through 3-13 were, for the most part, reasonably well correlated with the earlier UT results. For a given strip coupon, sites with larger grain diameters tended to have higher attenuations and higher FOM values. The notable exception was the V-Die-A strip. For that specimen, attenuation and FOM values tended to be larger near the OD than near the billet center (see figures 3-50 and 3-51). However, metallography performed on the adjacent rough-cut slab found average grain diameters to be slightly larger near the billet center than near the billet OD (see table 3-14).

A second round of metallographic studies was carried out on the V-Die-A rough-cut specimen to check the original results. The locations of the 12 metallographic coupons used in the original study and the four coupons used in the new study are shown in figures 3-71(a) and 3-71(b), respectively. The four new coupons had different dimensions in the hoop direction (ranging from 1/4″ to 5/8″) so that there was no possibility of misidentifying their locations within the V-Die-A rough-cut specimen. The coupons were polished and etched to reveal views of the microstructure as seen looking radially inward from the billet OD. The grain structures are illustrated in figure 3-72. Average grain sizes were deduced using the MCL and P(L) methods as before. The results of the old and new grain size measurements are compared in table 3-15 and

are quite similar. The quoted values are averages of the MCL and P(L) estimates using the combined XY data, and for the old results, averages over the three viewing directions at a given radial site are listed. One sees that for both V-Die-A metallographic studies, the average grain size tends to be slightly larger near the billet center than near the billet OD, in apparent conflict with the UT data.

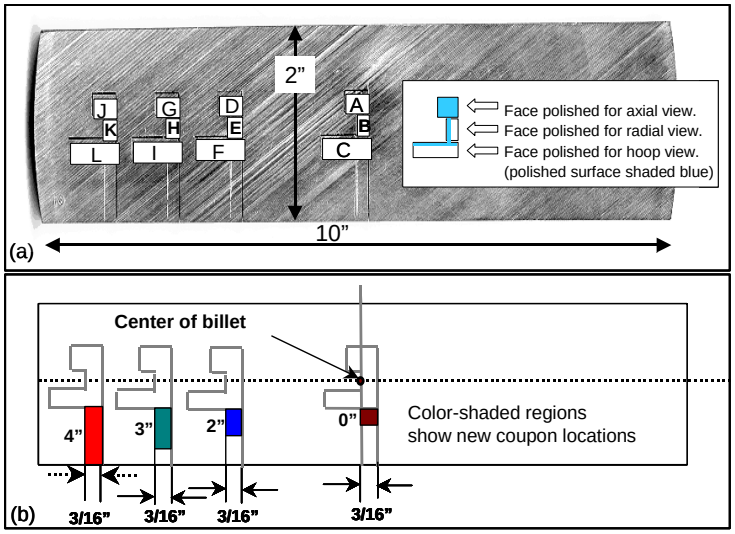

FIGURE 3-71. (a) LOCATIONS AND DESIGNATIONS OF THE 12 ORIGINAL METALLOGRAPHY COUPONS FROM EACH ROUGH-CUT SPECIMEN AND (b) LOCATIONS AND SHAPES OF THE FOUR NEW METALLOGRAPHY COUPONS FOR V-DIE-A

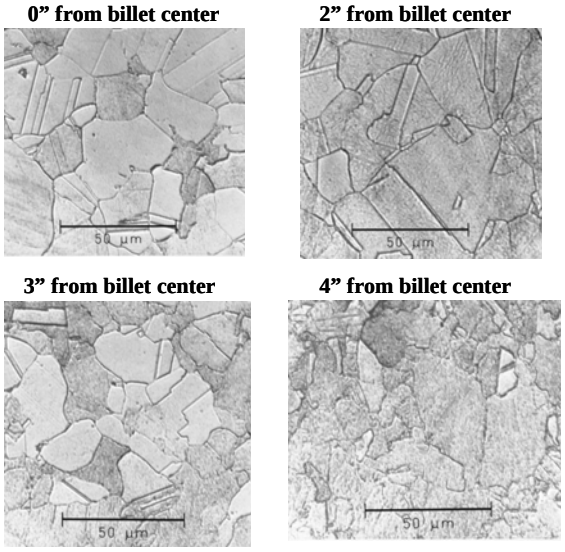

FIGURE 3-72. LOCAL MICROSTRUCTURES OF THE FOUR NEW METALLOGRAPHY COUPONS FROM THE V-DIE-A ROUGH-CUT SLAB
(Grain size estimates are deduced from similar photographs covering larger areas.)

TABLE 3-15. BEST ESTIMATES OF AVERAGE GRAIN DIAMETERS AT RADIAL SITES IN THE V-DIE-A METALLOGRAPHY SLAB

Site	Average Grain Diameter (microns)	
	V-Die-A 4 New Coupons	V-Die-A 12 New Coupons
0″	23.31	23.85
2″	25.35	22.01
3″	116.36	15.88
4″	15.18	20.00

Note: Site coordinate is the distance from the billet center.

From the original C-scans of the uncut billets and the measurements on the rectangular coupons, it was known that backscattered grain noise levels and other UT properties vary with position. The metallographic studies show that the billet microstructures vary with position as well and are presumably responsible for the UT property variations. One possible explanation for the V-Die-A anomaly would be that microstructural variations with position are sufficiently large in the vicinity of the V-Die-A strip coupon, or the microstructures of the UT property strip and the metallography slab are significantly different. To test this hypothesis, the remnants of the strip coupons and metallography slabs were scanned to create C-scan images of backscattered noise levels for comparison with the original strip coupon noise images shown in figures 3-19 through 3-22. This task was complicated by three factors: (1) the UT inspection system used in the original noise scans had been replaced with a new system from a different manufacturer, making direct absolute noise level comparisons impossible; (2) in the original scans, the depth zone from which grain noise was acquired extended beyond the 0.5″ thickness available in the metallography slab; and (3) the surfaces of the metallography slabs were not smooth, being rough EDM cuts for the IN718 specimens and rough saw cuts for the Waspaloy specimen. Nonetheless, it was hoped that the new scans would reveal how grain noise varied with position in the metallography slabs for comparison with the variations seen earlier in the UT property strips.

The same 15-MHz focused transducer employed earlier was used for the new scans, but the water path was adjusted to focus the beam about 0.3″ below the entry surface (side 2 of each specimen) and the depth gate for noise acquisition was narrowed to about 0.1″-0.5″. Useable grain noise images for the Waspaloy metallography slab could not be obtained because of strong scattering from the saw-cut ridges on the entry surface. However, useable grain noise images were obtained for the three IN718 cases, and these are shown in figures 3-73 through 3-75. Note that each figure contains three images. The rightmost two images are the new C-scans of the metallography slab and strip coupon remnants, respectively, with both scans carried out at the same gain. The holes in the metallography slab where coupons were removed are clearly visible. The leftmost image in each figure is the original backscattered grain noise C-scan image (see figures 3-19 through 3-22) of the 10″ long strip coupon with the amplitude-to-color mapping altered so that the lower half of the image resembles the new scan of the 4.5″ long strip coupon

remnant. For each of the three IN718 cases, the old and new images of the lower half of the strip coupon show similar variations of noise with position, as expected. For GFM-A and V-Die-B, the noise patterns in the original strip coupon and the metallography slab remnant are reasonably similar, with the noise tending to be largest near the billet center and decreasing as the OD is approached. For the V-Die-A case, however, there are some noticeable differences between the noise patterns in the property strip and the metallography slab, particularly near those areas where the small metallography coupons were removed. Of the four metallography sites (0″, 2″, 3″, and 4″), the noise level in the original V-Die-A property strip is clearly highest at 4″ from the billet center. For the corresponding metallography slab, however, the noise level at 0″ appears to be slightly higher than those at 2″, 3″, and 4″. One concludes that the microstructures of the strip coupon and metallography slab are likely more dissimilar for V-Die-A than for the other two IN718 cases.

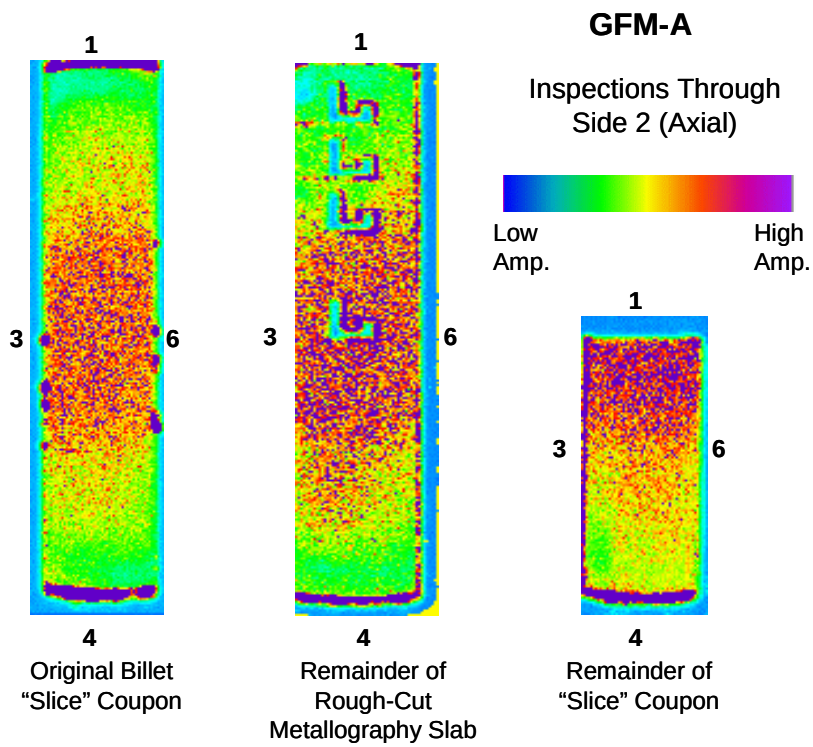

FIGURE 3-73. BACKSCATTERED GRAIN NOISE C-SCANS OF THE GFM-A STRIP COUPON AND METALLOGRAPHY SLAB

Thus, it appears that the variation of microstructure with position within the studied region of the V-Die-A billet was sufficiently large that grain sizes within the rough-cut metallography specimen were not indicative of those in the companion UT specimen at similar radial depths. Cutting new metallography coupons from the V-Die-A UT property specimens themselves were considered. However, this was not done because of (1) a desire to keep those specimens intact and (2) the fact that the GFM-A and V-Die-B metallography coupons provided sufficient data to quantify the relationship between grain size and UT properties in IN718 material.

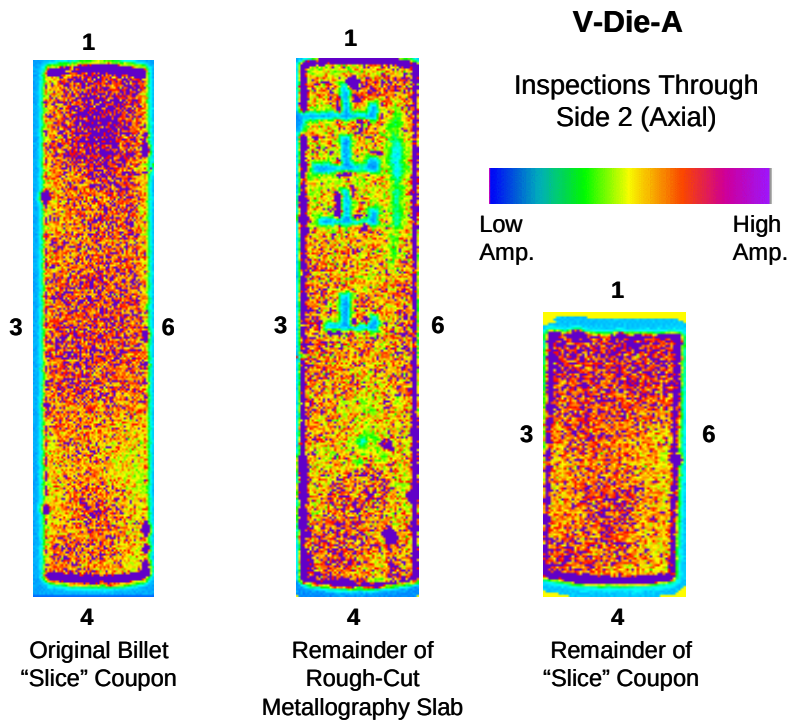

FIGURE 3-74. BACKSCATTERED GRAIN NOISE C-SCANS OF THE V-DIE-A STRIP COUPON AND METALLOGRAPHY SLAB

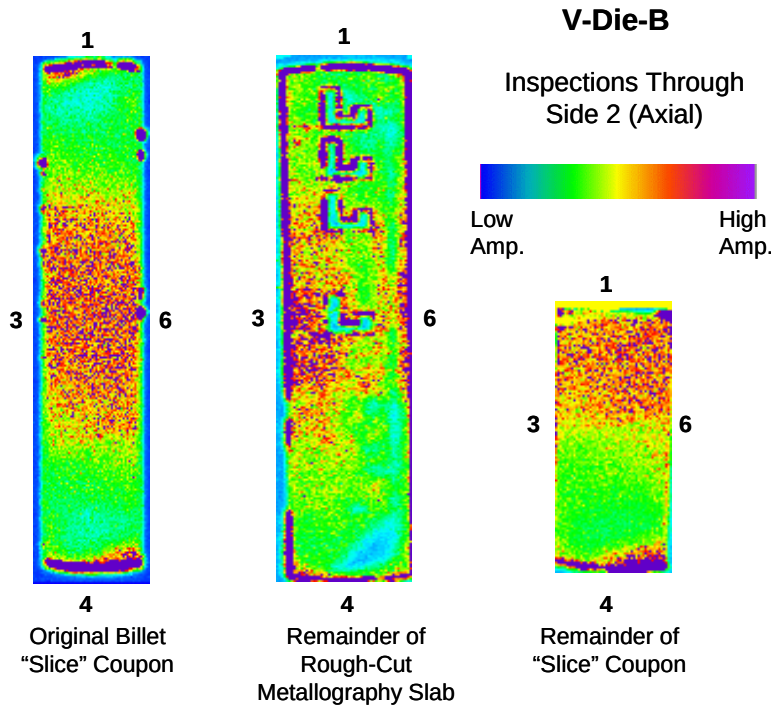

FIGURE 3-75. BACKSCATTERED GRAIN NOISE C-SCANS OF THE V-DIE-B STRIP COUPON AND METALLOGRAPHY SLAB

3.1.5.4 Correlations Between UT Properties and Average Grain Diameters.

Figure 3-76 displays the manner in which average grain diameter depends on radial position in each of the four strip coupons. The best estimates of the average grain diameters, as viewed from the radial, axial, and hoop directions, have been plotted versus radial depth from the billet center. For the V-Die-A strip, results are shown for both the original set of 12 metallography coupons and the auxiliary set of 4 newer coupons, with the latter results labeled radial-new in the figure.

Figure 3-76 can be compared with similar plots in figures 3-50 and 3-51, showing the dependence of UT attenuation and noise FOM on the radial coordinate of the measurement site. Comparing the three figures for a given strip specimen, one sees that increasing measured grain size is generally associated with increasing attenuation and increasing FOM. The lone exception is the V-Die-A strip. For that case, the attenuation and noise tend to be highest near the 3″ or 4″ sites, while the measured grain size is highest near the billet center. For the V-Die-A case, there is reason to believe that the microstructure of the metallography slab is somewhat different than that of the property measurement strip, and this likely accounts for the minor divergence between the trends of the UT properties and the measured grain diameters.

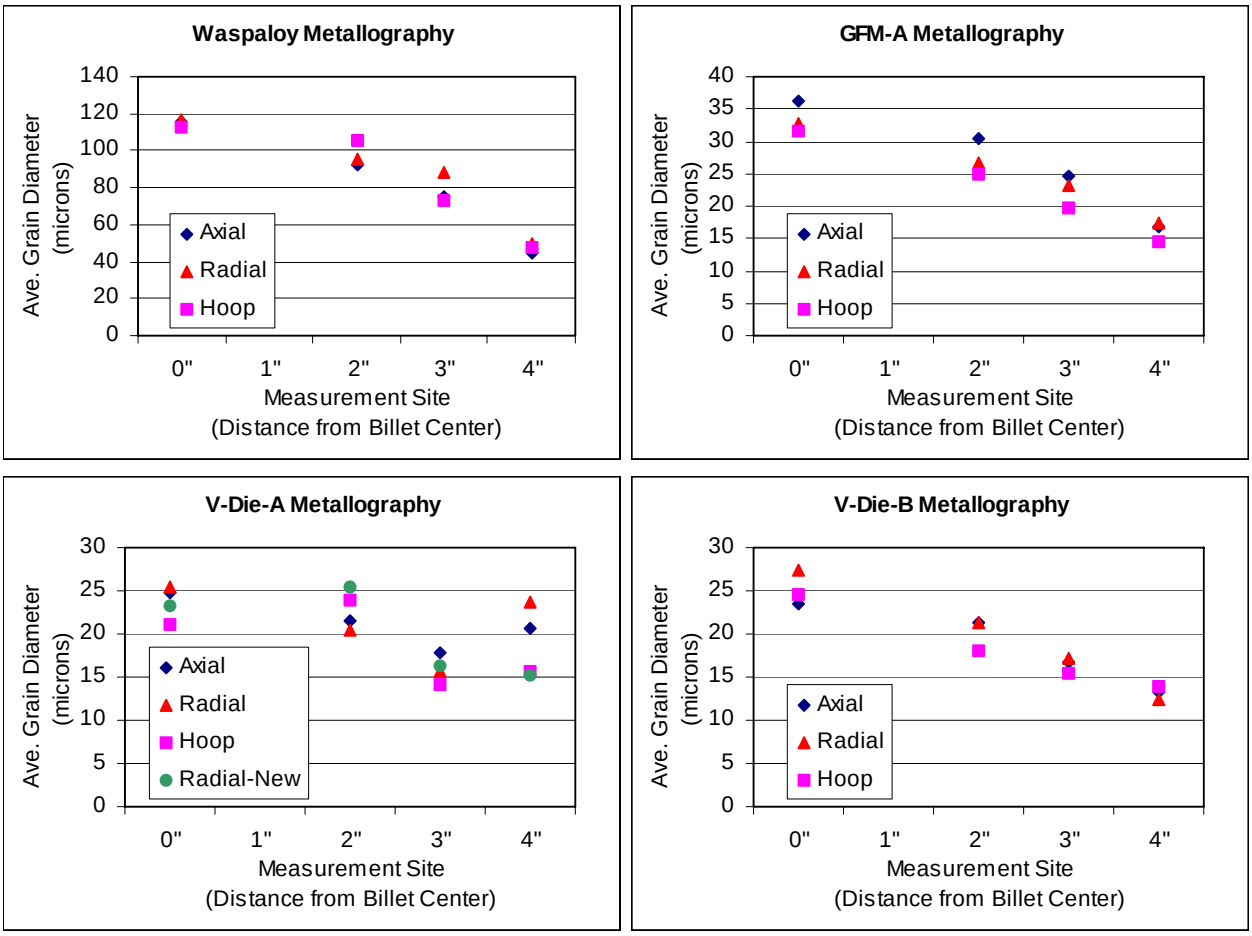

FIGURE 3-76. BEST ESTIMATES OF GRAIN DIAMETERS VERSUS RADIAL POSITION

Measured attenuation and FOM values are plotted versus the mean grain diameter in figures 3-77 and 3-78, respectively. The UT property values are specifically those at 7.5 MHz. One can make similar plots at other frequencies using tables 3-6 and 3-7 and tables 3-10 through 3-13. Each plotted point in figures 3-77 and 3-78 represents a UT measurement made at one site on one billet specimen for one particular inspection direction. Thus, in the upper left panel of each figure there are 12 points shown for each strip specimen: four inspection sites per specimen and three inspection directions per site. The UT result for a given sound propagation direction has been plotted against the grain diameter measured using metallography coupons whose viewing direction was parallel to that of the propagation direction. For example, at the billet center (0″ site) the attenuation or FOM value for radial propagation is plotted against the measured grain diameter for metallography coupon B. For the V-Die-A case, the grain diameters are those measured using the original suite of 12 metallography coupons. Because the correspondence between the grain diameters and UT properties is suspect for the V-Die-A strip, the V-Die-A results have been omitted from the lower two panels of figures 3-77 and 3-78. The lower panels show a much stronger correlation between grain diameter and UT properties than is seen in the upper panels, which include the V-Die-A results.

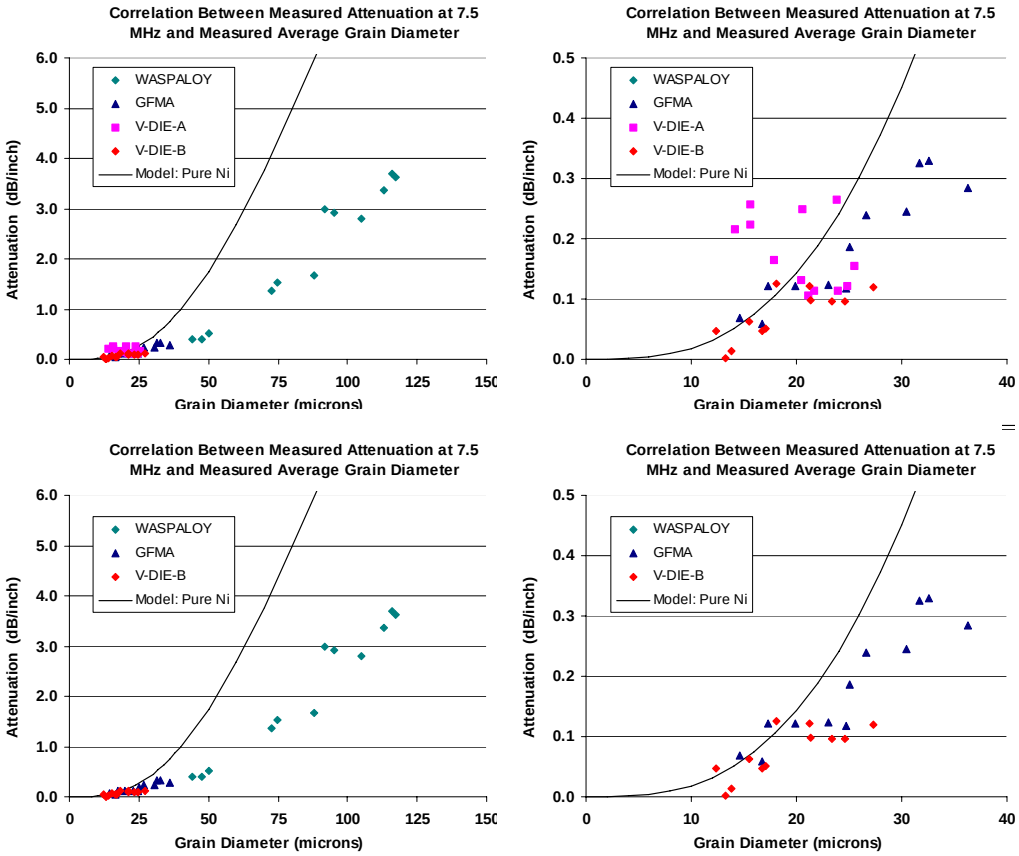

FIGURE 3-77. RELATIONSHIP BETWEEN AVERAGE GRAIN DIAMETER AND MEASURED ATTENUATION (AT 7.5 MHz) FOR EACH OF THE FOUR STRIP COUPONS (Each right-hand panel shows a blowup of the low-diameter region of the left-hand panel. V-Die-A data are included in the upper two panels and omitted from the lower two panels.)

For comparison, figures 3-77 and 3-78 also display predicted curves for equiaxed pure Ni microstructures with randomly oriented grains. As before, attenuation and FOM values, as functions of the mean grain diameter, were predicted using the formalisms of references 40-44, assuming an exponential P(L) curve in each case. For the range of diameters shown in figures 3-77 and 3-78, the predicted attenuation and FOM values at 7.5 MHz increase systematically with grain diameter. At larger grain diameters, predicted attenuation and FOM both decrease and eventually approach zero in the limit where the grain diameter exceeds the specimen thickness. The measured attenuation and FOM values of the Ni alloy specimens tend to increase with grain diameter in manners that are similar in form to those predicted by the models. However, the average rise rates for the measured data, which are slightly different for the IN718 and Waspaloy cases, are somewhat lower than those predicted for pure Ni. This may indicate that the single-crystal elastic constants of the two alloys are significantly different from those of pure Ni. Alternatively, it may be connected with the decision to exclude twin boundaries from the grain size analysis; this choice effectively increases the measured grain diameters and thus alters the rise rates of the attenuation-versus-grain size and FOM-versus-grain size curves.

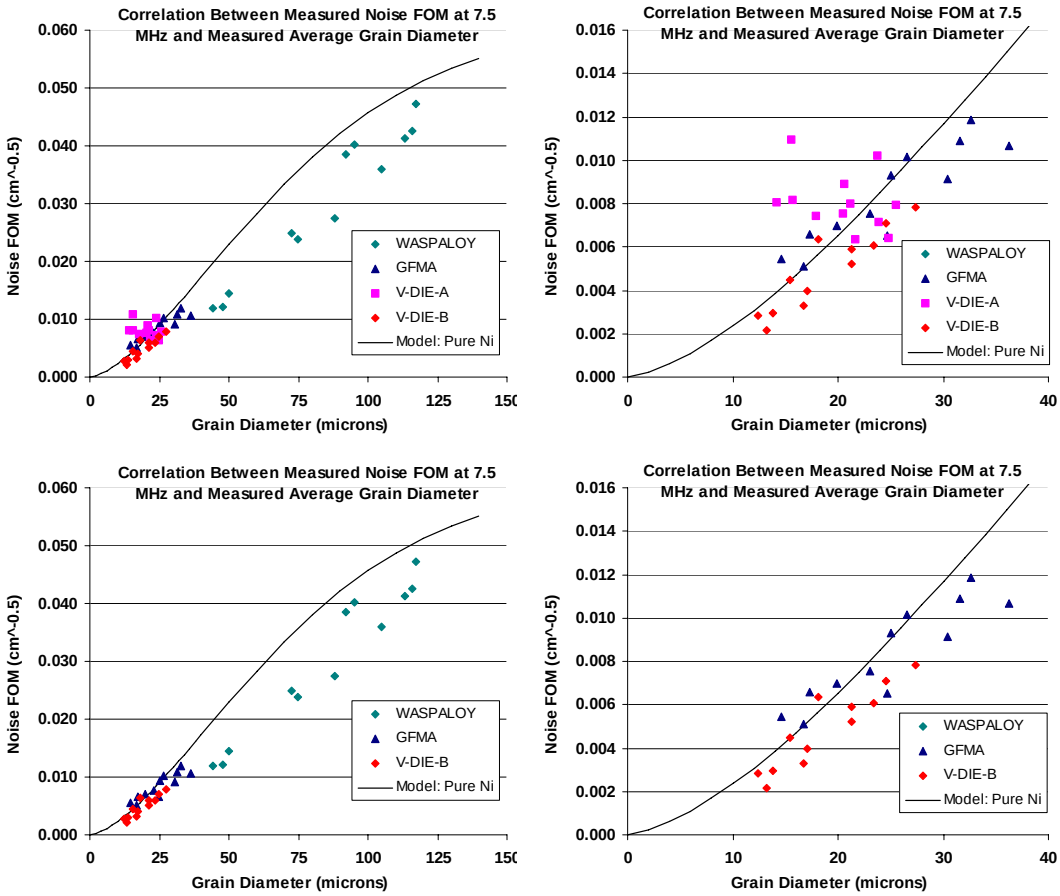

FIGURE 3-78. RELATIONSHIP BETWEEN AVERAGE GRAIN DIAMETER AND MEASURED NOISE FOM (AT 7.5 MHz) FOR EACH OF THE FOUR STRIP COUPONS
(Each right-hand panel shows a blowup of the low-diameter region of the left-hand panel. V-Die-A data are included in the upper two panels and omitted from the lower two panels.)

3.1.5.5 Estimating Single-Crystal Elastic Constants of Two Ni Alloys.

The single-crystal elastic constants of IN718 and Waspaloy are not presently known. The possibly of deducing them from the UT and metallography study was not envisioned in the original ETC Phase II proposal, but has emerged as a beneficial windfall.

If one assumes that the grain sizes have been properly measured from an attenuation and scattering point of view, then an approach can be crafted to estimate the single-crystal elastic constants for each alloy from the UT and metallography data in hand. The approach is illustrated in figure 3-79 using data from the IN718 GFM-A specimen measured at a site 2″ from the billet center. The starting points are model expressions that relate UT wave speeds [46] and attenuation [43] to details of the microstructure. It was assumed that IN718 and Waspaloy have single-phase cubic crystalline structures like that of pure Ni. The three independent elastic constants for a cubic-phase microstructure {C11, C12, C44} were varied until the predicted longitudinal and shear-wave velocities for polycrystalline specimens and the predicted attenuation near 7.5 MHz matched the measured results. Three averaging schemes for relating polycrystalline sound velocities to elastic constants were investigated (the so-called Voigt, Reuss, and Hill averages), and each gave rise to slightly different results. The upper portion of figure 3-79 lists the experimental velocity and attenuation values used in the by-hand fitting process, and the predicted quantities for a near-optimal set of elastic constants. There, the Hill averaging scheme was used for the predicted velocities. Model attenuation values were again obtained using the on-line attenuation calculator developed by Joe Turner [40], which requires the density, elastic constants, and average grain diameter as inputs. The lower portion of figure 3-79 compares the measured and predicted attenuation-versus-frequency curves for the fitted set of IN718 elastic constants, namely {C11, C12, C44} = {242, 140, 110 GPa}. For this set, the measured and predicted velocity and attenuation values are in reasonably good agreement with one another. Slightly better agreement can likely be achieved by fine-tuning the elastic constant values, and future study along those lines is planned.

The preliminary fitting study was completed using the UT property and metallography data for the Waspaloy, GFM-A, and V-Die-B specimens. The results are summarized in table 3-16. At each measurement site, UT property and grain size results for the three propagation directions have been averaged to estimate corresponding values for a perfectly isotropic specimen. The averaged grain diameters and attenuation values at each site, which are inputs to the fitting procedure, are listed in the table. Other inputs are the measured density, longitudinal-wave velocity, and shear-wave velocity, which can be found in tables 3-2, 3-4, and 3-5, respectively. The single-crystal elastic constants deduced by fitting to the measured data at each site are listed in the rightmost nine columns of table 3-16. Separate results are shown for each of the three model approaches (Voigt, Reuss, and Hill) that relate average sound velocities to the elastic constants and density of the specimen. At a given measurement site, the three approaches led to roughly similar sets of elastic constants, typically differing by several percent from one another. Site-to-site differences in the {C11, C12, C44} values for a fixed choice of the velocity averaging scheme (e.g., the Hill average) are on the same order, namely, from 0%-10% in most cases. In addition, table 3-16 shows that the average of the deduced elastic stiffness constants value oversites in GFM-A is reasonably similar to the average oversites in V-Die-A. This is

as expected since both specimens are of the same (nominal) IN718 alloy. For comparison, the single-crystal elastic constants of pure Ni are C11 = 250 GPa, C12 = 160 GPa, and C44 = 118.5 GPa.

Specimen:	GFMA
Measurement Site:	2" from billet center
Measured Ave. Grain Diameter (a):	27.35 microns
Measured Longitudinal Velocity (a):	0.5808 cm/usec
Predicted Longitudinal Velocity:	0.5811 cm/ usec (H Ave.)
Measured Shear-wave Velocity (b):	0.3087 cm/usec
Predicted Shear-Wave Velocity:	0.3087 cm/usec (Hi Ave.)
Measured Attenuation at 7.5 MHz (a):	0.0101 N/cm = 0.22 dB/inch
Predicted Attenuation at 7.5 MHz:	0.0105 N/cm = 0.23 dB/inch
Model Elastic Constants:	C11 = 242 GPa
	C12 = 140 Gpa
	C44 = 110 Gpa

Notes: (a) Averaged over radial, axial, hoop directions.
(b) Measured for radial propagation.

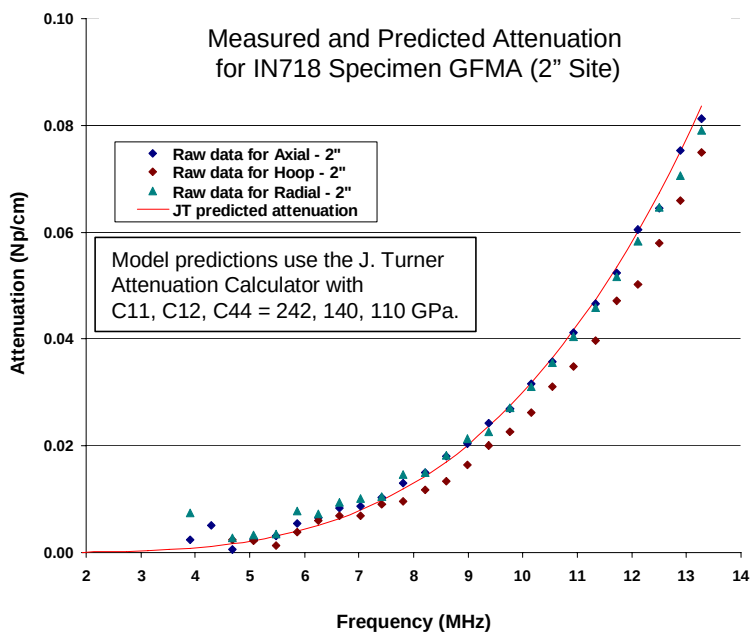

FIGURE 3-79. EXAMPLE OF DETERMINING IN718 SINGLE-CRYSTAL ELASTIC CONSTANTS BY FITTING TO MEASURED VELOCITY AND ATTENUATION DATA

The initial efforts to extract single-crystal elastic constants from the measured data appear promising. Further work is planned to develop software that will automate the fitting process, resulting in more optimal fits at each measurement site. The introduction of FOM data into the fitting process will also be explored. In addition, efforts will be undertaken to test the approach using polycrystalline specimens for which the single-crystal elastic constants are known. For example, equiaxed, untextured specimens of pure Ni could be procured and studied. Efforts along these lines are currently underway, and preliminary findings have been published [47]. Additional investigations are in progress, and it is expected that results will be published in the scientific literature at an appropriate time.

TABLE 3-16. PRELIMINARY VALUES OF DEDUCED SINGLE-CRYSTAL ELASTIC CONSTANTS FOR THE V-DIE-B, GFM-A, AND WASPALOY BILLET SPECIMENS

	V-Die-B		Deduced Elastic Constants								
	Average over radial, axial, hoop		Voigt Average			Reuss Average			Hill Average		
Site	Grain Dia. (microns)	Attenuation (dB/inch)	c12	c11	c44	c12	c11	c44	c12	c11	c44
0″	25.12	0.1038	137	248	94	135	252	102	136	250	99
2″	20.23	0.1151	140	242	97	138	246	113	138	246	104
3″	16.44	0.0534	139	244	96	137	248	109	137	248	102
4″	13.15	0.0210	130	262	87	130	262	90	131	260	90
		Average over sites:	136.5	249	93.5	135	252	103.5	135.5	251.0	98.8

	GFM-A		Deduced Elastic Constants								
	Average over radial, axial, hoop		Voigt Average			Reuss Average			Hill Average		
Site	Grain Dia. (microns)	Attenuation (dB/inch)	c12	c11	c44	c12	c11	c44	c12	c11	c44
0″	33.52	0.3132	139	244	96	137	248	109	138	246	104
2″	27.35	0.2229	142	238	99	139	244	117	140	242	110
3″	22.53	0.1213	140	242	97	138	246	113	139	244	107
4″	16.20	0.0827	145	232	102	141	240	130	142	238	118
		Average over sites:	141.5	239	98.5	138.75	244.5	117.25	139.8	242.5	109.8

	Waspaloy		Deduced Elastic Constants								
	Average over radial, axial, hoop		Voigt Average			Reuss Average			Hill Average		
Site	Grain. Dia. (microns)	Attenuation (dB/inch)	c12	C11	c44	c12	c11	c44	c12	c11	c44
0″	115.38	3.5626	143	264	101	141	268	109	142	266	106
2″	97.40	2.8959	144	262	102	141	268	109	142	266	106
3″	78.50	1.5187	143	264	101	141	268	109	142	266	106
4″	47.36	0.4407	143	264	101	141	268	109	142	266	106
		Average over sites:	143.25	263.5	101.25	141	268	109	142.0	266.0	106.0

Note: The measured average grain diameter and attenuation (at 7.5 MHz) used in the fitting process are listed in the second and third columns from the left. Deduced elastic constants are in GPa units.

3.2 SUMMARY.

As part of the ongoing effort to quantify and improve inspection practices, the ETC has investigated the UT properties of Ni alloy, cylindrical billets used in the fabrication of rotating jet engine components. A primary goal of the study was to determine, for representative 10″ diameter billets, the manner in which longitudinal velocity, attenuation, and backscattered grain noise capacity depend on position and inspection direction. UT attenuation and backscattered noise capacity are frequency-dependent. Currently, most Ni alloy billet inspections are performed using 5-MHz transducers, but it may be desirable in the future to improve sensitivity by increasing the inspection frequency. In the Ni survey study, it was endeavored to measure attenuation and noise capacity within the frequency range of greatest present and future interest, namely, from about 5 to 12.5 MHz.

UT property measurements are most easily carried out on rectangular specimens, which were used in this study. To construct a coherent picture of how properties vary with position and sound propagation direction, a two-stage, coupon-cutting scheme was adopted. Rectangular strip coupons with approximate dimensions of 2″ x 2″ x 10″ were cut along billet diameters and used for UT measurements in the axial and hoop directions. The strip coupons were later cut into 1″ thick slices for UT measurements in the radial direction. It was decided by consensus that two Ni alloys would be studied: IN718 and Waspaloy. Two different forging methods known as GFM and V-Die are commonly used to transform IN718 cast ingot into finished billet, and it was desired that both be studied. Budgetary considerations allowed for the study of a total of four strip coupons and their associated slices.

The UT properties of Ni alloy billets are dependent in part on the casting and forging history. A lack of cylindrical symmetry during forging leads to noncylindrically symmetric UT properties, as evidenced by the noise-banding patterns that are seen in routine multizone inspections of billets. From earlier studies, it was known that changes in velocity and attenuation values are generally well correlated with changes in backscattered noise levels. Thus, backscattered noise patterns could be used to identify coupon sites with different UT properties. Noise-banding patterns seen in multizone inspections of 10″ diameter candidate billets were used to select the sites where strip coupons were cut. The final choices and their designations were:

- V-Die-A: Strip coupon from a high-noise band in an IN718 V-Die billet.
- V-Die-B: Strip coupon from a low-noise band in the above V-Die billet.
- GFM-A: Strip coupon from a high-noise band in an IN718 GFM billet.
- Waspaloy: Strip coupon from high-noise band in a Waspaloy billet.

The strip coupons were cut from the billets using EDM methods, and the sound entry surfaces for the UT measurements were ground smooth. The density of each strip was determined in the standard manner by dividing the measured mass by the computed volume, resulting in 8.26 gm/cc for each of the IN718 strips and 8.21 gm/cm for the Waspaloy strip.

Before detailed UT property measurements were performed, each strip coupon was scanned at normal incidence through the four large (2″ x 10″) surfaces using planar and focused transducers. The object was to produce C-scan images of back-wall echo TOF, back-wall echo amplitude, and backscattered grain noise amplitude. TOF images indicated that the sonic velocity was nearly constant within a given strip coupon. However, back-wall amplitude and backscattered noise images showed significant variations with position, principally with radial depth in the billet. Sites with low back-wall amplitude (i.e., high attenuation) tended to have high backscattered noise levels. Moreover, at a given radial position in a given strip coupon, the back-wall attenuation or grain noise level was nearly identical for axial and hoop sound propagation. Thus, the results of the preliminary scans were consistent with the hypothesis that the billet microstructures had approximately equiaxed, randomly oriented grains whose mean diameter varied systematically with position. It was also noted that the V-Die-A and V-Die-B strip coupons, which were cut from high- and low-noise bands of the same IN718 billet, differed significantly in their attenuation and grain noise levels near the coupon ends (OD regions) but had very similar values near their centers. Such a coalescing of UT property values at the billet

center were shown in an earlier study using coupons cut from high- and low-noise bands of Ti-6-4 billets. It indicates that the asymmetries in the mechanical working of a billet, which led to noise banding and other property variations in the hoop direction, have a diminished effect near the billet center.

The preliminary back-wall and backscattered noise C-scans revealed that the UT properties of the strip coupons were primarily dependent on radial depth and were approximately symmetric about the billet center. It was, thus, decided that detailed property measurements for each strip coupon would be made at sites along a single billet radius, rather than along a full diameter. Five sites were selected, which were located 0″, 1″, 2″, 3″, and 4″ from the billet center. At each site velocity, attenuation and grain noise capacity were carefully measured in each of the three principal directions. For sonic beam propagation in the axial and hoop directions, UT measurements were made on the intact strip coupons. For measurements in the radial direction, the strip coupons were cut into approximately 1″ thick slices centered at the five sites.

Except for a limited number of shear-wave velocity measurements, all UT property measurements were made in pulse/echo mode with the specimens immersed in distilled water.

Detailed velocity measurements were made using 0.25″ diameter planar transducers at normal incidence. The velocity at each measurement site was determined from the average time delay between successive back-wall echoes. Early measurements for selected cases using both 5- and 10-MHz planar transducers found very little difference between the two measured velocities, i.e., typically less than one-tenth of 1 percent. Consequently, the dependence of velocity on frequency was deemed to have little impact on practical inspections, and subsequent velocity measurements were made using only the 10-MHz transducer.

Two competing immersion methods for detailed attenuation measurements were explored. One was based on comparing the first back-wall echo in the metal specimen to that in an FQ reference block of similar thickness, and a second was based on comparing the first three metal back-wall echoes with one another. Each method yielded an attenuation-versus-frequency curve within the bandwidth of the 10-MHz, 0.25″ diameter broadband planar transducer that was used. It was found that good agreement between the two methods could be obtained if (1) the spectra of the back-wall echoes being used to determine the valid frequency range for the measurement were examined; (2) the results where the sonic beam interacted appreciably with the lateral edges of the coupon were discounted; and (3) the same equipment gain setting was used when acquiring all echoes that contributed to the measured attenuation at a given site. After these preliminary measurements were completed, the second method was selected as the primary measurement modality since it was believed to be more accurate for low-attenuation cases.

The goal of the detailed backscattered noise measurements was to determine the frequency-dependent FOM parameter that quantifies the noise-generating capacity of the microstructure. The FOM value depends solely on the microstructure of the metal and, ideally, is independent of the means used to measure it. At each measurement site, a well-characterized 15-MHz, F7, focused transducer was scanned above the metal specimen and several hundred noise A-scans were acquired and stored. A back-wall echo from an FQ block served as a reference echo, which

was analyzed to deduce a measurement system efficiency factor. The FOM-versus-frequency curve was then extracted from the stored noise data using the independent scatterer noise model, which relates the average noise spectrum to the FOM and various measurement system parameters. The results are considered to be trustworthy in the frequency range where the attenuation is accurately known and the average backscattered noise spectrum is appreciable.

The backscattered noise study afforded an opportunity to test some predictions of the independent scatterer noise model. In preliminary studies, the model was used to predict the depth dependence of the rms noise level from measured FOM-versus-frequency curves. The rms noise-versus-depth curves measured with focused probes typically display a pronounced maximum near the focal depth. The model was found to do a good job of predicting the overall shape and location of the focal maximum. However, the measured noise levels tended to be above the predicted result for times that were either well before or well beyond the focal maximum. One possible explanation, to be explored in future work, is that the departures from model predictions are due to multiple scattering events and the manner in which they contribute to the observed noise in and away from the focal zone. The determination of the grain noise FOM from measured noise data requires analysis of backscattered noise RF waveforms within some designated time gate. Various gate choices were explored, but for the quoted results, a time gate that bracketed the focal zone was used. This choice was made because the noise model is believed to be most reliable in that region and because the grain noise level is highest there, thus reducing the impact of residual electronic noise. The deduced FOM value also depends on the assumed rate at which energy is lost by the sonic beam during propagation. The sensitivity of deduced FOM values to uncertainty in the energy loss attenuation was also explored. For the quoted results, it was assumed the energy loss attenuation to be equivalent to the attenuation measured in the back-wall echo study. In general, the attenuation of surface echoes has contributions due to both energy loss and beam distortion. However, for fine-grained metals like the specimens in this study, the attenuation of surface echoes is believed to be dominated by the energy loss effect.

For each of the three properties of interest, 60 measurement trials were conducted, corresponding to four billet strip specimens, five measurement sites per strip, and three inspection directions per site.

For the set of 60 measurements, longitudinal velocities were found to range over 0.5805 ±0.0009 cm/μsec (or ±0.15%) for the IN718 specimens and over 0.6008 ±0.0006 cm/μsec (or ±0.10%) for the Waspaloy specimens. No obvious trends were observed in the manner in which velocity varied with position. The minor velocity variations within each of the four billet strips may simply reflect the inherent errors in the measurement process. In practice, the small velocity variations seen in these Ni alloy billets, in and of themselves, are expected to have no significant impact on inspectability. The sonic velocity influences the radiation pattern within the billet that is produced by the insonifying transducer. Sizeable velocity inhomogeneities can shift the focal depth and alter the degree of focus at the focal zone. For the specimens studied, the velocity variations are very small and are unlikely to cause any noticeable changes in the radiation pattern.

In contrast to the velocity behavior, attenuation and FOM values varied significantly with both frequency and position. In particular, it was found that

- the attenuation and FOM values varied significantly with radial position in each of the billet strips studied, being largest near the billet center (0″) for Waspaloy, GFM-A, and V-Die-B, and largest near the OD for V-Die-A.

- on average, at a given measurement site in a given strip, there was little difference between the UT properties for the axial, radial, and hoop directions.

- averaged over radial position, the attenuation or FOM value increased for the sequence: V-Die-B, V-Die-A, GFM-A, and Waspaloy.

- attenuation and FOM values tended to be well correlated: sites with higher (lower) attenuation also had higher (lower) FOM.

The attenuation and FOM values varied widely over the suite of specimens, with values for both properties being much larger for Waspaloy than for IN718. Averaged over all the coupons and all inspection directions, the Waspaloy attenuation at 5 MHz (0.56 dB/inch) was 15 times larger than the IN718 attenuation (0.036 dB/inch). At 7.5 MHz, the average Waspaloy attenuation was 16 times larger (2.41 dB/inch versus 0.15 dB/inch). The average FOM values for Waspaloy at 5 and 7.5 MHz were larger than the corresponding averages for IN718 by factors of 3 and 4, respectively. Within a given billet strip coupon, attenuation values at these frequencies varied by as much as an order of magnitude with position, and FOM values varied by as much as a factor of 3.

Models for simulating inspections often assume that the attenuation can be approximated as a power law in frequency:

$$\textit{Attenuation in N/cm units} = C\ (\textit{frequency in MHz})^{p}$$

For this reason, each measured attenuation-versus-frequency curve was fit to such a power law. For the Ni billet specimens in the frequency range of interest, power-law fits in virtually all cases yielded powers in the $3 < p < 4$ range. For some sites in the Waspaloy strip specimen, the attenuation values were too large to permit accurate measurement above about 8 MHz for the transducer and sample thicknesses used. However, the summary tables and graphs in this study are complete for 5 MHz (the center frequency for existing Ni billet inspections) and for 7.5 MHz (the likely center frequency for a next-generation inspection with improved sensitivity).

For each of the Ni alloy billet specimens studied, the variations of properties with position were such that the attenuation and noise FOM tended to increase or decrease together as the measurement site was changed. This behavior is expected for specimens with equiaxed grains—as the mean grain size increases, the attenuation and noise FOM both increase. However, this trend is not always seen in jet engine materials. For example, for the Ti alloy billet specimens studied under ETC Phase I, the direction of maximum back-wall attenuation was usually the direction of minimum grain noise, leading to an inverse relationship between attenuation and noise amplitudes. These two different trends were attributed to the role of recrystallization

during the billet formation process. In Ni alloys, there is a significant amount of recrystallization that occurs due to mechanical working of the billet during its formation. This evidently led to nearly equiaxed grains in the Ni billet specimens under study. In contrast, very little or no recrystallization occurs during the working of Ti alloy billets. Hence, the large-scale macrograins present in the Ti ingot become elongated in the axial direction, and these elongated macrograins cause sonic beam distortions that led to an inverse relationship between noise FOM and attenuation.

The systematic variation of attenuation and FOM with position will make some locations within billets more difficult to inspect than others. For a given defect, SNR will vary with defect position, generally being smaller at locations having larger FOM values. The UT properties reported in this study can be used as inputs to model calculations that simulate billet inspections and estimate SNR values.

A second goal of the study was to correlate the measured UT properties with the local billet microstructures. To this end, small metallography coupons were cut from a 1/2″ thick slab that was adjacent in the billet to the strip coupon used for UT property measurements. For each of the four strip coupons studied, there were 12 metallography coupons: three each from sites located 0″, 2″, 3″, and 4″ from the billet center. The collection of 12 coupons provided axial, radial, and hoop views of the microstructure at each of the four inspection sites.

Grain size information was deduced from micrographs of the polished and etched metallography coupons. Tracings of the grain boundaries were made from apparent twin boundaries that were identified and excluded since it is believed that such boundaries do not play a major role in determining UT attenuation and backscattered noise levels. The grain boundary tracings were then digitized and analyzed. Two different approaches, known as the MCL and P(L) methods, were used to deduce average grain diameters from a given image. Each method found the grains to be relatively equiaxed at a given site, i.e., there was no general tendency for the grains to be elongated in the radial, axial, or hoop directions. Overall, the average diameter estimates provided by the two methods were very similar, with the P(L) estimate tending to be about 5% below the MCL method. The results of the two methods were averaged to obtain best estimates of the grain diameters at the various measurement sites. Average grain diameters ranged from about 13-34 microns in the IN718 specimens and from about 47 to 115 microns in the Waspaloy specimens.

For each billet strip studied, the measured average grain diameter tended to vary systematically with radial position. For the most part, the measured grain diameters were well correlated with the UT properties; for a given strip coupon, sites with larger grain diameters tended to have higher attenuations and higher FOM values. The notable exception was the V-Die-A strip. Follow-up studies revealed that backscattered noise levels at corresponding points in the V-Die-A strip coupon and the adjacent metallography slab were dissimilar, suggesting different mean grain sizes. The fact that grain diameters measured in the V-Die-A metallography slab were not representative of those in the property strip is likely responsible for the lack of correlation between the UT properties and grain diameters for that specimen. Setting aside the V-Die-A results, the remaining data served to quantify the relationship between grain diameter on the one hand and UT attenuation and backscattered noise FOM on the other. For both IN718 and

Waspaloy, the tables and graphs in this study allowed one to deduce attenuation and FOM values from knowledge of the mean grain diameter and vice versa. The significant grain diameter variations, with radial depth in the billet strips, were documented. There are also significant microstructural variations in the hoop and axial directions, as indicated by the noise-banding patterns.

In the future, it may be possible to estimate the average grain diameter at a given site in a billet under inspection from systematic measurements of backscattered grain noise. One would have to measure the backscattered noise level as a function of depth between the billet OD and the interior site in question by varying the focal depth of the interrogating sound beam. For analysis purposes, the depth region would be partitioned into thin layers and the grain size within each layer would be estimated in a bootstrapped fashion. Beginning with the layer closest to the OD, one would estimate the local average grain diameter by locating that value for which measured noise characteristics best matched the model predictions. The grain diameter in the first layer would determine attenuation losses that impact the analysis of noise from the second and deeper layers. One could systematically proceed layer by layer, estimating the mean grain size in each layer that best accounted for the observed noise, taking into consideration the accumulating effects of attenuation as one proceeded deeper into the billet. Tables 3-6, 3-7, and 3-10 through 3-14, which relate attenuation and noise FOM to grain size, would be instrumental in such a process.

It was noted that the measured attenuation and FOM values of the Ni alloy specimens tend to increase with grain diameter in manners that are very similar in form to those predicted by the models for pure Ni microstructures containing randomly oriented, equiaxed grains. However, the average rise rates for the measured data, which are slightly different for the IN718 and Waspaloy cases, are lower than those predicted for pure Ni. This indicated that the single-crystal elastic constants of the two alloys are somewhat different from those of pure Ni.

The single-crystal elastic constants of IN718 and Waspaloy are not presently known, but an approach for deducing them from the UT and metallography work is being explored. This may prove to be an added benefit of the ETC-sponsored research that was not envisioned in the original proposal. The approach is based on varying the three independent elastic constants for a cubic-phase microstructure {C11, C12, and C44} until model-predicted velocities and attenuation best match the experimental values. The initial efforts to extract single-crystal elastic constants from the measured IN718 and Waspaloy data appear promising, and further work is planned to refine and test the approach.

4. SYNTHETIC INCLUSION SAMPLES.

4.1 INTRODUCTION.

Ni alloys such as IN718, Waspaloy, IN901, IN100, and René 95 are used extensively in high-temperature jet engine applications. The basic UT properties of unflawed Ni alloy billets were the subject of the previous section. Equally important are the sonic properties of defects in these materials, since detectability is determined in part by the difference in UT impedance (sound velocity times density) between the defect and the host metal. Multiple defect types exist in forged billets, including dirty white spots, clean white spots, segregation, and slag. In powder metal alloys, ceramic particles, porosity, and powder-lot anomalies are seen. Typically, dirty white spots contain a microstructure of Nb-lean alloy with fine oxides and nitrides. Typical segregation defects consist of Nb-rich regions in billets that produce undesirable, brittle phases. Slag defects are Ca-rich ceramic phases originating from the ESR melting step and typically result from poor ingot surface preparation.

This section describes the selection and manufacture of synthetic defect seeds and their embedding in IN718 material. Micrographs of the seeds themselves and of destructive analysis of some of the blocks are included. UT data in the form of velocity measurements and C-scan images were used to develop conclusions regarding defect detection in production inspections.

4.2 SYNTHETIC DEFECTS.

Three types of synthetic defects were made for this study: dirty white spot, clean white spot, and freckle. White spots are Nb- and Ti-lean regions in IN718. There are two basic types: dirty white spots and clean white spots. So-called dirty white spots are generally contaminated drop-in of the crown or torus above the melt during vacuum arc remelting. Clean white spots fall into one of several categories: discrete white spots occur by drop-in from crown or torus, dendritic white spots occur by drop-in from shrinkage, and solidification white spots are thought to occur as a result of an instability in solidification conditions during the final VAR process. Freckles are generally considered to be macrosegregation as a result of instabilities in the convective flow of Nb-rich liquid during solidification. The freckle regions typically possess higher volume fractions of the Laves phase and/or δ-Ni_3Nb.

The synthetic defect seeds were chosen to lie within the composition range of defects found in production. Jackman, et al. [48] described the white spot compositions; Wlodek and Field [49] described the freckle compositions and phase analyses. The chemical composition of the seeds and the IN718 parent material are presented in table 4-1.

TABLE 4-1. COMPOSITIONS, IN WEIGHT PERCENT, OF SYNTHETIC DEFECTS

Defect	Ni	Fe	Cr	Nb	Ti	Al	Mo	C	O	B	N
White Spot	55.9	19.2	17.7	3.0	0.6	0.4	3.2	0.008	0	0.004	0
Freckle	49.4	14.5	17.1	13.2	1.7	0.7	3.4	0.14	0	0.004	0
Dirty White Spot	55.8	18.7	16.7	2.9	2.2	0.6	3.1	0.008	0.2	0.004	0.2
IN718	52.8	18.5	19.0	5.1	1.1	0.5	3.0				

Note: Synthetic defects fabricated for this work are shown along with the IN718 base material.

The white spot and freckle compositions were prepared by vacuum induction and casting into a rectangular slab mold. The dirty white spot composition was prepared by VAR, where TiO_2 and TiN were used to achieve the prescribed oxygen and nitrogen contents.

After casting, the defect slabs were HIPped at 1100°C, 210 MPa for 3 hours to close any solidification shrinkage. Then the defect slabs were cut in half, and one-half of each defect slab was press forged 50% at 982°C. This forging step was to create within the synthetic defects the microstructure that would be present in a production defect after billetizing or forging and to assure that the synthetic defect would have directional features consistent with the forgings into which they would be placed.

Small samples with smooth surfaces were machined for speed of sound and density measurements from cast plus HIPped defect material and also from cast, HIP, and forged material. Optical microscopy and electron backscatter diffraction analysis have been performed to determine the constituent phases of the synthetic inclusions of the selected compositions.

Figures 4-1 and 4-2 display microstructures of the synthetic white spot composition. Figure 4-1 displays the as-cast plus HIP microstructure, which contains large grains, some larger than the field of view, with linear arrays of particles that may represent regions of interdendritic microsegregation. Figure 4-2 displays the microstructure of the white spot composition after forging at 982°C. The grain boundaries are jagged, suggesting some warm-work that has not been fully recovered, with some vertical slip lines present in the field of view.

Figures 4-3 and 4-4 display the microstructure of the synthetic freckle composition. Figure 4-3 displays the as-cast plus HIP microstructure, which contains primary Ni dendrites and an interdendritic eutectic of fine-scale Ni and Cr_2Nb-type C14 Laves phase, identified by electron backscatter diffraction. Figure 4-4 displays the microstructure of the freckle composition after forging at 982°C; the microstructural features are compacted relative to those of figure 4-3.

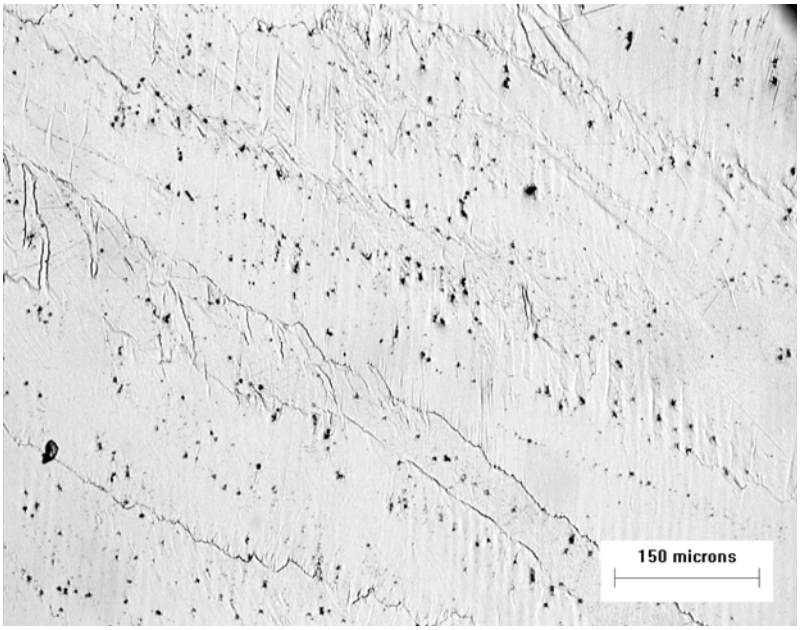

FIGURE 4-1. MICROSTRUCTURE OF WHITE SPOT CASTING

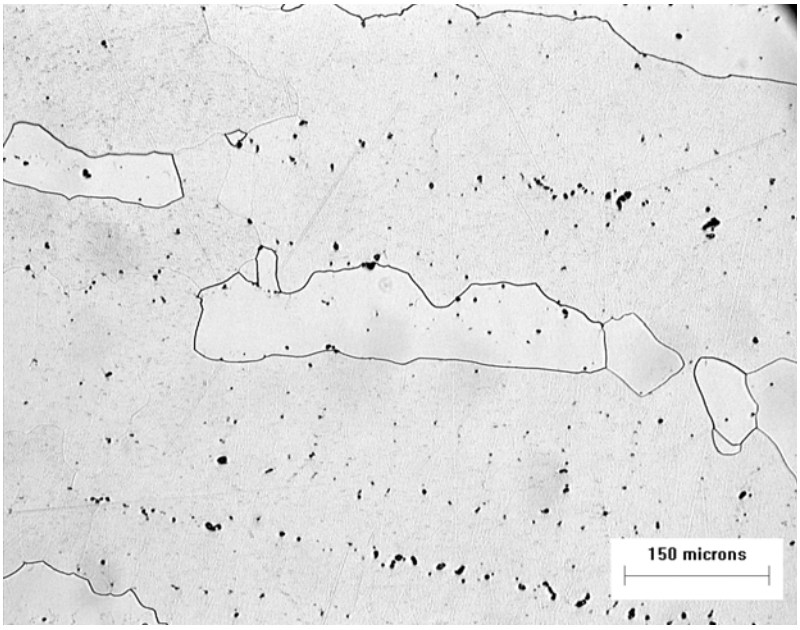

FIGURE 4-2. MICROSTRUCTURE OF WHITE SPOT FORGING

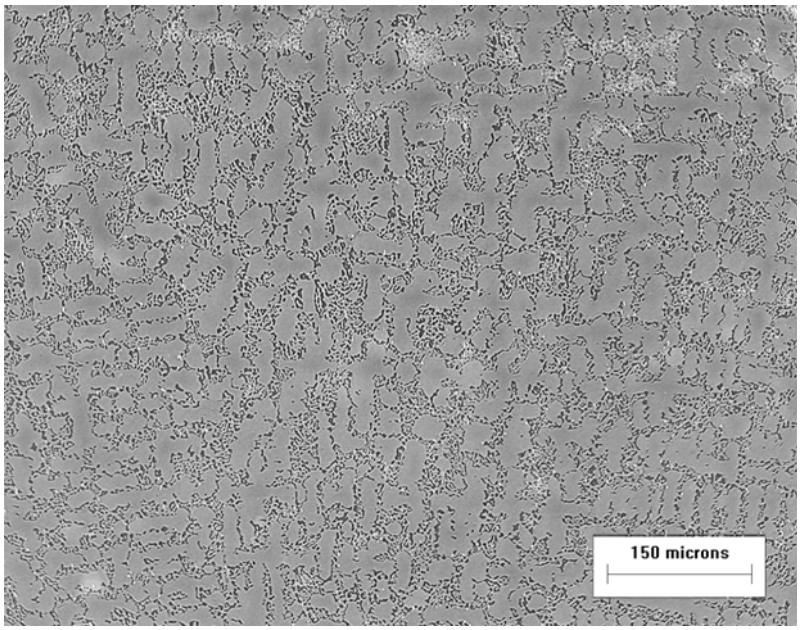

FIGURE 4-3. MICROSTRUCTURE OF FRECKLE INGOT
(The microstructure contains primary gamma-Ni dendrites and a gamma-Laves eutectic.)

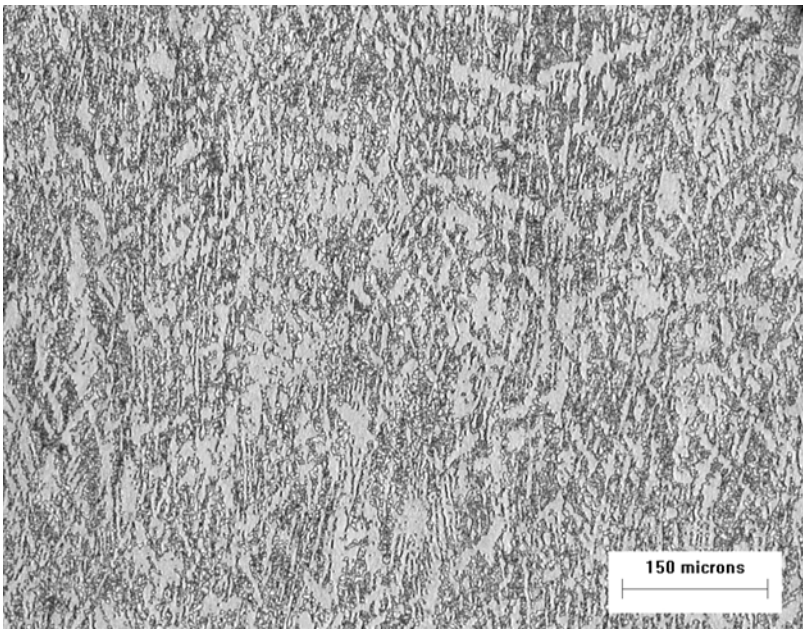

FIGURE 4-4. MICROSTRUCTURE OF FRECKLE FORGING, EXHIBITING REFINEMENT DUE TO FORGING

Figures 4-5 and 4-6 display the microstructure of the synthetic dirty white spot composition. Figure 4-5 displays the as-cast plus HIP microstructure, which contains large grains, larger than the field of view, with clumps of smaller particles that arose from the intentional TiO_2 and TiN additions.

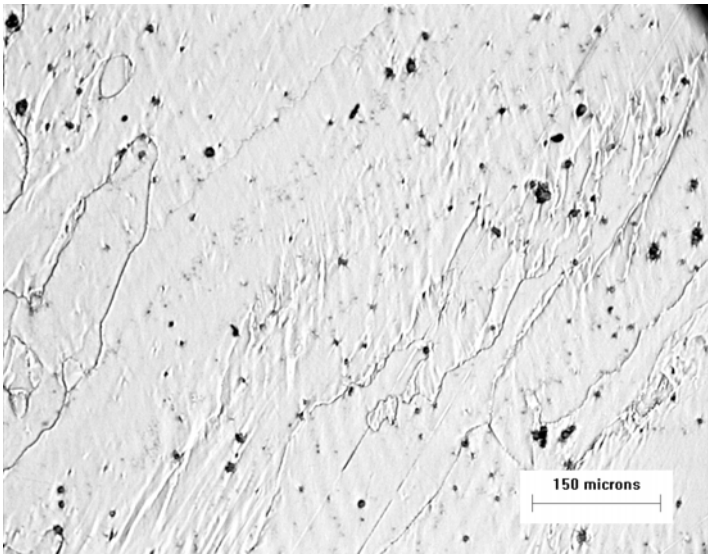

FIGURE 4-5. MICROSTRUCTURE OF DIRTY WHITE SPOT BUTTON

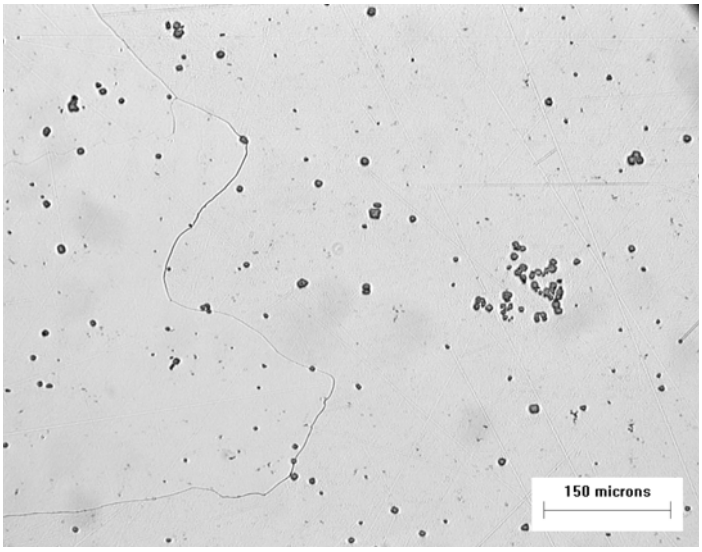

FIGURE 4-6. MICROSTRUCTURE OF DIRTY WHITE SPOT FORGING

Figure 4-6 displays the microstructure of the dirty white spot composition after forging at 982°C. The grain boundaries are seen to be jagged, similar to those in the forged white spot of figure 4-2. In addition, (vertical) slip lines are present in the field of view and clumps of dark particles are present.

For each of the three defect compositions, rectangular coupons were fabricated from the HIPped and forged material. These were used for round-robin measurements of density and velocity carried out at GE (Schenectady, NY), P&W (West Palm Beach, FL), and ISU (Ames, IA). The velocity results are listed in table 4-2. Measurements made at different installations were generally found to be in good agreement. Shear-wave measurements, made using contact transducers, were generally difficult due to the inhomogeneity of the specimens and their relatively small size. For a given propagation direction, the shear-wave speed often depended significantly on the polarization direction of the wave. For the measurements performed at ISU and P&W, the polarization direction was varied to locate the slowest and fastest shear-wave speeds, which were tabulated. In some cases (for example, in the side 3 direction of dirty white spot specimen), reliable shear-wave speed measurements were not feasible due to the specimen and probe dimensions. The reflectivity of a defect in a host billet is expected to depend upon the impedance mismatch between the defect and host metal, with UT impedance defined as the product of sound velocity and density. Thus, in addition to sound velocity, density was also measured for each of the three rectangular synthetic defect specimens. Measured densities were 8.267, 8.246, and 8.227 gm/cc for white spot, freckle, and dirty white spot specimens, respectively.

TABLE 4-2. RESULTS OF UT VELOCITY MEASUREMENTS ON RECTANGULAR COUPONS OF SYNTHETIC Ni BILLET DEFECT MATERIAL

Specimen	Side	Thickness (mm)	ISU		GE		P&W	
			L-wave Velocity (mm/μsec)	S-wave Velocity (mm/μsec)	L-wave Velocity (mm/μsec)	S-wave Velocity (mm/μsec)	L-wave Velocity (mm/μsec)	S-wave Velocity (mm/μsec)
White Spot	1	10.684	5.60	3.07-3.31	5.65	3.27	5.61	3.14-3.30
	2	12.410	5.66	2.98-3.35	5.75		5.68	3.07-3.32
	3	12.514	5.74	2.94-3.41	5.78		5.75	3.12-3.35
Freckle	1	10.558	5.78	3.12-3.16	5.79	3.18	5.79	3.08-3.18
	2	12.555	5.84	3.06-3.13	5.85		5.84	3.05-3.16
	3	12.419	5.84	3.05-3.15	5.86		5.85	3.06-3.14
Dirty White Spot	1	4.312	5.88	3.12-3.17	6.03	2.99	5.91	
	2	7.268	5.90		5.97		5.92	
	3	7.323	5.94		6.07		5.95	

4.3 FLAT-BOTTOM HOLE BLOCK.

A #1 FBH block was designed and machined from the sample billet that was selected for manufacturing the synthetic defect seed blocks. The geometry of this block is shown in figure 4-7. Five #1 FBHs were drilled 1/2″ deep in alloy 718 to provide a reference standard for

the UT measurement of noise levels in the IN718 billet material and the measurement of defect signal amplitudes in the seeded blocks.

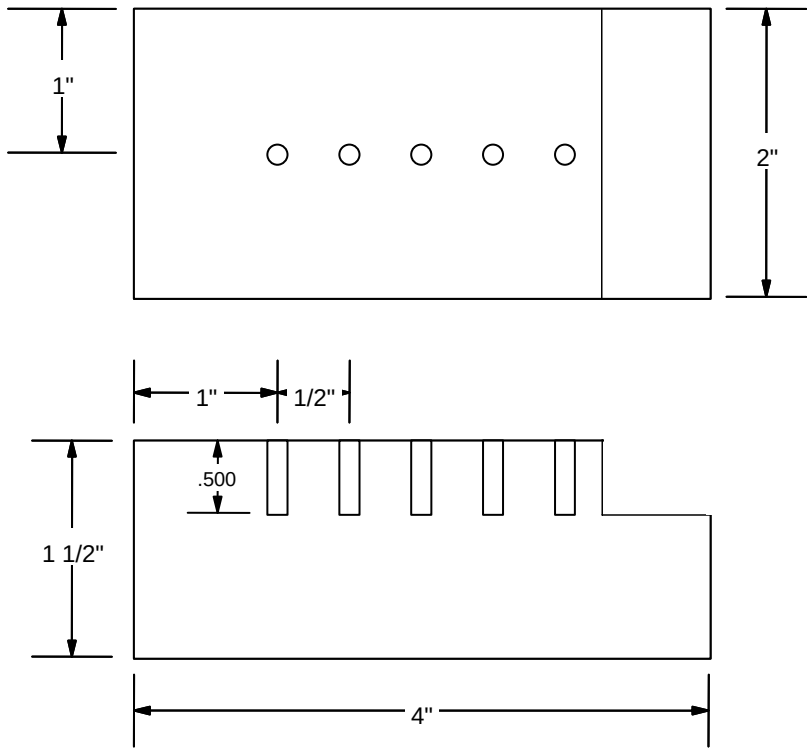

FIGURE 4-7. #1 FBH IN718 BLOCK DESIGN

The F number is used to describe the focusing characteristics of a given UT transducer, with F/n denoting a transducer whose ratio of focal length in water to element diameter n. C-scan images were acquired from the FBH block using a 10-MHz F/7 transducer, as shown in figure 4-8. The mean material noise level, on an 8-bit scale (0-255), was 42.6 at a receiver attenuation setting of -6 dB or equivalently 4.26 at -26 dB. The five FBH targets scanned left to right at -26 dB gave 8-bit amplitudes of 209, 215, 214, 220, and 208, respectively. The average FBH amplitude level is 213.2, with error bars of +6.8 and -5.2. This yields an average SNR of 213.2: 4.26, or approximately 50:1, and also suggests the holes are very consistent.

The five images of the FBHs in figure 4-8 show that they do not lie along a straight line. However, the entry points of the drilled holes did lie along a straight line on the block surface. This suggests that the drill bits wandered in their progress from the block surface to the 1/2″ depth.

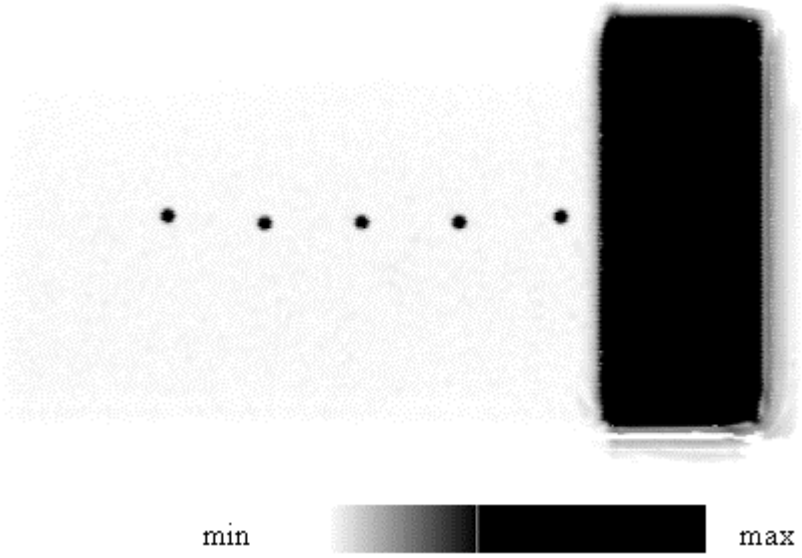

FIGURE 4-8. ULTRASONIC C-SCAN OF #1 FBH IN718 BLOCK

4.4 TRIAL SEED BLOCK DESIGN.

Prior to the manufacture of the final blocks containing the seeded defects, four smaller blocks were fabricated and studied. These were used to assess the fabrication procedure and to evaluate the bonding of the synthetic seeds to the IN718 parent material. In addition, the UT response of the bond between the cap and the base portions of the IN718 block was investigated using these test blocks. The basic test block design is shown in figure 4-9.

Following this design, four separate test blocks were made. Three contained only one type of defect each, i.e., either freckle, dirty white spot, or white spot compositions. The fourth block contained two defects of each seed type. The initial IN718 blocks were machined to size and ultrasonically inspected to ensure that no prior flaws existed in the parent material. The caps were cut off using wire EDM and ground flat. Seed pockets were drilled in the block base and mating surfaces cleaned. The blocks and seeds were assembled and electron beam (EB)-welded in a vacuum. Next, they were HIPped at 970°C for 3 hours at 210 MPa. The HIP temperature was selected to be just below the delta-Ni_3Nb solvus temperature. This prevented grain growth by delta-phase pinning of the grain boundaries and was a sufficiently high temperature that large-scale delta precipitation was not possible.

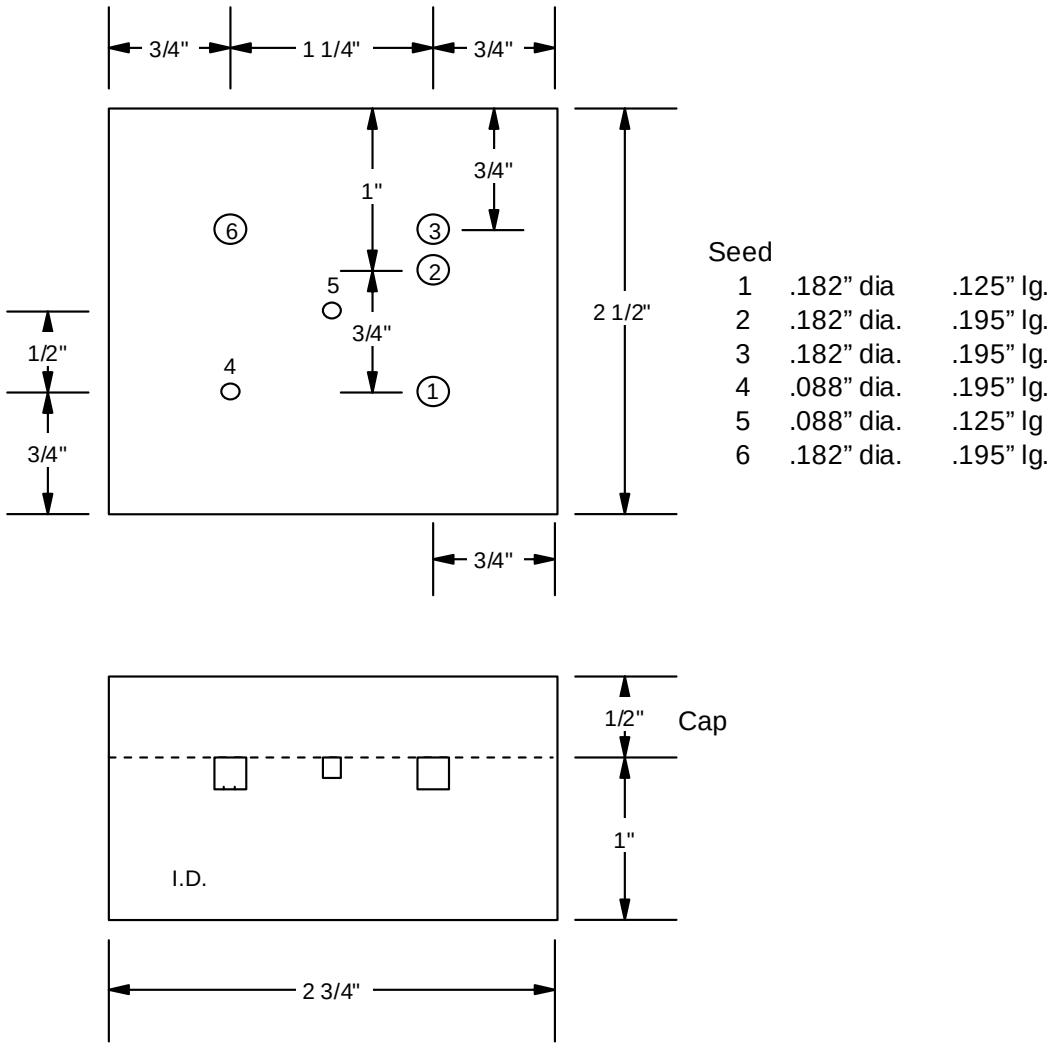

FIGURE 4-9. TRIAL BLOCK DESIGN

Seeds were numbered 1 through 6 in each block, as shown in figure 4-9. The blocks were denoted freckle, white spot, dirty white spot, and composite based on seed type. UT C-scans of the blocks were made using a 10-MHz F/4 transducer, and the resulting images are shown in figure 4-10. The UT reflections from the front and back surfaces of each seed in each block were examined. For well-bonded, weakly scattering inclusions, one expects the echoes from the front and back surfaces of the defect to have similar amplitudes and opposite phases. Cases with anomalous differences in the amplitudes of the front- and back-surface reflections, or those having high amplitude signals between the arrival times of the front- and back-surface reflections, were noted. The noteworthy cases are listed in table 4-3. Based on the UT data, the abnormal seeds were cut out of the test blocks by EDM and examined using optical microscopy.

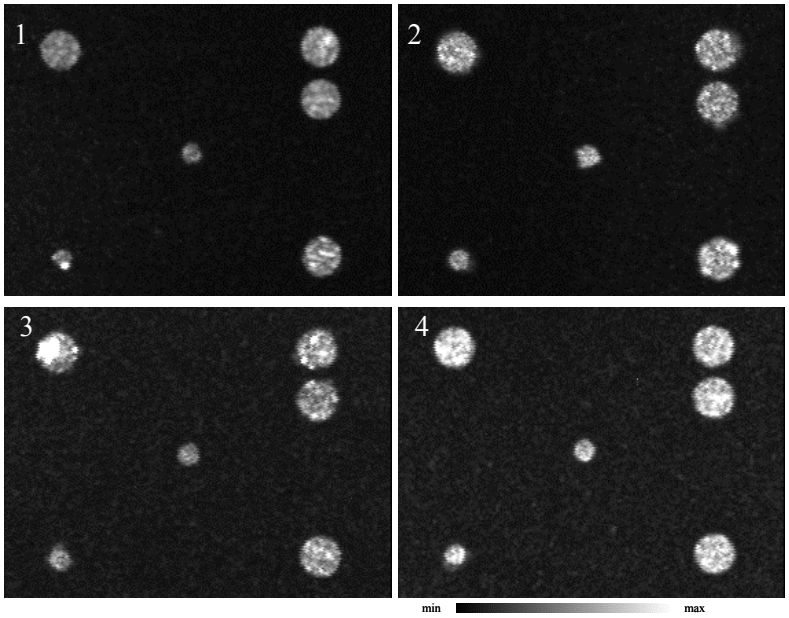

FIGURE 4-10. ULTRASONIC C-SCANS OF TRIAL BLOCKS
(C-scan images of the freckle (1), white spot (2), dirty white spot (3), and Composite (4) test blocks using a 10-MHz F/4 transducer.)

TABLE 4-3. ANOMALOUS INDICATIONS FROM IN718 TRIAL BLOCKS

Seed	UT Observation
Freckle 1	Abnormally strong front and back pulses
Freckle 2	Abnormally strong front and back pulses, back pulse much higher than front
Freckle 3	Abnormally strong front and back pulses
White Spot 1	Internal structure
White Spot 2	Internal structure, big void back wall, that verberated
White Spot 3	Internal structure, big void back wall, that verberated
Dirty White Spot 1	Back-wall or crack in seed, back wall could be internal crack
Dirty White Spot-6	Abnormally strong front pulse, strongly voided front
Composite 1 (Freckle)	Back-wall echo had high amplitude and was disorganized in time domain
Composite 2 (Dirty White Spot)	Internal structure
Composite 3 (White Spot)	Internal structure

Note: C-scan data for these seeds gave higher than expected ultrasonic reflections. These seeds were cut out and destructively analyzed.

In general, the interfaces between the synthetic flaws and the host metal, and those between the cap and base portions of the host metal itself, were found to be tight, conforming, absent of new phases, and void-free. Grain growth was seen across the cap/base interface, suggesting local mass transport. Such host/defect and host/host boundaries would generally be considered well-bonded. In some samples, local areas of poor bonding were identified, and representative examples are described below.

4.4.1 IN718-IN718 Interface.

As a baseline, figure 4-11 displays the microstructure of an IN718 to IN718 bond (cap to base). This particular bond is from the block containing dirty white spots and is typical of similar interfaces in all blocks. With reference to the figure, the as-HIPped microstructure contains small Ni_3Cb delta plates in the region away from the bond and small particles, presumably delta phase, near the bond line. The boundary grains are small and appear to cross the bond line, a sign of a good metallurgical bond from diffusion across this interface.

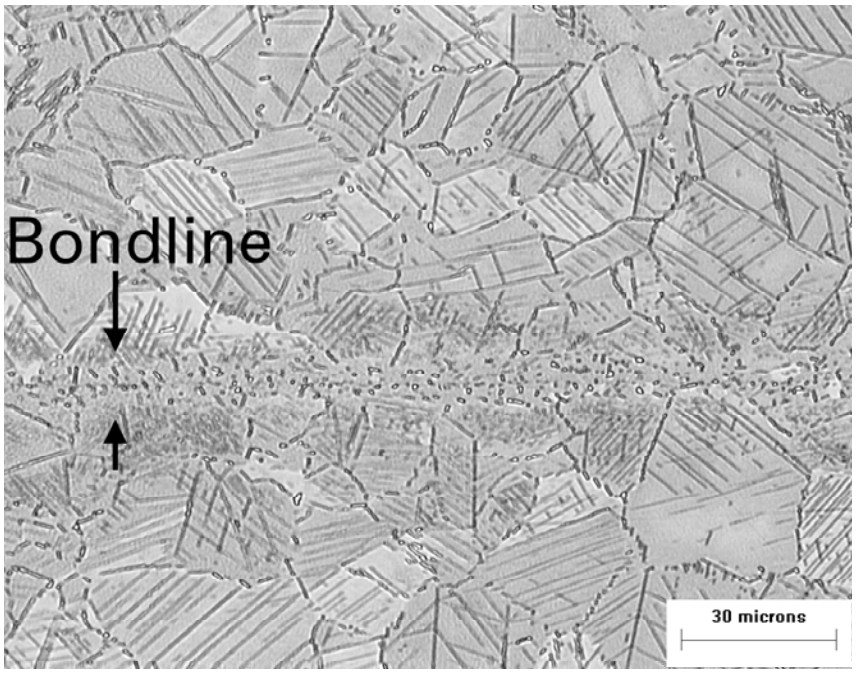

FIGURE 4-11. IN718 TO IN718 BOND LINE IN THE DIRTY WHITE SPOT TEST BLOCK

4.4.2 Freckle-IN718 Interface Defects.

Small discontinuities could typically be found on freckle-IN718 interfaces. Figure 4-12 shows a low-magnification view of the interface between IN718 and freckle seed 1; at this magnification, no discontinuities are apparent. At a higher magnification, figure 4-13 shows a portion of the interface between freckle seed 2 and IN718; there, small crack-like voids can be seen. Similar small voids could be found on all freckle seeds examined.

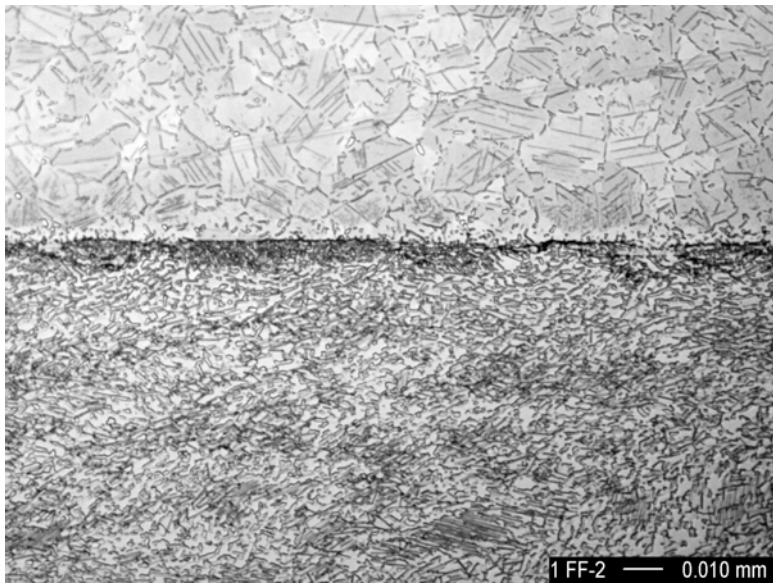

FIGURE 4-12. BOND BETWEEN FRECKLE SEED 1 (BOTTOM) AND IN718 (TOP)

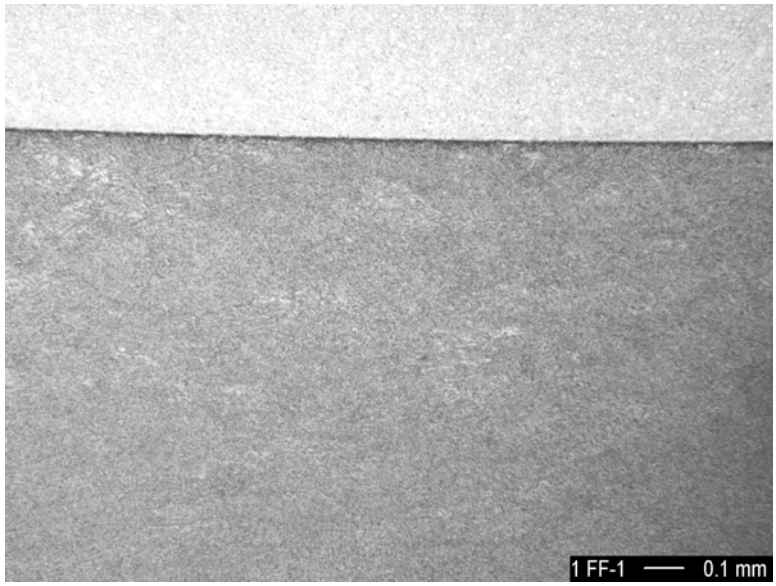

FIGURE 4-13. DETAIL OF BOND LINE BETWEEN FRECKLE SEED 2 (BOTTOM) AND IN718 (TOP) SHOWING SMALL DISCONTINUITIES

4.4.3 White Spot-IN718 Interface Defects.

Figure 4-14 shows large interior grains within white spot seed 1, which may be the source of the internal structure noted by ultrasound. For white spot seed 2, figure 4-15 shows the IN718 interface defect at a low magnification. There are small discontinuities present, particularly in the left half of the image. Additionally, a larger disbond was seen near the corner that circled the back surface of the seed. A similar ring disbond was also found around white spot seed 3.

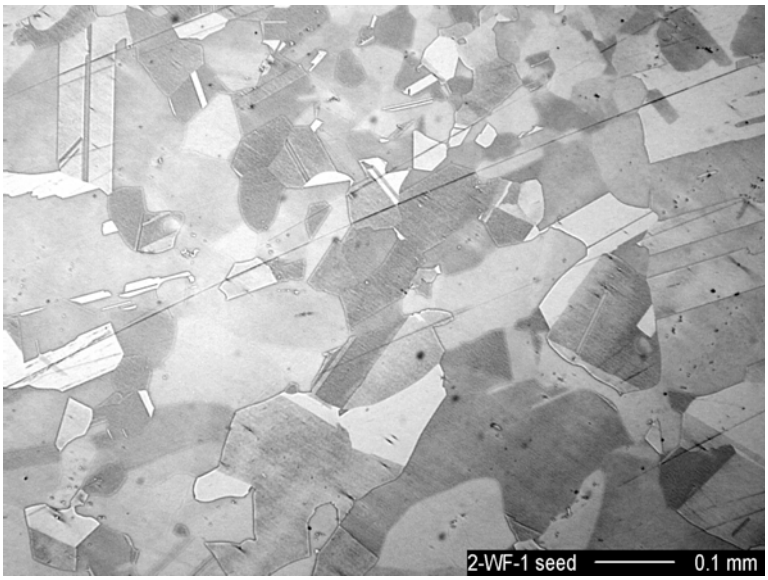

FIGURE 4-14. LARGE GRAIN STRUCTURE OF WHITE SPOT SEED 1
(This grain size is typical of that seen for all the white spot defects.)

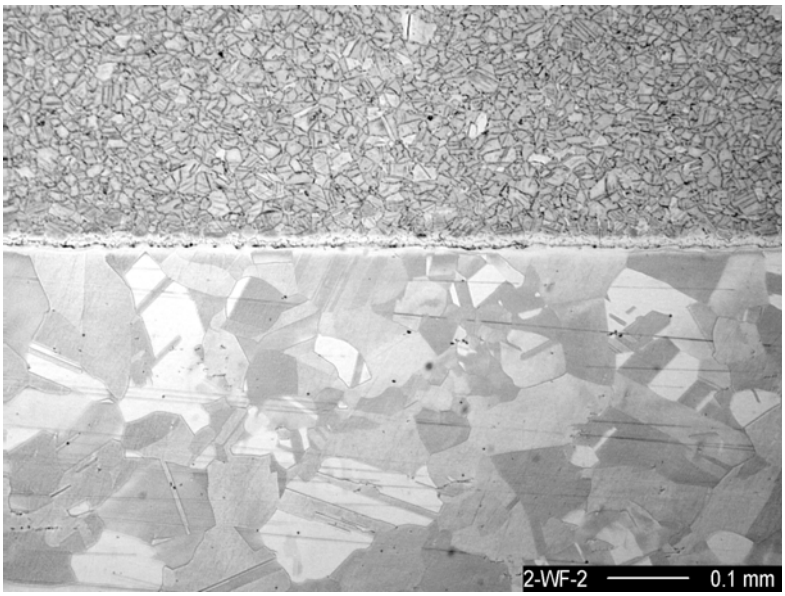

FIGURE 4-15. IN718 (TOP) AND WHITE SPOT SEED 2 (BOTTOM) INTERFACE

4.4.4 Dirty White Spot-IN718 Interface Defects.

Figure 4-16 shows a detailed IN718 dirty white spot 6 bond line in which large ceramic particles present at the surface of the synthetic defect did not bond to the IN718 host. These ceramics are presumably those present in the ingot and forging created by the TiO_2 and TiN additions.

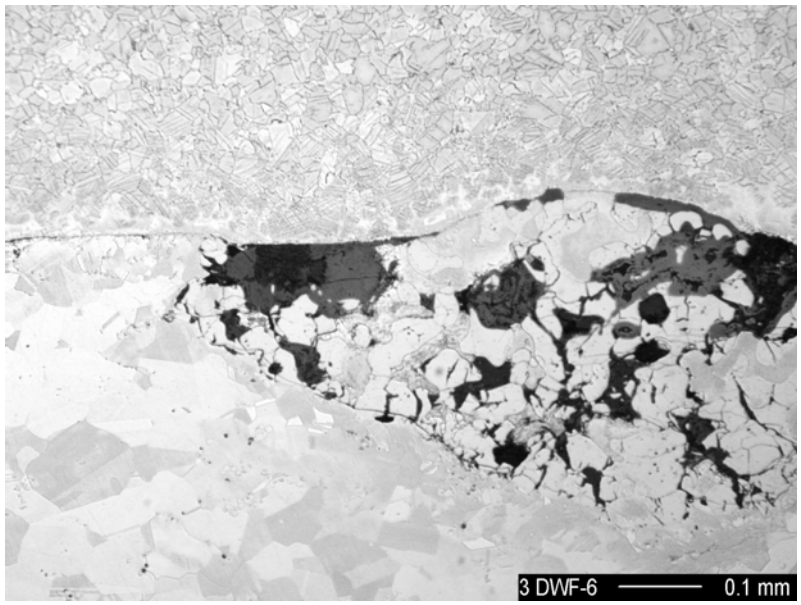

FIGURE 4-16. IN718 DIRTY WHITE SPOT 6 BOND LINE IN WHICH LARGE CERAMIC PARTICLES CREATE A NONBONDED REGION GREATER THAN 0.5 mm LONG

4.5 FINAL BLOCK DESIGN.

Based on experience from the trial block design, a new design was devised for the final blocks. White spot and dirty white spot grains are more than an order of magnitude larger than freckle grains (see figure 4-16). These grain sizes are consistent with the results of UT measurements (and with the difficulties in obtaining them). Seeds smaller than 0.185″ (~5.0 mm) would not likely accommodate a statistically significant number of the larger grains. In addition, the measured reflectivities of the nonvoided seeds in the trial Ni-based blocks were relatively small, ranging from about 0.1% to 1% of that of an equal area FBH.

As a result, the new design incorporated seeds on the order of a #3 FBH in diameter. Smaller seeds would be harder to fabricate, and direct UT velocity measurements on the seeds themselves (before insertion) would be difficult. In addition, smaller seeds would not likely provide accurate data in reflectivity studies because of competing grain noise.

Some of the seeds in the trial blocks showed good bonding to the host material while others did not. This demonstrated that good seed bonding was possible but the HIP parameters might need adjustment. The equipment used could not produce pressures greater than 210 MPa and the temperature could not be increased without causing large grain growth. The only parameter available for adjustment was HIP time, which was increased from 3 to 8 hours to permit plastic flow of the synthetic flaws and the achievement of metallurgical bonding.

Three IN718 blocks were machined with holes to accept seeds having nominal diameters of 0.185″ and nominal lengths of 0.205″. Figures 4-17 through 4-19 show the block designs and seed positions. The seeds themselves were again fabricated from forged batches of material having freckle, white spot, and dirty white spot compositions. The finished IN718 blocks into

which the seeds were inserted were assigned serial numbers beginning with letters FF, WF, and DWF for freckle, white spot, and dirty white spot seeds, respectively.

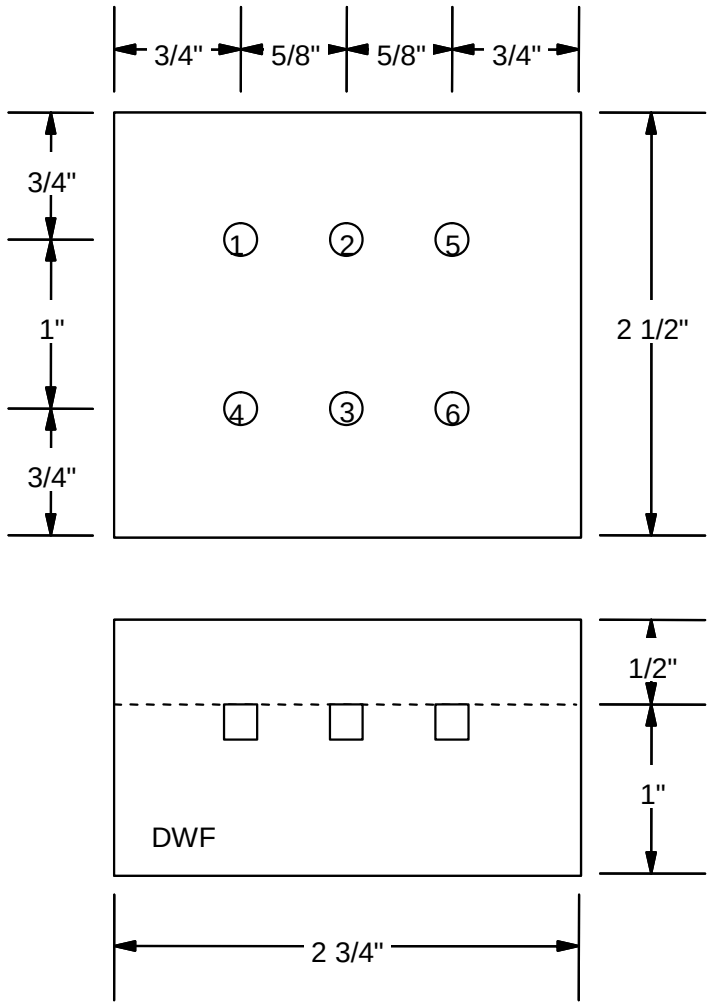

Sample	Length	Diameter
DWF-1	.203	.185
DWF-2	.201	.185
DWF-3	.199	.185
DWF-4	.200	.185
DWF-5	.205	.1855
DWF-6	.203	.185

FIGURE 4-17. DIMENSIONS AND SEED MAP FOR THE DIRTY WHITE SPOT SYNTHETIC SEED BLOCK

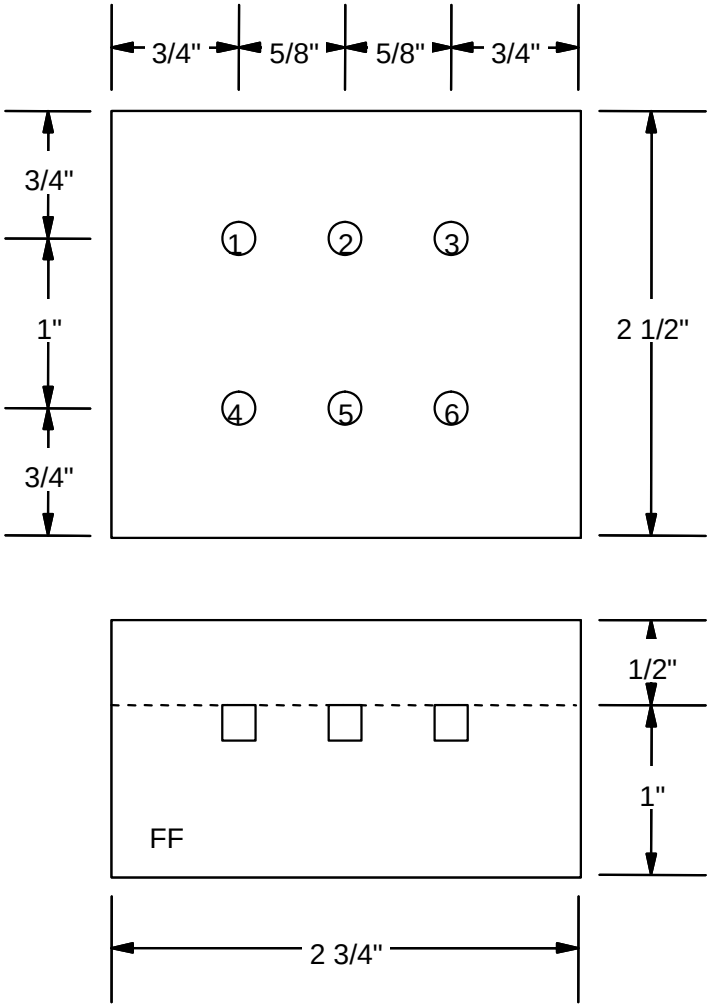

Sample	Length	Diameter
FF-1	.205	.185
FF-2	.205	.185
FF-3	.205	.185
FF-4	.205	.185
FF-5	.2055	.1855
FF-6	.205	.185

FIGURE 4-18. DIMENSIONS AND SEED MAP FOR THE FRECKLE SYNTHETIC SEED BLOCK

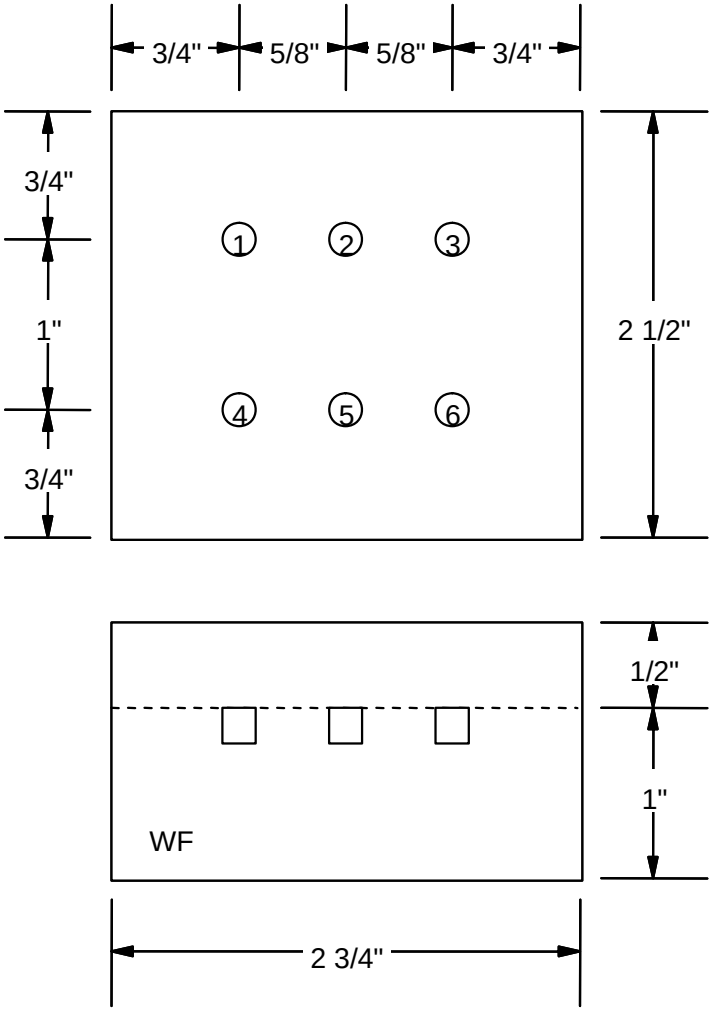

Sample	Length	Diameter
WF-1	.205	.185
WF-2	.205	.185
WF-3	.205	.185
WF-4	.2045	.1845
WF-5	.205	.185
WF-6	.197	.1845

FIGURE 4-19. DIMENSIONS AND SEED MAP FOR THE WHITE SPOT SYNTHETIC SEED BLOCK

The initial IN718 blocks were machined to size and ultrasonically inspected to ensure that no prior flaws existed in the parent material. The seeds were EDM'ed and machined to the lengths and diameters listed in table 4-4. The seed numbers in the table correspond to the seed numbers shown in the block drawings of figures 4-17 through 4-19.

TABLE 4-4. SEED TYPES AND DIMENSIONS FOR SYNTHETIC BLOCKS

Sample	Length (inches)	Diameter (inches)
FF-1	0.205	0.185
FF-2	0.205	0.185
FF-3	0.205	0.185
FF-4	0.205	0.185
FF-5	0.2055	0.1855
FF-6	0.205	0.185
WF-1	0.205	0.185
WF-2	0.205	0.185
WF-3	0.205	0.185
WF-4	0.2045	0.1845
WF-5	0.205	0.185
WF-6	0.197	0.1845
DWF-1	0.203	0.185
DWF-2	0.201	0.185
DWF-3	0.199	0.185
DWF-4	0.200	0.185
DWF-5	0.205	0.1855
DWF-6	0.203	0.185

Prior to insertion into the IN718 host blocks, each seed was ultrasonically characterized to determine its longitudinal and shear-wave velocities in the axial (nominally 0.205″) direction. Contact transducers were used having 1/4″ diameters and center frequencies of 15 and 5 MHz for longitudinal and shear-wave measurements, respectively. The results are shown in table 4-5.

For clean and dirty white spots, internal noise signals seen between the front- and back-surface echoes made measurements difficult; for shear-wave measurements, the SNR was not sufficient to accurately determine velocity. In addition, dirty white spot seeds had the poorest SNR for longitudinal measurements and the largest scatter in longitudinal velocity. Comparing tables 4-2 and 4-5, one sees that the velocities measured on the seeds themselves are in good agreement with the earlier measurements using rectangular coupons of seed material.

After the UT velocity measurements were completed, the blocks and seeds were assembled and EB-welded in a vacuum. The blocks were then HIPped at 970°C for 8 hours at 30 MPa. The top and bottom of each block was then lightly ground to remove any surface oxide and to provide clean, smooth surfaces for UT inspection. UT C-scans of the blocks were performed at 10 MHz with an F7 transducer. A representative C-scan is shown in figure 4-20. With reference to the figure, there is a high-amplitude spot on one of the inclusions in the block containing dirty white spots (upper row, center seed). The maximum amplitude from this inclusion was about twice

that of the other dirty white spot inclusions and equaled about 53% of the response from a #1 FBH in the calibration standard.

TABLE 4-5. SYNTHETIC SEED DIMENSIONS AND SOUND VELOCITIES

Sample	Length (mm)	Δ Time (L) (μsec)	C_L (mm/ μsec)	Δ Time (S) (μsec)	C_S (mm/ μsec)
FF-1	5.215	1.771	5.889	3.321	3.160
FF-2	5.210	1.798	5.795	3.293	3.164
FF-3	5.203	1.766	5.892	3.305	3.149
FF-4	5.203	1.766	5.892	3.283	3.170
FF-5	5.204	1.771	5.877	3.285	3.168
FF-6	5.204	1.776	5.860	3.267	3.186
WF-1	5.198	1.764	5.896	Attempts to measure shear data did not give sufficient SNR for precise velocity determinations.	
WF-2	5.212	1.788	5.830		
WF-3	5.213	1.800	5.792		
WF-4	5.210	1.814	5.744		
WF-5	5.223	1.776	5.882		
WF-6	5.011	1.706	5.875		
DWF-1	5.160	1.792	5.759	Attempts to measure shear data did not give sufficient SNR for precise velocity determinations.	
DWF-2	5.117	1.712	5.978		
DWF-3	5.277	1.811	5.828		
DWF-4	5.105	1.825	5.595		
DWF-5	5.063	1.532	6.610		
DWF-6	5.155	1.793	5.750		

Note: freckle, white spot, dirty white spot seed dimensions, and longitudinal and shear velocities are listed.

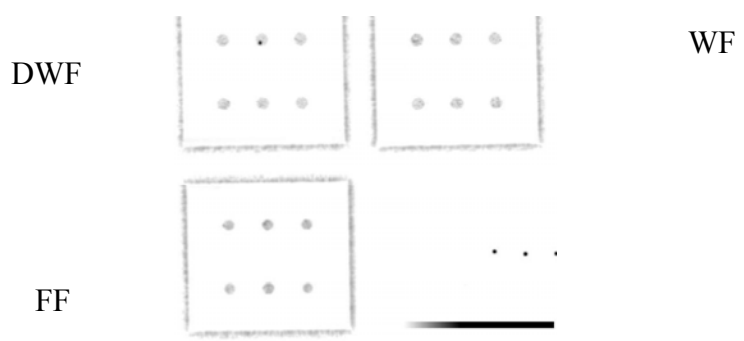

FIGURE 4-20. A 10-MHz F/7 C-SCAN OF BLOCKS CONTAINING SYNTHETIC DEFECTS
(Clockwise from lower left, the three defect blocks contain freckle, dirty white spot, and clean white spot defects, respectively. Image at lower right shows three of the #1 FBH in the reference block.)

Because of the abnormally large echo from one of the dirty white spot inclusions, it was decided to re-HIP all the blocks at the same conditions as before, viz. 970°C, 30 MPa, 8 hours. After this second HIP, the top and bottom surfaces of the blocks were again lightly machined and rescanned using the same 10-MHz F7 transducer. The resulting C-scan, shown in figure 4-21, was very similar to the earlier scan. Again, the same dirty white spot seed yielded an abnormally high peak amplitude. This amplitude was measured as 56% of the response from the average a #1 FBH in the calibration standard, quite close to the earlier result (53%). Thus, the re-HIP did not change the abnormally strong reflection from the dirty white spot in question. Since the block is believed to be well-bonded, it is possible that this strong reflection is from ceramic stringers that are present in dirty white spots.

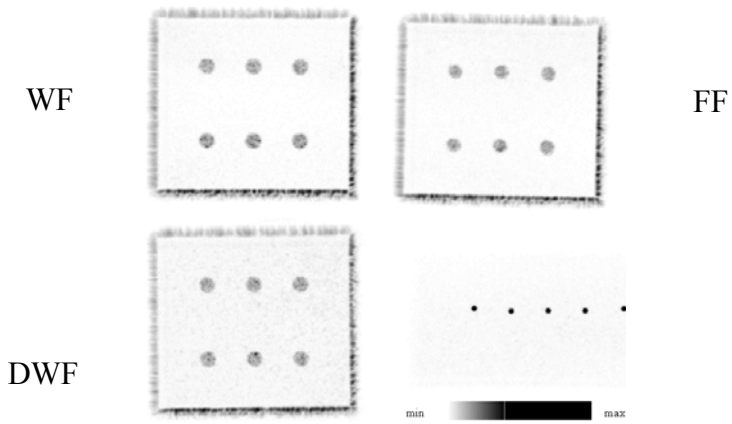

FIGURE 4-21. A 10-MHz C-SCAN OF BLOCKS WITH SYNTHETIC DEFECTS AFTER SECOND HIP
(Lower left block contains the dirty white spot inclusions, highly reflective seed is essentially unchanged. (Block rotated 180° from previous scan.) Lower right of picture shows five #1 FBHs from the companion reference standard block.)

4.6 SUMMARY.

In this study, to produce samples containing synthetic defects, three defect types were selected. Bulk compositions corresponding to the three classes of IN718 defects—white spots, dirty white spots, and freckles—were synthesized using melting and forging processes. The microstructure and UT properties of the bulk synthetic flaws were characterized. A procedure was developed to embed small coupons (seeds) of these defect materials as synthetic flaws in IN718 blocks. Three blocks were manufactured containing such synthetic flaws.

5. CONCLUSIONS.

The fundamental studies program has provided information that will be useful to the nondestructive evaluation community in the design of inspection methods for nickel (Ni) billets. Key results include the following:

- Ultrasonic (UT) velocity was found to be uniform for a given alloy. Since sonic velocity influences the UT beam radiation pattern, sizeable velocity variations can shift the focal depth and impact detectability. Given the uniformity of velocity measurements for IN718 and Waspaloy, it is unlikely that velocity variations will cause noticeable affects on detectability for these alloys.

- In contrast to velocity, attenuation and backscattered grain noise capacity were found to vary significantly with frequency and position. Attenuation and grain noises were highly correlated, i.e., billet regions of high attenuation and grain noise were also found to have high grain noise capacity. Attenuation and noise capacity values were generally found to be larger in Waspaloy than IN718.

- Grain size is the predominant factor controlling noise and attenuation in the Ni alloys studied in this program. In Ni processing, there is a significant amount of recrystallization that occurs due to mechanical working of the billet during the conversion process. This led to approximately equiaxed grains as determined by metallographic characterization performed during the program. As mean grain size increased, the attenuation and grain noise were also found to increase.

- Billet conversion practice was also found to affect the attenuation and grain noise characteristics of the alloys studied. Values of both properties were found to be lower for so-called V-Die processing than GFM.

- Attenuation and grain noise were found to be homogenous with little difference between the axial, radial, and hoop directions in a given measurement location.

- At a given location in a billet, attenuation and grain noise capacity were found to be approximately isotropic with little difference between the axial, radial, and hoop directions.

- Methods to produce synthetic defects with similar chemistries to naturally occurring defects were developed, and several specimens were fabricated that contain so-called white spot, dirty white spot, and freckle defects.

6. REFERENCES.

1. L. A. Jackman, G. E. Maurer, and S. Widge, "New Knowledge About 'White Spots' in Superalloys," *Advance Materials & Processes*, Vol. 5, May 1993, pp. 18-25.

2. P. Howard, D. Copley, and R. Gilmore, "Transducer Design for High Sensitivity Ultrasonic Inspection of Titanium," in *Rev. of Prog. in QNDE*, Vol.16A, D. O. Thompson and D. E. Chimenti, eds., Plenum Press, NY, 1997, pp. 893-900.

3. T. A. Gray, "Application of Measurement Models to Specification of Ultrasonic Inspections," in *Rev. of Prog. in QNDE*, Vol. 16B, D. O. Thompson and D. E. Chimenti, eds., Plenum Press, NY, 1997, pp. 2061-2068.

4. R. B. Thompson, F. J. Margetan, I. Yalda, C.-P. Chiou, and P. D., Panetta, "Coupling Microstructure Outputs of Process Models to Ultrasonic Inspectability Predictions," in *Rev. of Prog. in QNDE*, Vol. 17B, D. O. Thompson and D. E. Chimenti, eds., Plenum Press, NY, 1998, pp. 1847-1853.

5. J. A. Umbach and R. A. Roberts, "Ultrasonic Phased Array Transducers-Model and Experiment," presented at ASNT Fall Conference, October 1997.

6. K. Smith and L. Brasche, "Successful Implementation of FAA Research Address the Disk Inspection Initiative," in *Proceedings of the 5th Annual FAA/NASA/DOD Aging Aircraft Conference*, 2001.

7. R. J. Filkins, J. P. Fulton, T. C. Patton, and J. D. Young, "Recent Advances and Implementations of Flexible Eddy Current Probe Technology," in *Rev. of Prog. in QNDE*, Vol. 17B, D. O. Thompson and D. E. Chimenti, eds., Plenum Press, NY, 1998, pp. 1809-1816.

8. J. M. Amos and J. C. Chao, "Optimization of a Wide-Field Eddy Current Probe Using a Boundary Element Method Based Model," in *Rev. of Prog. in QNDE*, Vol.17A, D. O. Thompson and D. E. Chimenti, eds., Plenum Press, NY, 1998, pp. 275-282.

9. J. C. Chao, N. Nakagawa, D. A. Raulerson, and J. C. Moulder, "Boundary Element Method Based Probe Design Model Validation," in *Rev. of Prog. in QNDE*, Vol.16A, D. O. Thompson and D. E. Chimenti, eds., Plenum Press, NY, 1997, pp. 967-972.

10. W. Q. Meeker, V. Chan, R. B. Thompson, and C.-P. Chiou, "A Methodology for Predicting Probability of Detection for Ultrasonic Testing," in *Rev. of Prog. in QNDE*, Vol. 20B, D.O. Thompson and D.E. Chimenti, eds., AIP, Melville, NY, 2001, pp. 1972-1978.

11. R. H. Burkel, C.-P. Chiou, T. K. Keyes, W. Q. Meeker, J. H. Rose, D. J. Sturges, R. B. Thompson, and W. T. Tucker, "A Methodology for the Assessment of the Capability of Inspection Systems for Detection of Subsurface Flaws in Engine Components," FAA report DOT/FAA/AR-01/96, September 2002.

12. www. Sandia.gov

13. P. D. Panetta, F. J. Margetan, I. Yalda, and R. B. Thompson, "Ultrasonic Attenuation Measurements in Jet-Engine Titanium Alloys," in *Rev. of Prog. in QNDE*, Vol. 15B, D. O. Thompson and D. E. Chimenti, eds., Plenum Press, NY, 1996, p. 1525.

14. P. D. Panetta, F. J. Margetan, I. Yalda, and R. B. Thompson, "Observation and Interpretation of Microstructurally Induced Fluctuations of Back-Surface Signals and Ultrasonic Attenuation in Titanium Alloys," ibid., Vol. 16B, 1997, p. 1547.

15. F. J. Margetan, P. D. Panetta, and R. B. Thompson, "Ultrasonic Signal Attenuation in Engine Titanium Alloys," in *Rev. of Prog. in QNDE*, Vol. 17B, D. O. Thompson and D. E. Chimenti, eds., Plenum Press, NY, 1998, pp. 1469-1476.

16. P. D. Panetta, R. B. Thompson, F. J. Margetan, and I. Yalda, "Ultrasonic Microstructural Characterization and Modeling of Attenuation in Ti-17 and Ti-6Al-4V Alloys," *Nondestructive Evaluation and Materials Properties*, O. Buck and P. Liaw, eds., TMS, Warrendale, OH, 1998.

17. P. D. Panetta, R. B. Thompson, and F. J. Margetan, "Use of Electron Backscatter Diffraction in Understanding Texture and the Mechanisms of Backscattered Noise Generation in Titanium Alloys," in *Rev. of Prog. in QNDE*, Vol. 17A, D. O. Thompson and D. E. Chimenti, eds., Plenum Press, NY, 1998, pp. 89-96.

18. R. B. Thompson, P. Panetta, and F. J. Margetan, "Relationship of the Ultrasonic Backscattering Coefficient of Titanium Alloys to Microstructure," Materials and Processes Affordability: Keys to the Future, H. S. Kliger, B. J. Rasmussen, L. A. Pilato, and T. B. Tolle, eds., SAMPE, Covina, CA, 1998, pp. 1448-1457.

19. F. J. Margetan, H. Wasan, and R. B. Thompson, "An Experimental Study of Microstructure-Induced Ultrasonic Signal Fluctuations in Jet-engine Titanium Alloys," *Rev. of Prog. in QNDE*, Vol. 19B, D. O. Thompson and D. E. Chimenti, eds., AIP, Melville, NY, 2000, pp. 1433-1440.

20. F. J. Margetan, T. A. Gray, and R. B. Thompson, "A Technique for Quantitatively Measuring Microstructurally Induced Ultrasonic Noise," *Review of Progress in QNDE*, Vol. 10B, D. O. Thompson and D. E. Chimenti, eds., Plenum Press, NY, 1991, pp. 1721-1728.

21. F. J. Margetan and R. B. Thompson, "Microstructural Noise in Titanium Alloys and its Influence on the Detectability of Hard-Alpha Inclusions," *Review of Progress in QNDE*, Vol. 11, D. O. Thompson and D. E. Chimenti, eds., Plenum Press, NY, 1992, pp. 1717-1724.

22. F. J. Margetan, R. B. Thompson, I. Yalda-Mooshabad, and Y. K. Han, "Detectability of Small Flaws in Advanced Engine Alloys," ISU Center for NDE, July 1993. (This 221-page report summarizes 3 years of U.S. Air Force sponsored research on the use of

ultrasound to detect defects in titanium engine components and discusses at some length the underlying noise models that are used to deduce the FOM from measured noise data.)

23. Edward J. Nieters, Robert S. Gilmore, David C. Copley, Patrick J. Howard, Robert C. Trzaskos, John D. Young, Michael E. Keller, and William J. Leach, "A Multizone Technique for Billet Inspection," *Review of Progress in QNDE*, Vol. 14B, D. O. Thompson and D. E. Chimenti, eds., Plenum Press, NY, 1995, p. 2137.

24. P. J. Howard and R. S. Gilmore, "Ultrasonic Noise and the Volume of the Ultrasonic Pulse," *Review of Progress in QNDE*, 15, D. O. Thompson and D. E. Chimenti, eds., Plenum Press, NY, 1996, p. 1495.

25. P. Haldipur, F. J. Margetan, L. Yu, and R. B. Thompson, "Ultrasonic Attenuation Measurements in Jet-Engine Nickel Alloys," *Review of Progress in QNDE*, Vol. 20, D. O. Thompson and D. E. Chimenti, eds., AIP, Melville, NY, 2001, pp. 1338-1345.

26. A. Minachi, F. J. Margetan, and R. B. Thompson, "Reconstruction of a Piston Transducer Bean Using Multi-Gaussian Beams (MGB) and Its Applications," in *Review of Progress in QNDE*, Vol. 17A, D. O. Thompson and D. E. Chimenti, eds., Plenum, NY, 1998, pp. 907-914.

27. F. J. Margetan, R. B. Thompson, and T. P. Lerch, "An Analytical Approximation for a Common Ultrasonic Grain Noise Diffraction Integral," *Review of Progress in QNDE*, Vol. 18A, D. O. Thompson and D. E. Chimenti, eds., Kluwer/Plenum, NY, 1999, p. 45.

28. F. J. Margetan, R. B. Thompson, and I. Yalda-Mooshabad, "Modeling Ultrasonic Microstructural Noise in Titanium Alloys," *Review of Progress in QNDE*, 12, D. O. Thompson and D. E. Chimenti, eds., Plenum Press, NY, 1993, pp. 1735-1743.

29. F. J. Margetan, R. B. Thompson, and I. Yalda-Mooshabad, "Backscattered Microstructural Noise in Ultrasonic Toneburst Inspections," *Journal of Nondestructive Evaluation*, Vol. 13, Plenum Press, NY, 1994, pp. 111-136.

30. F. J. Margetan, I. Yalda-Mooshabad, and R. B. Thompson, "Estimating Ultrasonic Signal-to-Noise Ratios for Inspections of Cylindrical Billets," *Review of Progress in QNDE*, Vol. 13, D. O. Thompson and D. E. Chimenti, eds., Plenum Press, NY, 1994, pp. 1737-1744.

31. F. J. Margetan, K. Y. Han, I. Yalda, Scot Goettsch, and R. B. Thompson, "The Practical Application of Grain Noise Models in Titanium Billets and Forgings," *Review of Progress in QNDE*, Vol. 14, D. O. Thompson and D. E. Chimenti, eds., Plenum Press, NY, 1995, pp. 2129-2136.

32. F. J. Margetan, I. Yalda and R. B. Thompson, "Predicting Gated-Peak Grain Noise Distributions for Ultrasonic Inspections of Metals," *Review of Progress in QNDE*, Vol. 15, D. O. Thompson and D. E. Chimenti, eds., Plenum Press, NY, 1996, pp. 1509-1516.

33. F. J. Margetan, I. Yalda, R. B. Thompson, J. Umbach, U. Suh, P. J. Howard, D. C. Copley, and R. Gilmore, "Ultrasonic Grain Noise Modeling: Recent Applications to Engine Titanium Inspections," *Review of Progress in QNDE*, Vol. 16, D. O. Thompson and D. E. Chimenti, eds., Plenum Press, NY, 1997, pp. 1555-1562.

34. F. J. Margetan, P. Haldipur, Linxiao Yu, R. B. Thompson, A. Degtyar, and H. Wasan, "Backscattered Ultrasonic Noise Measurements in Jet-Engine Nickel Alloys," *Review of Progress in QNDE*, Vol. 20, D. O. Thompson and D. E. Chimenti, eds., AIP, Melville, NY, 2001, pp. 1314-1321.

35. Anxiang Li, Ron Roberts, Pranaam Haldipur, Frank J. Margetan, and R. B. Thompson, "Computational Study of Grain Scattering Effects in Ultrasonic Measurements," *Review of Progress in QNDE*, Vol. 22, D. O. Thompson and D. E. Chimenti, eds., AIP, Melville NY, in press.

36. Pranaam Haldipur, F. J. Margetan, Linxiao Yu, and R. B. Thompson, "A Study of Ultrasonic Property Variations Within Jet-Engine Nickel Alloy Billets," *Review of Progress in QNDE*, Vol. 21B, D. O. Thompson and D. E. Chimenti, eds., AIP, Melville, NY, 2002, pp. 1502-1509.

37. P. Haldipur, F. J. Margetan, and R. B. Thompson, "Correlation Between Local Ultrasonic Properties and Grain Size Within Jet-Engine Nickel Alloy Billets," *Review of Progress in QNDE*, Vol. 22, D. O. Thompson and D. E. Chimenti, eds., AIP, Melville, NY, in press.

38. Pranaam Haldipur, "Model-Based Interpretation on Ultrasonic Data in Nickel-Based Superalloys," Ph.D. Dissertation, Material Science Engineering Dept., Iowa State University, Ames, Iowa, in preparation.

39. C. P. Chiou, Isaac Yalda, F. J. Margetan, and R. B. Thompson, "The Use of Ultrasonic Flaw and Noise Models in Designing Titanium Test Blocks," *Review of Progress in QNDE*, 17B, D. O. Thompson and D. E. Chimenti, eds., Plenum Press, NY, 1998, pp. 2069-2076.

40. J. A. Turner, "On-line Attenuation Calculator," may be accessed at http://em-jaturner.unl.edu

41. J. A. Turner and R. L. Weaver, "Radioactive Transfer and Multiple Scattering of Diffuse Ultrasound in Polycrystalline Media," *J. Acoust. Soc. Am.* V. 96, pp. 3675-3683, 1994.

42. R. L. Weaver, "Diffusivity of Ultrasound in Polycrystals," *J. Mech. Phys. Solids* 38, 55-86, 1990.

43. F. E. Stanke and G. S. Kino, "A Unified Theory for Elastic Wave Propagation in Polycrystalline Materials," *J. Acoust. Soc. Am.* V. 75, pp. 665-681, 1984.

44. J. H. Rose, "Ultrasonic Backscatter from Microstructure," *Review of Progress in QNDE*, Vol. 11B, D. O. Thompson and D. E. Chimenti, eds., Plenum Press, NY, 1992, pp. 1677-1684.

45. Frank J. Margetan, Pranaam Haldipur, and Yanming Guo, "Determination of Grain Diameter Estimates From Grain-boundary Tracings," a "How-To-Manual" which also demonstrates the use of the GmSize3 software, Center for NDE at Iowa State University, May 2002.

46. R. B. Thompson, J. F. Smith, S. S. Lee, and G. C. Johnson, "A Comparison of Ultrasonic and X-Ray Determinations of Texture in Thin Cu and Al Plates," *Metallurgical Transactions A*, Vol. 20A, November 1989, pp. 2431-2446.

47. P. Haldipur, F.J. Margetan, and R.B. Thompson, "Estimation of Single-Crystal Elastic Constants From Ultrasonic Measurements on Polycrystalline Specimens," *Rev. of Prog. in QNDE*, Vol. 23, D.O. Thompson and D.E. Chimenti, eds., AIP, Melville, NY, 2004, in press.

48. Laurence A. Jackman, Gernant E. Maurer, and Sunil Widge, "White Spots in Superalloys," In *Superalloys 718, 625, 706, and Various Derivatives*, E. A. Loria, ed., *The Minerals, Metals & Materials Society*, Warrendale, PA, 1994, pp. 153-166.

49. S. T. Wlodek and R. D. Field, "Freckles" in Cast and Wrought Products, In *Superalloys 718, 625, 706, and Various Derivatives*, E. A. Loria, ed., 1994, *The Minerals, Metals & Materials Society*, Warrendale, PA, pp. 167-176.

APPENDIX A—DEFECT CHARACTERIZATION OF NATURALLY OCCURRING ANOMALIES

In addition to work with synthetic defects, five naturally occurring anomalies were ultrasonically and metallographically characterized in cooperation with members of the Specialty Metals Processing Consortium. Members of the consortium provided specimens and production inspection information for five indications. Samples were ultrasonically characterized at Iowa State University and metallographically characterized by the Original Equipment Manufacturer members of the Engine Titanium Consortium. The results of the characterization are provided in this appendix. Details of the ultrasonic characterization procedure are provided in Appendix B. A summary of the anomaly characterization is provided in table A-1.

TABLE A-1. ANOMALY CHARACTERIZATION DATA SUMMARY

Indication Number	Material Description	UT Response (%Full) Screen Height	Anomaly Type
1	IN 718 VIM/VAR	NA	Entrapped slag
2	IN 718 VIM/ESR/VAR	80% +2.5 dB	Entrapped slag
3	IN 718 VIM/ESR/VAR	80% +2.5 dB	Entrapped slag
4	Waspaloy VIM/ESR/VAR	100%	Nonmetallic inclusion
5	Waspaloy VIM/ESR/VAR	100%	Nonmetallic inclusion

Ni Billet Indication #1 – General Information

- Found in 10" triple melt Inconel 718 billet
- Indication determined to be entrapped slag

Ni Billet Indication # 1 – Sample sectioning and naming convention

Micrograph Orientation

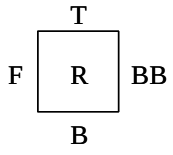

Cube Orientation

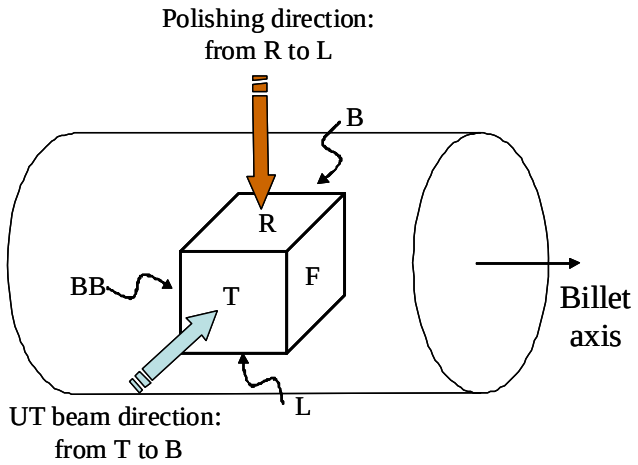

Ni Billet Indication # 1 – Ultrasonic Measurements

Ni Real Indication #1: Image Orientation

Transducer P2: Panametrics V307 5MHz/1.0” dia. 8” PTF
Transducer PA: Megasonics IHM 20MHz/0.25” dia. 2” SF

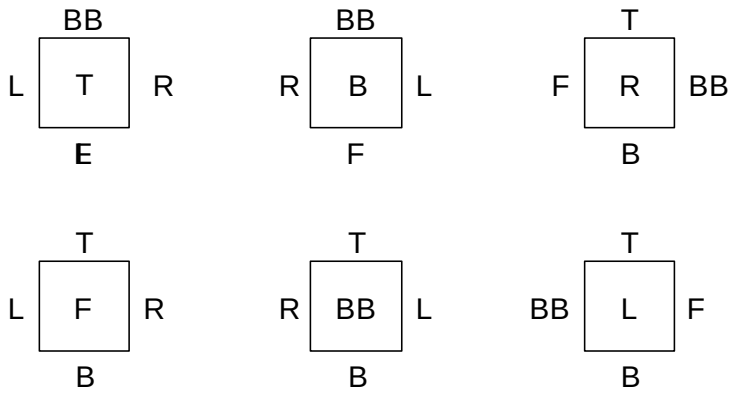

Ni Billet Indication # 1 – Ultrasonic Measurements

5 MHz C-Scan Images (P2 transducer)

All are 200 by 200 pixels at 5 mils scan increments

Sides BB and F have no indication

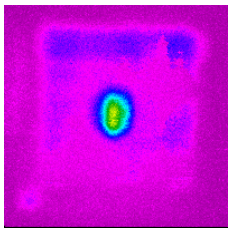

Side T
Gain=43 dB

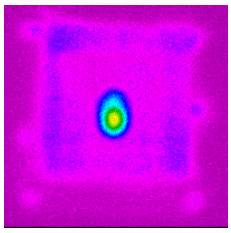

Side B
Gain=43 dB

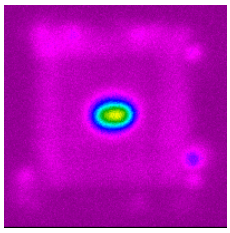

Side R
Gain=37 dB

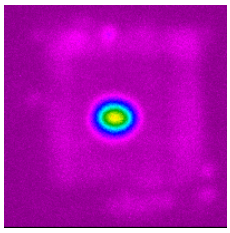

Side L
Gain=37 dB

Ni Billet Indication # 1 – Ultrasonic Measurements

20 MHz C-Scan Images (PA transducer)

All are 500 by 500 pixels at 2 mils scan increments

Arrows: Surface air bubble

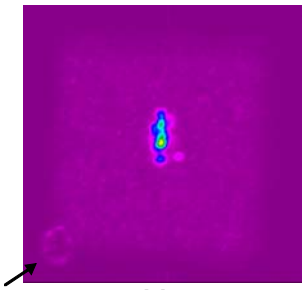

Side T
Gain=30 dB

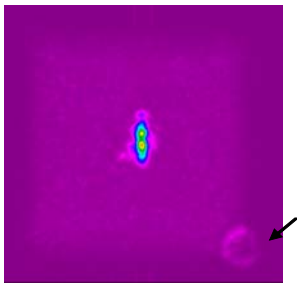

Side B
Gain=30 dB

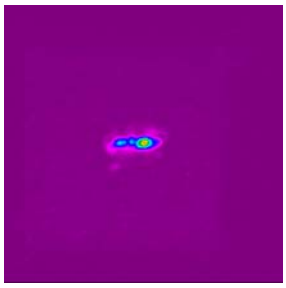

Side R
Gain=24 dB

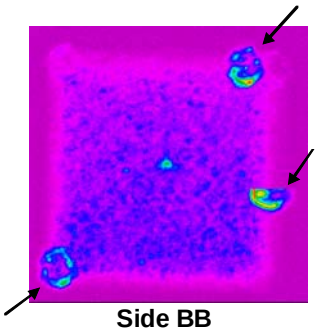

Side BB
Gain=43? dB

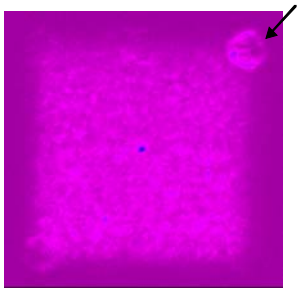

Side F
Gain=38 dB

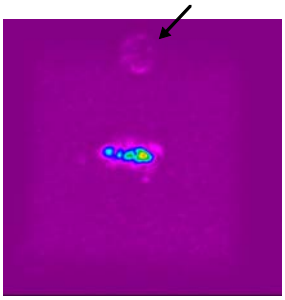

Side L
Gain=28 dB

Ni Billet Indication # 1 – 10X magnification

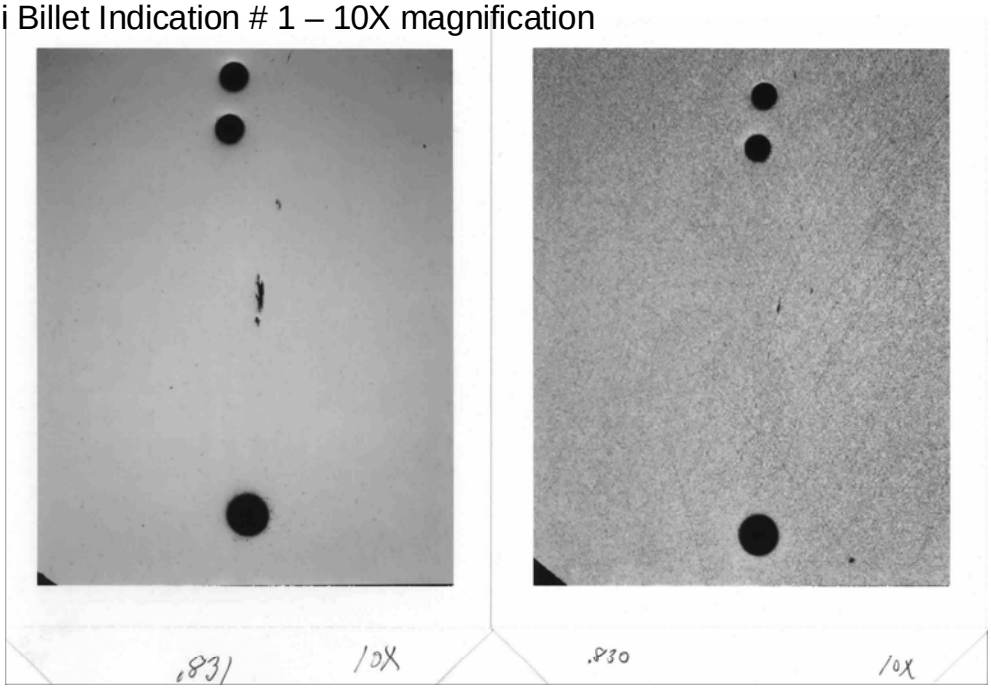

NOTE: the numbers on the right-hand side indicate the magnification (10x) and the polishing depth of slice measured from original top surface of R side (0.830” and 0.831”)

Ni Billet Indication # 1 – 10X magnification

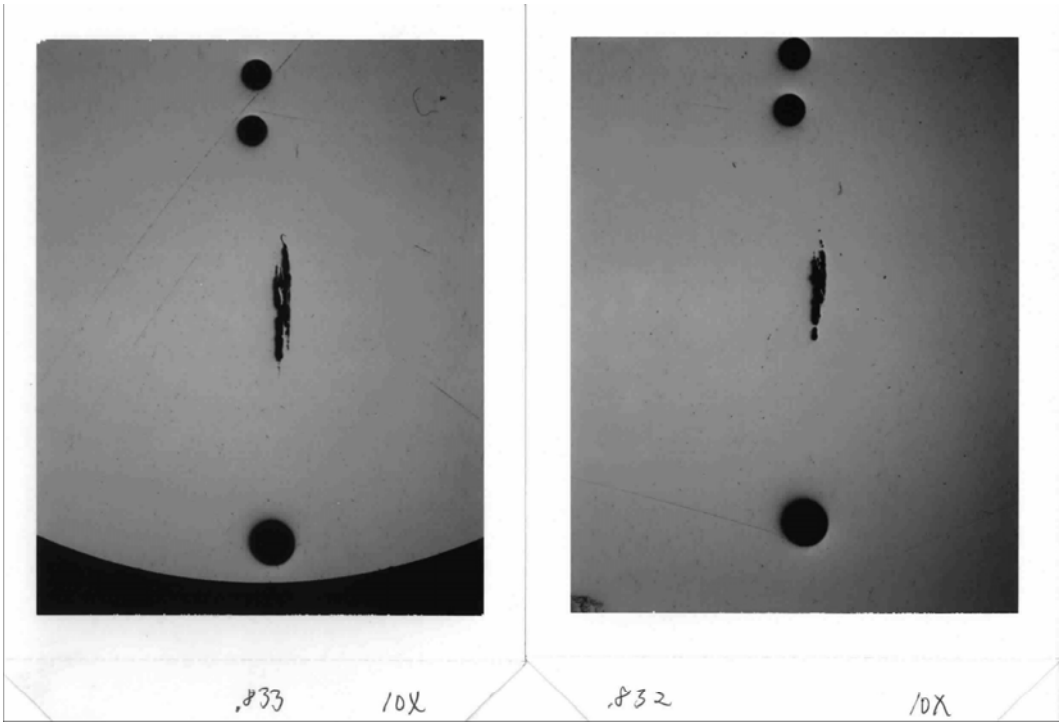

Ni Billet Indication # 1 – 10X magnification

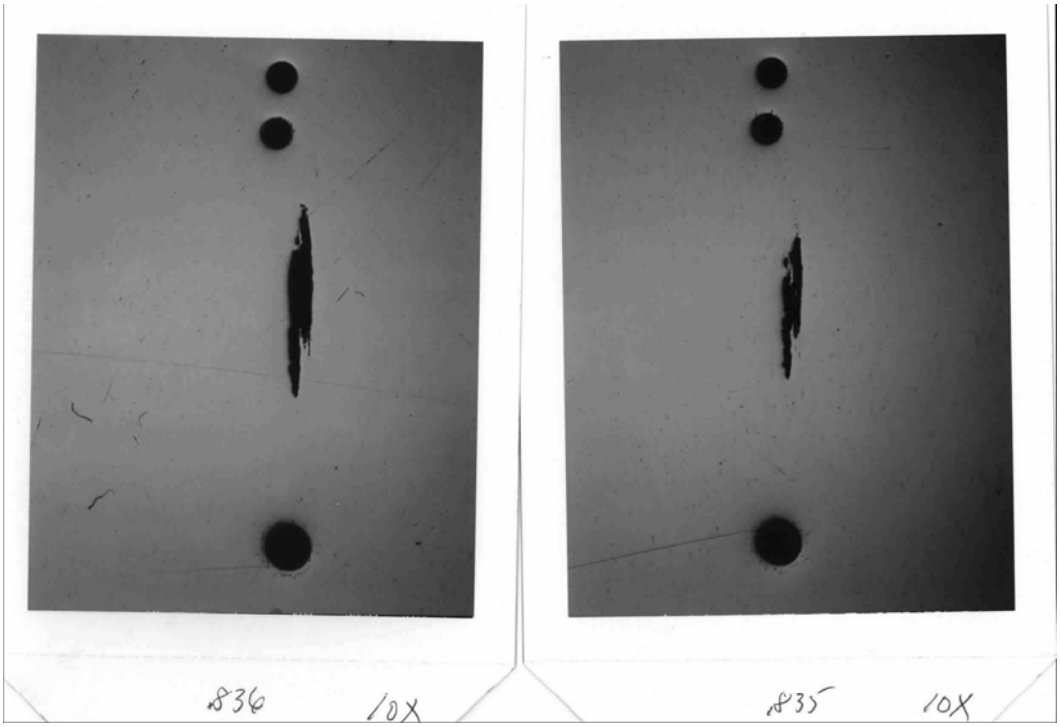

Ni Billet Indication # 1 – 10X magnification

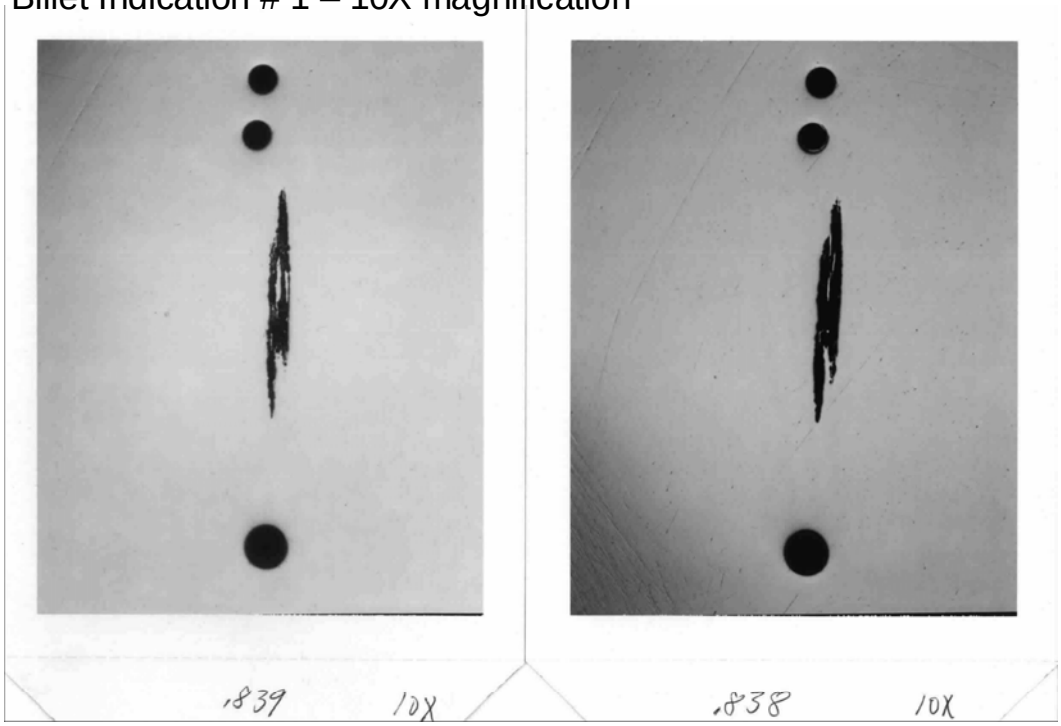

Slice 0.839” is where the chemical analysis was performed

Ni Billet Indication # 1 – 10X magnification

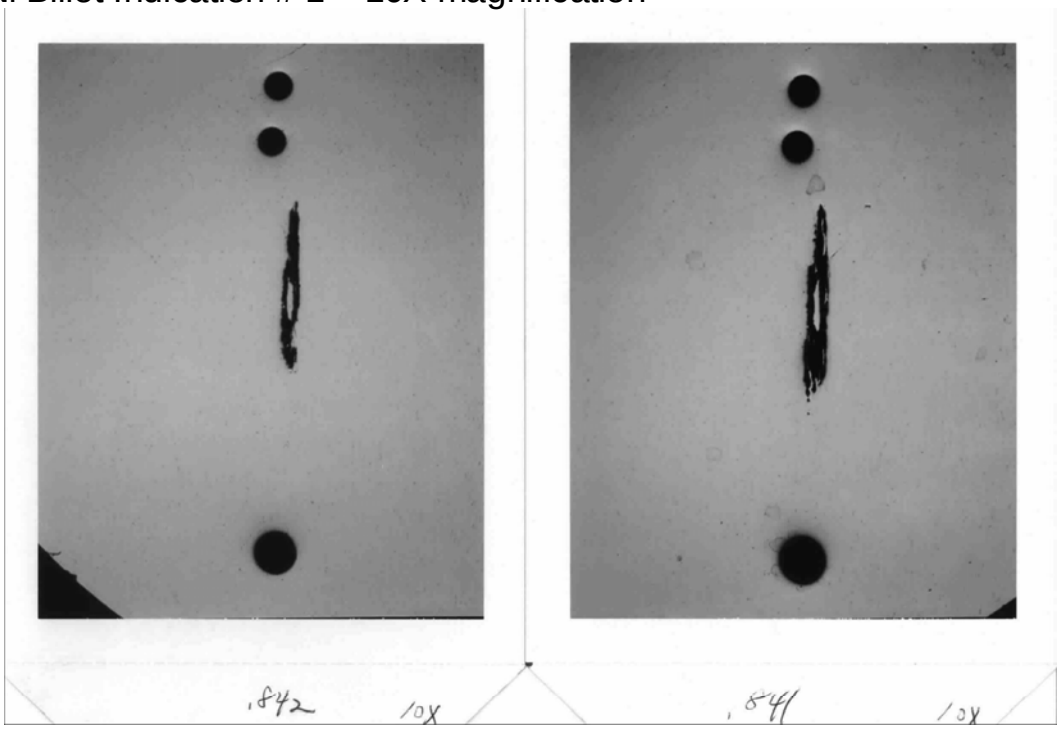

Ni Billet Indication # 1 – 10X magnification

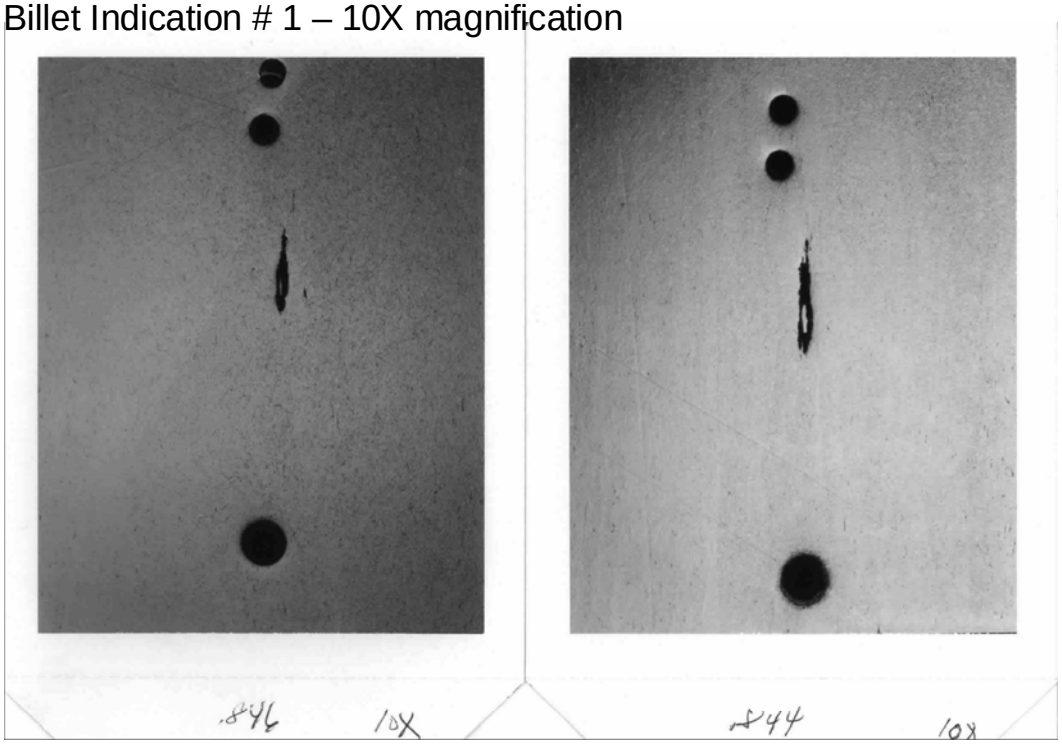

Due to technical problem, after slice 0.846" the sectioning jumps directly to the last slice 0.861" at which Indication cross section was no longer seen.

Ni Billet Indication # 1 – 100X composite micrographs

Slice 830

Slice 831

Slice 832

Slice 833

Ni Billet Indication # 1 – 100X composite micrographs

Slice 835

Slice 836

Slice 838

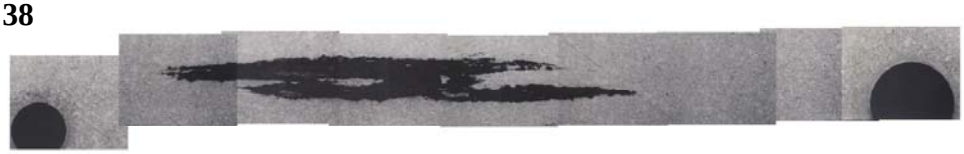

Slice 839

Ni Billet Indication # 1 – 100X composite micrographs

Slice 841

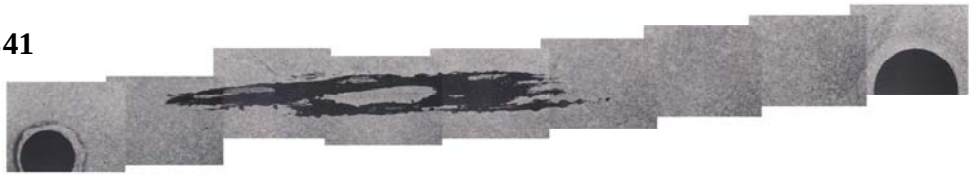

Slice 842

Slice 844

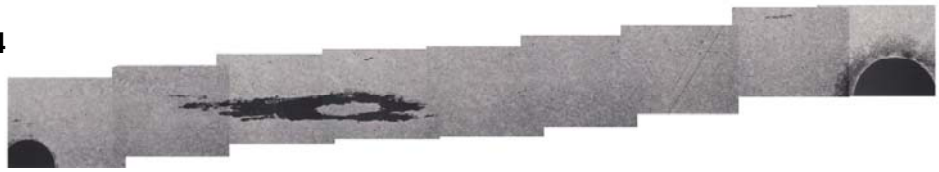

Slice 846

Ni Billet Indication # 1 – SEM analysis performed at slice 0.839”

Inco 718 triple melt
Matrix scan

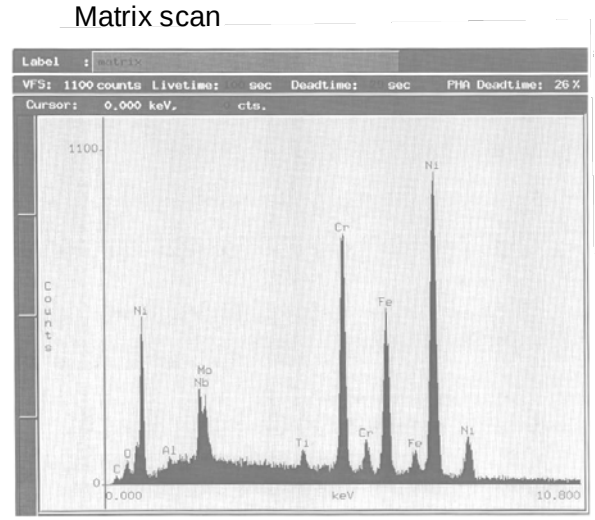

Tue Jan 2 13:48:41 2001

matrix

Refit _Al-K' _Al-K" _Si-K' _Si-K" _Fe-L' _Fe-L" _Ca-K' _Ca-K"
Refit _Nb-L' _Ti-K" _Cr-K" _Mo-L' _Mo-L"
Filter Fit Method
Chi-sqd = 0.97 Livetime = 100.0 Sec.
Standardless Analysis

Element	Relative k-ratio	Error (1-Sigma)	Net Counts	Error (1-Sigma)
Nb-L	0.04238	+/- 0.00216	3924	+/- 200
Ti-K	0.01040	+/- 0.00076	789	+/- 58
Cr-K	0.20137	+/- 0.00225	12274	+/- 137
Fe-K	0.19081	+/- 0.00456	8866	+/- 212
Ni-K	0.52874	+/- 0.00796	18124	+/- 273
Mo-L	0.02279	+/- 0.00179	2012	+/- 158
Al-K	0.00136	+/- 0.00022	231	+/- 37
Si-K	0.00097	+/- 0.00027	157	+/- 44
Fe-L	---	---	532	+/- 104
Ni-L	---	---	5502	+/- 118
C -K	---	---	165	+/- 23
O -K	---	---	488	+/- 52
Ca-K	0.00116	+/- 0.00052	114	+/- 51

Adjustment Factors	K	L	M
Z-Balance:	0.00000	0.00000	0.00000
Shell:	1.00000	1.00000	1.00000

PROZA Correction Acc.Volt.= 20 kV Take-off Angle=35.00 deg
Number of Iterations = 4

Element	k-ratio (calc.)	ZAF	Atom %	Element Wt %	Wt % Err. (1-Sigma)
Nb-L	0.0408	1.499	3.84	6.12	+/- 0.31
Ti-K	0.0100	1.007	1.23	1.01	+/- 0.07
Cr-K	0.1940	0.962	20.90	18.66	+/- 0.21
Fe-K	0.1838	0.965	18.50	17.73	+/- 0.42
Ni-K	0.5093	1.034	52.25	52.67	+/- 0.79
Mo-L	0.0220	1.423	1.90	3.12	+/- 0.25
Al-K	0.0013	2.894	0.82	0.38	+/- 0.06
Si-K	0.0009	2.069	0.40	0.19	+/- 0.05
Ca-K	0.0011	1.010	0.16	0.11	+/- 0.05
Total			100.00	100.00	

Ni Billet Indication # 1 – SEM analysis performed at slice 0.839”
SEM analysis locations – 200X photograph

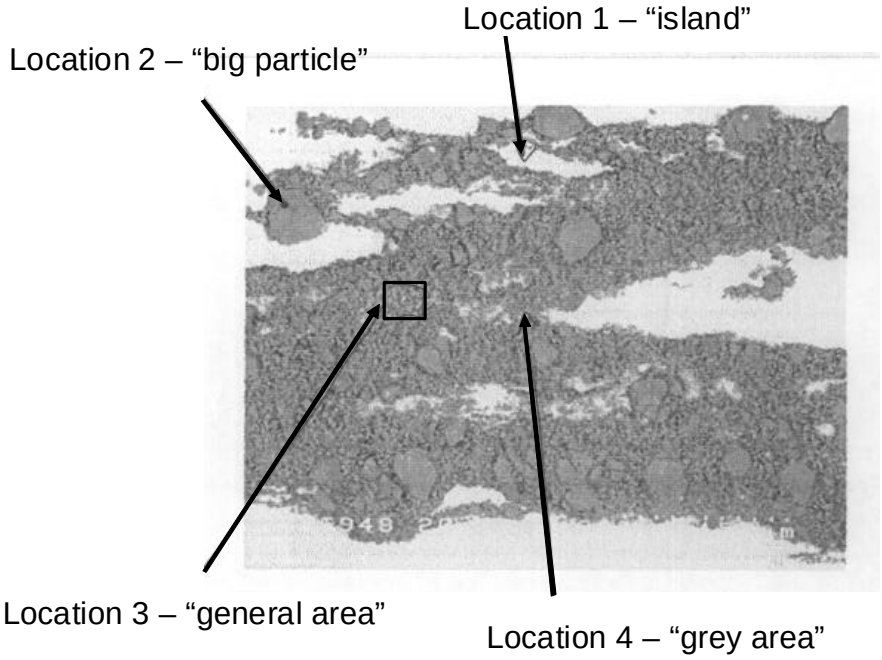

Ni Billet Indication # 1 – SEM analysis performed at slice 0.839”

Inco 718 triple melt
Location 1 – “island scan”

Tue Jan 2 13:28:54 2001

light colored "islands"/photo 6948

Refit _Al-K' _Al-K" _Si-K' _Si-K" _Fe-L' _Fe-L" _Ca-K' _Ca-K"
Refit _Nb-L' _Ti-K" _Mo-L' _Mo-L"
Filter Fit Method
Chi-sqd = 1.99 Livetime = 100.0 Sec.
Standardless Analysis

Element	Relative k-ratio	Error (1-Sigma)	Net Counts	Error (1-Sigma)
Nb-L	0.04696	+/- 0.00234	4081	+/- 203
Ti-K	0.01562	+/- 0.00084	1112	+/- 60
Cr-K	0.19424	+/- 0.00344	11112	+/- 197
Fe-K	0.18379	+/- 0.00475	8016	+/- 207
Ni-K	0.53327	+/- 0.00830	17156	+/- 267
Mo-L	0.02149	+/- 0.00193	1779	+/- 160
Al-K	0.00174	+/- 0.00025	277	+/- 39
Si-K	0.00064	+/- 0.00029	99	+/- 44
Fe-L	---	---	519	+/- 109
Ni-L	---	---	5817	+/- 128
C -K	---	---	698	+/- 33
O -K	---	---	485	+/- 55
Ca-K	0.00224	+/- 0.00057	204	+/- 52

Adjustment Factors	K	L	M
Z-Balance:	0.00000	0.00000	0.00000
Shell:	1.00000	1.00000	1.00000

PROZA Correction Acc.Volt.= 20 kV Take-off Angle=35.00 deg
Number of Iterations = 4

Element	k-ratio (calc.)	ZAF	Atom %	Element Wt %	Wt % Err (1-Sigma)
Nb-L	0.0451	1.496	4.24	6.75	+/- 0.34
Ti-K	0.0150	1.000	1.83	1.50	+/- 0.08
Cr-K	0.1867	0.965	20.19	18.01	+/- 0.32
Fe-K	0.1766	0.964	17.77	17.02	+/- 0.44
Ni-K	0.5125	1.033	52.56	52.94	+/- 0.82
Mo-L	0.0206	1.421	1.78	2.93	+/- 0.26
Al-K	0.0017	2.885	1.04	0.48	+/- 0.07
Si-K	0.0006	2.066	0.27	0.13	+/- 0.06
Ca-K	0.0022	1.024	0.32	0.22	+/- 0.06
Total			100.00	100.00	

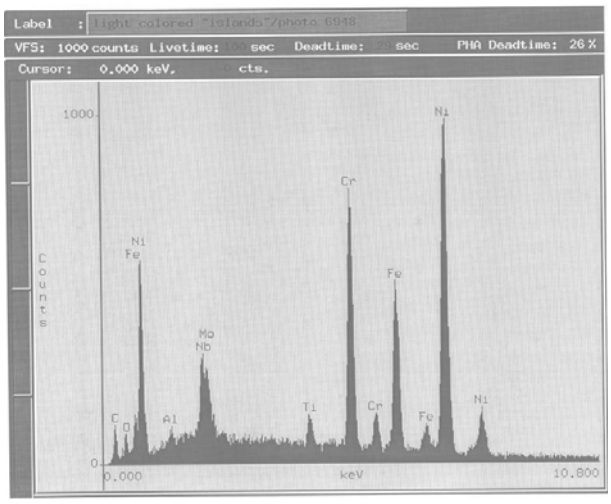

Ni Billet Indication # 1 – SEM analysis performed at slice 0.839”

Inco 718 triple melt
Location 2 – “large particle”

Tue Jan 2 13:20:04 2001

large particle/see photo 6948

Refit _Nb-L' _Nb-L" _Cr-K' _Cr-K" _Fe-K' _Fe-K" _Ni-K' _Ni-K" _Mo-L' _Mo-L" _Si-
Refit _Mo-L _Si-K _C -K'
Filter Fit Method
Chi-sqd = 1.36 Livetime = 100.0 Sec.
Standardless Analysis

Element	Relative k-ratio	Error (1-Sigma)	Net Counts	Error (1-Sigma)
Nb-L	0.00519	+/- 0.00165	211	+/- 67
Ti-K	0.01053	+/- 0.00204	352	+/- 68
Cr-K	0.00799	+/- 0.00138	215	+/- 37
Fe-K	0.00735	+/- 0.00196	150	+/- 40
Ni-K	0.02615	+/- 0.00305	395	+/- 46
Mo-L	0.00000	+/- 0.00001	0	+/- 0
Al-K	0.43626	+/- 0.00289	32334	+/- 214
Si-K	0.00000	+/- 0.00001	0	+/- 0
Fe-L	---	---	37	+/- 68
Ni-L	---	---	50	+/- 45
C -K	---	---	494	+/- 26
O -K	---	---	3523	+/- 66
Ca-K	0.50654	+/- 0.00536	21628	+/- 229

Adjustment Factors	K	L	M
Z-Balance:	0.00000	0.00000	0.00000
Shell:	1.00000	1.00000	1.00000

PROZA Correction Acc.Volt.= 20 kV Take-off Angle=35.00 deg
Number of Iterations = 5

Element	k-ratio (calc.)	ZAF	Atom %	Element Wt %	Wt % Err. (1-Sigma)
Nb-L	0.0042	1.577	0.23	0.66	+/- 0.21
Ti-K	0.0085	1.330	0.77	1.13	+/- 0.22
Cr-K	0.0064	1.234	0.50	0.79	+/- 0.14
Fe-K	0.0059	1.180	0.41	0.70	+/- 0.19
Ni-K	0.0210	1.142	1.34	2.40	+/- 0.28
Mo-L	0.0000	1.452	0.00	0.00	+/- 0.00
Al-K	0.3509	1.415	60.27	49.66	+/- 0.33
Si-K	0.0000	2.064	0.00	0.00	+/- 0.00
Ca-K	0.4074	1.096	36.48	44.66	+/- 0.47
Total			100.00	100.00	

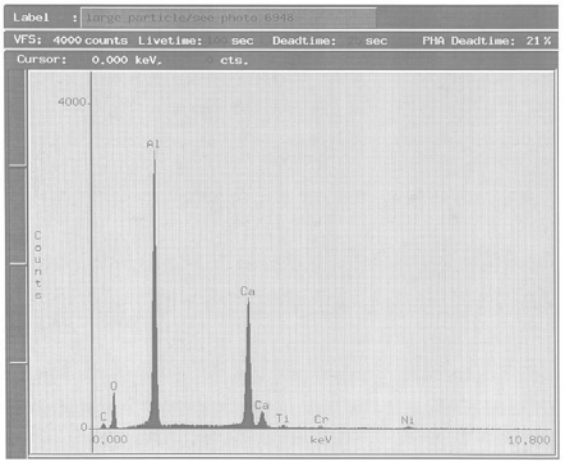

Ni Billet Indication # 1 – SEM analysis performed at slice 0.839”

Inco 718 triple melt
Location 2 – “white specks in large particle”

Tue Jan 2 13:25:08 2001

white specks in large particles/6948

Refit _Nb-L' _Nb-L" _Cr-K' _Cr-K" _Fe-K' _Fe-K" _Ni-K' _Ni-K" _Mo-L' _Mo-L" _Si-
Refit _Si-K _Fe-L _Ni-L _O -K'
Filter Fit Method
Chi-sqd = 1.34 Livetime = 100.0 Sec.
Standardless Analysis

Element	Relative k-ratio	Error (1-Sigma)	Net Counts	Error (1-Sigma)
Nb-L	0.00338	+/- 0.00191	152	+/- 86
Ti-K	0.15029	+/- 0.00336	5547	+/- 124
Cr-K	0.00654	+/- 0.00125	194	+/- 37
Fe-K	0.00394	+/- 0.00181	90	+/- 41
Ni-K	0.02423	+/- 0.00276	405	+/- 46
Mo-L	0.00103	+/- 0.00200	45	+/- 88
Al-K	0.22426	+/- 0.00193	18393	+/- 158
Si-K	0.00000	+/- 0.00001	0	+/- 0
Fe-L	---	---	0	+/- 0
Ni-L	---	---	0	+/- 0
C -K	---	---	464	+/- 28
O -K	---	---	2331	+/- 52
Ca-K	0.58633	+/- 0.00550	27704	+/- 260

Adjustment Factors	K	L	M
Z-Balance:	0.00000	0.00000	0.00000
Shell:	1.00000	1.00000	1.00000

PROZA Correction Acc.Volt.= 20 kV Take-off Angle=35.00 deg
Number of Iterations = 4

Element	k-ratio (calc.)	ZAF	Atom %	Element Wt %	Wt % Err. (1-Sigma)
Nb-L	0.0028	1.396	0.15	0.39	+/- 0.22
Ti-K	0.1247	1.309	12.37	16.32	+/- 0.36
Cr-K	0.0054	1.259	0.48	0.68	+/- 0.13
Fe-K	0.0033	1.188	0.25	0.39	+/- 0.18
Ni-K	0.0201	1.137	1.41	2.28	+/- 0.26
Mo-L	0.0009	1.341	0.04	0.11	+/- 0.22
Al-K	0.1860	1.588	39.75	29.54	+/- 0.25
Si-K	0.0000	1.730	0.00	0.00	+/- 0.00
Ca-K	0.4863	1.034	45.55	50.28	+/- 0.47
Total			100.00	100.00	

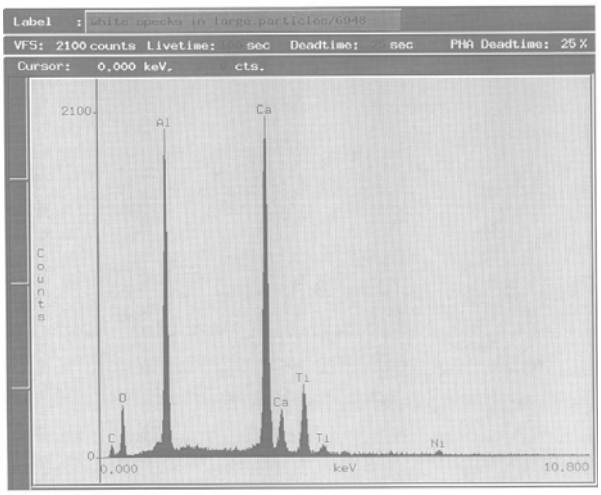

Ni Billet Indication # 1 – SEM analysis performed at slice 0.839”

Inco 718 triple melt
Location 3 – “general area”

Tue Jan 2 13:33:01 2001

general area in defect/photo 6948

Refit _Nb-L' _Nb-L" _Mo-L' _Mo-L" _Si-K' _Si-K" _Fe-L' _Fe-L"
Refit _Cr-K" _Fe-K' _Si-K _Fe-L _Ni-L' _C -K' _O -K'
Filter Fit Method
Chi-sqd = 1.52 Livetime = 100.0 Sec.
Standardless Analysis

Element	Relative k-ratio	Error (1-Sigma)	Net Counts	Error (1-Sigma)
Nb-L	0.01395	+/- 0.00202	628	+/- 91
Ti-K	0.02921	+/- 0.00223	1077	+/- 82
Cr-K	0.06085	+/- 0.00206	1801	+/- 61
Fe-K	0.05682	+/- 0.00488	1283	+/- 110
Ni-K	0.17441	+/- 0.00793	2904	+/- 132
Mo-L	0.01006	+/- 0.00222	432	+/- 95
Al-K	0.28156	+/- 0.00212	23056	+/- 174
Si-K	0.00000	+/- 0.00001	0	+/- 0
Fe-L	---	---	0	+/- 0
Ni-L	---	---	548	+/- 54
C -K	---	---	307	+/- 24
O -K	---	---	3198	+/- 57
Ca-K	0.37314	+/- 0.00445	17604	+/- 210

Adjustment Factors	K	L	M
Z-Balance:	0.00000	0.00000	0.00000
Shell:	1.00000	1.00000	1.00000

PROZA Correction Acc.Volt.= 20 kV Take-off Angle=35.00 deg
Number of Iterations = 4

Element	k-ratio (calc.)	ZAF	Atom %	Element Wt %	Wt % Err. (1-Sigma)
Nb-L	0.0107	1.569	0.66	1.68	+/- 0.24
Ti-K	0.0224	1.234	2.12	2.76	+/- 0.21
Cr-K	0.0467	1.160	3.82	5.42	+/- 0.18
Fe-K	0.0436	1.119	3.21	4.88	+/- 0.42
Ni-K	0.1338	1.113	9.31	14.89	+/- 0.68
Mo-L	0.0077	1.492	0.44	1.15	+/- 0.25
Al-K	0.2160	1.776	52.19	38.37	+/- 0.29
Si-K	0.0000	2.031	0.00	0.00	+/- 0.00
Ca-K	0.2863	1.078	28.25	30.86	+/- 0.37
Total			100.00	100.00	

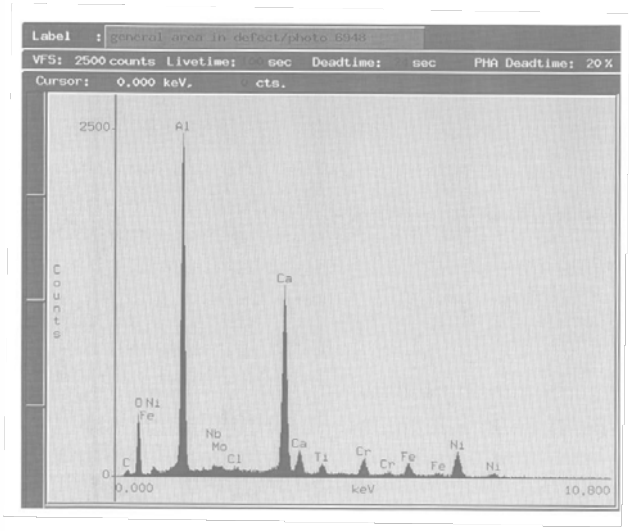

Ni Billet Indication #2 – General Information

- Found in 10" triple melt Inconel 718 billet
- Amplitude was 80% plus 2.5 dB with a #2 FBH equal to 80%
- Depth was 2.7" and the length was 0.375 " in billet.
- Indication determined to be entrapped slag

Ni Billet Indication # 2 – Ultrasonic Measurements

Cube Information

- Dimension close to 1” cube with error around 20 mils all sides.
- UT scans were performed at ISU using a Utex WinSpect system.
- UT data include single A-scans at peak positions, C-scan images, and volumetric A-scans at C-scan scan grids using both 5 and 15 MHz transducers.
- Additional A-scans were obtained from fused quartz block as reference waveforms.

Billet/Cube Orientation

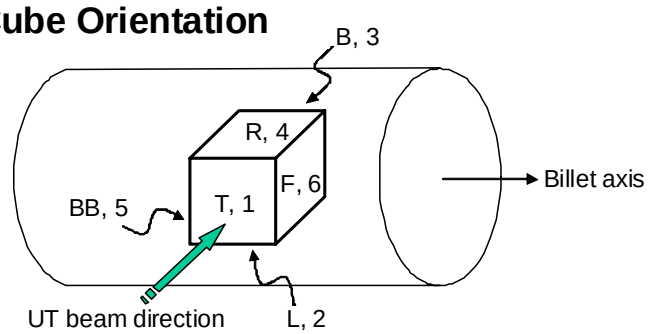

Ni Billet Indication # 2 – Ultrasonic Measurements

Cube UT Scan Information

Transducers:

PB: Panametrics V319 15MHz/0.5” dia. 90mm PTF;
P2: Panametrics V307 5MHz/1.0” dia. 8” PTF

Scan Parameters:

All scan files used 250 MHz sampling rate, 1 ms gate width and 4 time averages.
P2 files are 71x71 pixels (scan positions) at 10 mils spatial increment.
PB files are 141x141 pixels (scan positions) at 5 mils spatial increment.

Ni Billet Indication # 2 – Ultrasonic Measurements

P2 (5MHz) C-scan Images

Sides 5 and 6 were masked by P2’s internal structure in time trace

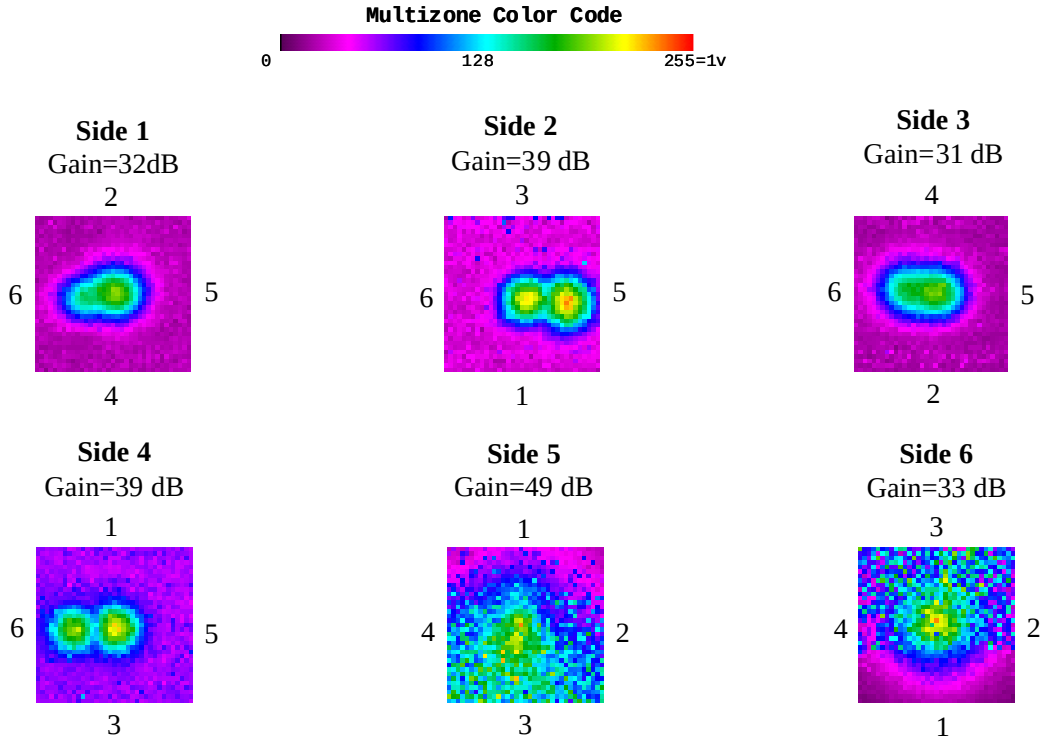

Ni Billet Indication # 2 – Ultrasonic Measurements

PB (15MHz) C-scan Images

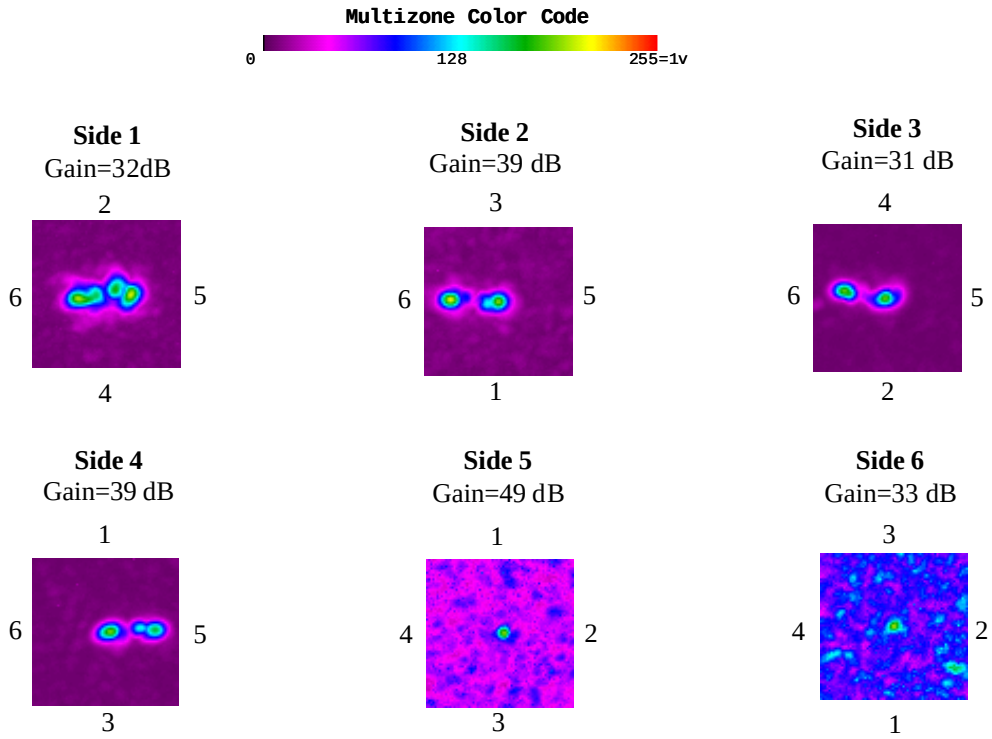

Ni Billet Indication # 2 – 100X composite micrograph

Slice 1

Slice 2

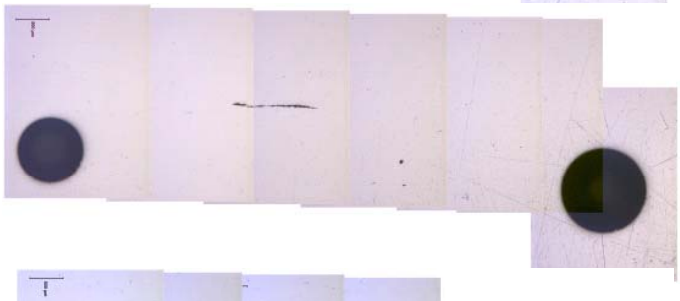

500 µm

Slice 3

Slice 4

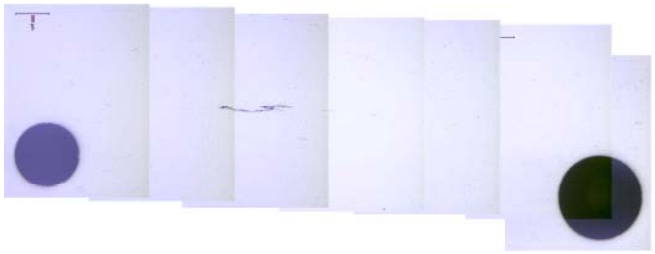

Slice 5

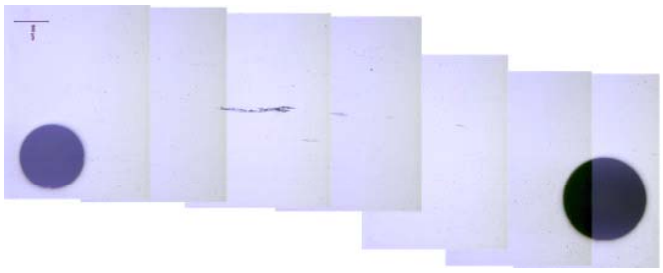

500 µm

Slice 6

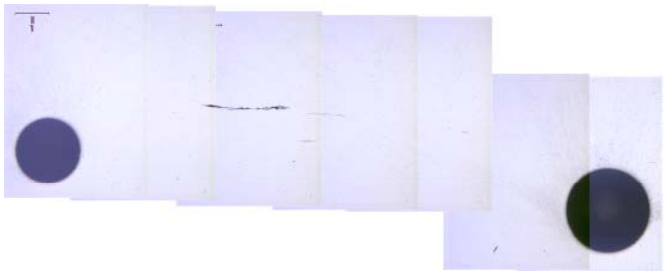

Ni Billet Indication # 2 – 100X composite micrograph

Slice 7

Slice 8

500 µm

Slice 9

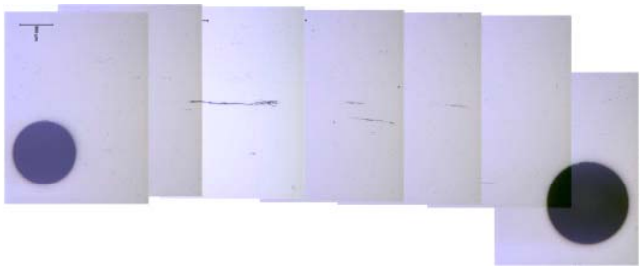

Slice 10

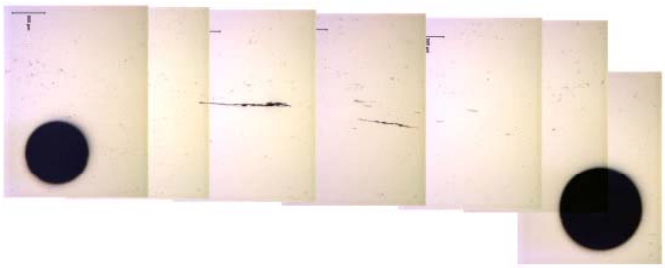

Slice 11

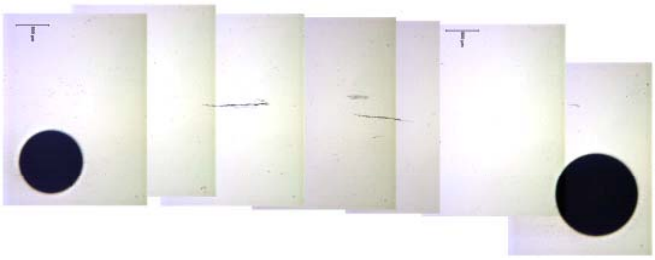

Slice 12

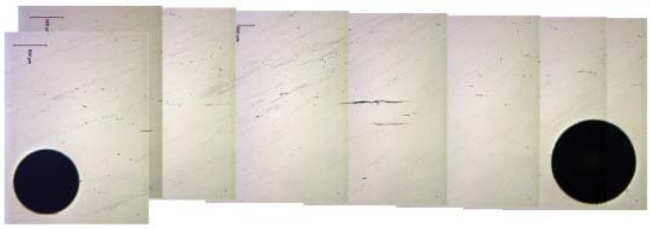

Ni Billet Indication # 2 – 100X composite micrograph

Slice 13

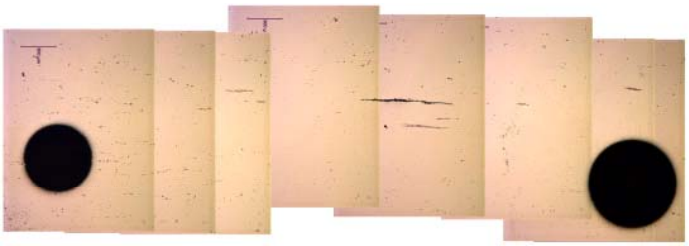

Slice 14

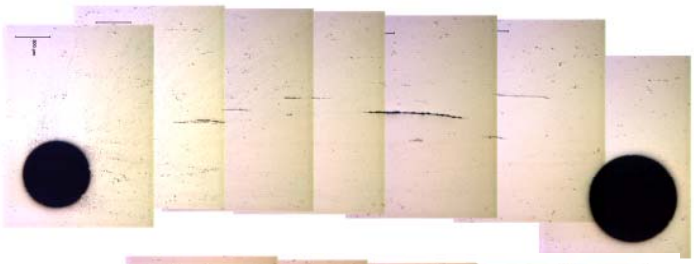

500 µm

Slice 15

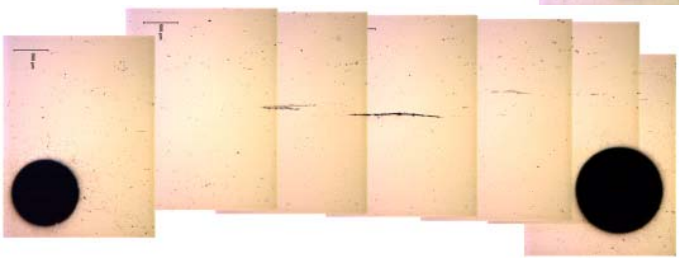

Slice 16

Slice 17

Slice 18

Ni Billet Indication # 2 – 100X composite micrograph

Slice 19

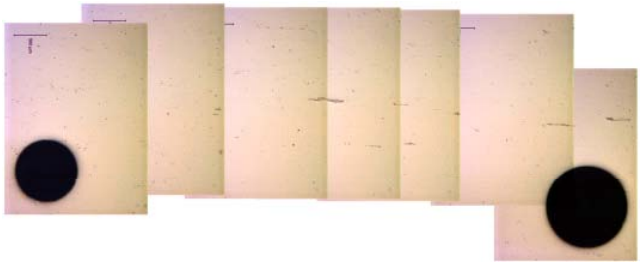

Slice 20

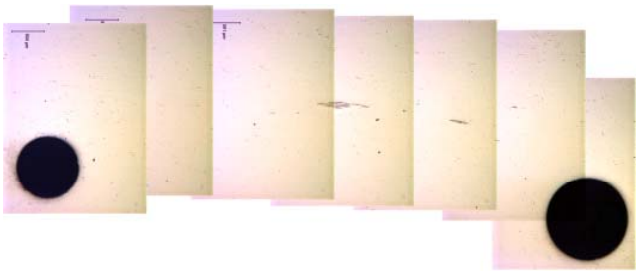

500 µm

Slice 21

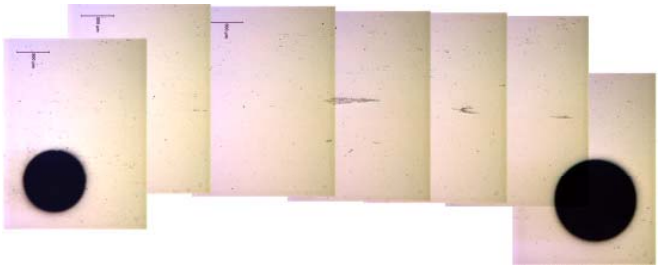

Slice 22

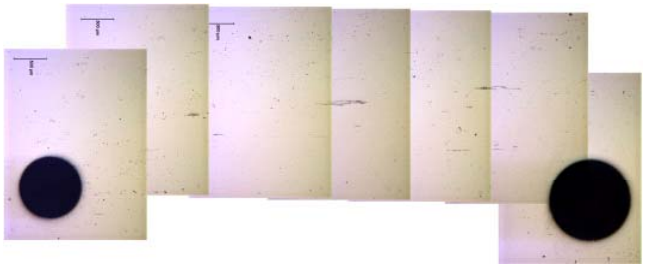

Slice 23

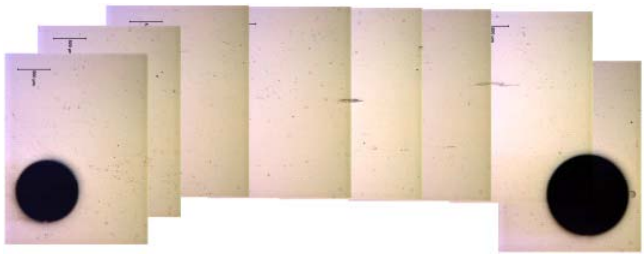

Slice 24

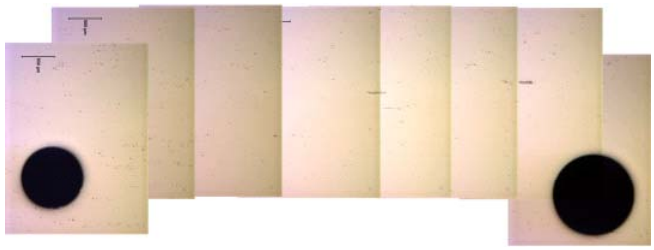

Ni Billet Indication # 2 – 100X composite micrograph

Slice 25

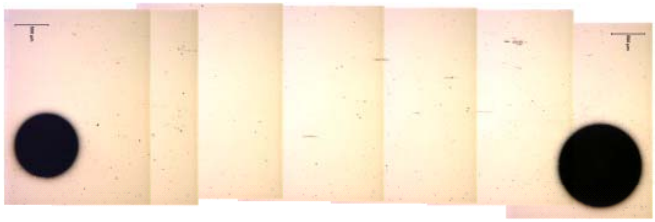

Slice 26

500 µm

Slice 27

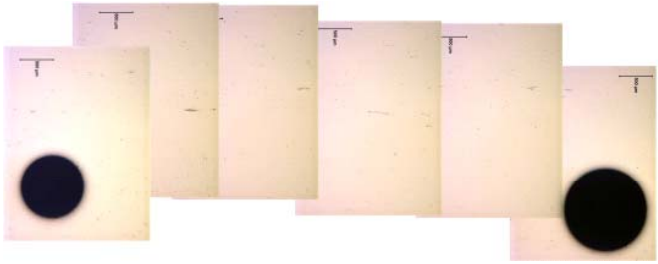

Slice 28

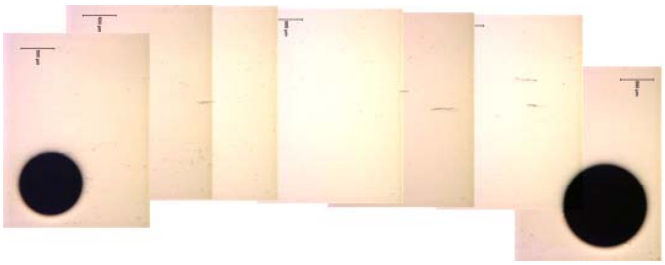

Slice 29

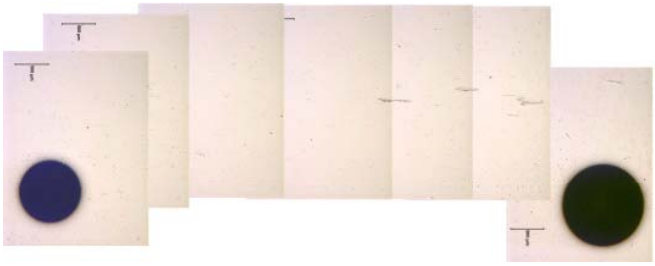

Slice 30

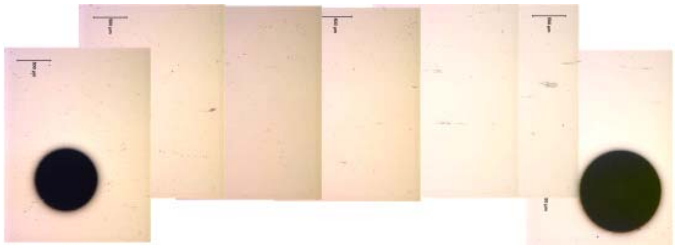

Ni Billet Indication # 2 – 100X composite micrograph

Slice 31

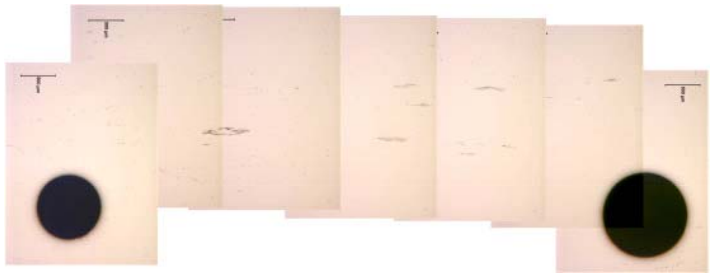

Slice 32

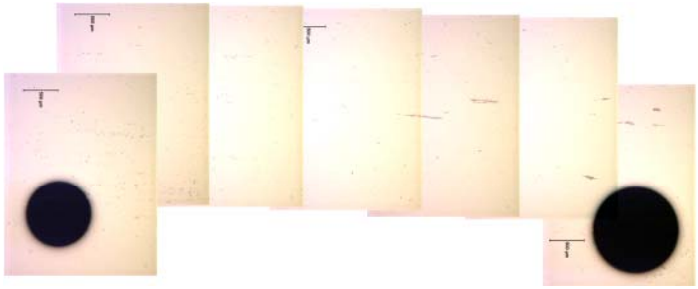

500 µm

Slice 33 **No indication present**

Slice 34

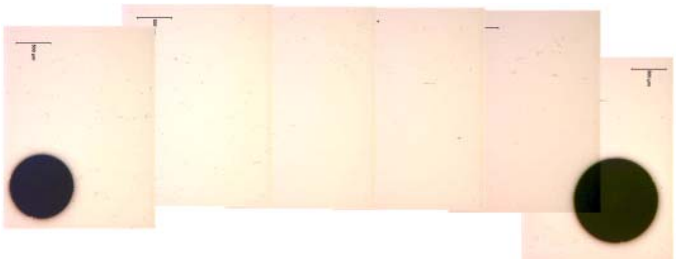

Slice 35

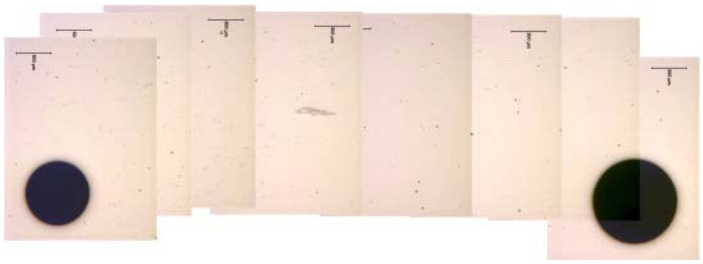

Slice 36

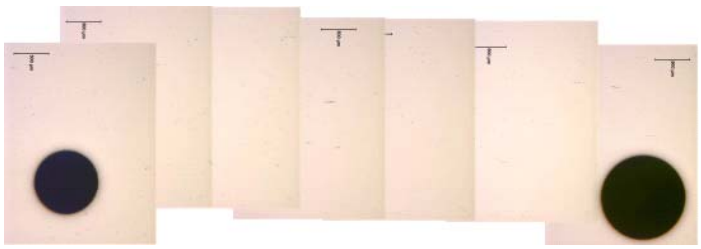

Ni Billet Indication # 2 – 100X composite micrograph

Slice 37 **No indication present**

Slice 38 **No indication present**

500 µm

Slice 39

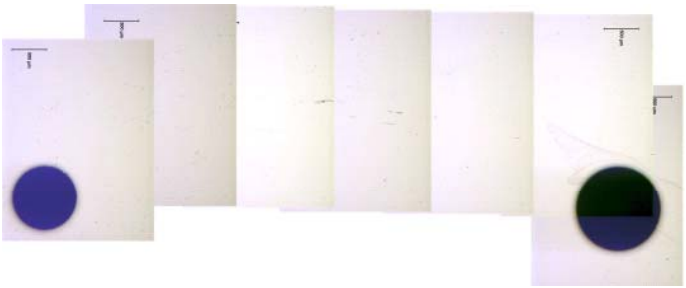

Ni Billet Indication # 2 – SEM analysis

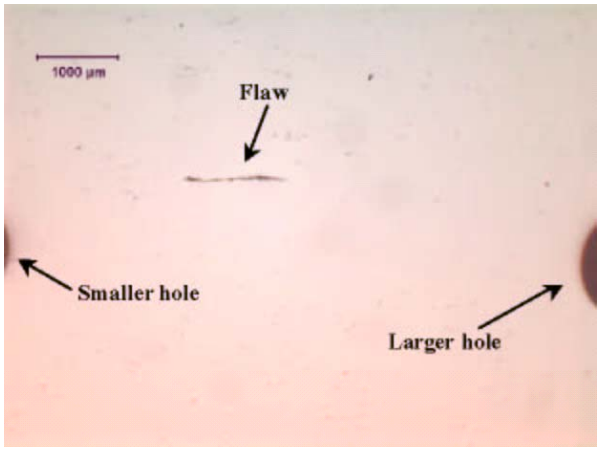

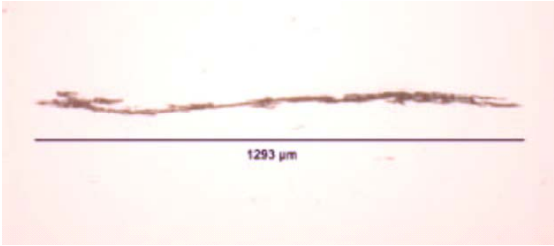

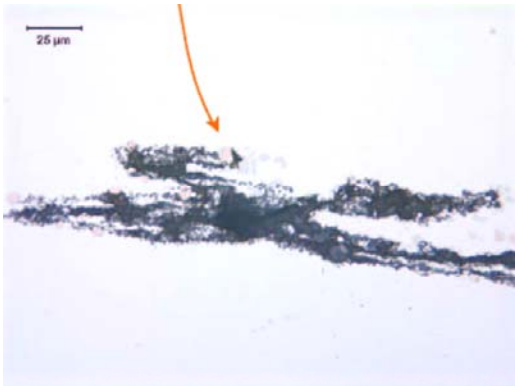

Ni Billet Indication # 2 – SEM analysis

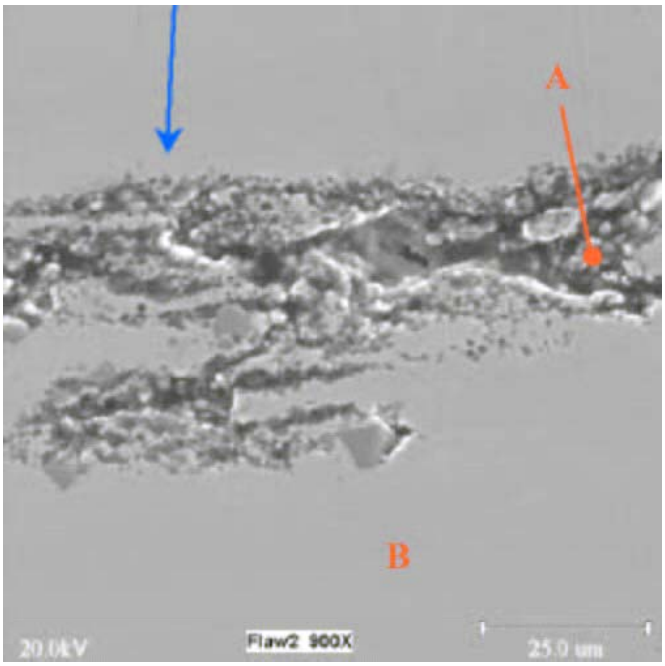

Ni Billet Indication # 2 – SEM analysis

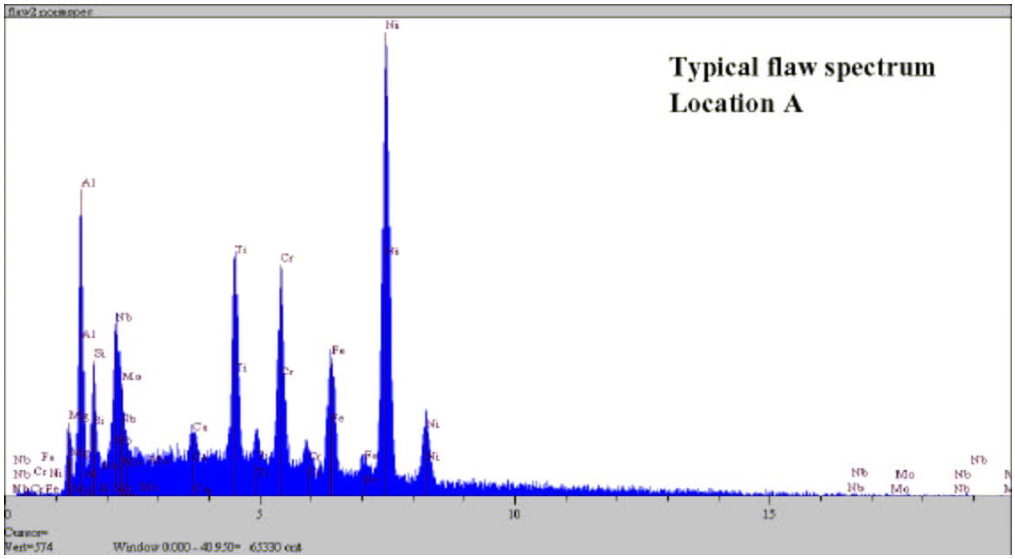

Ni Billet Indication # 2 – SEM analysis

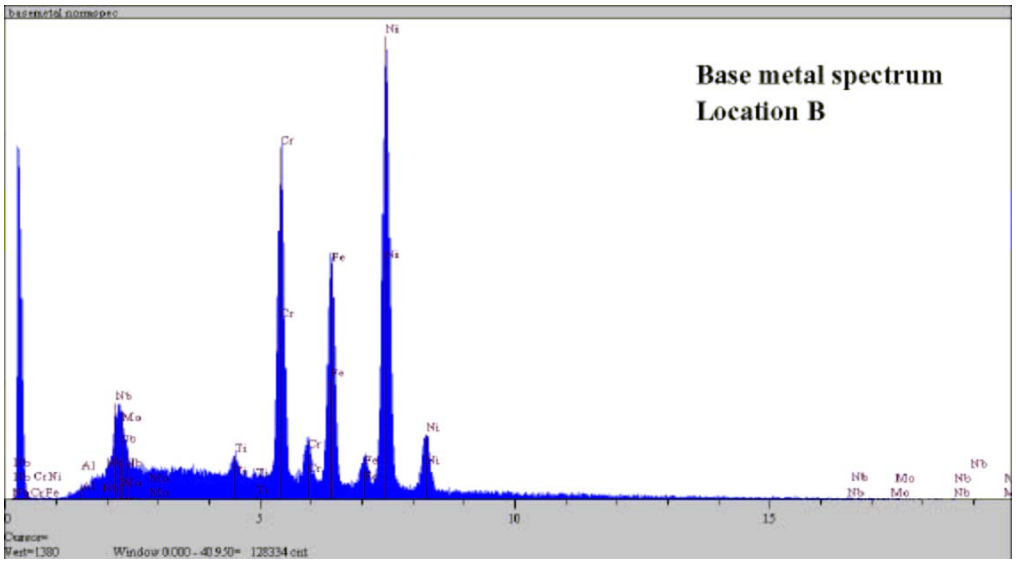

Ni Billet Indication # 2 – SEM analysis

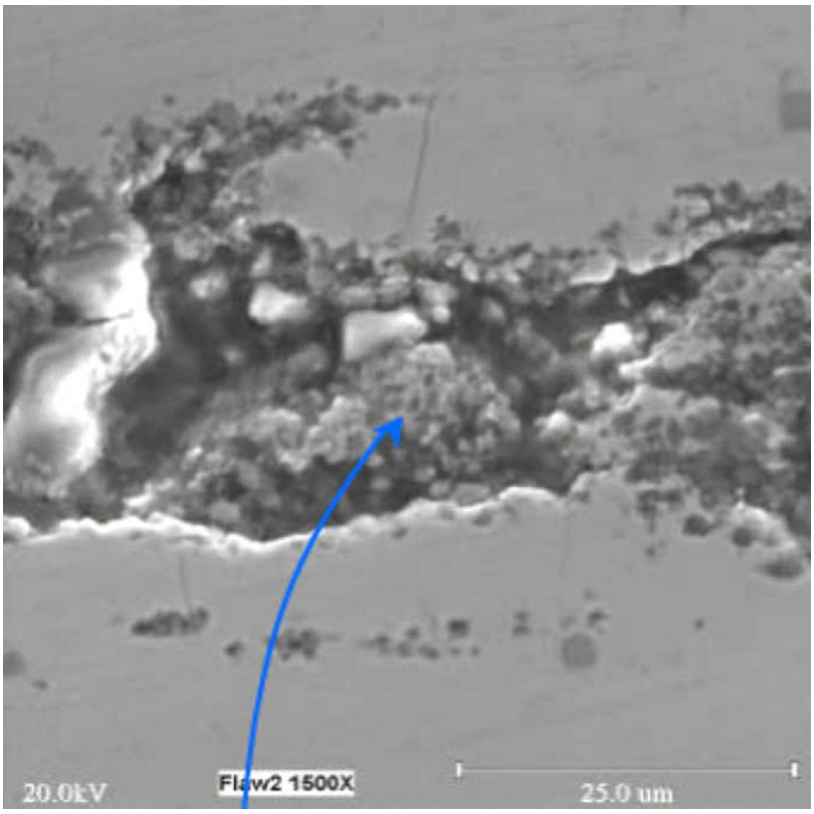

Location C

Ni Billet Indication # 2 – SEM analysis

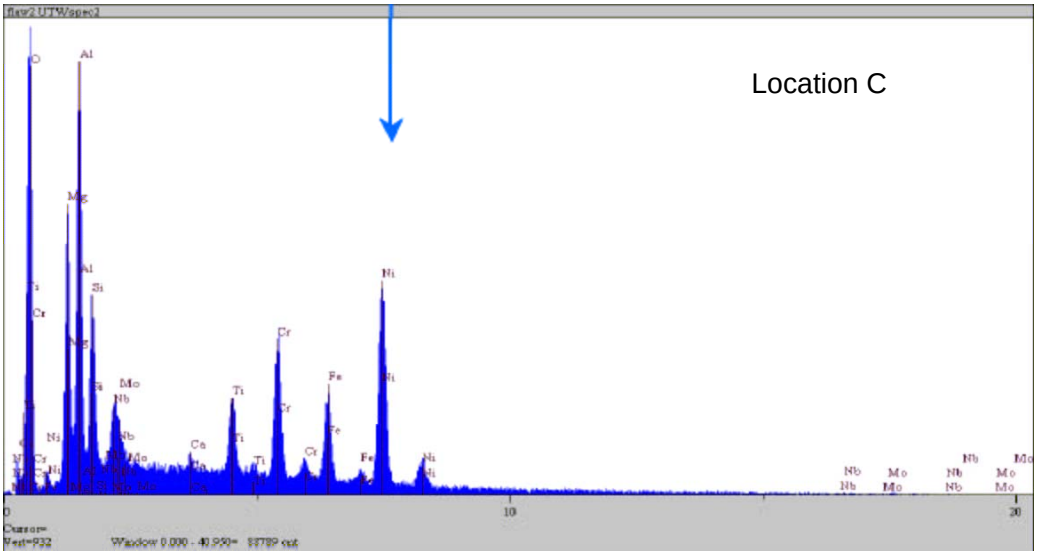

Ni Billet Indication #3 – General Information

- **Billet:** double melt 718, 10” diameter
- **Calibration:** #3 flat-bottom hole at 80% of full screen height
- **Indication Amplitude:** 80% of full screen height
- **Depth:** 5.265”
- **Length:** 0.35”
- **Source:** Dirty white spot

Ni Billet Indication # 3 – Sectioning and naming convention

Cube Block Orientation and Naming System

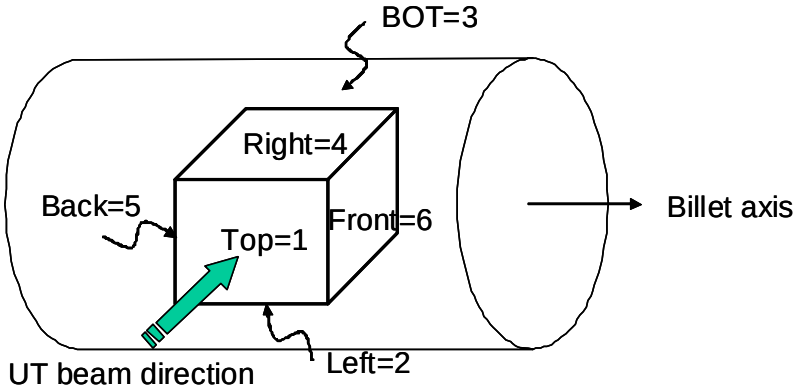

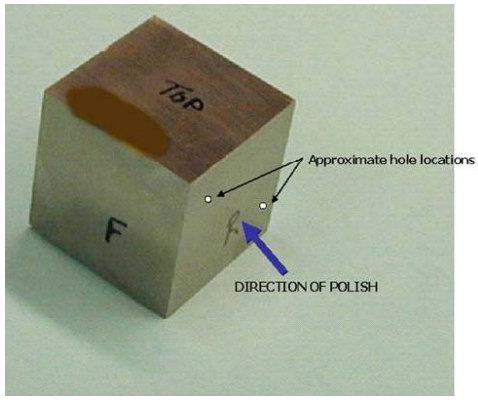

Ni Billet Indication # 3 – Ultrasonic Measurements

C-scan Images

50 MHz

Side 1

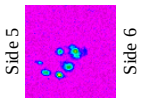

0.4" X 0.4"
Gain=35 dB

Side 3

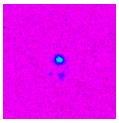

0.5" X 0.5"
Gain=34 dB

15 MHz

Side 1

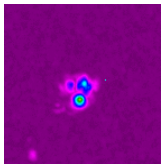

0.7" X 0.7"
Gain=26 dB

Side 2

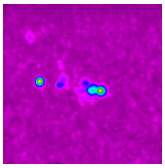

0.7" X 0.7"
Gain=34 dB

Side 3

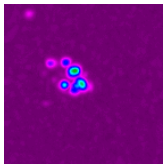

0.7" X 0.7"
Gain=22 dB

Side 4

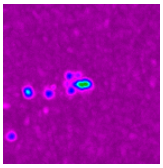

0.7" X 0.7"
Gain=32 dB

Side 5

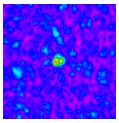

0.5" X 0.5"
Gain=45 dB

Side 6

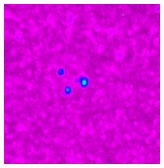

0.7" X 0.7"
Gain=37 dB

Multizone Color Code

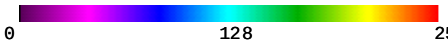

Image resolution: All are of 0.005" scan increment (in-between pixels)
Orientation: side 5 on left and side 6 on right for sides 1~4; side 2 on left and side 4 on right for sides 5~6

Ni Billet Indication # 3 – 100X composite micrograph
Sectioning occurred at 0.002” increments

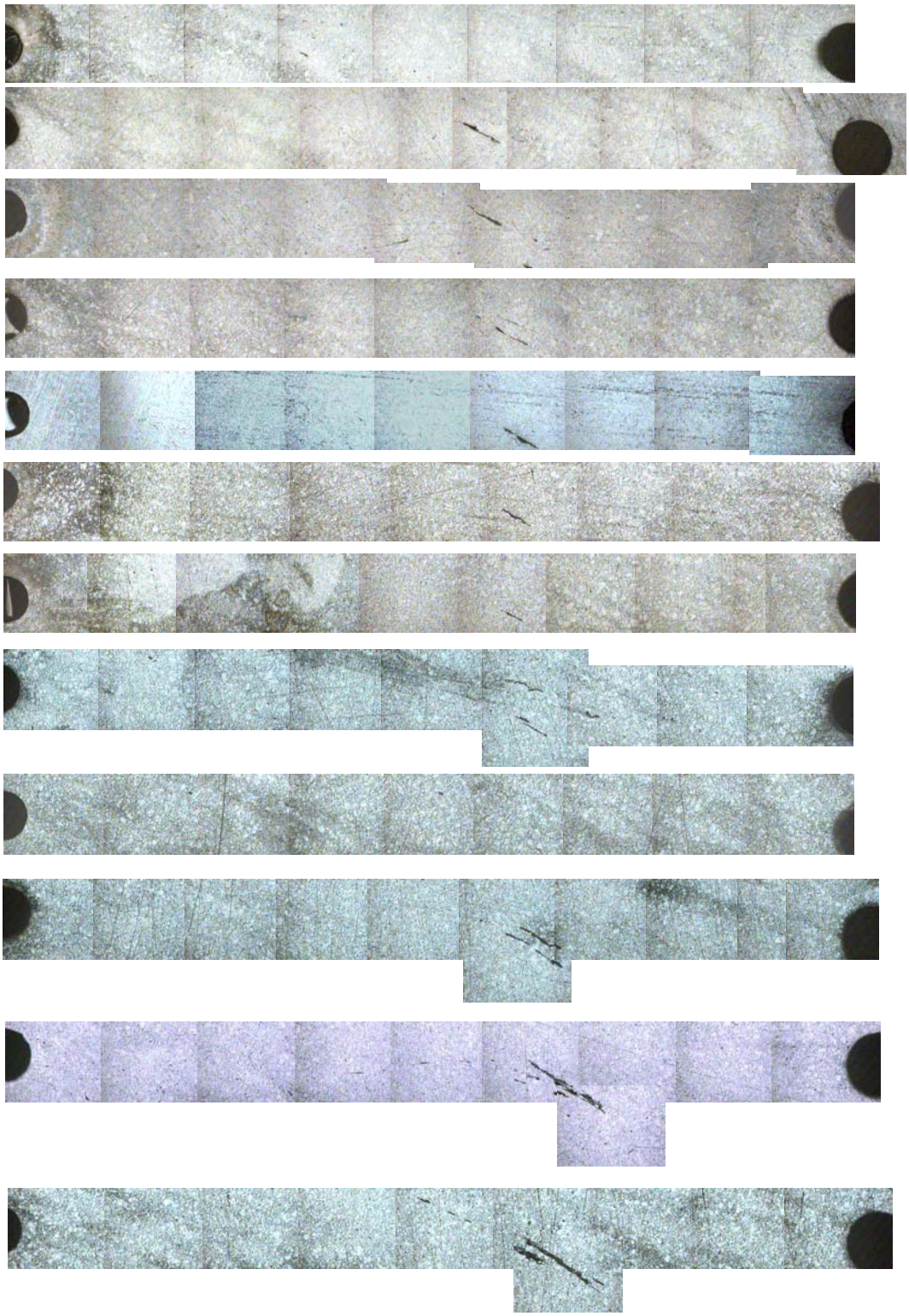

Ni Billet Indication # 3 – 100X composite micrograph
Sectioning occurred at 0.002” increments

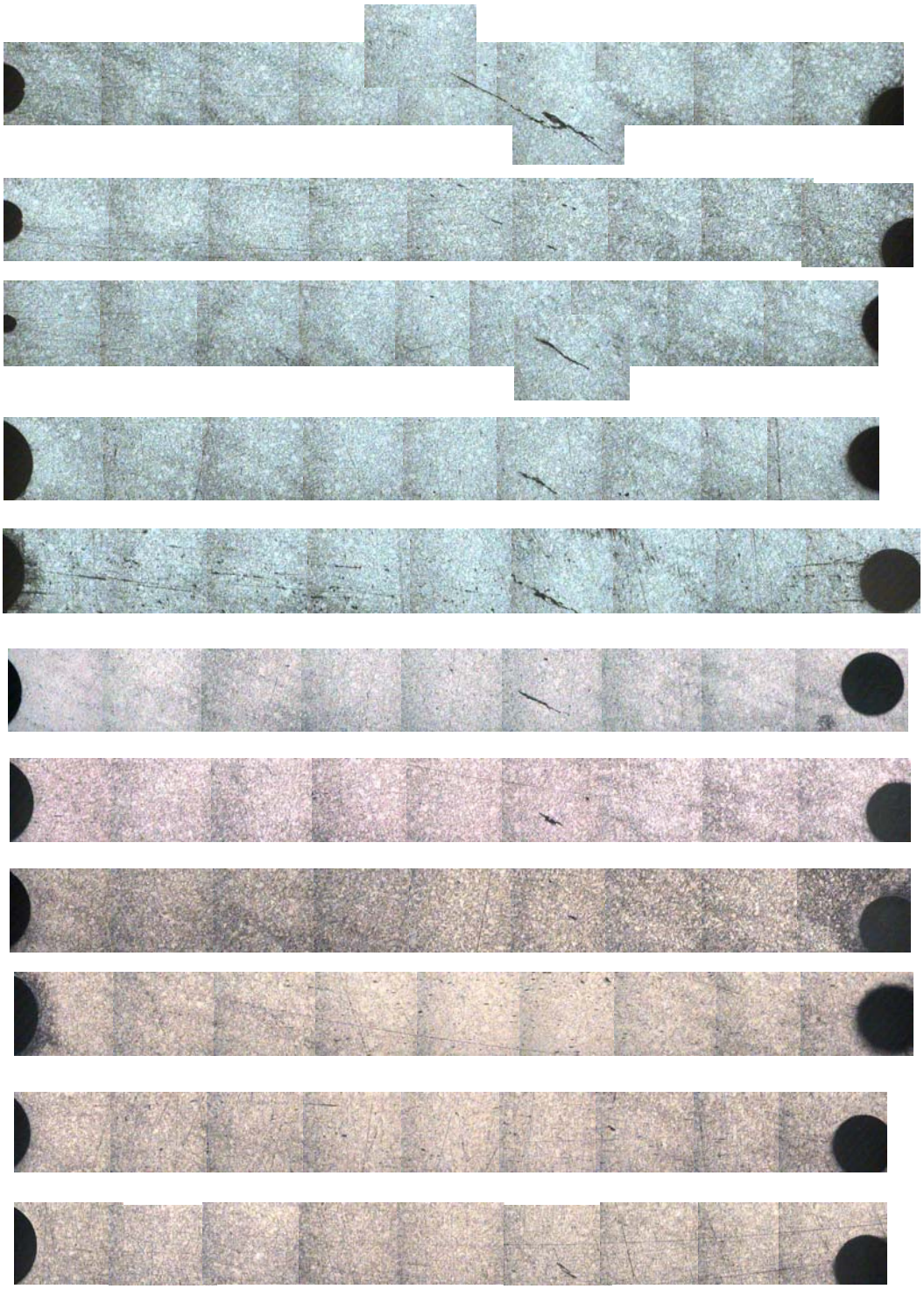

Ni Billet Indication # 3 – 100X composite micrograph
Sectioning occurred at 0.002” increments

#40

#41

#42

#43

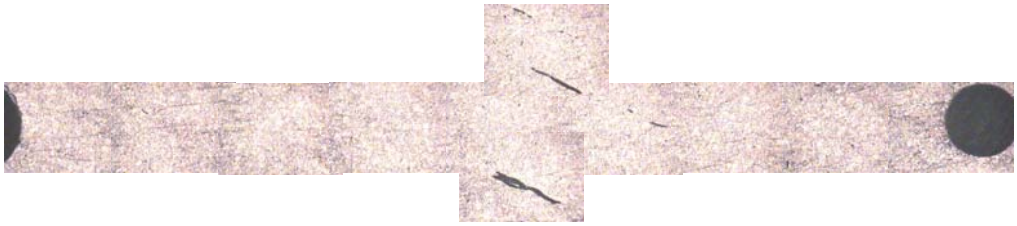

#44

#45

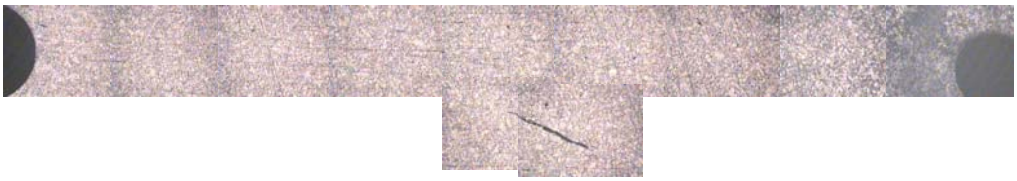

#46

#47

Ni Billet Indication # 3 – 100X composite micrograph
Sectioning occurred at 0.002” increments

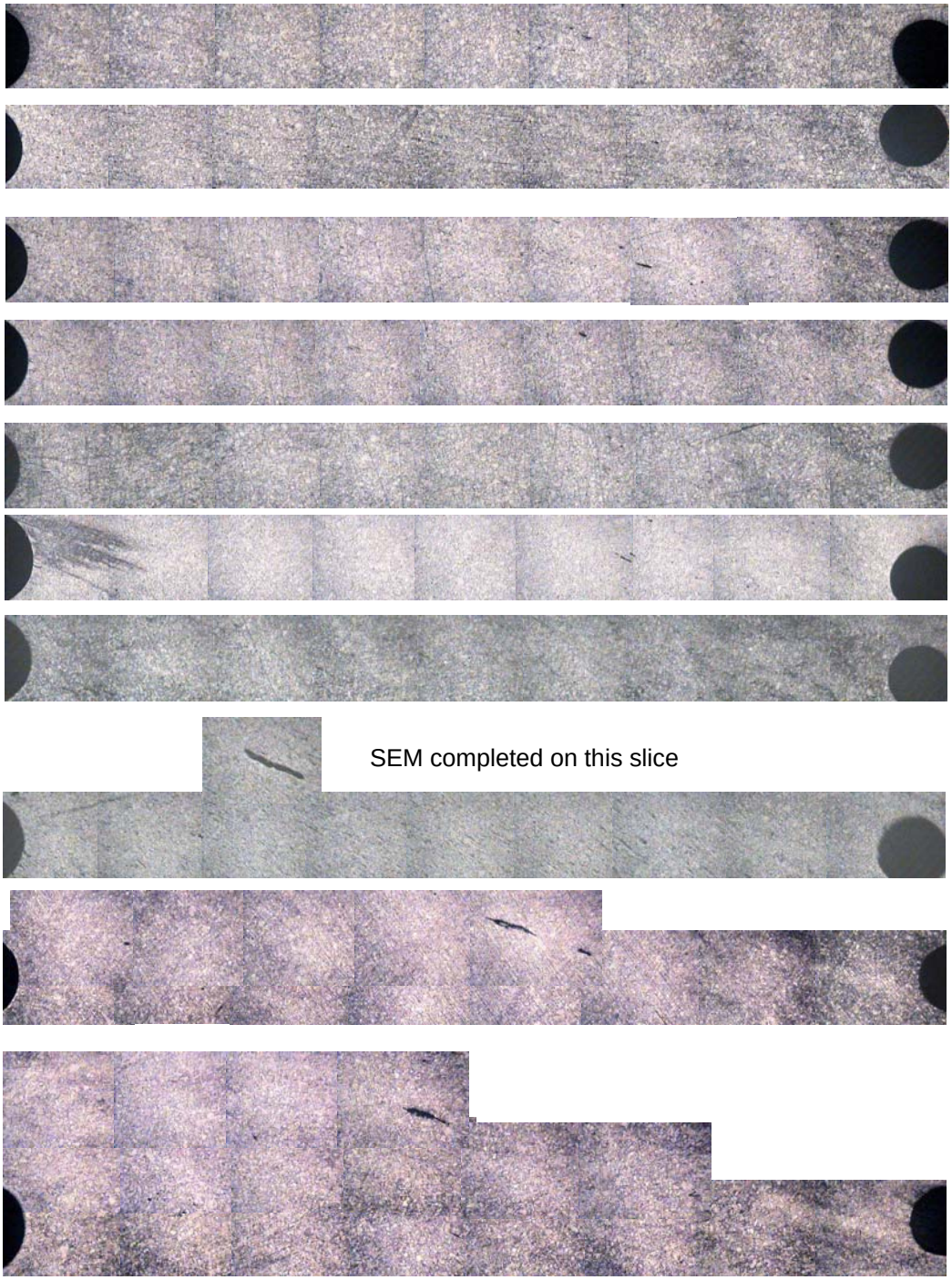

Ni Billet Indication # 3 – 100X composite micrograph
Sectioning occurred at 0.002” increments

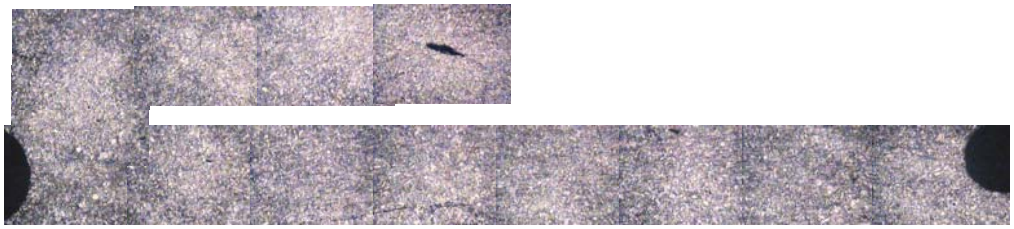

#58

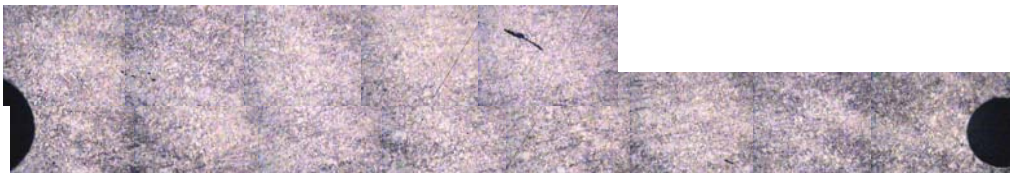

#59

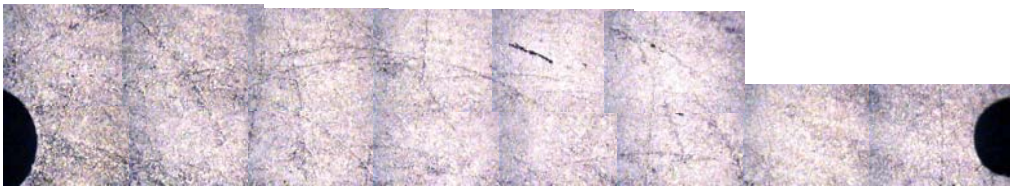

#60

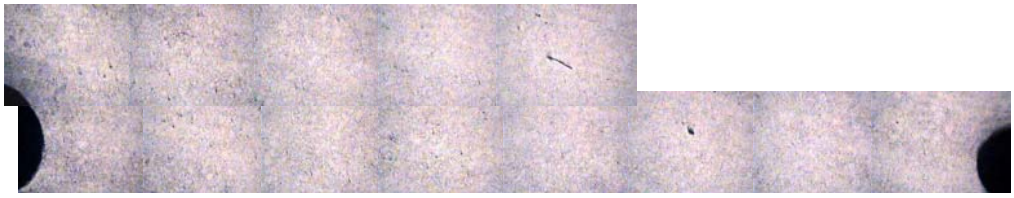

#61

#62

#63

#64

Ni Billet Indication # 3 – 100X composite micrograph
Sectioning occurred at 0.002” increments

#65

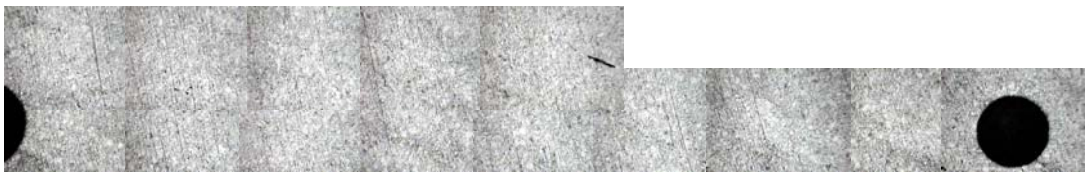

#66

#67

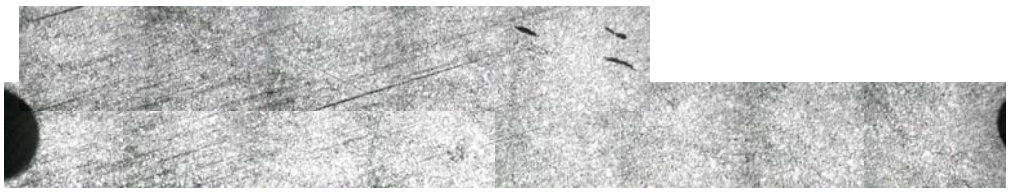

#68

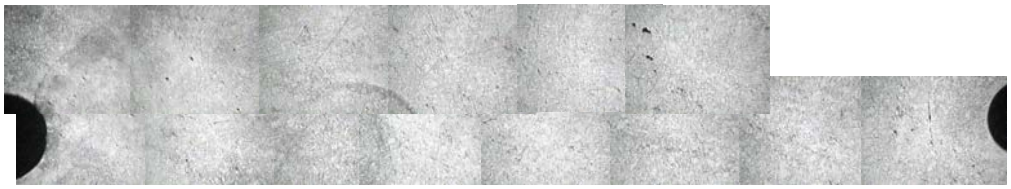

#69

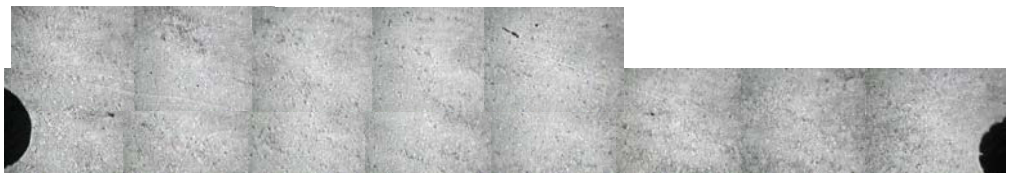

#70

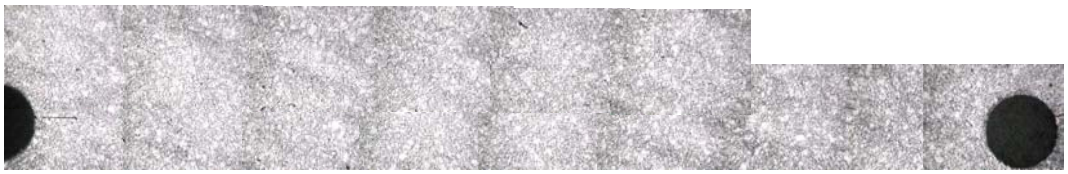

#71

Ni Billet Indication # 3 – SEM analysis performed at slice #55

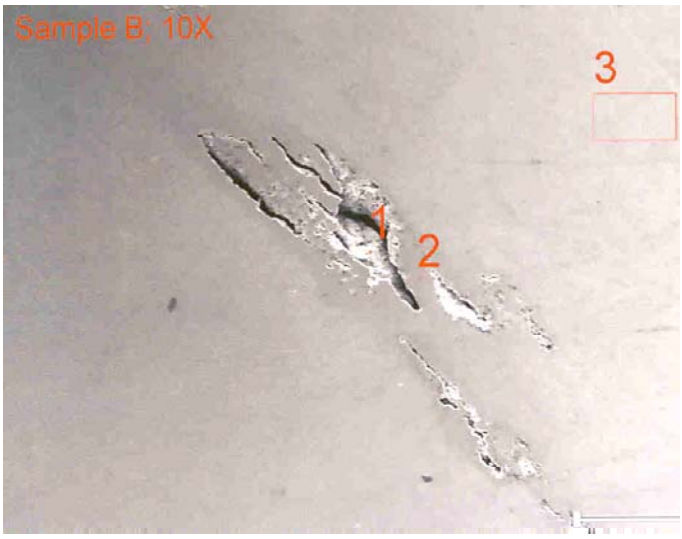

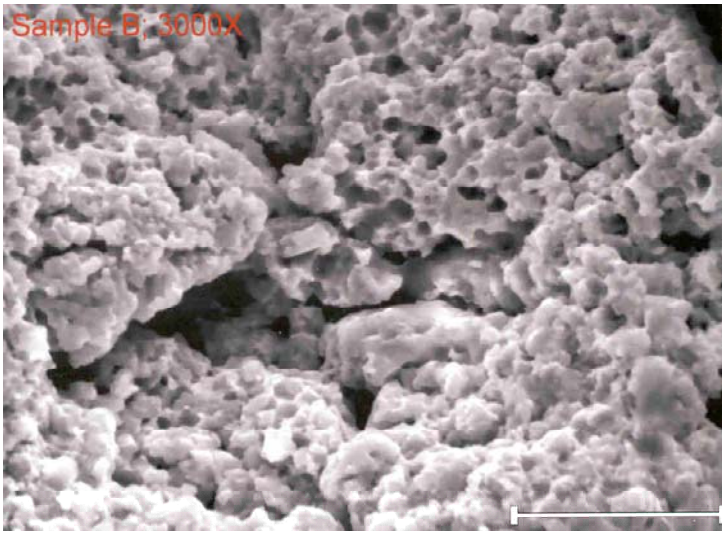

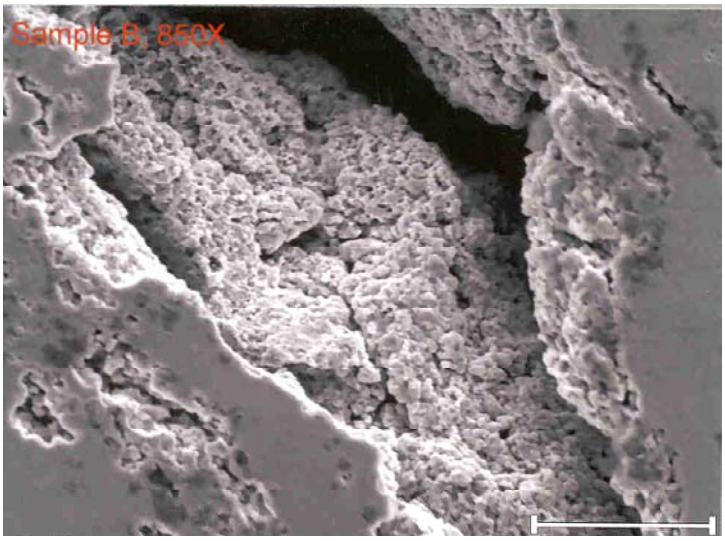

Ni Billet Indication # 3 – SEM analysis performed at slice #55

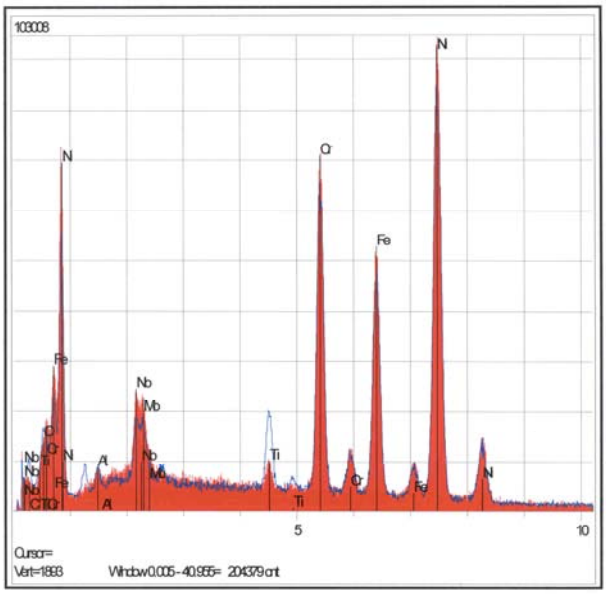

File: 103008	Job No.: 2276	Voltage: 20kV	Time: 100 Sec.

Comparison of area 1 and area 3
Base alloy away from contaminant – red
Overlay of contaminant - blue

Ni Billet Indication # 3 – SEM analysis performed at slice #55

File: 103006	Job No.: 2276	Voltage: 20kV	Time: 100 Sec.

Sample I.D: Photo 2276S001; Area 1; Contaminant

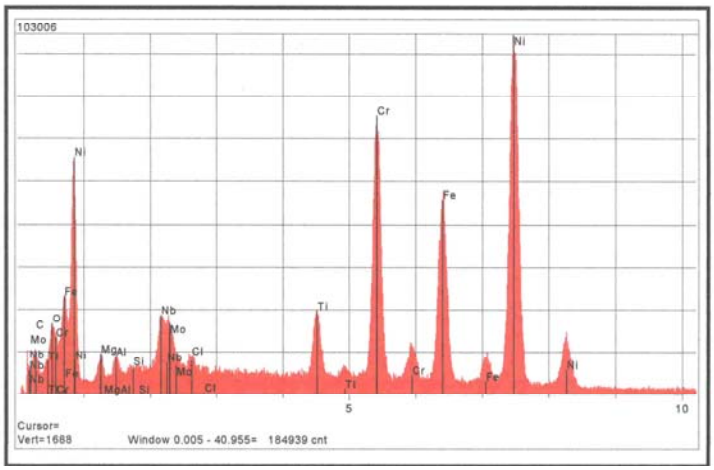

Ni Billet Indication # 3 – SEM analysis performed at slice #55

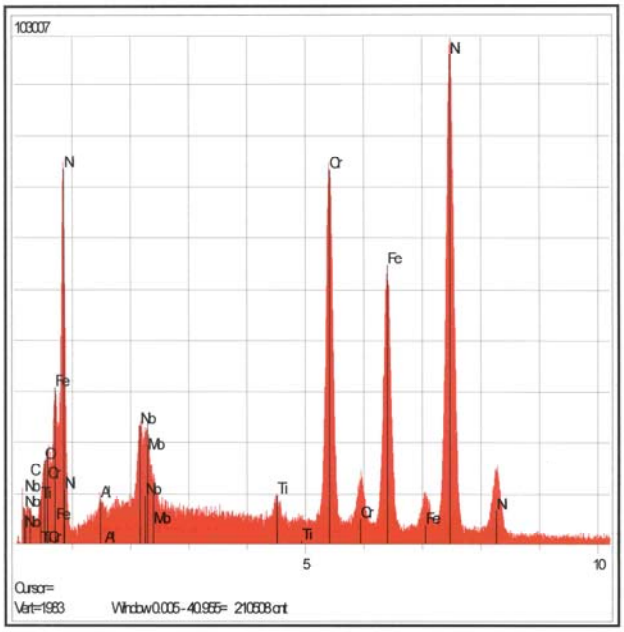

File:	103007	Job No.:	2276	Voltage:	20kV	Time:	100 Sec.

Base alloy away from contaminant – red

Ni Billet Indication # 3 – SEM analysis performed at slice #55

File:	103007	Job No.:	2276	Voltage:	20kV	Time:	100 Sec.

Sample I.D: Photo 2276S001; Area 2; Base alloy near Contaminant

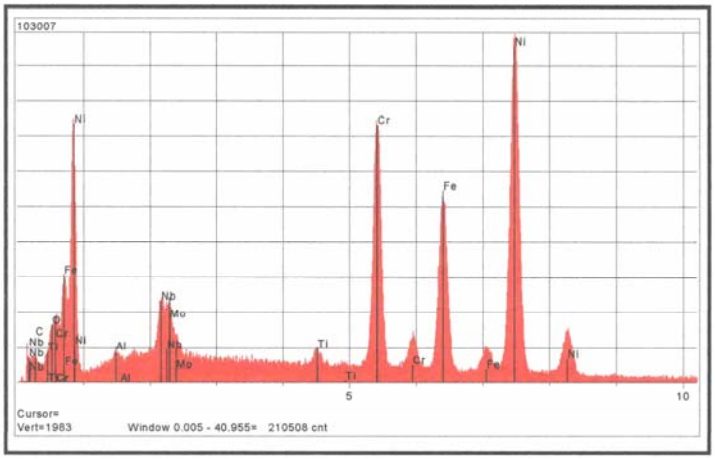

Ni Billet Indication # 3 – SEM analysis performed at slice #55

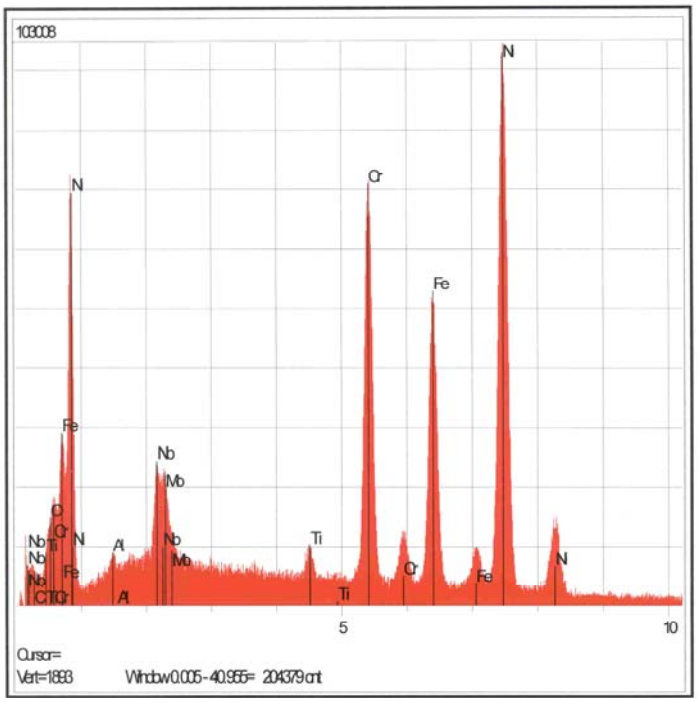

File: 103008	Job No.: 2276	Voltage: 20kV	Time: 100 Sec.

Base alloy away from contaminant – red

Ni Billet Indication # 3 – SEM analysis performed at slice #55

File: 103008	Job No.: 2276	Voltage: 20kV	Time: 100 Sec.

Sample I.D: Photo 2276S001; Area 2; Base alloy away from Contaminant

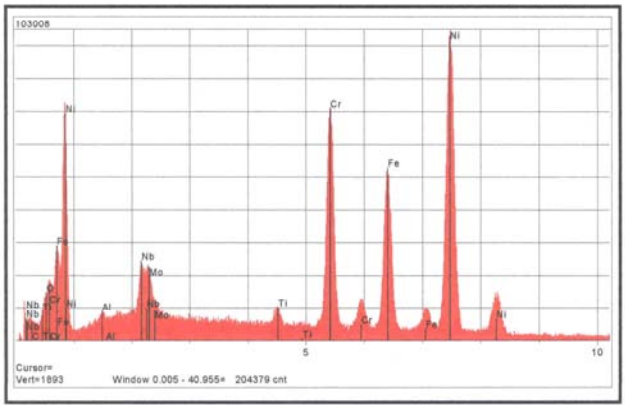

Ni Billet Indication # 3 – SEM analysis performed at slice #55

File: 103008	Job No.: 2276	Voltage: 20kV	Time: 100 Sec.

Sample I.D: Photo 2276S001; Area 3; Base alloy away from Contaminant – red overlay contaminant - blue

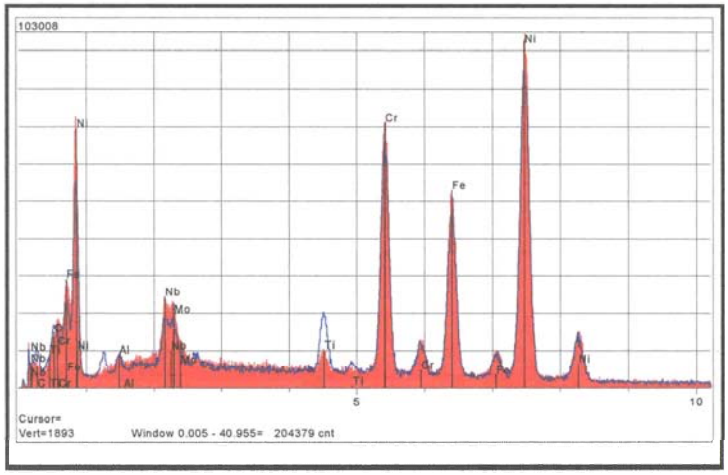

Ni Billet Indication #4 – General Information

- Alloy = Waspaloy
- Melt method = VIM-VAR (Vacuum Induction Melting followed by Vacuum Arc Remelting)
- Billet Diameter = 11”.
- Calibration was in accordance industry standards. The required flat bottom hole (FBH) size is a 5/64” diameter. Calibration reflectors were positioned at approximately 0.92” and 6.6” below the sound entry surface. These reflectors were gated and electronically DAC was used.
- Calibration amplitude = 80% of full screen height (FSH).
- Reject level = 100% of the required FBH (i.e. 80% FSH).
- Alarm threshold = 60% FSH (75% of the calibration height).
- Maximized indication amplitude = 98% FSH (122% of a #5 FBH)
- Indication length ~ 0.420” ; depth ~ 5.6”
- Transducer Information:
    a. Frequency = 3.5 MHZ
    b. Transducer Size = 0.75” by 1.0” rectangular
    c. Cylindrically Focussed at 7.00”
    d. Beam Diameter = 0.090 in cylindrical direction (scanning direction)
    e. Longitudinal Wave
    f. Water path set at 4.50”
- Indication: nonmetallic inclusion typical of Waspaloy

Ni Billet Indication #4 – Naming convention for sectioning

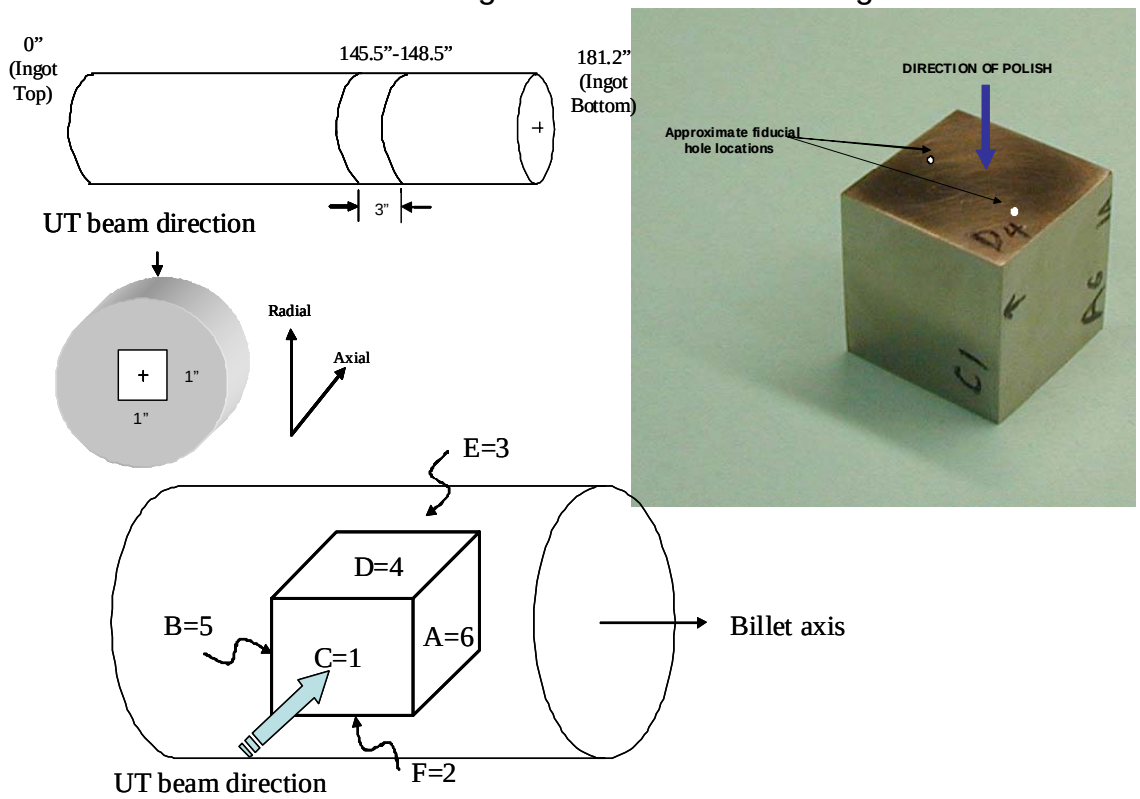

Ni Billet Indication #4 – Ultrasonic Measurements

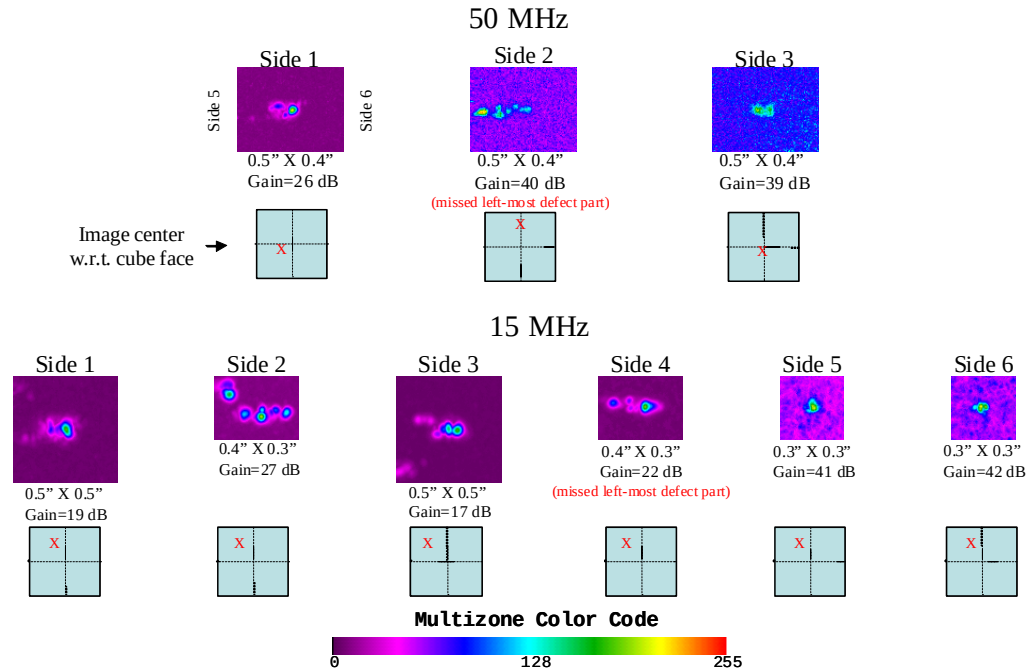

Image resolution: All are of 0.005” scan increment (in-between pixels)
Orientation: side 5 on left and side 6 on right for sides 1~4; side 2 on left and side 4 on right for sides 5~6

Ni Billet Indication #4 – Ultrasonic Measurements

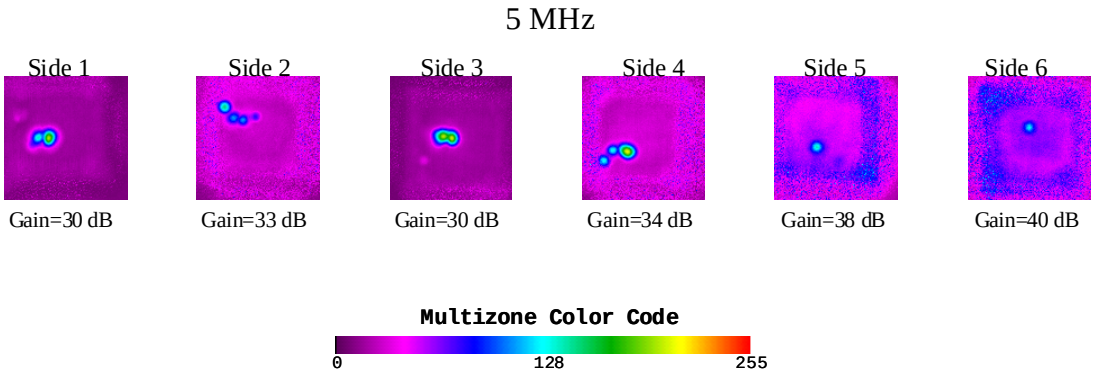

Image resolution: All are 1.1” by 1.1” of 0.01” scan increment (in-between pixels)
Orientation: side 5 on left and side 6 on right for sides 1~4; side 2 on left and side 4 on right for sides 5~6

Ni Billet Indication #4 – 100X composite micrograph
Sectioning at 0.002” increments

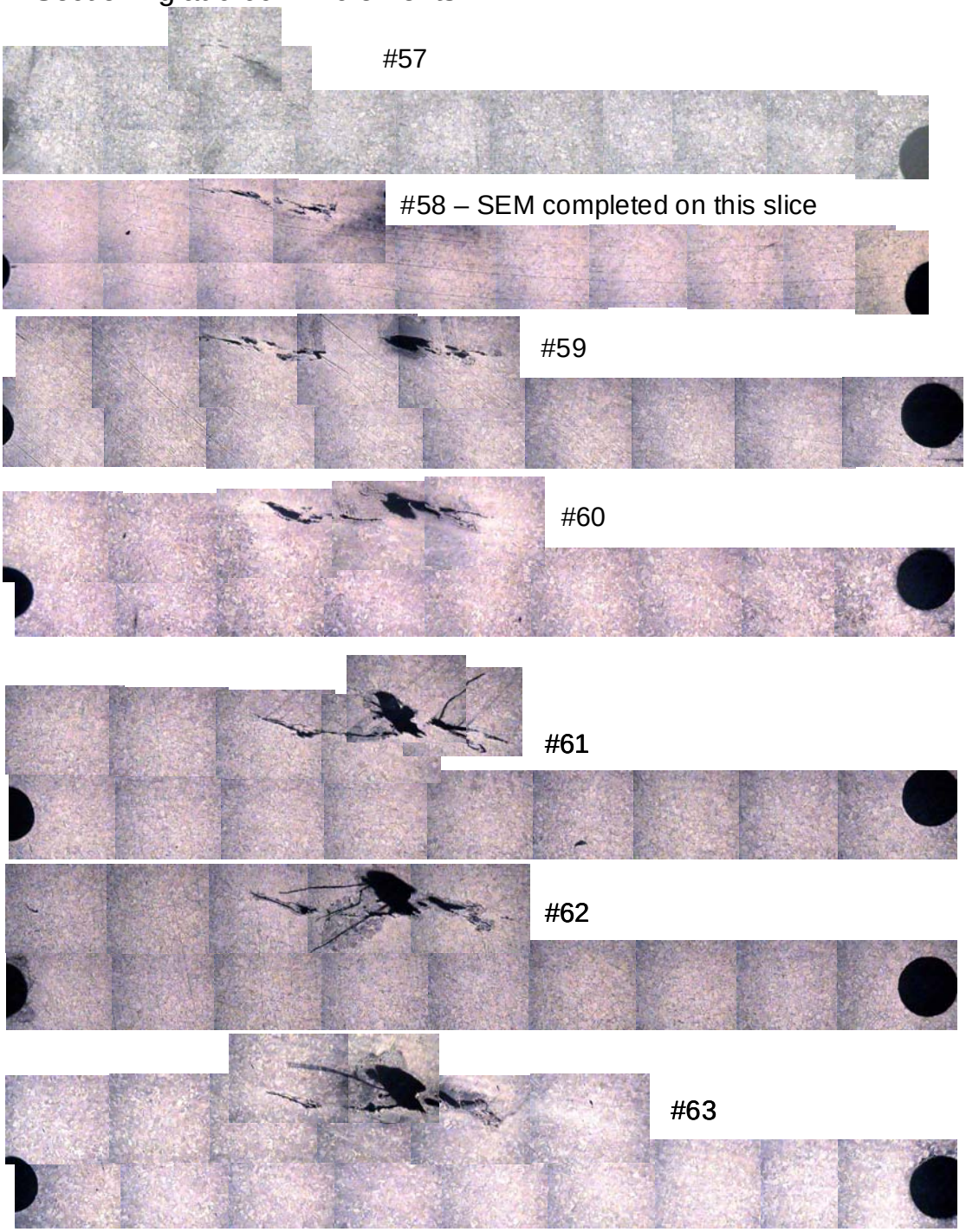

Ni Billet Indication #4 – 100X composite micrograph
Sectioning at 0.002” increments

Ni Billet Indication #4 – 100X composite micrograph
Sectioning at 0.002” increments

#70

#71

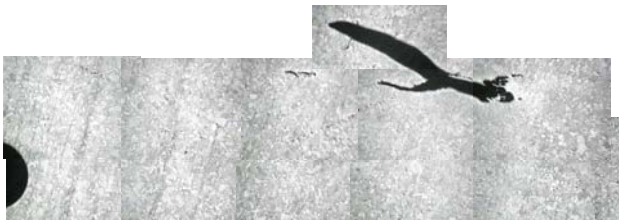

#72

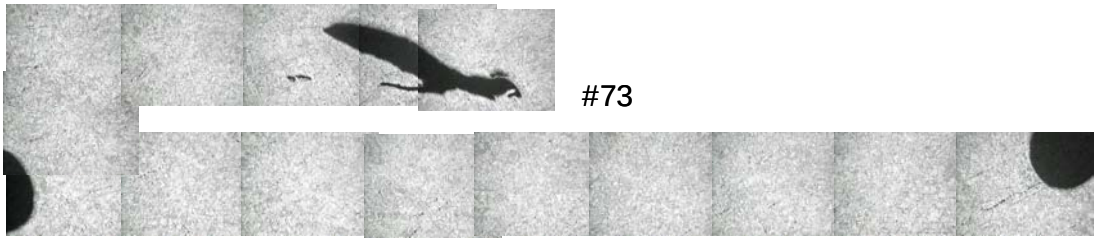

#73

#74

#75

Ni Billet Indication #4 – 100X composite micrograph
Sectioning at 0.002” increments

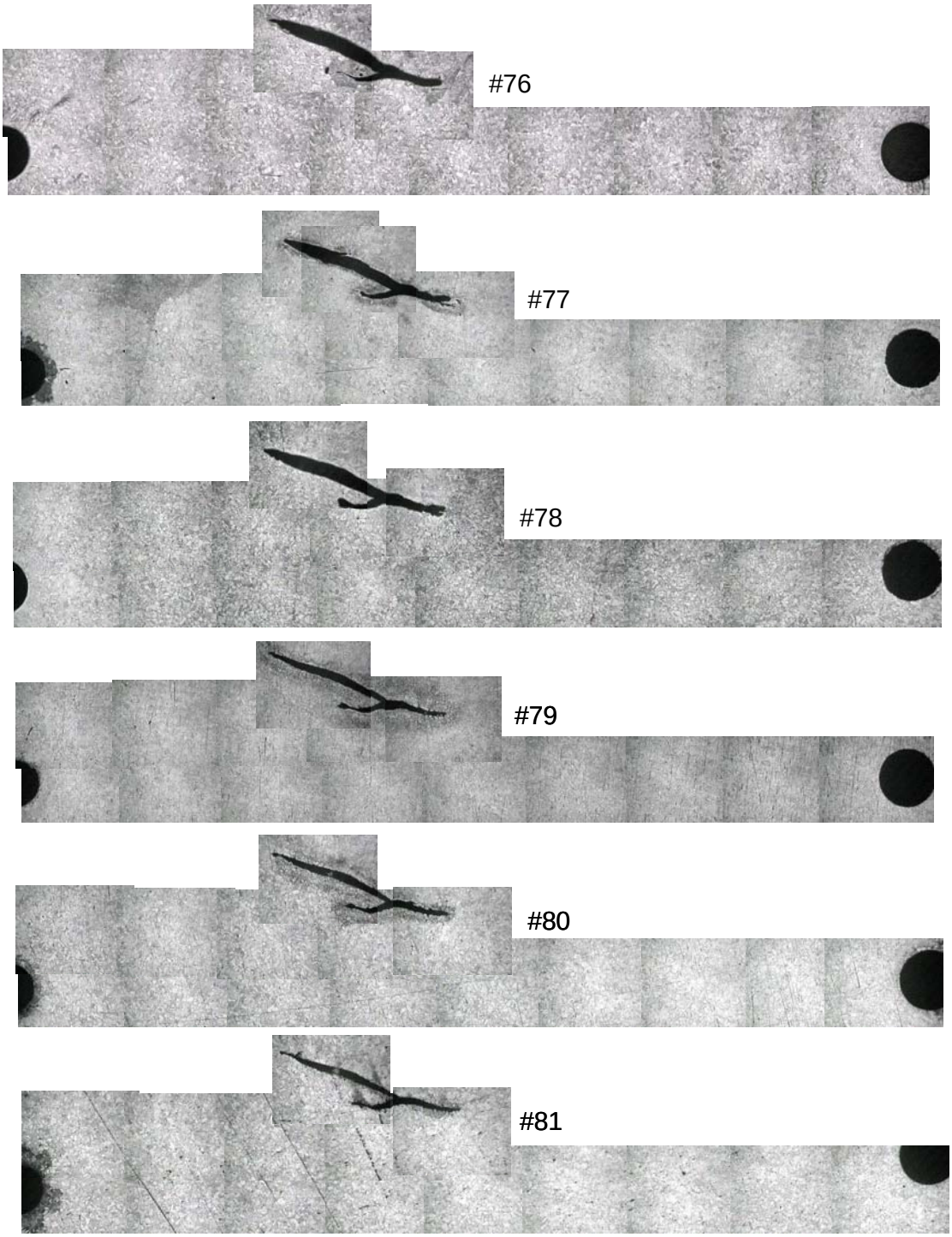

Ni Billet Indication #4 – 100X composite micrograph
Sectioning at 0.002” increments

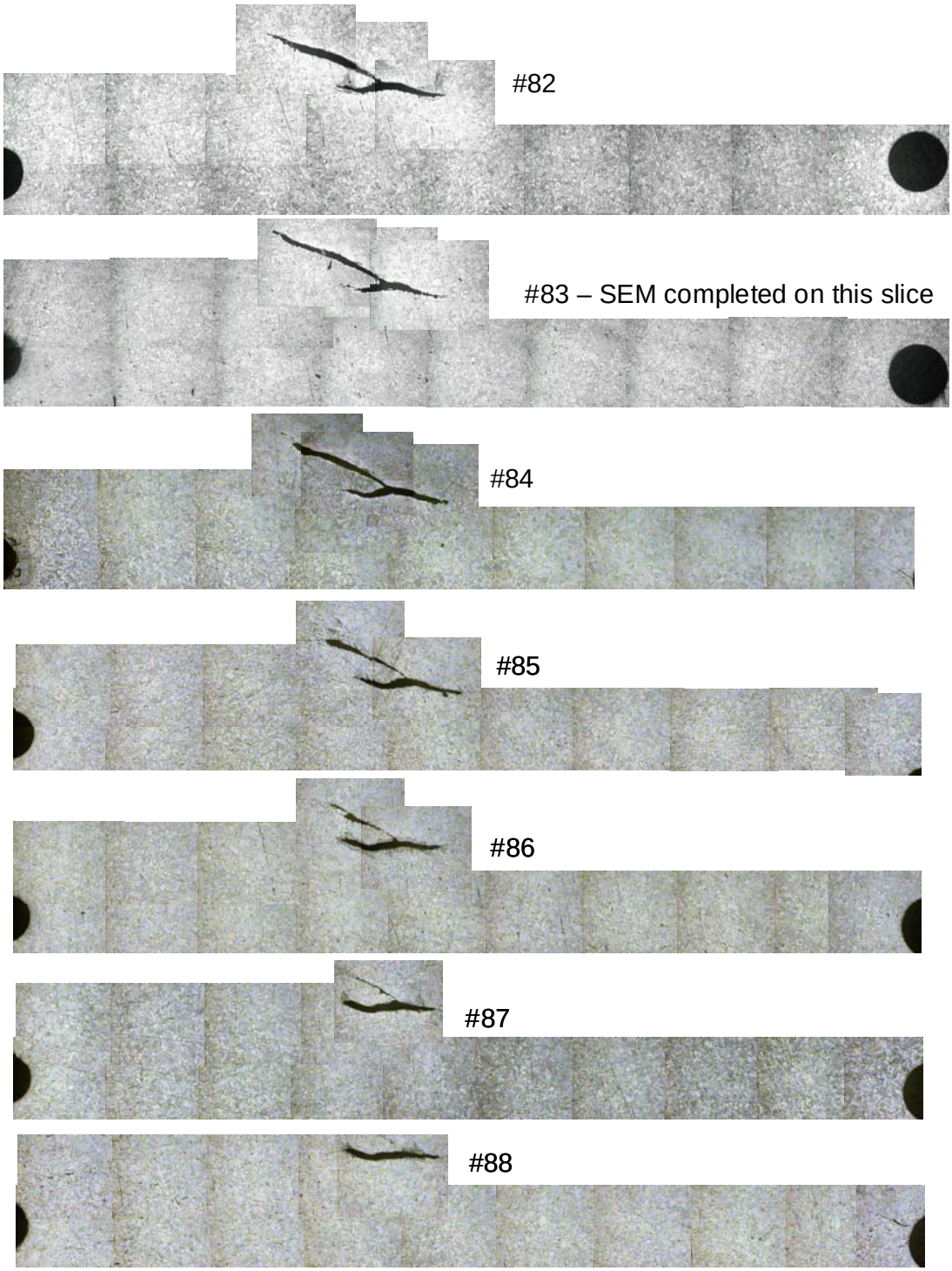

Ni Billet Indication #4 – 100X composite micrograph
Sectioning at 0.002” increments

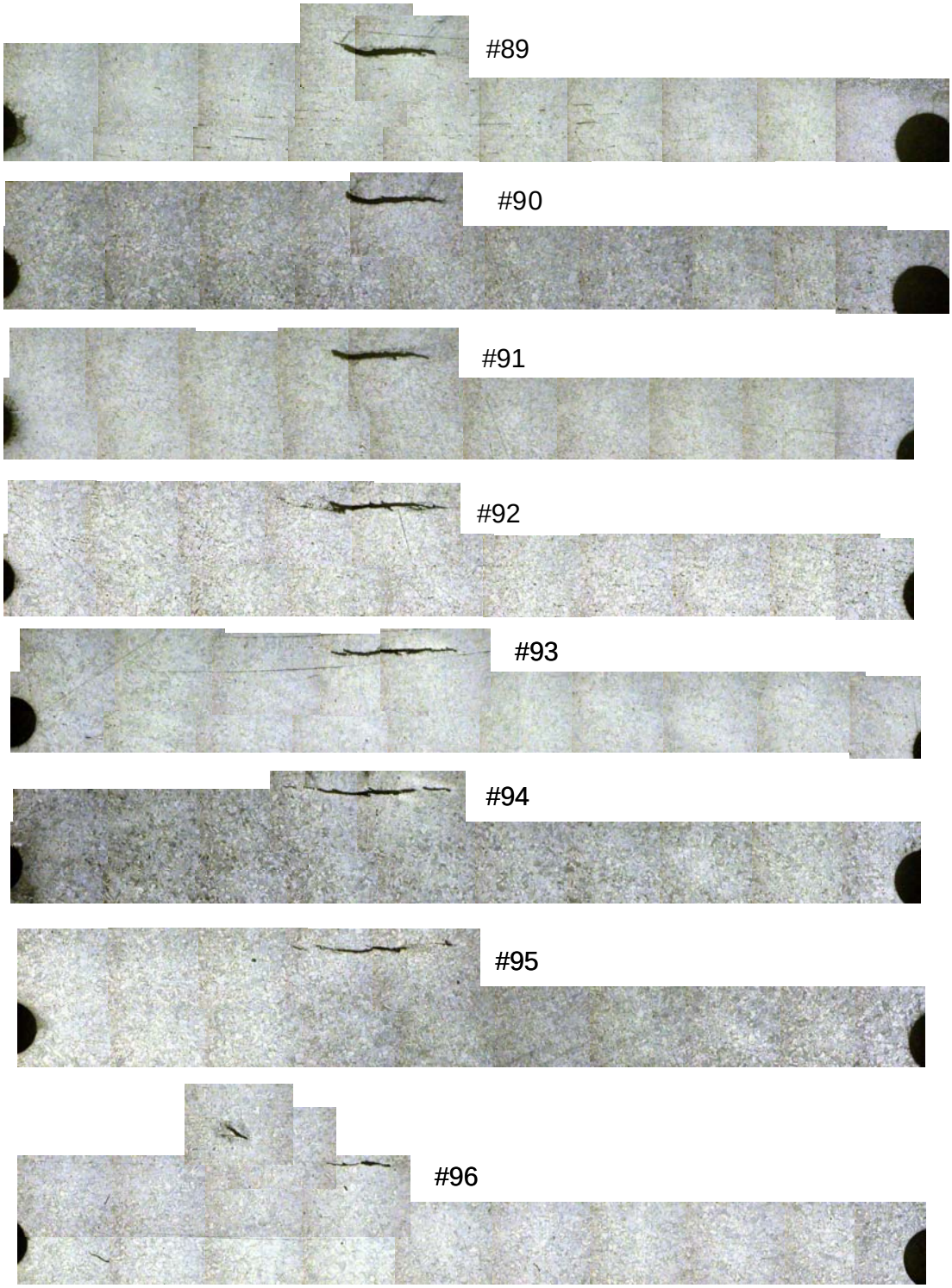

Ni Billet Indication #4 – 100X composite micrograph
Sectioning at 0.002” increments

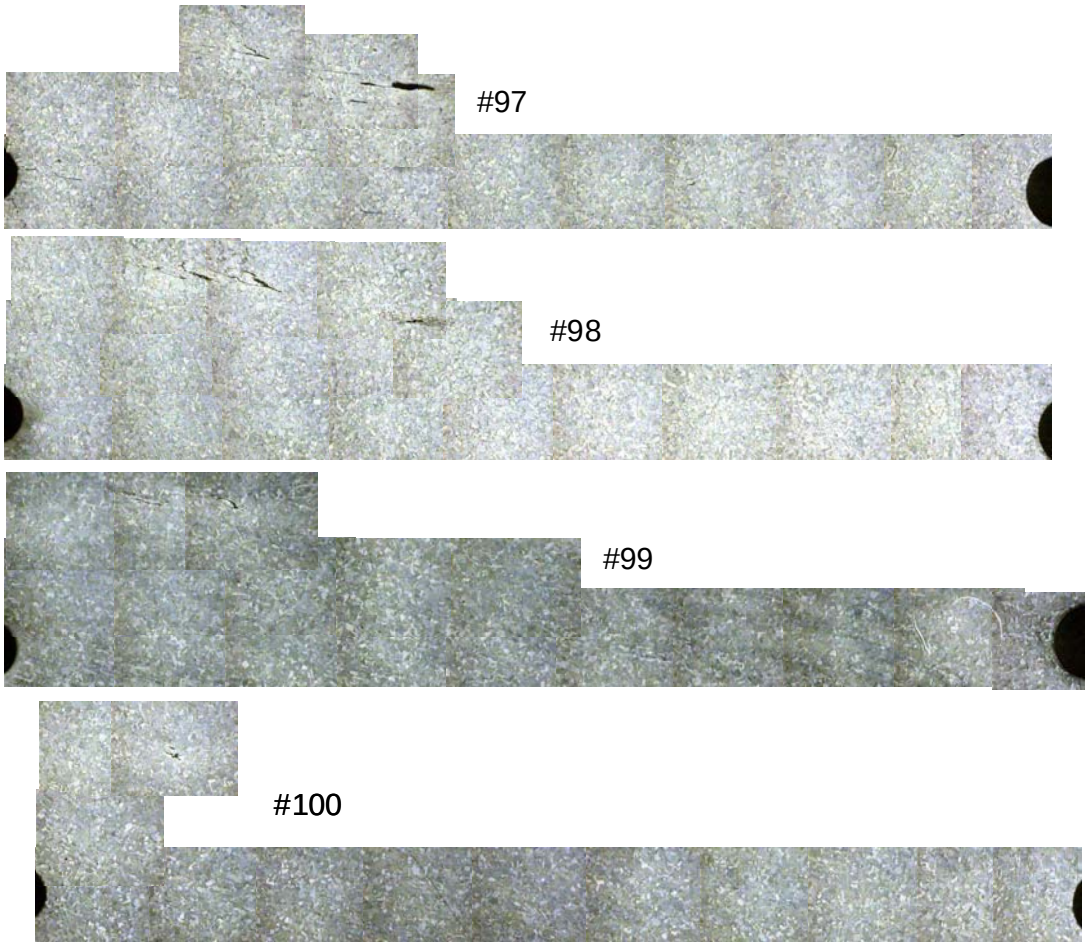

Ni Billet Indication #4 – SEM analysis performed at slice #58
0.18834” polished in from side D

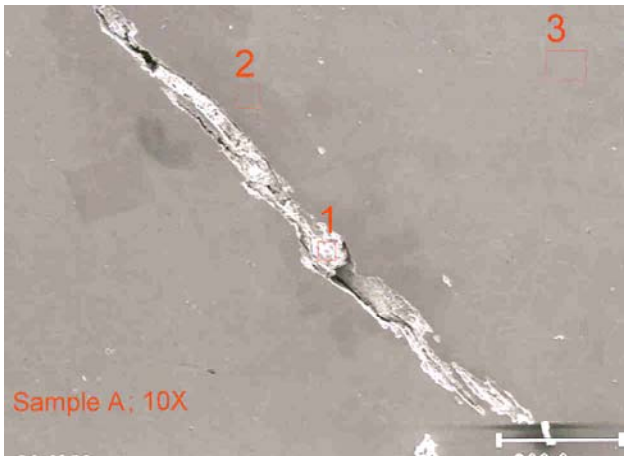

10X

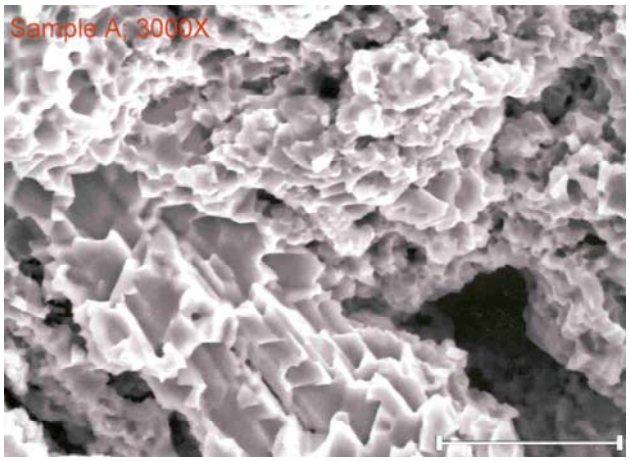

3000X

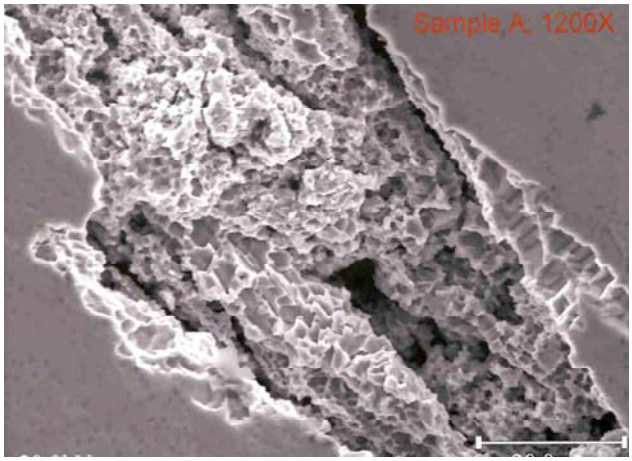

1200X

Ni Billet Indication #4 – SEM analysis performed at slice #58
0.18834” polished in from side D

Polish #58

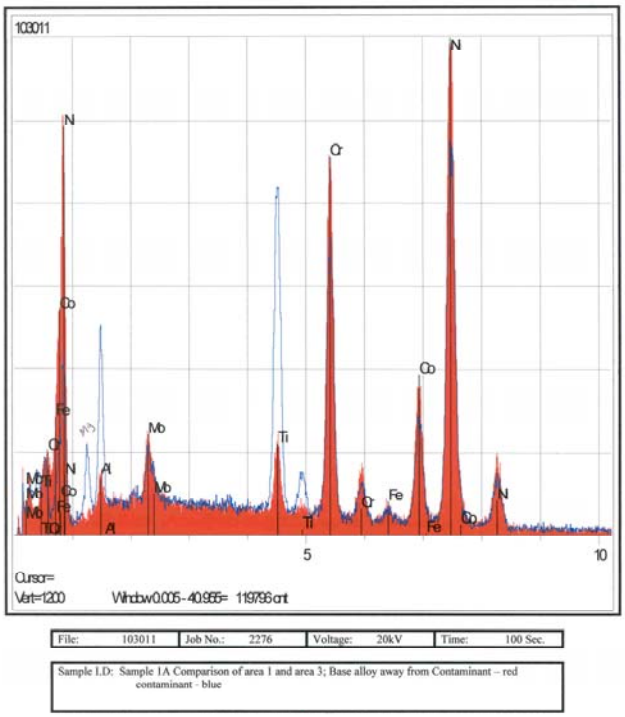

Ni Billet Indication #4 – SEM analysis performed at slice #58
0.18834” polished in from side D

Polish #58

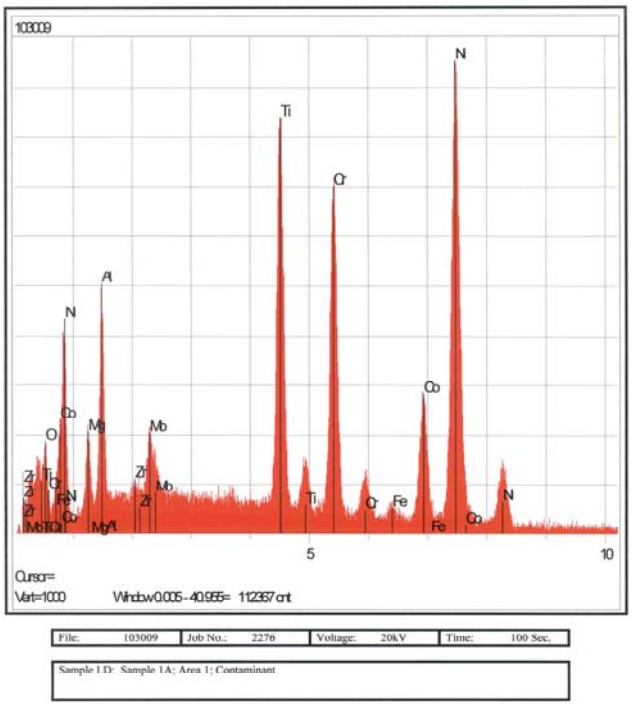

Ni Billet Indication #4 – SEM analysis performed at slice #58
0.18834” polished in from side D

Polish #58

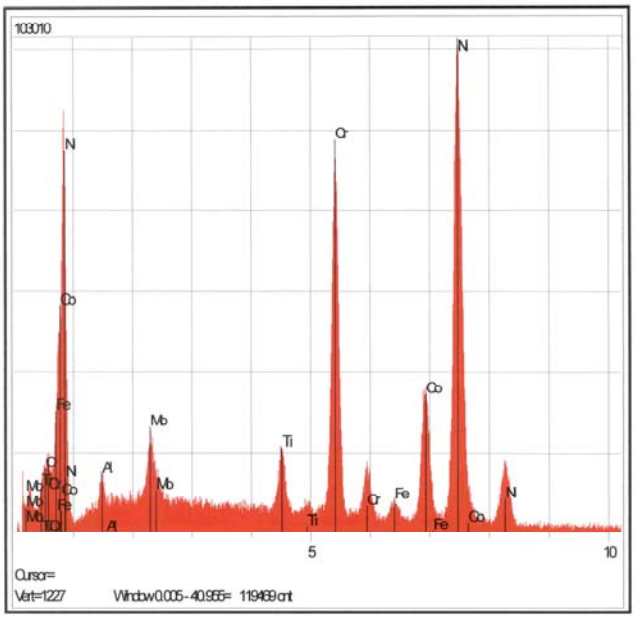

File: 103010	Job No.: 2276	Voltage: 20kV	Time: 100 Sec.

Sample I.D: Sample 1A; Area 2; Base alloy near Contaminant

Ni Billet Indication #4 – SEM analysis performed at slice #58
0.18834” polished in from side D

Polish #58

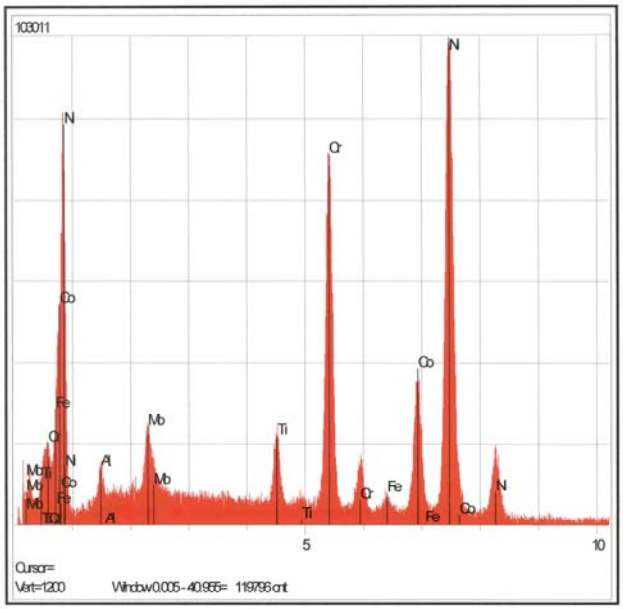

File: 103011	Job No.: 2276	Voltage: 20kV	Time: 100 Sec.

Sample I.D: Sample 1A; Area 3; Base alloy away from Contaminant

Ni Billet Indication #4 – SEM analysis performed at slice #58
0.18834" polished in from side D

File: 103009	Job No.: 2276	Voltage: 20kV	Time: 100 Sec.

Sample I.D: Photo 2276S002; Area 1; Contaminant

Polish #58

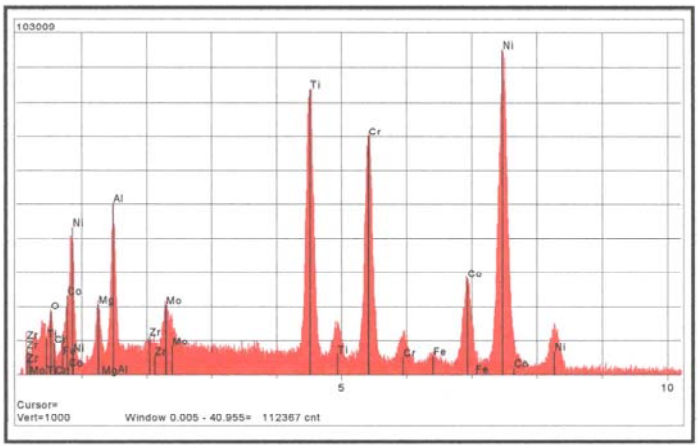

Ni Billet Indication #4 – SEM analysis performed at slice #58
0.18834" polished in from side D

File: 103011	Job No.: 2276	Voltage: 20kV	Time: 100 Sec.

Sample I.D: Photo 2276S002; Area 2; Base alloy away from Contaminant – red contaminant - blue

Polish #58

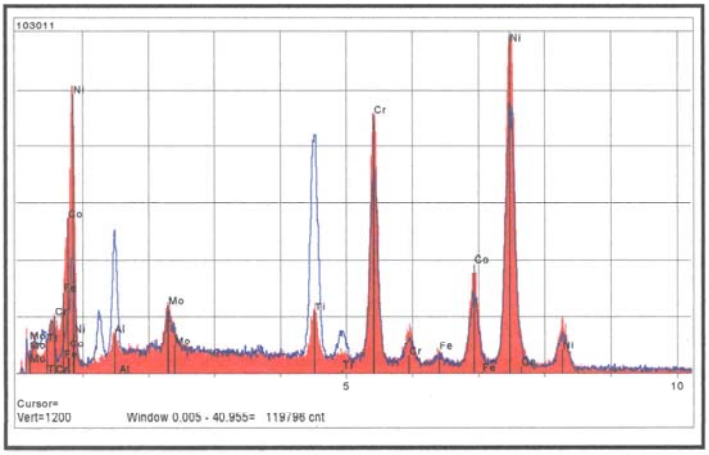

Ni Billet Indication #4 – SEM analysis performed at slice #58
0.18834" polished in from side D

File: 103010	Job No.: 2276	Voltage: 20kV	Time: 100 Sec.

Sample I.D: Photo 2276S002; Area 2; Base alloy near Contaminant

Polish #58

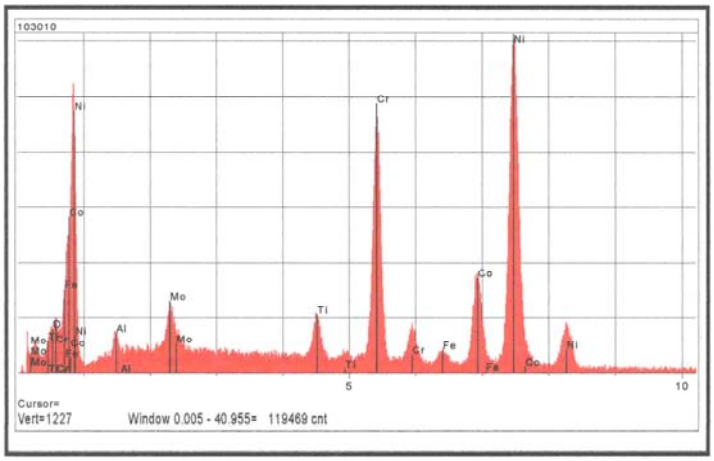

Ni Billet Indication #4 – SEM analysis performed at slice #58
0.18834" polished in from side D

File: 103011	Job No.: 2276	Voltage: 20kV	Time: 100 Sec.

Sample I.D: Photo 2276S002; Area 3; Base alloy away from Contaminant

Polish #58

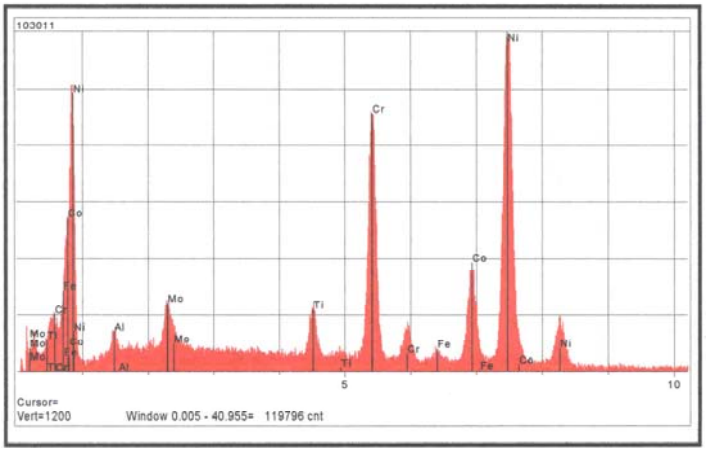

Ni Billet Indication #4 – SEM analysis performed at slice #83
0.23734" polished in from side D

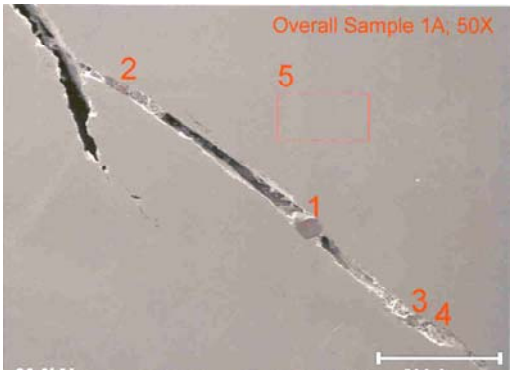

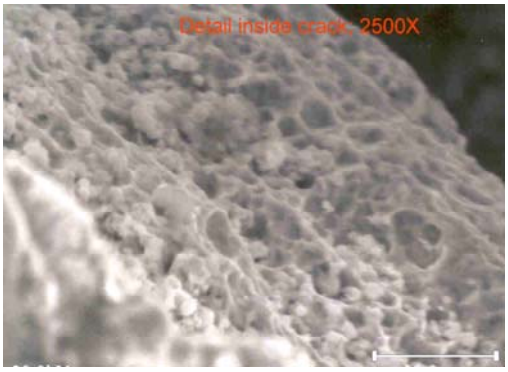

Ni Billet Indication #4 – SEM analysis performed at slice #83
0.23734" polished in from side D

File: 110805+6	Job No.: 2278	Voltage: 20kV	Time: 100 Sec.

Sample I.D: Mount 1A; blue = matrix; red = inside crack

Polish #83

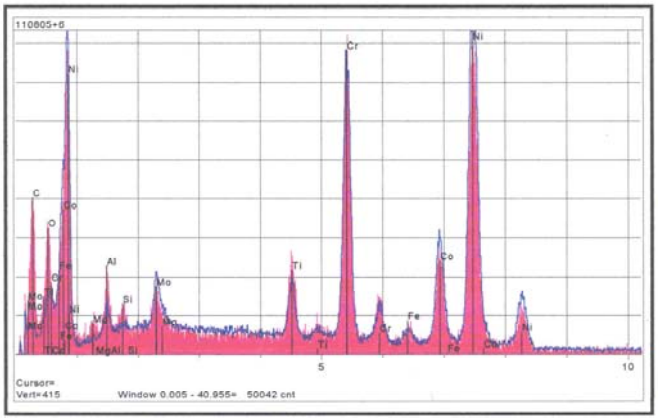

Ni Billet Indication #4 – SEM analysis performed at slice #83
0.23734" polished in from side D

File: 110806	Job No.: 2278	Voltage: 20kV	Time: 100 Sec.

Sample I.D: Mount 1A; inside crack

Polish #83

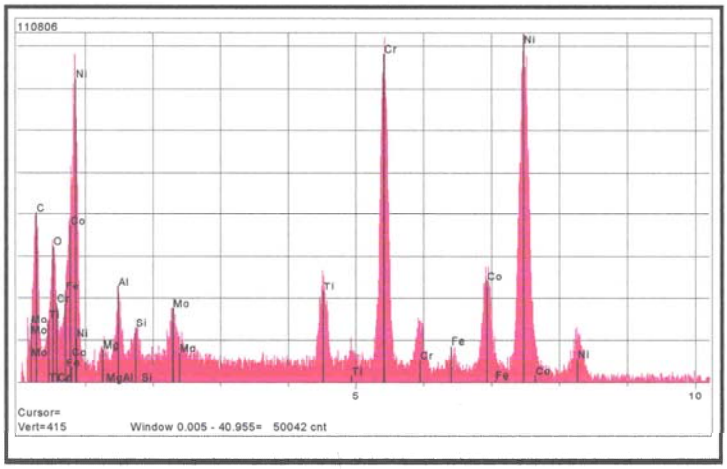

Ni Billet Indication #4 – SEM analysis performed at slice #83
0.23734" polished in from side D

File: 110801	Job No.: 2278	Voltage: 20kV	Time: 100 Sec.

Sample I.D: Mount 1A; Area 1 inclusion

Polish #83

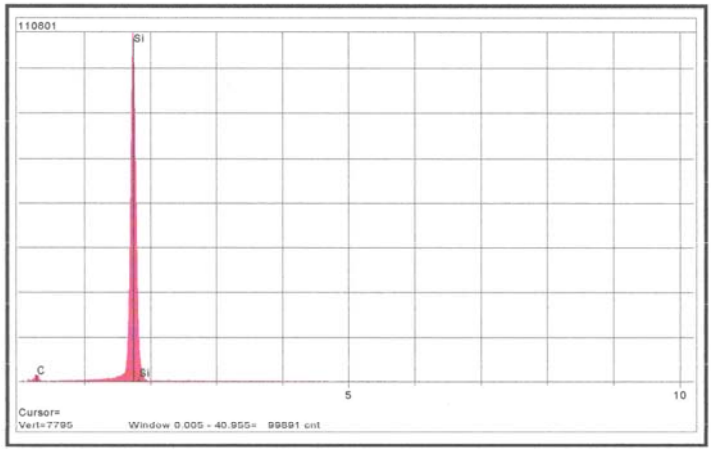

Ni Billet Indication #4 – SEM analysis performed at slice #83
0.23734” polished in from side D

File: 110802	Job No.: 2278	Voltage: 20kV	Time: 100 Sec.

Sample I.D: Mount 1A; Area 2 inclusion

Polish #83

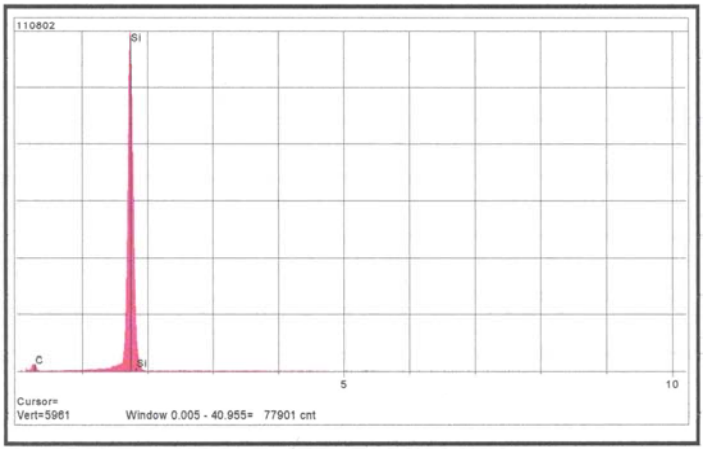

Ni Billet Indication #4 – SEM analysis performed at slice #83
0.23734” polished in from side D

File: 110805	Job No.: 2278	Voltage: 20kV	Time: 100 Sec.

Sample I.D: Mount 1A; Area 5 inclusion

Polish #83

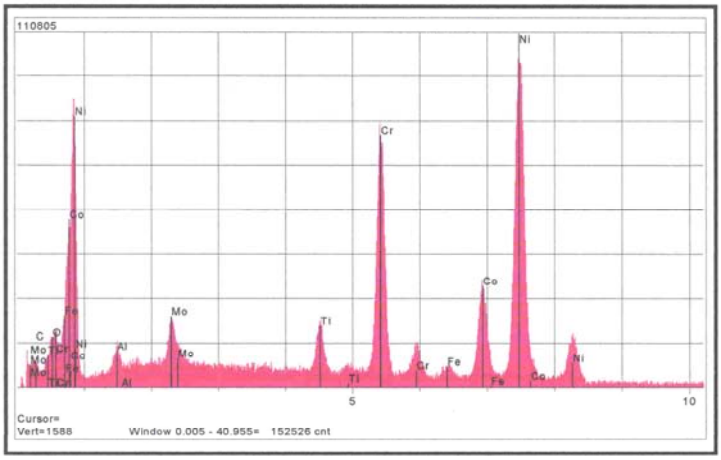

Ni Billet Indication #4 – SEM analysis performed at slice #83
0.23734" polished in from side D

File: 110804	Job No.: 2278	Voltage: 20kV	Time: 100 Sec.

Sample I.D: Mount 1A; Area 4 inclusion

Polish #83

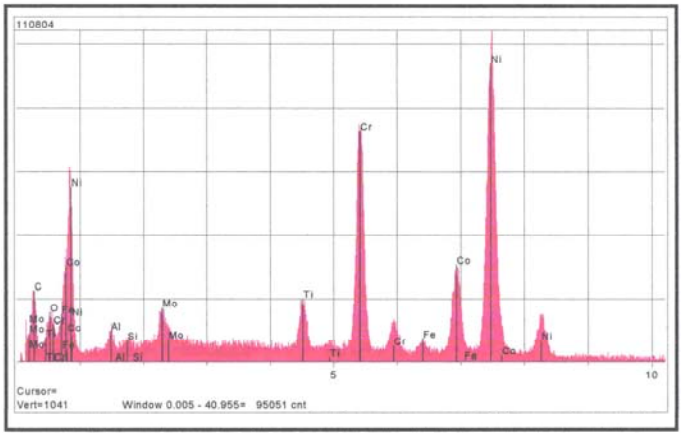

Ni Billet Indication #4 – SEM analysis performed at slice #83
0.23734" polished in from side D

File: 110804-5	Job No.: 2278	Voltage: 20kV	Time: 100 Sec.

Sample I.D: Mount 1A; Area 4+5; Blue= inclusions; Red= matrix

Polish #83

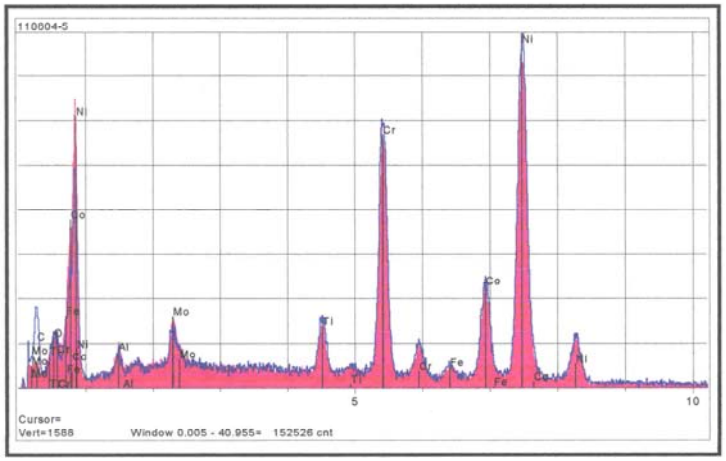

Ni Billet Indication #4 – SEM analysis performed at slice #83
0.23734” polished in from side D

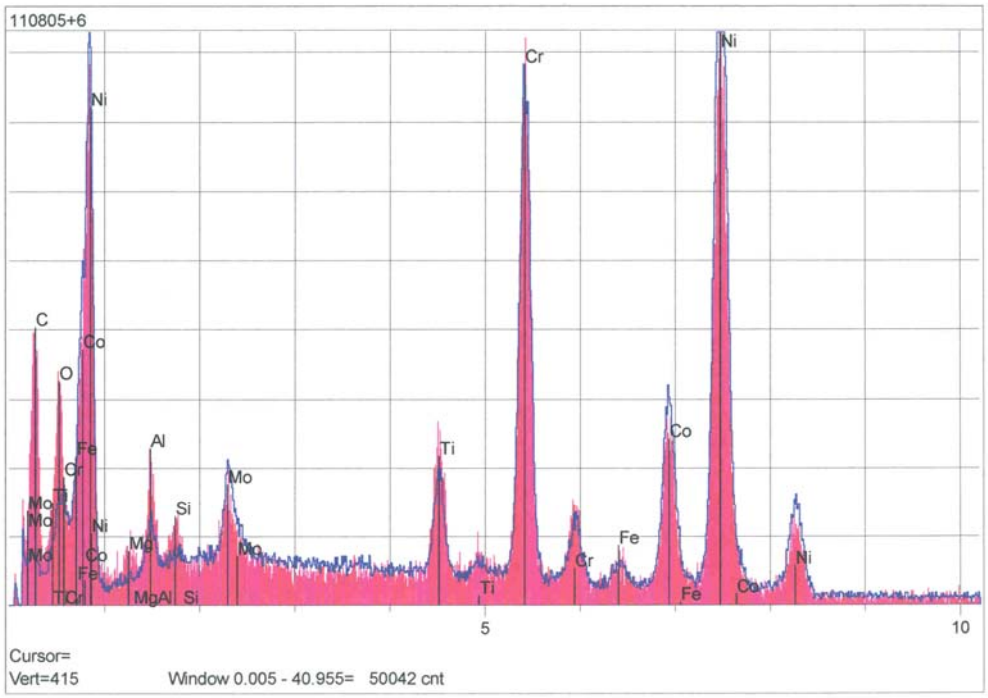

Ni Billet Indication #4 – SEM analysis performed at slice #83
0.23734” polished in from side D

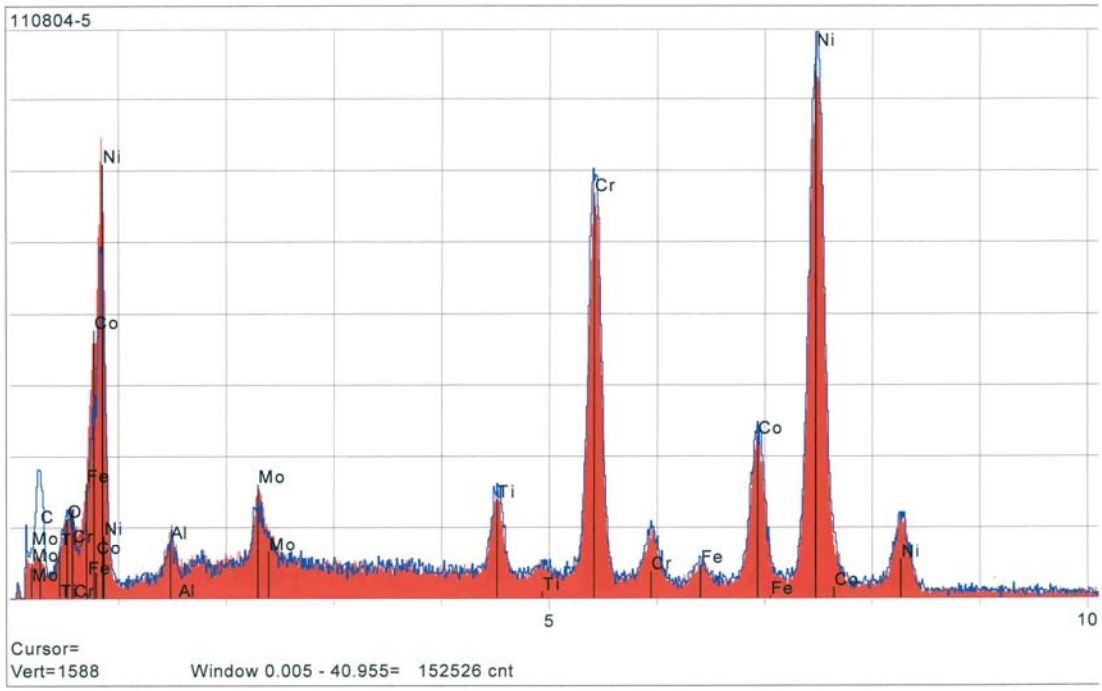

Ni Billet Indication #5 – General Information

- Alloy = Waspaloy
- Melt method = VIM-VAR (Vacuum Induction Melting followed by Vacuum Arc Remelting)
- Billet Diameter = 11”
- Calibration was in accordance industry standards. The required flat bottom hole (FBH) size is a 5/64” diameter. Calibration reflectors were positioned at approximately 0.92” and 6.6” below the sound entry surface. These reflectors were gated and electronic DAC applied.
- Calibration amplitude = 80% of full screen height (FSH)
- Reject level = 100% of the required FBH (i.e. 80% FSH)
- Alarm threshold = 60% FSH (75% of the calibration height).
- Maximized indication amplitude = 80% FSH (100% of a #5 FBH)
- Indication length ~ 0.670” ; depth ~ 4.0”
- Transducer Information:
    a. Frequency = 3.5 MHZ
    b. Transducer Size = 0.75” by 1.0” rectangular
    c. Cylindrically Focused at 7.00”
    d. Beam Diameter = 0.090 in cylindrical direction (scanning direction)
    e. Longitudinal Wave
    f. Water path set at 4.50”
- Indication: Nonmetallic inclusion

Ni Billet Indication #5 – Sample sectioning and naming convention

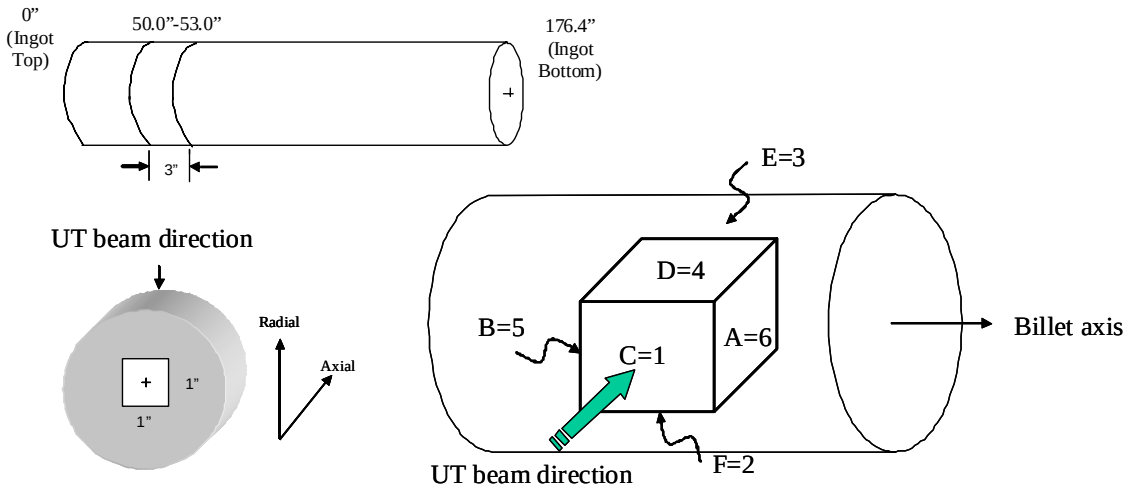

Ni Billet Indication #5 – Ultrasonic Measurements

Experimental C-scan Images

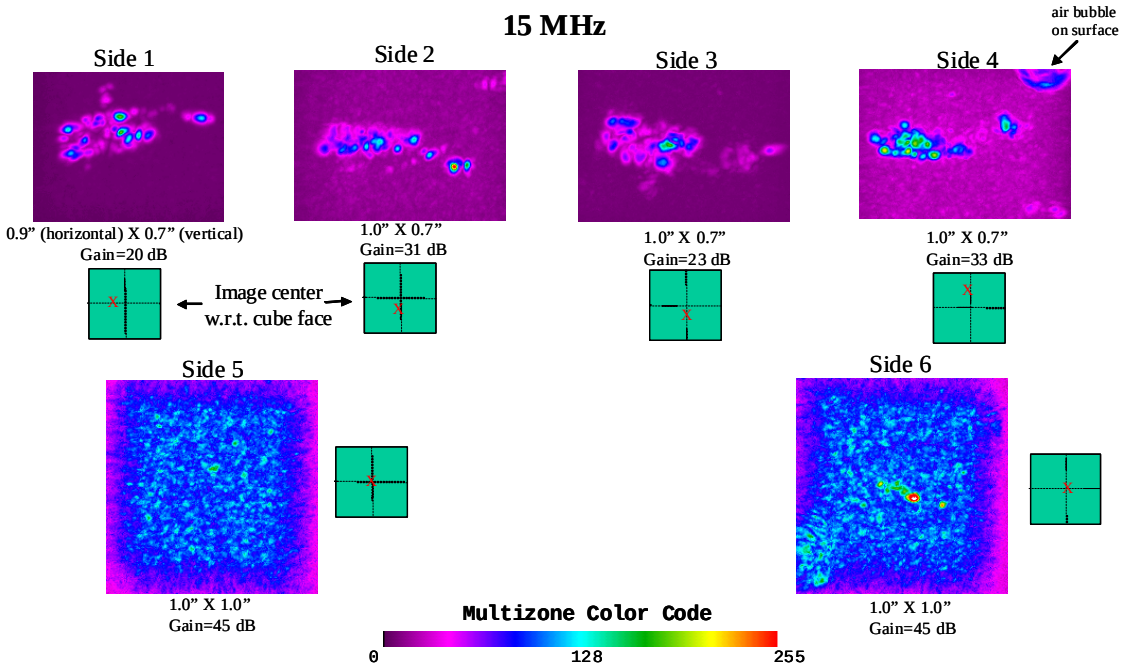

Image resolution: All are of 0.005" scan increment (in-between pixels)
Orientation: side 5 on left and side 6 on right for sides 1~4; side 2 on left and side 4 on right for sides 5~6

Experimental C-scan Images (conti.)

5 MHz

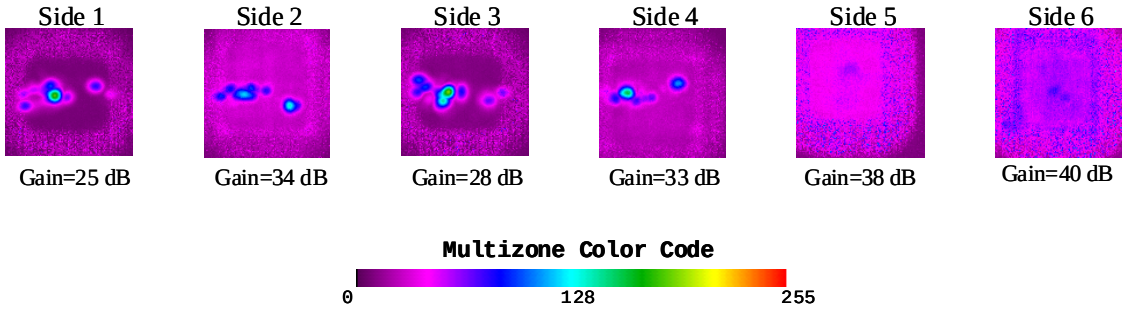

Image resolution: All are 1.1” by 1.1” centered; of 0.01” scan increment (in-between pixels)
Orientation: side 5 on left and side 6 on right for sides 1~4; side 2 on left and side 4 on right for sides 5~6

50 MHz

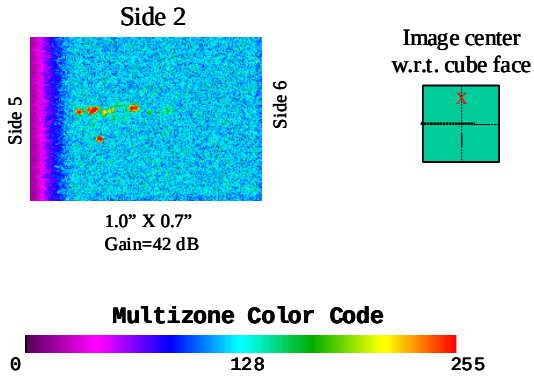

Image resolution: 0.005” scan increment (in-between pixels)
Orientation: side 5 on left and side 6 on right

Ni Billet Indication #5 -100X composite micrograph
Sectioning occurred at 0.002” increments, not all slices shown

Slice 1

Slice 5

Slice 11

Slice 13

Slice 16

Slice 18

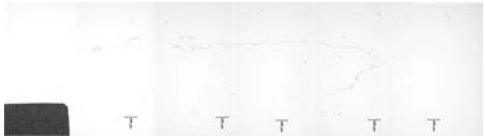

Slice 21

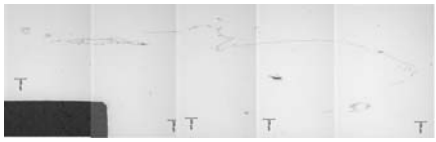

Slice 23

Ni Billet Indication #5 - 100X composite micrograph
Sectioning occurred at 0.002” increments, not all slices shown

Slice 25

Slice 27

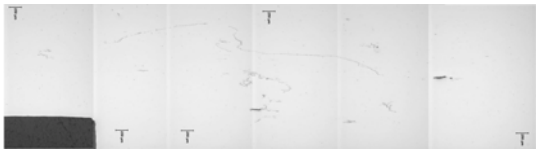

Slice 29

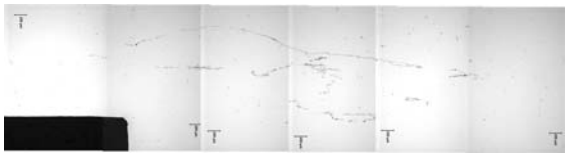

Slice 31

Slice 33

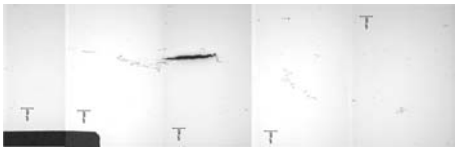

Slice 34

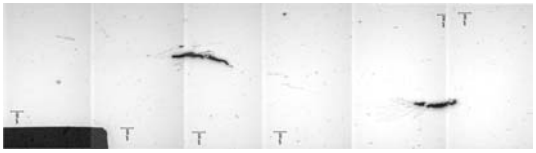

Slice 35

Ni Billet Indication #5 - 100X composite micrograph
Sectioning occurred at 0.002” increments, not all slices shown

Slice 36

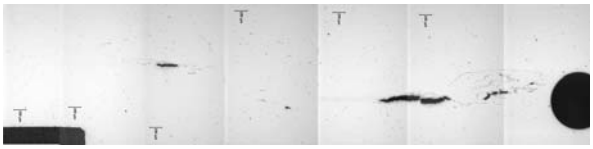

Slice 37

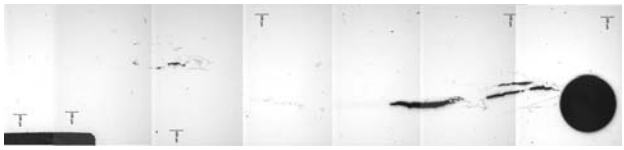

Slice 39

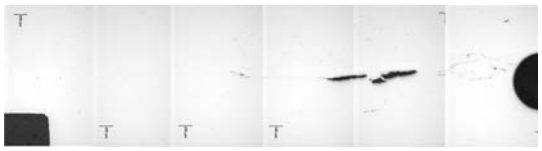

Slice 40

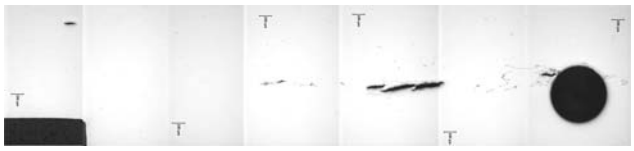

Slice 41

Slice 42

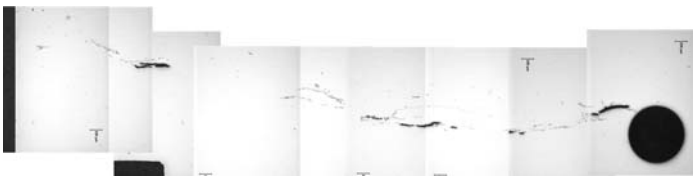

Slice 43

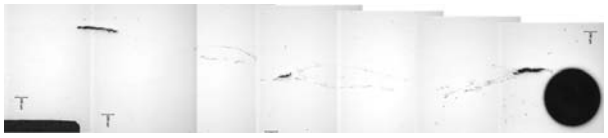

Ni Billet Indication #5 - 100X composite micrograph
Sectioning occurred at 0.002” increments, not all slices shown

Slice 44

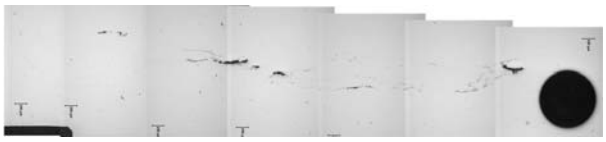

Slice 46

Slice 47

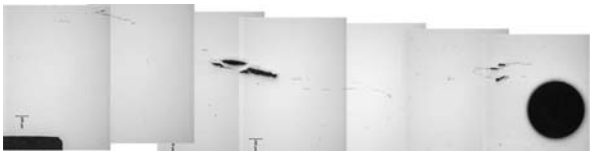

Slice 49

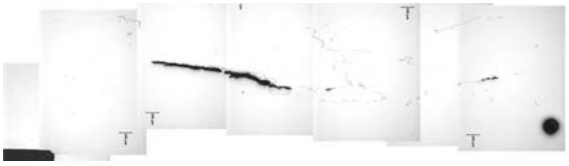

Slice 50

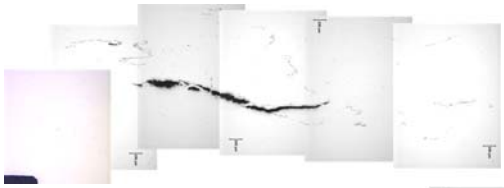

Slice 51

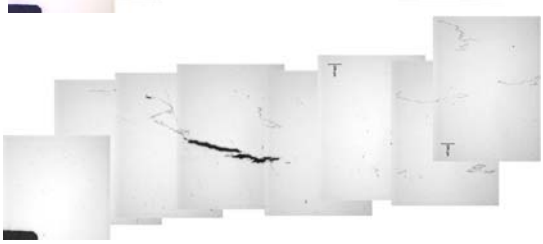

NI Billet Indication #5 – 100X composite micrograph
Sectioning occurred at 0.002” increments, not all slices shown

Slice 52

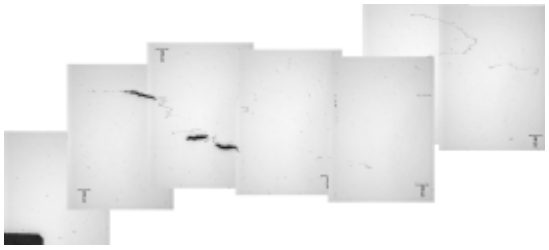

Slice 53

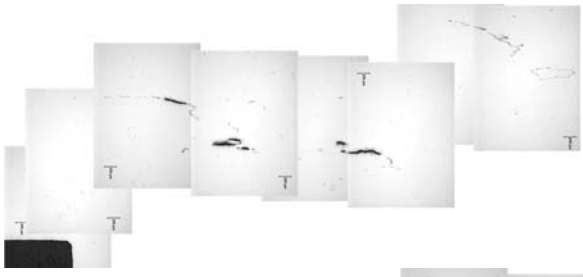

Slice 55

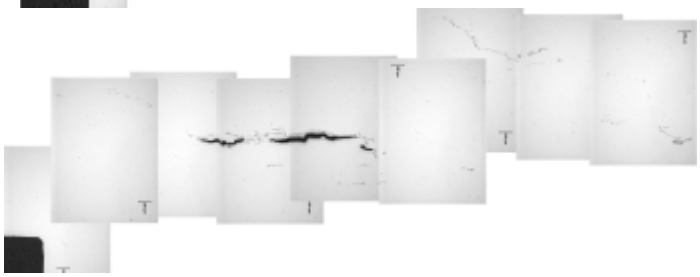

Slice 56

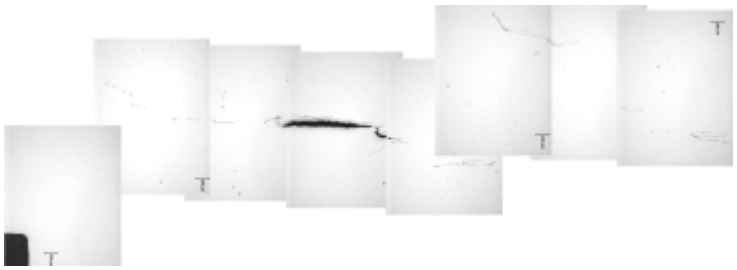

Slice 57

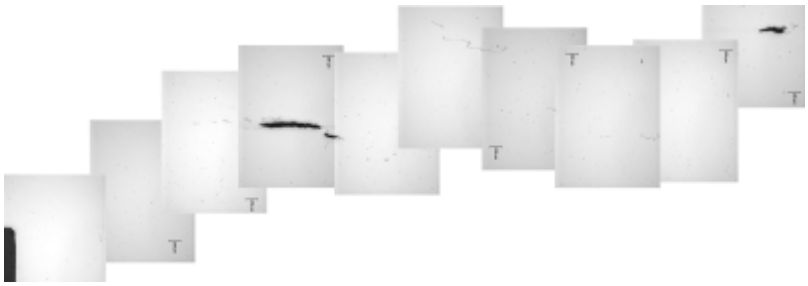

APPENDIX B—ULTRASONIC DATA ACQUISITION PROCEDURE FOR ETC REAL DEFECTS

Using a Sonix Immersion System

by C. Thomas Chiou, Mike Keller, Jeff Umbach and Andrei Degtyar

Last update: 04-17-01

1. Introduction

This procedure is written for internal use in ETC-II Task 1.1.1 Fundamental Studies and other related tasks. The objective is to acquire UT a-scan, c-scan and multiple b-scan (volumetric a-scan) data of naturally occurring defects embedded in a small Ti- or Ni-based cube block. The target readers are NDE staff with sufficient experience in use of a Sonix immersion system. Some technical details has been included here in an attempt to make this document self-contained. Section 2 lists the basic requirements of system components and accessories. Section 3 lays out the experimental setups of the reference and defect data acquisition, for which the step-by-step procedures are described in Sections 6 and 7. Other supporting materials are provided in the remaining sections. For clarification of several key terminologies, the readers are referred to Section 9.

2. System Requirements

The designated scan hardware is a computerized Sonix immersion scan system produced in the 1990's (or later) with three-axis scan capability, controlled by Sonix FlexSCAN-C software version 4.0 (or higher). Sonix default pulser/receiver such as DPR-35+ should be used if equipped, but other typical pulser/receivers such as Panametrics 505x series can be substituted. A standard transducer search tube (mounting pole) and a mechanical transducer manipulator capable of two angular position controls are assumed to be parts of the scan system. The defect specimen should have been sectioned down to a minimum size (typically around 1" cube) with the defect centered in the block. Knowledge of defect depth on each of the six sides is expected. The front and back surfaces of the defect cube block in the three orthogonal directions should also be made as parallel as possible. The accessories include a sample stand, a thermometer, transducer sets and fused-quartz reference sets. The specifications and usage of each accessory component are as follows.

2.1 Sample stand

A three- or four-legged flat stand of circular (or rectangular) shape with minimal size of 4" diameter (or side) is needed to support the cube sample and the reference plate in the scan tank. This stand should be made of rust-free materials such as stainless steel, titanium or epoxy glass, and the stand legs must be adjustable with good precision for leveling.

2.2 Thermometer

A thermometer is needed to measure the water temperature of the scan tank from which the water attenuation can be estimated. The precision of the thermometer should be within 1 degree Celsius or Fahrenheit.

2.3 Transducer Set

Minimally, two focused transducers are needed to acquire the UT data. Both should generally be spherically focused with central frequencies around 5MHz for one and at least 15 MHz for the other. Assuming a maximum 0.5" defect depth below all six sides of the defect cube block, all transducers must have at least a 2" true focal length (see Section 9.1 for definition) for good focusing. The size and focal length combination of the transducer should be carefully selected so that the beam entry area will not be larger than the 1" square surface of the defect cube block. The typical transducer set used consisted of a 5MHz, 1" diameter, 8" true focal length transducer and a 25 MHz, 0.25" diameter, 2" true focal length transducer.

In order to determine the key transducer parameters such as the true focal lengths, geometric focal lengths and equivalent diameters (Section 9.1), all transducers must also be characterized. The transducer characterization task may be performed at ISU before a procedure is specified and tested at other sites in the future.

2.4 Reference Set

Minimally one (two recommended) fused-quartz plate is needed for the above-mentioned transducers to take reference waveforms (a-scans). These reference waveforms will be used by UT models to estimate the "system efficiency factor" of the scan system (Section 3.1). The plate thickness should be 1" (used with 5MHz transducer) and 0.5" (used with 15 MHz transducer and above) for the primary and the second optional plates, respectively. The size of the plate(s), normally 2"-4" in diameter (or per side), should fit with the service area of the sample stand. Like the defect cube block, the front and back surfaces of the plate(s) should also be parallel.

3. Experimental Setups

3.1 Basic Setups

One of the objectives of acquiring UT data with this procedure is to support UT modeling activities. The UT models used in ETC are based on ISU's Thompson-Gray measurement model framework[1]. In order to predict real defect signals at absolute levels as seen on the oscilloscope, these UT models require a separate reference experiment from which the scan system response or "system efficiency factor" can be estimated. Thus, the data acquisition actually consists of two parts: the main task is to acquire the defect data from the cube block, and the other is to obtain the reference waveforms from, as mentioned in Section 2.4 above, the fused-quartz set(s). The setup of these two experiments, both in immersion mode, are illustrated below.

In Figure 3.1, a focused transducer (specified in Section 2.3) is normalized (Section 3.4) to the front surface of a fused-quartz plate of thickness $Y_{r,s}$. Given the UT speeds in water and fused-quartz (Sections 9.2 and 9.3), plate thickness, and the transducer focal length, the waterpath is set (see Section 9.4 for formula) to $Y_{r,w}$ such that the geometric focal length

(section 9.1) is on the back surface of the fused-quartz plate. Echoes from the back surface, i.e. the reference waveforms (a-scans), are to be acquired in this experiment. Note that additional spacers need to be placed between the fused-quartz plate and the stand, which ensures water to be the backing medium. This is important for UT models to set up correct interface parameters without ambiguity.

In Figure 3.2, the <u>same</u> transducer is similarly normalized to the front surface of the defect cube block. However, a different waterpath $Y_{d,w}$ is used so that true focal length is on the nearest (front) surface of the defect, for which the defect depths $Y_{d,s}$ in all six sides should have been measured (Section 1). Prior to transducer normalization, the stand needs to be leveled with respect to the paths of the scan bridge (Section 3.2). It is also assumed that both front and back surfaces of the defect block are in parallel to the leveled stand surface (Section 1). In this experiment, single-shot a-scans, two-dimensional c-scans, and three-dimensional b-scans (see Section 9.1 for definition) will be acquired.

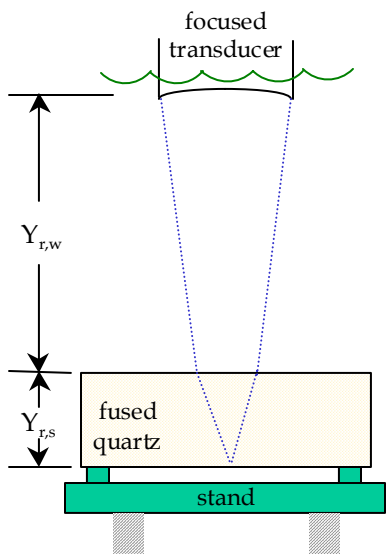

Figure 3.1 Reference Experiment

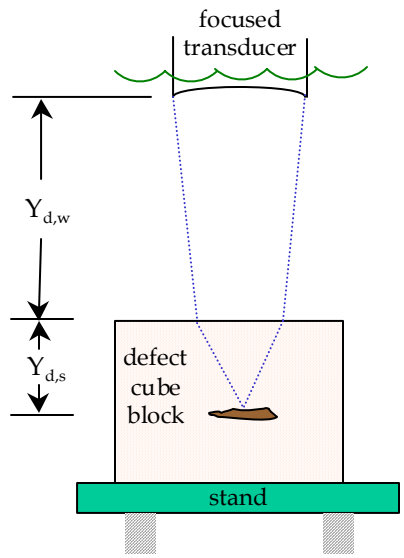

Figure 3.2 Defect Experiment

<u>It should be pointed out that all hardware connections (such as the co-axial cables and transducer search tube) and settings (such as damping, pulse rate, energy level on pulser/receiver unit) must be kept the same for both the reference and defect experiments. The only adjustable setting is the gain (or attenuation on Panametrics models) of the pulser/receiver unit</u>. This is to ensure the accuracy of the system efficiency factor as stated above.

In order to warrant the best possible data obtained in an optimal condition of a given scan system, extra care should also be taken on the specimen placement issues. Specimen placement involves the leveling of the specimen and orienting the specimen with respect to the scan system coordinates. These are the subjects of the following subsections.

3.2 Specimen Leveling

For a typical linear scan, the rule of thumb is to maintain a constant distance between the beam entry surface and the transducer face. This constant distance can in turn be related to the planar path that the scan bridges move about, assuming there is no bending of the scan bridges (see Section 4.2). This ensures the alignment of the specimen and the scan bridges to avoid the fluctuations of beam focusing and signal time-of-flight. This is referred as "specimen leveling with constant water path", and the surface to be leveled is often the front surface of the specimen. A common technique of leveling a front surface is to perform a lengthy line scan on that surface. During the scanning, the amount of change in time-of-flight of an echo from the front surface, as seen on the oscilloscope, determines the degree of tilting of the surface. One can then adjust, for instance, the screws of the sample stand to correct the tilt. However, given the relatively large size of the transducer (1" diameter for the 5MHz transducer) and small dimension of the defect block (~1" cube), this technique does not work well in this case. The solution here is to level the surface of the sample stand instead. The leveling of the sample stand ensures the same for the front and back surfaces of the defect cube block, since they are parallel to each other as was required (Section 1). For the reference fused-quartz plate, the leveling is not as crucial because only single-shot a-scans are acquired.

3.3 Specimen Orientation

Based on past experience with the Sonix system, issues related to specimen orientation have frequently been the source of error and confusion. Often the c-scan images were rotationally disoriented or mirror-inverted from the actual specimen layout. The problem arises largely from the inconsistency between the specimen orientation (in the water tank) and the Sonix scan plan. To avoid such difficulty, <u>it is recommended that the Sonix scan plan be set up to match exactly with the actual specimen orientation</u>. As an example, Figure 3.3a illustrates a hypothetical specimen orientation and the matching Sonix c-scan line paths (see Section 9.5 for detailed scan/step direction settings under FlexSCAN-C's Scan Setup menu). If the "bottom-up" image convention (with origin at lower-left corner) is followed, then the orientation of the c-scan image, as depicted in Figure 3.3b, should match correctly with that of the specimen. It is also recommended to keep a drawing of the specimen orientation with respect to the scan plan and a copy of the details of the scan plan settings for future reference.

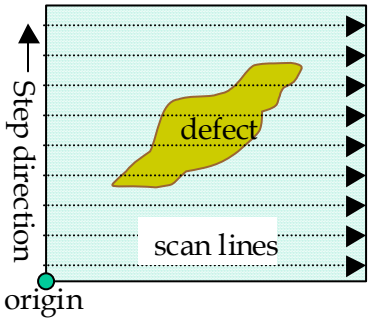

Figure 3.3.a specimen and scan orientations

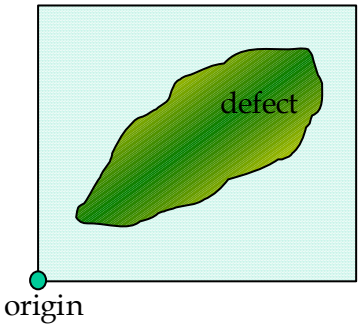

Figure 3.3b resulting c-scan image

3.4 Transducer Normalization

In addition to specimen leveling, the normalization of the transducer is also an important but often difficult task. By “normalization” we mean to orient the transducer with respect to the beam entry surface in such a way that the sound beam enters the specimen with minimum energy loss and achieves the optimal focusing. For spherically focused transducers, a popular “ring wave” method of normalization has proven reliable. The "ring wave" method takes advantage of the time-of-flight difference between the outer transducer “ring wave” and inner main beam. As depicted in Figure 3.4b, when the transducer is very close to a flat surface, the central main component of the beam takes a longer time to travel back and forth than the outer “ring” components do. This results in a separation of the time domain front surface echo into a small leading “ring” signal and a large trailing main signal as shown in Figure 3.4b. If the transducer is well fabricated, the “ring” signal will reach its maximum when the transducer is perpendicular to the surface such that all ring components travel using the same amount of time. This phenomenon thus provides a practical way to “normalize” a focused transducer of axial symmetry. The degree of time separation between the ring and main components depends on the size, focal length and frequency of the transducer. For the 5MHz, 1” diameter, spherically focused transducer with focal length 8” at about 0.5” above a flat surface, the time separation is substantial. For a higher frequency transducer with shorter focal length and smaller diameter, the separation becomes less clear. In this case, the inseparable main and ring signals should be viewed as a whole and maximized in the process of transducer normalization.

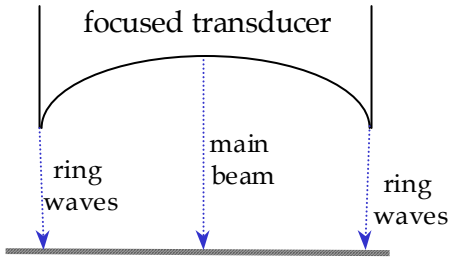

Figure 3.4a "ring-wave" setup

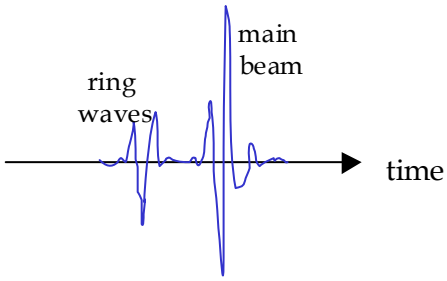

Figure 3.4b corresponding a-scan

4. System Calibration

In addition to an optimal experimental setup, a thorough system calibration process is the key to data accuracy and should be conducted BEFORE any data acquisition. In this procedure, there are three elements in the system calibration process: pulser/receiver, mechanical scan bridges, and oscilloscope. <u>It is also strongly recommended to follow all calibration procedures described in FlexSCAN-C user's guide.</u>

Pulser/Receiver

Important electronic parts like the pulser/receiver are often overlooked in the calibration process. While the accuracy of other aspects of the pulser/receiver matters, the single most critical function of the pulser/receiver for this procedure is the gain (or attenuation) setting, the only adjustable electronic parameters in the system (recall Section 3.1). Extra care should be taken in operating this setting. For example, the receiver of Panametrics 5052 is rated maximum output voltage of $\pm$0.5 volt into 50 Ohms. Any signal that has peak-to-peak amplitude exceeding 1 volt is subjected to distortion and loss of data accuracy. Thus, <u>it is vital to maintain a linear undistorted operation of the gain (attenuation) setting in the pulser/receiver unit and acquire measurements in this linear range</u>. A simple test of the linearity is to measure the peak-to-peak amplitude of a stationary signal (within the maximum output limit) with a sequence of gain settings that lie in the expected range of operation. The amplitude change in measurement should be linearly proportional to that in the gain settings. Proper remedy needs to be made if significant deviation from the linearity is observed.

Mechanical Scan Bridges

Typical problems with mechanical scan parts are scan bridge bending due to aging and scan "backlash" effects. Severe scan bridge bending may cause data loss and/or incorrect data registration. For example, heavy weight over time can cause the center of a scan bridge to buckle downward, which leads to a shorter waterpath in the central portion of scan. For a fixed narrow time gate in which UT data are digitized, a portion of the target UT signal may then shift out in this central scan path depending on the amount of bending. The misalignment problem

may also arise when the beam entry surface of specimen has variable curvature. Because of these shortcomings, at most times it is good idea to turn ON the "front surface follower" feature in Gate Control window of FlexSCAN-C.

The "backlash" effect frequently originates from excessive "looseness" in the lead screws of the mechanical scan bridge. This looseness can cause misalignment problem in data when scanned in bi-directional mode (i.e. taking data in both scan and return pass of a scan line). One way to determine the amount of backlash is to scan an object of well-defined shape and examine the degree of distortion in the c-scan image, especially the outlines of the object image. In FlexSCAN-C, the backlash effect may be compensated by software operation (Scan -> Backlash Correction). In any event, it is recommended to scan only in unidirectional mode (scan -> Scan Setup -> Bidirectional OFF) to reduce this effect.

Oscilloscope

The Sonix digital oscilloscope comes with default settings, as seen in the A/D Offset of A/D 8100 window, for the vertical baseline position of signal trace. Normally, these default settings are sufficient to keep the trace baseline in the middle (zero) of the scope display. In situations that the signal baseline deviates substantially from this zero position, the A/D Offset setting must be adjusted accordingly.

Another problem with the Sonix digital scope is a constant time trace offset as seen in some systems using an external pulser/receiver unit. This is possibly due to inconsistent timing between the trigger signal and the initial transmitted pulse in the combination of pulser/receiver and Sonix A/D card. This offset, typically causing 1-2 s longer in a time-of-flight reading, should be pre-determined and compensated as much as possible. One way to determine this time trace offset is to take a time-of-flight measurement from a specimen of known thickness, e.g. the 1" fused-quartz reference plate. This can be done as follows:

First proceed with the procedures of leveling the sample stand, transducer normalization with respect to sample stand, and determining the water wave speed as described in Sections 3.2, 3.4 and 9.2. Next, place the fused-quartz plate on the sample stand, manually lower the transducer to be in contact with the front surface of fused-quartz plate, and then carefully remove the fused-quartz plate from below. In this way, an exact 1" waterpath is readily set for a time-of-flight measurement of the front surface echo from the sample stand surface. Follow Section 9.4 to calculate the time-of-flight and compare that with the Sonix scope reading. The difference is the offset needed to be compensated in all future time-of-flight measurements. Note that this time trace offset depends on system loading (the combination of pulser/receiver, transducer, cables, etc.) and must be re-calibrated if any system component and/or major setting changes.

5. Data Format

Three types of UT data are acquired in this procedure: a-scan, multiple b-scan, and c-scans. By default, FlexSCAN-C generates a UT scan data file using the traditional DOS naming system: XXXXXXXX.YYY where X's are the user supplied file name (8 characters maximum) and Y's are the three-character file extension assigned by FlexSCAN-C.

Files with **CS1** extension are binary c-scans stored either in Sonix proprietary format or TIFF format. The former format can be read by any image processing software supporting RAW format. The actual data follow the first 9276-bytes header. Note that the image origin is at the lower left corner stored in row major. The TIFF format is one of the popular public-domain file formats and should be supported by most image processing software. From the programming point of view, the Sonix proprietary format is the preferred format because it is easier to work with.

Files with **RF** extension are multiple-line b-scans stored in a Sonix proprietary format, which is a special version of multi-page TIFF format. Files of this type can be accessed by FlexSCAN-C directly. Some image processing software also support this format.

Files with **TXT** extension are numeral "screen dump" of a-scan traces and can be opened by any text file editor. It contains a short header followed by waveform data points in 256-level integer, separated by commas. It is always a good practice to maintain a concise file naming convention and provide such convention along with the corresponding data structure in a "readme" file for future reference and use.

6. Reference Waveform Acquisition

To ensure best data quality and minimal errors, it is advised to follow the steps below when acquiring the reference waveform. The transducer should have been mounted on the angular manipulator, which is in turn attached to the search tube of the scan bridge.

The following steps need only to be done once for each new fused-quartz plate:

- Measure and record the dimensions and weight of the fused-quartz plate. Deduce the density accordingly and check with the tabulated generic value (Section 9.3) if applicable. Take necessary action if the difference is significant.
- Measure and record the UT speeds of the fused-quartz plate and check with the tabulated generic values (Section 9.3) if applicable. Take necessary action if the difference is significant.

The following steps need to be done for each transducer loaded with the system at the beginning of the scans:

- Determine the time trace offset (Section 4.3).
- Measure and record the UT speed in water (Section 9.2).
- Measure and record water temperature within 1-degree precision.

Steps below are to be done for both low-frequency (5 MHz) and high-frequency transducers with matching fused-quartz plate:

- Measure and record the UT speed in water (Section 9.2) when water quality/temperature changes significantly during the scans. Be sure to update the new water speed in FlexSCAN-C (under Edit->Configuration->couplant velocity).

- Measure and record water temperature within 1-degree precision when temperature changes significantly during the scans.
- Normalize transducer with respect to front surface using "ring wave" method (Section 3.4).
- Calculate the time-of-flight prediction of the front surface echo so that the *geometric focus* is set on the back surface (Section 9.2). Use the pre-determined plate thickness in the calculation.
- Manipulate FlexSCAN-C's digital scope to locate the front surface echo. Adjust waterpath until front surface echo appears at the predicted time instance as calculated in the last step. Be sure to account for the time trace offset if any (Sections 3.1 and 4.3, and Figure 3.1).
- Manipulate FlexSCAN-C's digital scope to display the back surface echo.
- Measure the time-of-flight of the back surface echo. Check measurements against the predictions. Make correction if necessary.
- Adjust both pulser/receiver's gain setting (or attenuation setting on Panametrics 505x series) and the A/D Gain setting in FlexSCAN-C's A/D 8100 window so that the peak back surface waveform is about at 80% full screen height. Also set the time scale of FlexSCAN-C's digital scope so that time resolution is sufficient (at least 20 time trace data points across the signal duration).
- Check and adjust the baseline offset (A/D offset in A/D 8100 window) if necessary (Section 4.3).
- Record all Sonix system settings. This can be done by properly arranging all FlexSCAN-C's setting windows on the screen and then print screen from File menu.
- Record all other experimental settings.
- Take single-shot a-scan waveform of back surface echo. The time average feature should be turned ON to reduce noise. Use highest average number available. A-scan waveform data is obtained by entering File -> Export … -> Scope to ASCII. Record peak-to-peak amplitude of the waveform.

7. Defect Data Acquisition

To ensure best data quality and minimal errors, it is advised to follow the steps below when acquiring the defect data. The defect depth in each side of the defect cube block should have been determined previously. The transducer should have been mounted on the angular manipulator, which is in turn attached to the search tube of the scan bridge.

The following steps need only to be done once for each new defect cube block:

- Measure and record the UT speeds of the defect cube block and check with the tabulated generic values (Section 9.3) if applicable. Take necessary action if the difference is significant.
- Measure and record the dimensions and weight of the defect cube block. Deduce the density accordingly and check with the tabulated generic value (Section 9.3) if applicable. Take necessary action if the difference is significant.

The following steps need to be done for each transducer loaded with the system at the beginning of the scans. This step can be skipped if it has been done in reference data acquisition.

- Measure and record the UT speed in water (Section 9.2).
- Measure and record water temperature within 1-degree precision.
- Determine the time trace offset (Section 4.3).
- Go to Edit -> Configuration -> Image Format to set c-scan format to Sonix proprietary format.

The steps below are to be done for both low-frequency (5 MHz) and high-frequency transducers. For each transducer, repeat the applicable steps on every accessible side of the cube block:

- Measure and record the UT speed in water (Section 9.2) when water quality/temperature changes significantly during the scans. Be sure to update the new water speed in FlexSCAN-C (under Edit->Configuration->couplant velocity).
- Measure and record water temperature within 1-degree precision when temperature changes significantly during the scans.
- Level the sample stand and set the defect cube block on the stand (Section 3.2).
- Maintain a consistent and precise orientation of the defect cube block with respect to the scan system coordinates (Section 3.3).
- Normalize transducer with respect to front surface of the defect cube block using "ring wave" method (Section 3.4).
- Calculate the time-of-flight prediction of the front surface echo so that the *true focus* is set on the nearest defect surface (Section 9.4). Calculate the prediction for the time-of-flight of defect signal from the pre-determined defect depth. Also calculate the prediction for the time-of-flight of back surface echo from the pre-determined cube dimensions.
- Manipulate FlexSCAN-C's digital scope to locate the front surface echo. Adjust waterpath until front surface echo appears at the predicted time instance. Be sure to account for the time trace offset if any (Section 4.3).
- Manipulate FlexSCAN-C's digital scope to locate the defect signal and back surface echo.
- Measure the time-of-flight of the defect signal and back surface echo. Check measurements against the predictions. Make correction if necessary.
- Adjust both pulser/receiver's gain (or attenuation on Panametrics 5052x series) setting and the A/D Gain setting in FlexSCAN-C's A/D 8100 window so that the maximum defect waveform is about at 80% full screen height (Section 9.5).
- Check and adjust the baseline offset (A/D offset in A/D 8100 window) if necessary (Section 4.3).
- Set proper time gate location and width for defect signal in FlexSCAN-C's Gate Control window. Make sure the sampling rate is at least 100 MHz (Section 9.5). Also turn on Front Follow gate (Sections 4.2 and 9.5).

- Record all Sonix system settings. This can be done by properly arranging all FlexSCAN-C's setting windows on the screen and then print screen from File menu.
- Record the cube block orientation drawing and all other experimental settings.
- Take single-shot a-scan waveform of defect at peak position with time average feature ON. This is done by entering File -> Export … -> Scope to ASCII. Record peak-to-peak amplitude of the defect waveform.
- Turn OFF time average feature (time averaging requires time-consuming multiple data acquisitions at the same scan which is not possible in high-speed scans such as c- or b-scans. The scan speed will be greatly compromised if this feature is not turned off).
- Go to Scan -> Scan Setup. Set all necessary parameters for c-scan. Make sure the scan and step increments are 5 mils for 5 MHz scan, and 2 mils for high-frequency scans, respectively (see example in Section 9.5).
- Go to Scan -> Scan Go to dry run c-scan data acquisition.
- Make changes such as scan sizes (pixels) in Scan Setup if necessary.
- Repeat last three steps until data quality criterion is met.
- Follow the last four steps to acquire b-scan data (see example in Section 9.5).

8. Key Parameter Calculations/Settings

In this section, the methods of calculation for all key parameters used in this procedure are given. In support of these calculations and clarification of the procedure contents, some key terms are first described. Examples of Sonix scan settings are also attached for future reference.

8.1 Key Terminology

Time-of-flight (TOF) in UT NDE is the round-trip time that ultrasound travels in a medium (or media) between transducer face and a point of interest, or between two points of interest. The horizontal time axis as seen on oscilloscope measures the time-of-flight of signals.

Waterpath is the distance between the transducer face and the front surface of the specimen in an immersion test.

Geometric and true focal lengths and equivalent diameter are the most important transducer parameters for a spherically focused transducer. Geometric focal length is the axial length (measured from the transducer face) as determined by geometric optics with respect to a given lens curvature. True focal length is the one most transducer specifications refer to, indicating the actual focal depth. Usually true focal length is shorter than geometric focal length. Equivalent diameter is the transducer size (diameter) produced by transducer characterization procedure, not necessarily the same as the manufacturer's specification.

Multiple-line B-scan takes an a-scan (waveform) at each scan position in a two-dimensional c-scan path. The results are three-dimensional a-scan data covering the volume being scanned.

8.2 UT speed in water

A simple measurement of the longitudinal-wave speed in water can be done by using two reference signals from a flat surface. In most cases, the front surface echoes are conveniently used as the reference signals. First normalize the transducer with respect to the flat surface (Section 3.4). Measure the TOF, T_1, of a reference point on the front surface echo, say, at the peak position. Secondly, move the transducer up or down a known distance, D, perpendicular to the flat surface. In a Sonix immersion system, this can be easily done by moving the motorized vertical scan bridge on which the transducer search tube attaches. The distance moved can be monitored in the Motor window in FlexSCAN-C. Next, measure the TOF, T_2, of the same peak reference point on the front surface echo at the new position. Finally, by simple physics of motion,

$$\text{water speed} = \frac{2D}{|T_2 - T_1|}$$

where | | means the absolute difference. For example, let D=2 inch=5.08cm, T_1=30 μs (microsecond; 1 μs =10^{-6} second) and T_2=98.65 μs then water speed = 0.148 cm/μs (0.0583 in/μs) which is typical for tap water at 70°F. This water speed should also match with the "couplant velocity" in FlexSCAN-C (accessed from Edit menu -> Configuration -> Couplant Velocity).

8.3 UT speeds in defect cube block/fused-quartz plate

Longitudinal-wave speed in cube block/fused-quartz plate can be measured similar to that in water. The difference is that the back surface echo taken from the defect cube block or fused-quartz plate (without moving the transducer up or down) replaces the second front surface echo in the case of water. For example, let the TOF of front surface be 20μs and TOF of back surface echo be 28.2 μs. From the above formula, the longitudinal-wave speed in a 1" Ti-6Al-4V cube block is 0.62 cm/μs. Shear-wave speed, however, requires the use of a shear-wave transducer measured in contact mode. One can take the first and the second bounces of the back surface echoes as the reference signals. If no shear-wave transducer is available, the values in Table 8.1 may be used.

Table 8.1 UT and material properties of several frequently used materials in ETC

Material	**Longitudinal-wave speed (cm/μs)**	**Shear-wave speed (cm/μs)**	**Density (g/cm^3)**
Water	0.148	NA	1.00
Ti-64	0.620	0.319	4.43
IN718	0.610	0.326	7.86
Fused-quartz	0.597	0.309	2.20

8.4 Waterpath

Given transducer focal lengths, wave-speeds in water and in the specimen, the correct waterpath and the corresponding TOF can be easily computed. Let the geometric and true focal lengths be F_g and F_t, respectively. Also denote longitudinal wave-speeds in water, fused-quartz and defect cube block as V_w, V_f, and V_s. For the reference experiment, the following formula applies:

$$F_g = Y_{r,w} + \frac{V_f}{V_w} Y_{r,s}$$

For the defect experiment, the parameters change slightly in the same formula:

$$F_t = Y_{d,w} + \frac{V_s}{V_w} Y_{d,s}$$

where the subscripted Y's are the waterpaths and specimen thickness/depths described in Section 3.1 and Figures 3.1 and 3.2. The corresponding TOF_r for the back surface echo (measured from beginning of the time trace) is the sum of TOF for front surface echo (also from beginning) and TOF for the back surface echo (measured after the front surface echo) in the reference experiment:

$$TOF_r = TOF_{r,w} + TOF_{r,s} = \frac{2Y_{r,w}}{V_w} + \frac{2Y_{r,s}}{V_s}$$

Likewise, TOF_d for the defect in the defect experiment is

$$TOF_d = TOF_{d,w} + TOF_{d,s} = \frac{2Y_{d,w}}{V_w} + \frac{2Y_{d,s}}{V_s}.$$

8.5 Examples of Sonix FlexSCAN-C scan settings

Figures 8.1 through 8.5 are the actual scan settings used in the first Ni real defect. Most settings should be suitable for future use except those specifics on transducer characteristics and defect size. Figures 8.1 and 8.2 are examples of the SCAN SETUP menu in Sonix FlexSCAN-C settings for low-frequency (5 MHz) and high-frequency c-scans, respectively. Figure 8.3 shows the SCAN SETUP menu for high frequency b-scan. Figures 8.4 and 8.5 are examples of screen snap shot of Sonix FlexSCAN-C showing the various settings for low-frequency (5 MHz) and high-frequency scans.

9. Further Contact

Questions/corrections/comments are welcome and should be forwarded to

C. Thomas Chiou (515)294-0299 cchiou@cnde.iastate.edu

Mike Keller (513)552-4643 mike_keller@geae.com

Jeff Umbach (561)796-6047 umbachj@pwfl.com

Andrei Degtyar (860)565-3987 degtyaa@pweh.com

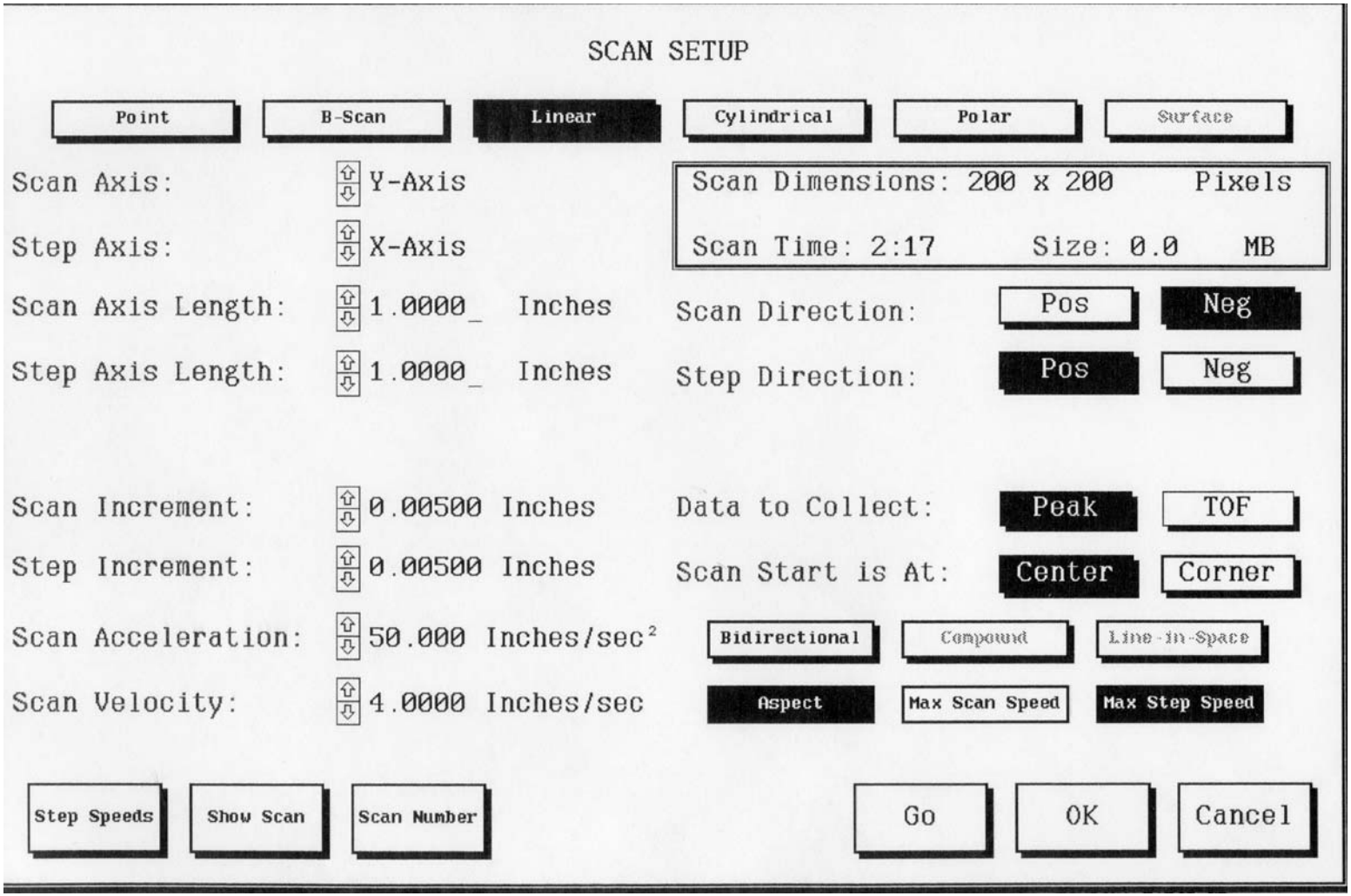

Figure 8.1 The SCAN SETUP menu in Sonix FlexSCAN-C for low-frequency (5 MHz) c-scan settings

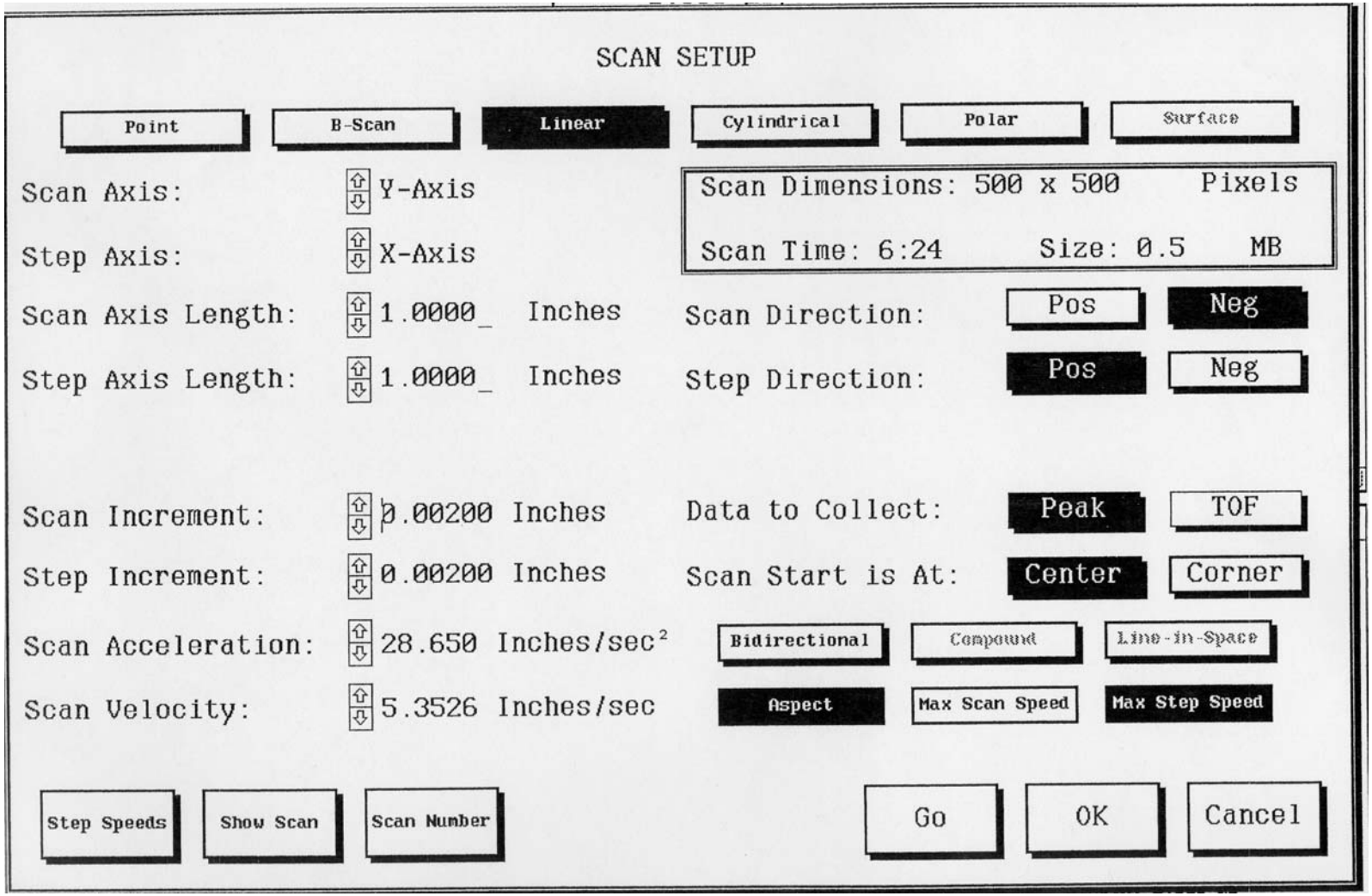

Figure 8.2 The SCAN SETUP menu in Sonix FlexSCAN-C for high frequency c-scan settings

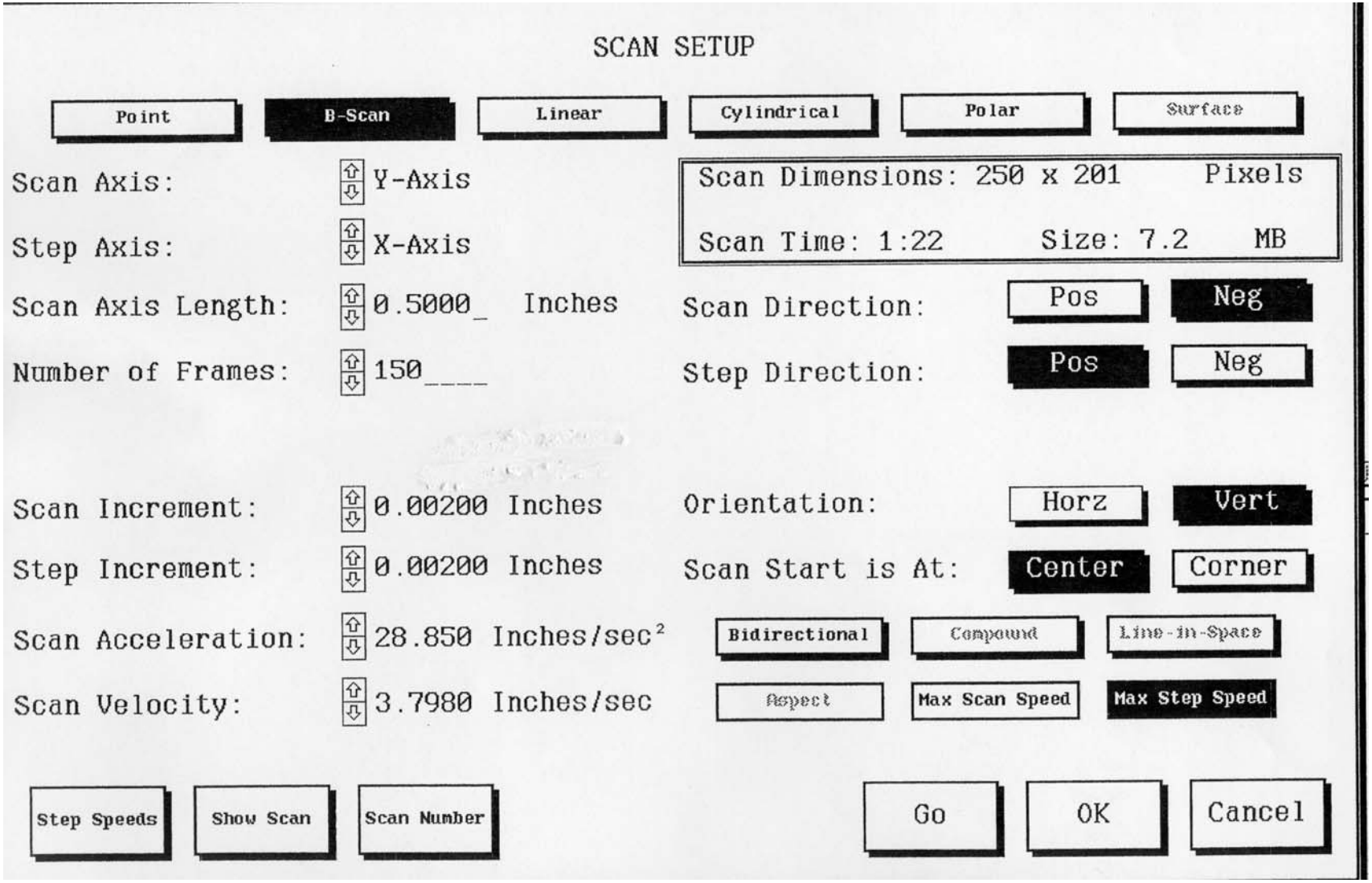

Figure 8.3 The SCAN SETUP menu in Sonix FlexSCAN-C for high frequency b-scan settings

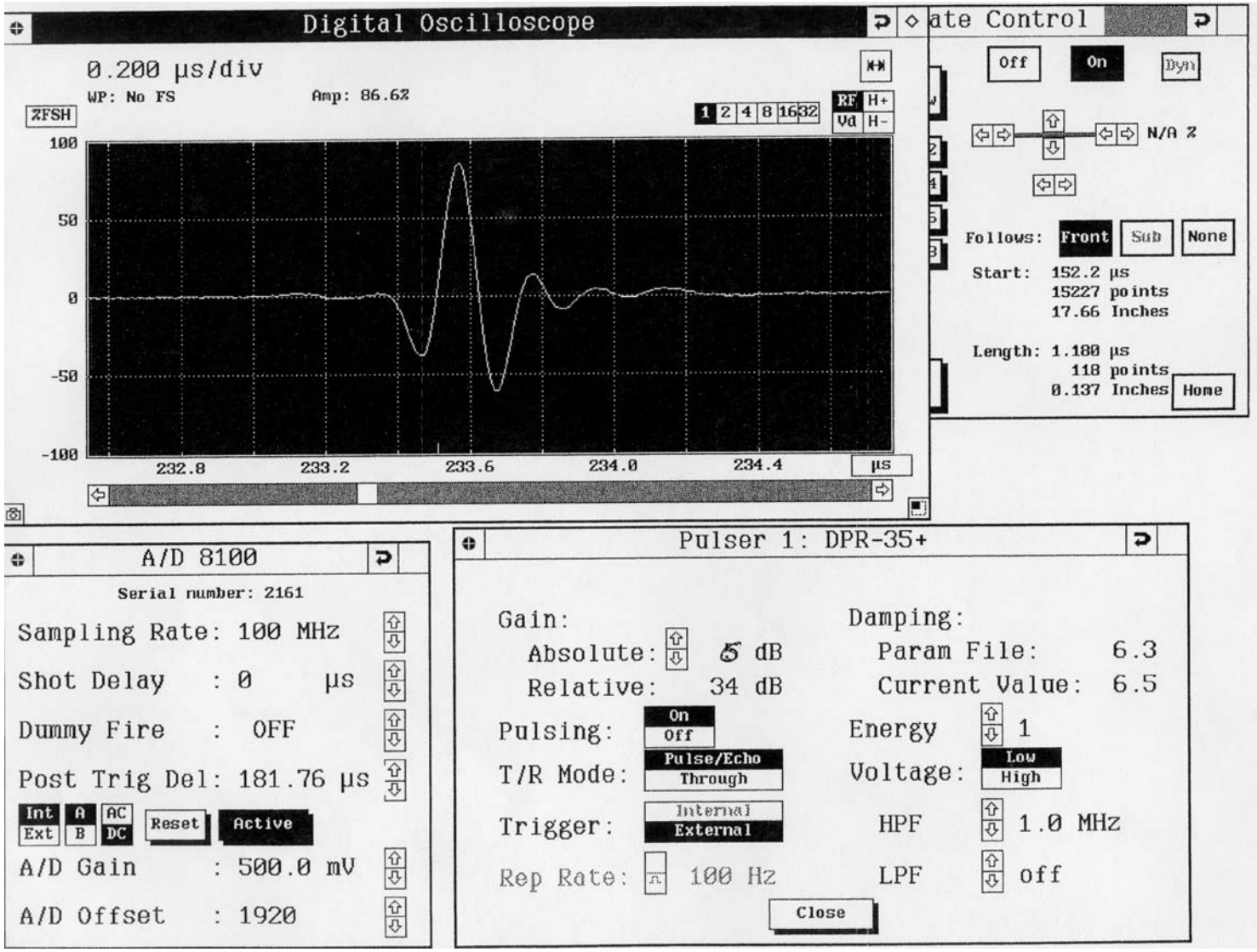

Figure 8.4 A screen snap shot of Sonix FlexSCAN-C shows the various settings for low-frequency (5 MHz) scan

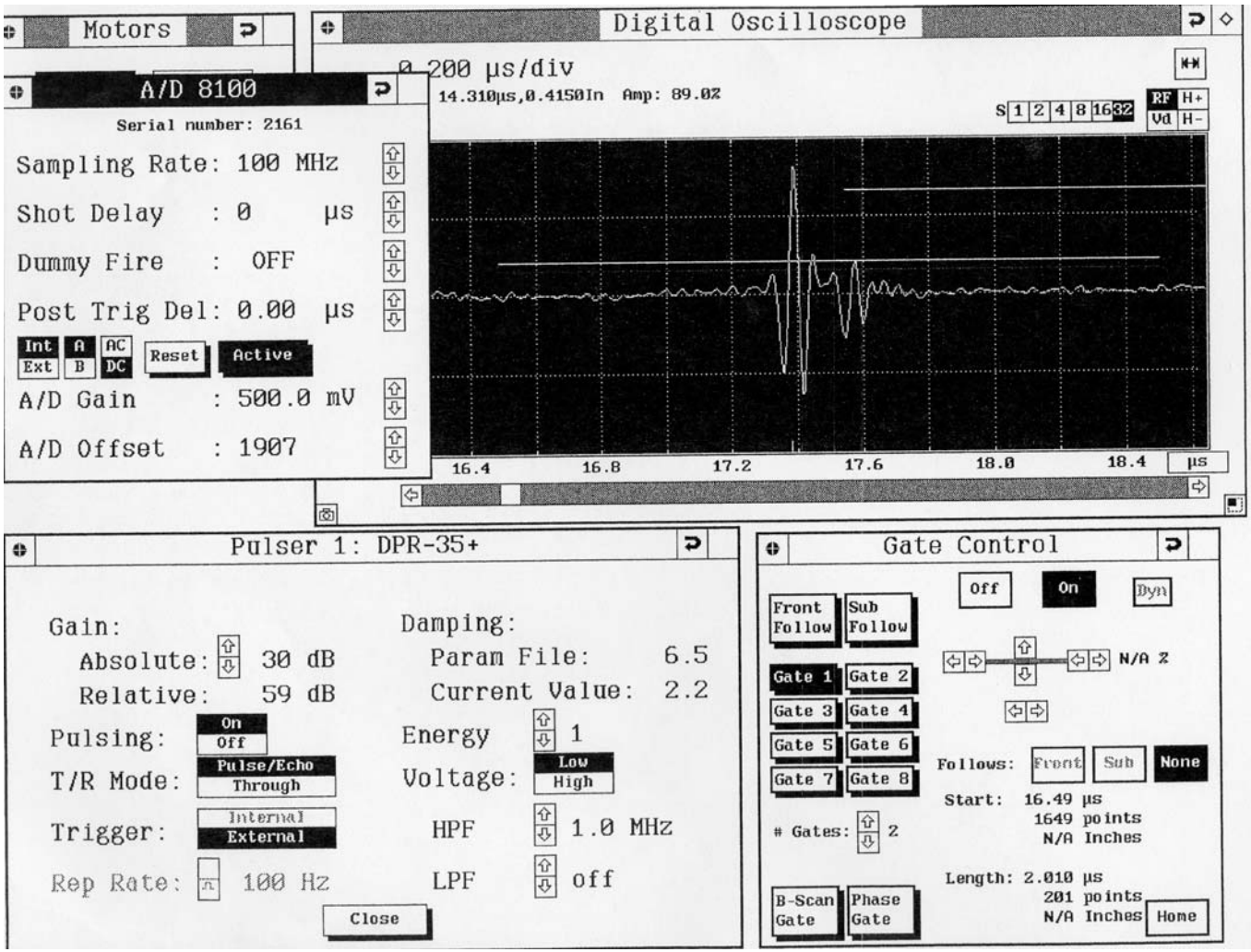

Figure 8.5 A screen snap shot of Sonix FlexSCAN-C shows the various settings for high-frequency scan

[1] Gray, T. A., "Application of Measurement Models to Specification of Ultrasonic Inspections", in Review of Progress in QNDE, Vol. 16B, edited by D. O. Thompson and D. E. Chimenti, Plenum, New York, 1997, pp. 2061-2068.